

**UC Davis**

**UC Davis Electronic Theses and Dissertations**

**Title**

Photooxidants in Aerosol Liquid Water: Organic Triplet Excited State, Hydroxyl Radical, and Singlet Molecular Oxygen

**Permalink**

<https://escholarship.org/uc/item/8xq5h3qf>

**Author**

Ma, Lan

**Publication Date**

2022

Peer reviewed|Thesis/dissertation

Photooxidants in Aerosol Liquid Water: Organic Triplet Excited State, Hydroxyl Radical, and Singlet Molecular Oxygen

By

LAN MA  
DISSERTATION

Submitted in partial satisfaction of the requirements for the degree of

DOCTOR OF PHILOSOPHY

in

Agricultural and Environmental Chemistry

in the

OFFICE OF GRADUATE STUDIES

of the

UNIVERSITY OF CALIFORNIA

DAVIS

Approved:

---

Cort Anastasio, Chair

---

Qi Zhang

---

Tran Nguyen

Committee in Charge

2022

## ABSTRACT

Atmospheric waters – including fog/cloud drops and aerosol liquid water (ALW) – are important sites for the transformations of atmospheric species and the formation of aqueous secondary organic aerosols (aqSOA). These chemical processes largely occur through reactions with photoformed oxidants such as hydroxyl radical ( $\bullet\text{OH}$ ), singlet molecular oxygen ( $^1\text{O}_2^*$ ), and oxidizing triplet excited states of organic matter ( $^3\text{C}^*$ ). Despite this, there are few measurements of these photooxidants, especially in extracts of ambient particles. Moreover, ALW – which has high solute concentrations – has great potential to produce aqSOA, but the chemistry in ALW is poorly understood. To address this gap, in this work we measured photooxidant concentrations and formation kinetics in dilute aqueous particle extracts and extrapolated the results to ALW conditions. We also studied the kinetics of triplet reactions with biomass burning phenols under ALW conditions.

In chapter 2, we investigated kinetics of six highly substituted phenols that are potentially important in ALW with the triplet excited state of 3,4-dimethoxybenzaldehyde. Second-order rate constants at pH 2 are all fast,  $(2.6\text{-}4.6) \times 10^9 \text{ M}^{-1} \text{ s}^{-1}$ , while values at pH 5 are 2-5 times smaller. Rate constants are reasonably described by a quantitative structure-activity relationship with phenol oxidation potentials. Triplet-phenol kinetics are unaffected by ammonium sulfate, sodium chloride, galactose (a biomass-burning sugar), or Fe(III). In contrast, ammonium nitrate increases the rate of phenol loss by making  $\bullet\text{OH}$ , while Cu(II) inhibits phenol decay. Our results suggest that phenols with high  $K_H$  can be an important source of aqSOA in ALW, with  $^3\text{C}^*$  typically the dominant oxidant.

In chapter 3, we evaluated how dissolved organic matter (DOM) and Cu(II) inhibit  $^3\text{C}^*$  probe decay, which can cause an underestimation of  $^3\text{C}^*$  concentrations. Our overarching goal is to find a triplet probe that has low inhibition by DOM and Cu(II), and low sensitivity to  $^1\text{O}_2^*$ . We tested 12 potential probes from a variety of compound classes and found that (phenylthiol)acetic acid (PTA) seems well suited for ALW

conditions, with mild inhibition and fast rate constants with triplets. We evaluated the performance of both PTA and syringol (SYR) as triplet probes in several aqueous extracts of particulate matter. While PTA is less sensitive to inhibition than SYR, it measures lower triplet concentrations, possibly because it is less sensitive to weakly oxidizing triplets.

In chapter 4, we measured photooxidant concentrations in illuminated aqueous particle extracts as a function of particle dilution and used the resulting oxidant kinetics to extrapolate to ALW conditions. Extracts were prepared from winter (WIN) and summer (SUM) particles from Davis, California. As particle mass gets more concentrated,  $\bullet\text{OH}$  concentrations in WIN remain relatively unchanged, while they increase in SUM. In both winter and summer samples,  $^3\text{C}^*$  concentrations increase rapidly with particle mass concentrations and then plateau under more concentrated conditions.  $^1\text{O}_2^*$  in WIN increases linearly with particle mass while in SUM it approaches a plateau. Under ambient aerosol liquid water conditions we predict a ratio of concentrations of  $^1\text{O}_2^* : ^3\text{C}^* : \bullet\text{OH}$  of  $10^3 - 10^2 : 10^2 : 1$  with  $\bullet\text{OH}$  concentrations on the order of  $10^{-14}$  M (including mass transport from the gas phase). Although  $\bullet\text{OH}$  is often considered the main sink for organic compounds in the aqueous phase, the much higher concentrations of  $^3\text{C}^*$  and  $^1\text{O}_2^*$  in aerosol liquid water suggest these photooxidants are more important sinks for many organics in particle water.

In chapter 5, we investigate the seasonal variation of photooxidants by measuring their concentrations in dilute aqueous extracts of ambient particles. Based on UV/Vis and aerosol mass spectrometer data, we categorized our 18 samples into four groups: Winter & Spring (Win-Spr) influenced by residential wood combustion; Summer & Fall (Sum-Fall) without wildfire influence; summer fresh biomass burning particles from wildfires (FBB), and aged biomass burning plumes (ABB). The concentration ratio of  $^1\text{O}_2^* : ^3\text{C}^* : \bullet\text{OH}$  in dilute particle extracts is  $(150 - 1500) : (10 - 300) : 1$ , respectively, while this ratio in ALW is predicted to be  $(100 - 1000) : (10 - 150) : 1$ . FBB has the highest mass absorption coefficient (MAC) and highest average  $^1\text{O}_2^*$  concentration but lowest average quantum yields ( $\Phi$ ) for

formation of all three photooxidants. Win-Spr and ABB have similar MAC and higher average  $\Phi$  of oxidants, indicating aging tends to enhance quantum yields. Sum-Fall has the lowest  $^1\text{O}_2^*$  due to low DOC, but highest  $\Phi_{1\text{O}_2^*}$ .  $^1\text{O}_2^*$  and  $^3\text{C}^*$  determined by SYR are linearly correlated with DOC and appear to be independent of sample type.

## ACKNOWLEDGMENTS

First and foremost, I wish to thank my advisor, Professor Cort Anastasio. I am very grateful that he offered me a great opportunity to explore the wonder of science and pursue my doctorate degree. His enthusiasm, inquisitiveness, and devotion on research has made great influence on me. He is always an extraordinary mentor, treating me with kindness, patience, and understanding. He taught me to how to be a good researcher, inspired me when I was in dilemma, and encouraged me when I was down. Thanks to his continuous support, I am able to accomplish this unforgettable journey. I have been so lucky to have worked with him.

A warm thanks to Professor Qi Zhang and Nguyen Tran, for their insights as both members of my qualifying exam and dissertation committees. I also thank the other members in my qualifying exam Professor Michael Kleeman and Anthony Wexler, for their valuable suggestions and guidance.

I thank the Anastasio group that also provide me with huge support: Ted Hullar, Alexander McFall, Stephanie Arciva, Aaron Lieberman, and Laura Heinlein, for their help with experimental training, resolving research problems, and fixing instruments. I also would like to express my gratitude to three undergraduate researchers who have worked with me over the last five years – Chrystal Guzman, Theodore Tran, and Reed Worland. Their intelligence and diligence provided high quality assistance, allowing me to work more efficiently. A warm thanks to Professor Qi Zhang’s group – Professor Qi Zhang, Wenqing Jiang and Christopher Niedek for their collaboration in chemical characterization of samples and insightful discussion and perspectives on my research. I also thank Dr. Keith Bein and people in Air Quality Research Center for their help with sample collection.

I thank all of my sources of fundings: The National Science Foundation, Donald G. Crosby Fellowship in Environmental Chemistry, and the Jastro Shields Research Award that have supported me over the last five years.

Finally, with my deepest gratitude, I thank my family for their endless and unconditional love, support, and belief in me. I thank them for understanding me and standing behind me all the time no matter what decisions I made. I also thank my friends for their constant listening, accompany, and encouragement. Special thanks to Rocky and Norman, two bunnies, who always cure me with their cuteness.

## Table of Contents

<b>ABSTRACT</b> .....	<b>ii</b>
<b>ACKNOWLEDGMENTS</b> .....	<b>v</b>
<b>Chapter 1: Introduction</b> .....	<b>1</b>
1.1. Overview.....	1
1.2. Publications associated with this dissertation .....	5
1.3. References.....	6
<b>Chapter 2: Kinetics and Mass Yields of Aqueous Secondary Organic Aerosol from Highly Substituted Phenols Reacting with a Triplet Excited State</b> .....	<b>11</b>
ABSTRACT.....	11
2.1. Introduction.....	11
2.2. Materials and Methods.....	14
2.2.1. Chemicals and Solutions.....	14
2.2.2. Solution Illumination and Chemical Analysis .....	14
2.2.3. Kinetic Analysis.....	15
2.2.4. SOA Mass Yields ( $Y_{\text{SOA}}$ ).....	16
2.2.5. Oxidation Potentials.....	17
2.3. Results and Discussions .....	17
2.3.1. Oxidation Kinetics of Phenols by the Triplet Excited State of DMB .....	17
2.3.2. aqSOA Mass Yields.....	20
2.3.3. Effect of Solutes.....	21
2.3.4. Quantitative Structure-Activity Relationships .....	23
2.4. Atmospheric Implications.....	24
2.5. Acknowledgment .....	26
2.6. Figures.....	27
2.7. Supporting Information.....	33
2.8. References.....	57
<b>Chapter 3: An Evaluation of Probes to Measure Oxidizing Organic Triplet Excited States in Aerosol Liquid Water</b> .....	<b>63</b>
ABSTRACT.....	63
3.1. Introduction.....	63
3.2. Materials and Methods.....	66
3.2.1. Chemicals, Illuminations, and Kinetic Analysis .....	66
3.2.2. Relative Rate Method.....	66



3.2.3.	Inhibition Factors .....	66
3.2.4.	Quantifying Oxidizing Triplet Excited States of Organic Matter in PM Extracts .....	67
3.3.	Results and Discussion .....	68
3.3.1.	Inhibition Effects on Triplet Probes in an Aerosol Water Mimic .....	68
3.3.2.	Screening Potential Triplet Probes.....	70
3.3.3.	Kinetic Study on PTA .....	73
3.3.4.	Dependence of $IF_{PTA}$ on SYR+Cu concentrations and EDC .....	74
3.4.	Determination of [ $^3C^*$ ] in PME using PTA as the triplet probe .....	76
3.5.	Acknowledgements.....	79
3.7.	Figures.....	80
3.8.	Supporting Information.....	87
3.9.	References.....	110

**Chapter 4: Predicting Photooxidant Concentrations in Aerosol Liquid Water Based on Laboratory Extracts of Ambient Particles ..... 116**

ABSTRACT.....	116
4.1. Introduction.....	117
4.2. Experimental Methods .....	119
4.2.1. Chemicals.....	119
4.2.2. Particle Collection and Extraction .....	120
4.2.3. Sample Illumination and Chemical Analysis.....	121
4.2.4. Photooxidant Measurements .....	122
4.2.4.1. Hydroxyl radical ( $\bullet OH$ ).....	122
4.2.4.2. Oxidizing triplet excited states of organic matter ( $^3C^*$ ).....	123
4.2.4.3. Singlet molecular oxygen ( $^1O_2^*$ ).....	125
4.3. Results and Discussions .....	126
4.3.1. Testing Extractions and Rotary Evaporation .....	126
4.3.2. Ions and Light Absorption .....	127
4.3.3. Photooxidants in PM Extracts.....	128
4.3.3.1. Hydroxyl radical in PM extracts .....	129
4.3.3.2. Oxidizing triplet excited states of organic matter in PM extracts .....	132
4.3.3.3. Singlet molecular oxygen in PM extracts .....	134
4.3.4. Extrapolating Photooxidant Concentrations to ALW Conditions.....	135
4.3.4.1. Hydroxyl radical in ALW .....	136
4.3.4.2. Oxidizing triplet concentrations in ALW.....	139
4.3.4.3. Singlet molecular oxygen in ALW .....	141

4.4.	Conclusion and Uncertainties .....	143
4.5.	Financial Support .....	145
4.6.	Supporting Information.....	146
4.7.	References.....	174
<b>Chapter 5: Seasonal variation of photooxidant formation in aqueous extracts of ambient particles.....</b>		<b>182</b>
	ABSTRACT.....	182
5.1.	Introduction.....	183
5.2.	Experimental Methods .....	186
5.2.1.	Chemicals.....	186
5.2.2.	Particle Collection and Extraction .....	187
5.2.3.	Sample Illumination and Chemical Analysis.....	188
5.2.4.	Photooxidant Measurements .....	188
5.2.4.1.	Hydroxyl radical ( $\bullet\text{OH}$ ).....	188
5.2.4.2.	Singlet molecular oxygen ( $^1\text{O}_2^*$ ).....	190
5.2.4.3.	Oxidizing triplet excited state of organic matter ( $^3\text{C}^*$ ) .....	191
5.3.	Results and Discussion .....	192
5.3.1.	General Extract Characteristics.....	192
5.3.2.	Light Absorption in Particle Extracts.....	194
5.3.3.	Photooxidant Concentrations .....	198
5.3.3.1.	Normalization by sample duration.....	198
5.3.3.2.	Hydroxyl radical ( $\bullet\text{OH}$ ).....	198
5.3.3.3.	Singlet molecular oxygen ( $^1\text{O}_2^*$ ).....	202
5.3.3.4.	Oxidizing triplet excited states of brown carbon ( $^3\text{C}^*$ ).....	204
5.3.3.5.	Normalization by photon flux .....	206
5.3.4.	Quantum Yields for Photooxidants.....	207
5.3.4.1.	Hydroxyl radical .....	207
5.3.4.2.	Singlet molecular oxygen.....	209
5.3.4.3.	Oxidizing triplet excited states.....	210
5.3.5.	Extrapolation of Photooxidant Concentrations to ALW Conditions .....	212
5.4.	Conclusions, Implications, and Uncertainties.....	215
5.5.	Acknowledgement .....	217
5.6.	Financial Support .....	217
5.7.	Supporting Information.....	218
5.8.	References.....	269

**Chapter 6: Conclusion..... 278**

# Chapter 1: Introduction

## 1.1. Overview

Airborne particulate matter (PM) is one of the most important air pollutants, which impacts human health as well as climate change.<sup>1-4</sup> Organic compounds are major components of fine PM, accounting for 20% – 90% of aerosol mass.<sup>5</sup> Organic aerosols can be directly emitted from sources, such as biomass burning, which is classified as primary organic aerosol (POA). They can also be formed from the oxidation of volatile organic compounds (VOCs) in the atmosphere, which is termed secondary organic aerosol (SOA).<sup>6,7</sup> Traditionally, SOA is considered to be formed from gas-phase reactions.<sup>8,9</sup> However, recent studies have shown that semivolatile compounds in the gas phase can partition into the aqueous phase, including cloud, fog drops and aerosol water, and then undergo reactions to form low-volatility compounds (aqueous SOA, aqSOA), which could represent a critical pathway for SOA production.<sup>10-12</sup> Aqueous reactions favorably form more oxygenated products such as organic acids (e.g. oxalate), oligomers, and organosulfates.<sup>13-16</sup> A number of laboratory studies have shown that aqSOA can be efficiently formed under cloud/fog water conditions and significant aqSOA production has been observed in field studies.<sup>16-21</sup> However, less is known about chemical processes in aerosol liquid water (ALW), the liquid phase on particles. Compared to cloud/fog water, the liquid water content of aerosols is several orders of magnitude lower, thus it contains very high concentration of inorganic and organic species.<sup>22-24</sup> These high concentrations might lead to enhanced reaction rates and can more efficiently produce high molecular-weight compounds and brown carbon.<sup>12,15,25-27</sup> Modeled rates of aqSOA formation in ALW vary enormously, likely because reactant concentrations and chemical processes in particle water are poorly understood<sup>13,28-30</sup>. Understanding the formation rates of aqSOA in ALW requires reaction rate constants, as well as concentrations of oxidants and precursors.

Common aqueous oxidants include hydroxyl radical ( $\bullet\text{OH}$ ), nitrate and sulfate radicals, as well as photochemically-formed oxidants.<sup>20,21</sup> We are interested in photooxidants include hydroxyl radical ( $\bullet\text{OH}$ ), oxidizing triplet excited states of organic compounds ( $^3\text{C}^*$ ), and singlet molecular oxygen ( $^1\text{O}_2^*$ ) that have been measured in fog water and aqueous particle extracts.<sup>31</sup>  $\bullet\text{OH}$  is the most widely studied oxidant, which has high reactivity, with near diffusion-controlled rate constants with most organics.<sup>20</sup> Measured concentrations of  $\bullet\text{OH}$  in fog and cloud waters, as well as aqueous extracts of ambient particle and SOA are typically  $10^{-17}$  to  $10^{-15}$  M.<sup>31-37</sup>

$^3\text{C}^*$  is a class of photooxidants that are formed when dissolved organic chromophores (i.e., brown carbon (BrC)) such as aromatic carbonyls absorb sunlight.<sup>38</sup> Oxidizing  $^3\text{C}^*$  can react with phenols and biogenic volatile compounds to form aqSOA, and oxidize sulfite to sulfate.<sup>39-43</sup> Though  $^3\text{C}^*$  is less reactive than  $\bullet\text{OH}$ , measured  $^3\text{C}^*$  concentrations in fog water and ambient particle extracts range from  $10^{-15}$  to  $10^{-13}$  M, 10-100 times higher than  $\bullet\text{OH}$ .<sup>31,44</sup> For compounds (like phenols) that react rapidly with triplets,  $^3\text{C}^*$  can be as important an oxidant as  $\bullet\text{OH}$  in cloud and fog drops.<sup>31,45,46</sup> Moreover,  $^3\text{C}^*$  concentrations are expected to be higher in ALW because its production rate increases with dissolved organic carbon,<sup>47,48</sup> although organic compounds can also be important sinks for  $^3\text{C}^*$ , suppressing its steady-state concentration.<sup>49,50</sup>

Most or all triplets also transfer energy to dissolved oxygen to form another important photooxidant, singlet molecular oxygen.  $^1\text{O}_2^*$  concentrations in fog/cloud drops and dilute extracts of ambient particles and lab SOA are higher than  $\bullet\text{OH}$  and  $^3\text{C}^*$ , typically  $10^{-14}$  to  $10^{-12}$  M.<sup>31,33,35,37,51,52</sup> Since BrC is the main source of  $^1\text{O}_2^*$ , its concentration in ALW is predicted to increase to  $10^{-10}$  M as BrC concentration gets enhanced in ALW in previous work.<sup>31</sup> Though  $^1\text{O}_2^*$  is generally less reactive than  $\bullet\text{OH}$  and  $^3\text{C}^*$ , it can react quickly with electron-rich compounds and might be a competitive oxidant in ALW for select species due to its high concentration. However, measurements of photooxidants in illuminated particle water or particulate matter extracts are very limited and little is known about their concentrations or kinetics in ALW.

California air quality is often impacted by biomass burning (BB), including residential wood combustion in winter and frequent wildfires in summer and fall. Phenols are one of the most abundant classes of organic compounds emitted from BB due to the combustion of lignin,<sup>53-55</sup> and it is an important precursor of SOA in BB air masses.<sup>56,57</sup> Phenols not only react with oxidants in the gas phase,<sup>58-61</sup> they also have medium to high Henry's law constants ( $K_H$ ,  $10^3$  to  $10^9$  M atm<sup>-1</sup>), leading to their partitioning into the aqueous phase, where they can be oxidized to form aqSOA.<sup>42,45,62,63</sup> Previous studies from our group found that fog/cloud water reactions can dominate the formation of phenolic SOA compared to gas-phase paths.<sup>42,45,64,65</sup> However, the photochemistry of phenols has rarely been explored under ALW conditions, which could be a missing source for SOA.

The overall goal of our project is to assess the significance of phenolic SOA formation in aerosol liquid water. Evaluating its importance requires knowledge of the second-order rate constants for reactions of phenols with oxidants, concentrations of phenols and oxidants, and aqSOA mass yields. This dissertation focuses on the reactions of phenols with a model atmospheric triplet excited state as well as photooxidant concentration measurements in aqueous particle extracts and extrapolation to ALW conditions.

Reactions between <sup>3</sup>C\* and three of the base structures of biomass burning phenols (phenol, guaiacol, and syringol) have been studied in the dilute aqueous phase in previous works from our group. These reactions have rate constants near diffusion-controlled and produce SOA efficiently, with aqSOA mass yield near 1.<sup>42,45,64</sup> However, these simple phenols with moderate  $K_H$  values will have very little fraction partitioning to ALW because of its low water content. Therefore, substituted phenols with higher  $K_H$  appear to be more abundant organic species in particle water. However, little is known about the reactions of these phenols with <sup>3</sup>C\*. In chapter 2, we select six highly substituted phenols observed in biomass burning, measure their rate constants with an organic triplet excited state, and develop a quantitative structure-activity relationship. We examine the impacts of molar concentrations of salts and a cellulose-derived sugar,

and trace amounts of transition-metal ions, on the triplet kinetics. We also determine aqSOA mass yields from the phenol-triplet reactions.

In chapter 3, we evaluate the suitability of triplet probes under aqueous particle extract conditions. It is difficult to quantify  $^3\text{C}^*$  concentrations from dissolved organic matter (DOM) because DOM represents a complex mixture with a wide range of reactivities, which leads to the formed  $^3\text{DOM}^*$  also vary in reactivities including triplet energy and redox potentials.<sup>38,66</sup> One way to measure oxidizing  $^3\text{C}^*$  concentrations is with an electron transfer probe, whose loss due to the oxidation by  $^3\text{C}^*$  can be monitored and used to quantify  $^3\text{C}^*$ .<sup>44,67</sup> The commonly used probes in surface water are electron-rich phenols. However, DOM can play dual roles: acting as a photosensitizer to form  $^3\text{C}^*$ , but also as an antioxidant that inhibits triplet-induced oxidation. The latter can lead to underestimates of  $^3\text{C}^*$  concentrations by inhibiting probe decay.<sup>68-70</sup> Though phenol probes can resist this inhibition effect in low-DOC surface waters,<sup>68,71</sup> it is unclear if they are impacted in concentrated particle extracts with high DOC. Also, since  $^1\text{O}_2^*$  in ALW can be a competitive photooxidant with  $^3\text{C}^*$ ,<sup>31</sup> a high rate constants with  $^3\text{C}^*$  but a low value with  $^1\text{O}_2^*$  is required for the triplet probe so that it is relatively resistant to oxidation by  $^1\text{O}_2^*$ . In chapter 3, we evaluate the suitability of 12 triplet probes under aqueous particle extract conditions. We examine the susceptibility of the probes for inhibition and measure rate constants for probes with  $^1\text{O}_2^*$  and a model atmospheric triplet to gauge probe specificity. We identify a good candidate probe for triplets and compare its performance to a phenol probe in illuminated particle extracts.

In chapters 4 and 5, we sampled  $\text{PM}_{2.5}$  particles from November 2019 to October 2020 in Davis, CA. We measure photooxidant concentrations in aqueous particle extracts and extrapolated our photooxidant kinetics to ALW conditions. Due to the limited water amount of ALW, it is difficult to study chemistry in ALW directly. Kaur et al. measured  $\cdot\text{OH}$ ,  $^3\text{C}^*$ , and  $^1\text{O}_2^*$  concentrations as well as production rates and sinks in particle extracts as a function of particle dilution and extrapolated the results to aqueous aerosol conditions.<sup>31</sup> However, there are large uncertainties with this extrapolation since the PM extracts she studied

were approximately 1000 times more dilute than ALW. In chapter 4, we revisit this approach and attempt to reduce the uncertainty with higher DOM concentrations in our particle extracts. Moreover, we study both a winter PM sample as well as summer wildfire particles to explore differences in oxidant kinetics.

In chapter 5, we categorize one year of particle samples into four main types: winter samples influenced by residential wood combustion and high humidity; summer samples impacted by fresh wildfires; summer samples impacted by aged wildfires; and spring/summer samples with little to no biomass burning influence. We measure photooxidant concentrations ( $\bullet\text{OH}$ ,  $^1\text{O}_2^*$ ,  $^3\text{C}^*$ ) in water extracts of the particles, and investigate how the formation of photooxidants varies with particle type and optical properties. We also predict photooxidant concentrations in ALW for each sample type.

## 1.2. Publications associated with this dissertation

As listed below, Chapter 2 is published, Chapter 3-5 are in preparation for submission.

1. Chapter 2: Ma, L.; Guzman, C.; Niedek, C.; Tran, T.; Zhang, Q.; Anastasio, C. Kinetics and Mass Yields of Aqueous Secondary Organic Aerosol from Highly Substituted Phenols Reacting with a Triplet Excited State. *Environ. Sci. Technol.* **2021**, *55*, 5772–5781.
2. Chapter 3: Ma, L.; Worland, R.; Tran, T.; Jiang, W.; Niedek, C.; Zhang, Q.; Anastasio, C. An evaluation of probes to measure oxidizing triplet excited states in aerosol liquid water. In preparation for *Environmental Science and Technology*, **2022**.
3. Chapter 4: Ma, L.; Worland, R.; Jiang, W.; Niedek, C.; Guzman, C.; Bein, K. J.; Zhang, Q.; Anastasio, C. Predicting photooxidant concentrations in aerosol liquid water based on laboratory extracts of ambient particles. In preparation for *Atmospheric Chemistry and Physics*, **2022**.
4. Chapter 5: Ma, L.; Worland, R.; Heinlein, L.; Guzman, C.; Jiang, W.; Niedek, C.; Bein, K. J.; Zhang, Q.; Anastasio, C. Seasonal variation in light absorption photooxidant formation in aqueous extracts of ambient particles. In preparation for *Atmospheric Chemistry and Physics*, **2022**.



### 1.3. References

- (1) Sommers, W. T.; Loehman, R. A.; Hardy, C. C. Wildland fire emissions, carbon, and climate: science overview and knowledge needs. *For. Ecol. Manag.* **2014**, *317*, 1–8.
- (2) Pöschl, U. Atmospheric aerosols: composition, transformation, climate and health effects. *Angew. Chem. Int. Ed.* **2005**, *44*, 7520–7540.
- (3) Hallquist, M.; Wenger, J. C.; Baltensperger, U.; Rudich, Y.; Simpson, D.; Claeys, M.; Dommen, J.; Donahue, N. M.; George, C.; Goldstein, A. H.; et al. The formation, properties and impact of secondary organic aerosol: current and emerging issues. *Atmos. Chem. Phys.* **2009**, *9*, 5155–5236.
- (4) Kampa, M.; Castanas, E. Human health effects of air pollution. *Environ. Pollut.* **2008**, *151*, 362–367.
- (5) Kanakidou, M.; Seinfeld, J. H.; Pandis, S. N.; Barnes, I.; Dentener, F. J.; Facchini, M. C.; Van Dingenen, R.; Ervens, B.; Nenes, A.; Nielsen, C. J.; et al. Organic aerosol and global climate modelling: a review. *Atmos. Chem. Phys.* **2005**, *5*, 1053–1123.
- (6) de Gouw, J.; Jimenez, J. L. Organic aerosols in the Earth's atmosphere. *Environ. Sci. Technol.* **2009**, *43*, 7614–7618.
- (7) Bond, T. C.; Streets, D. G.; Yarber, K. F.; Nelson, S. M.; Woo, J.; Klimont, Z. A technology-based global inventory of black and organic carbon emissions from combustion. *J. Geophys. Res. Atmos.* **2004**, *109*.
- (8) Odum, J. R.; Hoffmann, T.; Bowman, F.; Collins, D.; Flagan, R. C.; Seinfeld, J. H. Gas/particle partitioning and secondary organic aerosol yields. *Environ. Sci. Technol.* **1996**, *30*, 2580–2585.
- (9) Pankow, J. F. An absorption model of gas/particle partitioning of organic compounds in the atmosphere. *Atmos. Environ.* **1994**, *28*, 185–188.
- (10) Ervens, B.; Turpin, B. J.; Weber, R. J. Secondary organic aerosol formation in cloud droplets and aqueous particles (aqSOA): a review of laboratory, field and model studies. *Atmos. Chem. Phys.* **2011**, *11*, 11069–11102.
- (11) Blando, J. D.; Turpin, B. J. Secondary organic aerosol formation in cloud and fog droplets: a literature evaluation of plausibility. *Atmos. Environ.* **2000**, *34*, 1623–1632.
- (12) Lim, Y. B.; Tan, Y.; Perri, M. J.; Seitzinger, S. P.; Turpin, B. J. Aqueous chemistry and its role in secondary organic aerosol (SOA) formation. *Atmospheric Chemistry & Physics Discussions* **2010**, *10*.
- (13) Ervens, B. Progress and problems in modeling chemical processing in cloud droplets and wet aerosol particles. In *Multiphase environmental chemistry in the atmosphere*; Hunt, S. W.; Laskin, A.; Nizkorodov, S. A., Eds.; ACS Symposium Series; American Chemical Society: Washington, DC, 2018; Vol. 1299, pp. 327–345.
- (14) Shrivastava, M.; Cappa, C. D.; Fan, J.; Goldstein, A. H.; Guenther, A. B.; Jimenez, J. L.; Kuang, C.; Laskin, A.; Martin, S. T.; Ng, N. L.; et al. Recent advances in understanding secondary organic aerosol: Implications for global climate forcing. *Rev. Geophys.* **2017**, *55*, 509–559.
- (15) Tan, Y.; Lim, Y. B.; Altieri, K. E.; Seitzinger, S. P.; Turpin, B. J. Mechanisms leading to oligomers and SOA through aqueous photooxidation: insights from OH radical oxidation of acetic acid and methylglyoxal. *Atmos. Chem. Phys.* **2012**, *12*, 801–813.
- (16) Sareen, N.; Carlton, A. G.; Surratt, J. D.; Gold, A.; Lee, B.; Lopez-Hilfiker, F. D.; Mohr, C.; Thornton, J. A.; Zhang, Z.; Lim, Y. B.; et al. Identifying precursors and aqueous organic aerosol formation pathways during the SOAS campaign. *Atmos. Chem. Phys.* **2016**, *16*, 14409–14420.

- (17) Sullivan, A. P.; Hodas, N.; Turpin, B. J.; Skog, K.; Keutsch, F. N.; Gilardoni, S.; Paglione, M.; Rinaldi, M.; Decesari, S.; Facchini, M. C.; et al. Evidence for ambient dark aqueous SOA formation in the Po Valley, Italy. *Atmos. Chem. Phys.* **2016**, *16*, 8095–8108.
- (18) Gilardoni, S.; Massoli, P.; Paglione, M.; Giulianelli, L.; Carbone, C.; Rinaldi, M.; Decesari, S.; Sandrini, S.; Costabile, F.; Gobbi, G. P.; et al. Direct observation of aqueous secondary organic aerosol from biomass-burning emissions. *Proc. Natl. Acad. Sci. USA* **2016**, *113*, 10013–10018.
- (19) Yu, L.; Smith, J.; Laskin, A.; George, K. M.; Anastasio, C.; Laskin, J.; Dillner, A. M.; Zhang, Q. Molecular transformations of phenolic SOA during photochemical aging in the aqueous phase: competition among oligomerization, functionalization, and fragmentation. *Atmos. Chem. Phys.* **2016**, *16*, 4511–4527.
- (20) Herrmann, H.; Schaefer, T.; Tilgner, A.; Styler, S. A.; Weller, C.; Teich, M.; Otto, T. Tropospheric aqueous-phase chemistry: kinetics, mechanisms, and its coupling to a changing gas phase. *Chem. Rev.* **2015**, *115*, 4259–4334.
- (21) McNeill, V. F. Aqueous organic chemistry in the atmosphere: sources and chemical processing of organic aerosols. *Environ. Sci. Technol.* **2015**, *49*, 1237–1244.
- (22) Nguyen, T. K. V.; Zhang, Q.; Jimenez, J. L.; Pike, M.; Carlton, A. G. Liquid water: ubiquitous contributor to aerosol mass. *Environ. Sci. Technol. Lett.* **2016**, *3*, 257–263.
- (23) Parworth, C. L.; Young, D. E.; Kim, H.; Zhang, X.; Cappa, C. D.; Collier, S.; Zhang, Q. Wintertime water-soluble aerosol composition and particle water content in Fresno, California. *J. Geophys. Res. Atmos.* **2017**, *122*, 3155–3170.
- (24) Faust, J. A.; Wong, J. P. S.; Lee, A. K. Y.; Abbatt, J. P. D. Role of Aerosol Liquid Water in Secondary Organic Aerosol Formation from Volatile Organic Compounds. *Environ. Sci. Technol.* **2017**, *51*, 1405–1413.
- (25) Renard, P.; Reed Harris, A. E.; Rapf, R. J.; Ravier, S.; Demelas, C.; Coulomb, B.; Quivet, E.; Vaida, V.; Monod, A. Aqueous phase oligomerization of methyl vinyl ketone by atmospheric radical reactions. *J. Phys. Chem. C* **2014**, *118*, 29421–29430.
- (26) De Haan, D. O.; Jansen, K.; Rynaski, A. D.; Sueme, W. R. P.; Torkelson, A. K.; Czer, E. T.; Kim, A. K.; Rafla, M. A.; De Haan, A. C.; Tolbert, M. A. Brown Carbon Production by Aqueous-Phase Interactions of Glyoxal and SO<sub>2</sub>. *Environ. Sci. Technol.* **2020**, *54*, 4781–4789.
- (27) Xia, S.-S.; Eugene, A. J.; Guzman, M. I. Cross photoreaction of glyoxylic and pyruvic acids in model aqueous aerosol. *J. Phys. Chem. A* **2018**, *122*, 6457–6466.
- (28) Ervens, B.; Volkamer, R. Glyoxal processing by aerosol multiphase chemistry: towards a kinetic modeling framework of secondary organic aerosol formation in aqueous particles. *Atmos. Chem. Phys.* **2010**, *10*, 8219–8244.
- (29) Lin, G.; Sillman, S.; Penner, J. E.; Ito, A. Global modeling of SOA: the use of different mechanisms for aqueous-phase formation. *Atmos. Chem. Phys.* **2014**, *14*, 5451–5475.
- (30) Washenfelder, R. A.; Young, C. J.; Brown, S. S.; Angevine, W. M.; Atlas, E. L.; Blake, D. R.; Bon, D. M.; Cubison, M. J.; de Gouw, J. A.; Dusanter, S.; et al. The glyoxal budget and its contribution to organic aerosol for Los Angeles, California, during CalNex 2010. *J. Geophys. Res.* **2011**, *116*.
- (31) Kaur, R.; Labins, J. R.; Helbock, S. S.; Jiang, W.; Bein, K. J.; Zhang, Q.; Anastasio, C. Photooxidants from brown carbon and other chromophores in illuminated particle extracts. *Atmos. Chem. Phys.* **2019**, *19*, 6579–6594.
- (32) Dorfman, L. M.; Adams, G. E. *Reactivity of the hydroxyl radical in aqueous solutions*; 0 ed.; National Bureau of Standards: Gaithersburg, MD, 1973.

- (33) Manfrin, A.; Nizkorodov, S. A.; Malecha, K. T.; Getzinger, G. J.; McNeill, K.; Borduas-Dedekind, N. Reactive Oxygen Species Production from Secondary Organic Aerosols: The Importance of Singlet Oxygen. *Environ. Sci. Technol.* **2019**, *53*, 8553–8562.
- (34) Arakaki, T.; Anastasio, C.; Kuroki, Y.; Nakajima, H.; Okada, K.; Kotani, Y.; Handa, D.; Azechi, S.; Kimura, T.; Tsuchiko, A.; et al. A general scavenging rate constant for reaction of hydroxyl radical with organic carbon in atmospheric waters. *Environ. Sci. Technol.* **2013**, *47*, 8196–8203.
- (35) Kaur, R.; Anastasio, C. Light absorption and the photoformation of hydroxyl radical and singlet oxygen in fog waters. *Atmos. Environ.* **2017**, *164*, 387–397.
- (36) Tilgner, A.; Herrmann, H. Tropospheric Aqueous-Phase OH Oxidation Chemistry: Current Understanding, Uptake of Highly Oxidized Organics and Its Effects. In *Multiphase environmental chemistry in the atmosphere*; Hunt, S. W.; Laskin, A.; Nizkorodov, S. A., Eds.; ACS Symposium Series; American Chemical Society: Washington, DC, 2018; Vol. 1299, pp. 49–85.
- (37) Anastasio, C.; McGregor, K. G. Chemistry of fog waters in California's Central Valley: 1. In situ photoformation of hydroxyl radical and singlet molecular oxygen. *Atmos. Environ.* **2001**, *35*, 1079–1089.
- (38) McNeill, K.; Canonica, S. Triplet state dissolved organic matter in aquatic photochemistry: reaction mechanisms, substrate scope, and photophysical properties. *Environ. Sci. Process. Impacts* **2016**, *18*, 1381–1399.
- (39) Wang, X.; Gemayel, R.; Hayeck, N.; Perrier, S.; Charbonnel, N.; Xu, C.; Chen, H.; Zhu, C.; Zhang, L.; Wang, L.; et al. Atmospheric photosensitization: A new pathway for sulfate formation. *Environ. Sci. Technol.* **2020**, *54*, 3114–3120.
- (40) Rossignol, S.; Aregahegn, K. Z.; Tinel, L.; Fine, L.; Nozière, B.; George, C. Glyoxal induced atmospheric photosensitized chemistry leading to organic aerosol growth. *Environ. Sci. Technol.* **2014**, *48*, 3218–3227.
- (41) Monge, M. E.; Rosenørn, T.; Favez, O.; Müller, M.; Adler, G.; Abo Riziq, A.; Rudich, Y.; Herrmann, H.; George, C.; D'Anna, B. Alternative pathway for atmospheric particles growth. *Proc. Natl. Acad. Sci. USA* **2012**, *109*, 6840–6844.
- (42) Smith, J. D.; Sio, V.; Yu, L.; Zhang, Q.; Anastasio, C. Secondary organic aerosol production from aqueous reactions of atmospheric phenols with an organic triplet excited state. *Environ. Sci. Technol.* **2014**, *48*, 1049–1057.
- (43) González Palacios, L.; Corral Arroyo, P.; Aregahegn, K. Z.; Steimer, S. S.; Bartels-Rausch, T.; Nozière, B.; George, C.; Ammann, M.; Volkamer, R. Heterogeneous photochemistry of imidazole-2-carboxaldehyde: HO<sub>2</sub> radical formation and aerosol growth. *Atmos. Chem. Phys.* **2016**, *16*, 11823–11836.
- (44) Kaur, R.; Anastasio, C. First measurements of organic triplet excited states in atmospheric waters. *Environ. Sci. Technol.* **2018**, *52*, 5218–5226.
- (45) Smith, J. D.; Kinney, H.; Anastasio, C. Aqueous benzene-diols react with an organic triplet excited state and hydroxyl radical to form secondary organic aerosol. *Phys. Chem. Chem. Phys.* **2015**, *17*, 10227–10237.
- (46) Ma, L.; Guzman, C.; Niedek, C.; Tran, T.; Zhang, Q.; Anastasio, C. Kinetics and Mass Yields of Aqueous Secondary Organic Aerosol from Highly Substituted Phenols Reacting with a Triplet Excited State. *Environ. Sci. Technol.* **2021**, *55*, 5772–5781.
- (47) McCabe, A. J.; Arnold, W. A. Reactivity of Triplet Excited States of Dissolved Natural Organic Matter in Stormflow from Mixed-Use Watersheds. *Environ. Sci. Technol.* **2017**, *51*, 9718–9728.

- (48) Canonica, S.; Freiburghaus, M. Electron-rich phenols for probing the photochemical reactivity of freshwaters. *Environ. Sci. Technol.* **2001**, *35*, 690–695.
- (49) Wenk, J.; Eustis, S. N.; McNeill, K.; Canonica, S. Quenching of excited triplet states by dissolved natural organic matter. *Environ. Sci. Technol.* **2013**, *47*, 12802–12810.
- (50) Gemayel, R.; Emmelin, C.; Perrier, S.; Tomaz, S.; Baboornian, V. J.; Fishman, D. A.; Nizkorodov, S. A.; Dumas, S.; George, C. Quenching of ketone triplet excited states by atmospheric halides. *Environ. Sci.: Atmos.* **2021**, *1*, 31–44.
- (51) Faust, B. C.; Allen, J. M. Aqueous-phase photochemical sources of peroxy radicals and singlet molecular oxygen in clouds and fog. *J. Geophys. Res.* **1992**, *97*, 12913.
- (52) Li, M.; Bao, F.; Zhang, Y.; Sheng, H.; Chen, C.; Zhao, J. Photochemical aging of soot in the aqueous phase: release of dissolved black carbon and the formation of 1O<sub>2</sub>. *Environ. Sci. Technol.* **2019**, *53*, 12311–12319.
- (53) Oros, D. R.; Simoneit, B. R. Identification and emission factors of molecular tracers in organic aerosols from biomass burning Part 1. Temperate climate conifers. *Applied Geochemistry* **2001**, *16*, 1513–1544.
- (54) Schauer, J. J.; Kleeman, M. J.; Cass, G. R.; Simoneit, B. R. Measurement of emissions from air pollution sources. 3. C<sub>1</sub>-C<sub>29</sub> organic compounds from fireplace combustion of wood. *Environ. Sci. Technol.* **2001**, *35*, 1716–1728.
- (55) Simoneit, B. R.; Schauer, J. J.; Nolte, C. G.; Oros, D. R.; Elias, V. O.; Fraser, M. P.; Rogge, W. F.; Cass, G. R. Levoglucosan, a tracer for cellulose in biomass burning and atmospheric particles. *Atmospheric Environment* **1999**, *33*, 173–182.
- (56) Akherati, A.; He, Y.; Coggon, M. M.; Koss, A. R.; Hodshire, A. L.; Sekimoto, K.; Warneke, C.; de Gouw, J.; Yee, L.; Seinfeld, J. H.; et al. Oxygenated Aromatic Compounds are Important Precursors of Secondary Organic Aerosol in Biomass-Burning Emissions. *Environ. Sci. Technol.* **2020**, *54*, 8568–8579.
- (57) Bruns, E. A.; El Haddad, I.; Slowik, J. G.; Kilic, D.; Klein, F.; Baltensperger, U.; Prévôt, A. S. H. Identification of significant precursor gases of secondary organic aerosols from residential wood combustion. *Sci. Rep.* **2016**, *6*, 27881.
- (58) Yee, L. D.; Kautzman, K. E.; Loza, C. L.; Schilling, K. A.; Coggon, M. M.; Chhabra, P. S.; Chan, M. N.; Chan, A. W. H.; Hersey, S. P.; Crouse, J. D.; et al. Secondary organic aerosol formation from biomass burning intermediates: phenol and methoxyphenols. *Atmos. Chem. Phys.* **2013**, *13*, 8019–8043.
- (59) Zein, A. E.; Coeur, C.; Obeid, E.; Lauraguais, A.; Fagniez, T. Reaction Kinetics of Catechol (1,2-Benzenediol) and Guaiacol (2-Methoxyphenol) with Ozone. *J. Phys. Chem. A* **2015**, *119*, 6759–6765.
- (60) Coeur-Tourneur, C.; Cassez, A.; Wenger, J. C. Rate coefficients for the gas-phase reaction of hydroxyl radicals with 2-methoxyphenol (guaiacol) and related compounds. *J. Phys. Chem. A* **2010**, *114*, 11645–11650.
- (61) Lauraguais, A.; Coeur-Tourneur, C.; Cassez, A.; Deboudt, K.; Fourmentin, M.; Choël, M. Atmospheric reactivity of hydroxyl radicals with guaiacol (2-methoxyphenol), a biomass burning emitted compound: Secondary organic aerosol formation and gas-phase oxidation products. *Atmos. Environ.* **2014**, *86*, 155–163.
- (62) Sagebiel, J. C.; Seiber, J. N. Studies on the occurrence and distribution of wood smoke marker compounds in foggy atmospheres. *Environmental Toxicology and Chemistry: An International Journal* **1993**, *12*, 813–822.

- (63) Sun, Y. L.; Zhang, Q.; Anastasio, C.; Sun, J. Insights into secondary organic aerosol formed via aqueous-phase reactions of phenolic compounds based on high resolution mass spectrometry. *Atmos. Chem. Phys.* **2010**, *10*, 4809–4822.
- (64) Yu, L.; Smith, J.; Laskin, A.; Anastasio, C.; Laskin, J.; Zhang, Q. Chemical characterization of SOA formed from aqueous-phase reactions of phenols with the triplet excited state of carbonyl and hydroxyl radical. *Atmos. Chem. Phys.* **2014**, *14*, 13801–13816.
- (65) Smith, J. D.; Kinney, H.; Anastasio, C. Phenolic carbonyls undergo rapid aqueous photodegradation to form low-volatility, light-absorbing products. *Atmos. Environ.* **2016**, *126*, 36–44.
- (66) Schmitt, M.; Moor, K. J.; Erickson, P. R.; McNeill, K. Sorbic acid as a triplet probe: reactivity of oxidizing triplets in dissolved organic matter by direct observation of aromatic amine oxidation. *Environ. Sci. Technol.* **2019**, *53*, 8087–8096.
- (67) Rosario-Ortiz, F. L.; Canonica, S. Probe compounds to assess the photochemical activity of dissolved organic matter. *Environ. Sci. Technol.* **2016**, *50*, 12532–12547.
- (68) Wenk, J.; von Gunten, U.; Canonica, S. Effect of dissolved organic matter on the transformation of contaminants induced by excited triplet states and the hydroxyl radical. *Environ. Sci. Technol.* **2011**, *45*, 1334–1340.
- (69) Wenk, J.; Canonica, S. Phenolic Antioxidants Inhibit the Triplet-Induced Transformation of Anilines and Sulfonamide Antibiotics in Aqueous Solution. *Environ. Sci. Technol.* **2012**, *46*, 5455–5462.
- (70) Canonica, S.; Laubscher, H.-U. Inhibitory effect of dissolved organic matter on triplet-induced oxidation of aquatic contaminants. *Photochem. Photobiol. Sci.* **2008**, *7*, 547.
- (71) Wenk, J.; Aeschbacher, M.; Sander, M.; von Gunten, U.; Canonica, S. Photosensitizing and Inhibitory Effects of Ozonated Dissolved Organic Matter on Triplet-Induced Contaminant Transformation. *Environ. Sci. Technol.* **2015**, *49*, 8541–8549.

## Chapter 2: Kinetics and Mass Yields of Aqueous Secondary Organic Aerosol from Highly Substituted Phenols Reacting with a Triplet Excited State

This work has been published as: L. Ma, C. Guzman, C. Niedek, T. Tran, Q. Zhang, and C. Anastasio, *Environ. Sci. Technol.*, 2021, **55**, 5772–5781.

### ABSTRACT

Biomass burning emits large amounts of phenols, which can partition into cloud/fog drops and aerosol liquid water (ALW) and react to form aqueous secondary organic aerosol (aqSOA). Triplet excited states of organic compounds ( $^3C^*$ ) are a likely oxidant, but there are no rate constants with highly substituted phenols that have high Henry's law constants ( $K_H$ ) and are likely important in ALW. To address this gap, we investigated the kinetics of six highly substituted phenols with the triplet excited state of 3,4-dimethoxybenzaldehyde. Second-order rate constants at pH 2 are all fast,  $(2.6 - 4.6) \times 10^9 \text{ M}^{-1}\text{s}^{-1}$ , while values at pH 5 are 2 to 5 times smaller. Rate constants are reasonably described by a quantitative structure-activity relationship with phenol oxidation potentials, allowing rate constants of other phenols to be predicted. Triplet-phenol kinetics are unaffected by ammonium sulfate, sodium chloride, galactose (a biomass-burning sugar), or Fe(III). In contrast, ammonium nitrate increases the rate of phenol loss by making hydroxyl radical, while Cu(II) inhibits phenol decay. Mass yields of aqueous SOA from triplet reactions are large and range from 59 to 99%. Calculations using our data along with previous oxidant measurements indicate that phenols with high  $K_H$  can be an important source of aqSOA in ALW, with  $^3C^*$  typically the dominant oxidant.

### 2.1. Introduction

Airborne particulate matter (PM) impacts human health, visibility and climate.<sup>1-3</sup> One of the major components of PM is secondary organic aerosol (SOA), which is formed by oxidation of volatile organic

compounds in the gas phase followed with condensation, as well as in cloud/fog drops and possibly aerosol liquid water (ALW).<sup>4-6</sup> Biomass burning (BB) is a major source of PM<sup>7</sup> and releases large amounts of soluble, reactive gases that can form SOA.<sup>8</sup> One major class of these gases is phenols, which are emitted from the combustion of lignin, with an estimated global source strength of 4.7 Tg yr<sup>-1</sup>.<sup>9-12</sup> Three of the most abundant phenols emitted from BB are phenol (C<sub>6</sub>H<sub>5</sub>OH or PhOH), guaiacol (2-methoxyphenol), and syringol (2,6-dimethoxyphenol), which represent the base structures of BB phenols.<sup>10,11</sup> Besides being oxidized in the gas phase, these three species have moderate Henry's Law constants ( $K_H = 10^3 - 10^4$  M atm<sup>-1</sup> at 278 K),<sup>13-15</sup> enabling them to partition into cloud/fog drops where they can react with a number of aqueous oxidants to form aqSOA.<sup>6,16-19</sup>

Triplet excited states of organic compounds (<sup>3</sup>C\*) are a class of aqueous oxidants that are formed when light-absorbing organics (i.e., brown carbon) absorb sunlight.<sup>20</sup> Triplets can react with gas-phase alkenes to make additional PM mass at the surface of particles,<sup>21,22</sup> convert glyoxal into highly oxygenated compounds,<sup>23,24</sup> and oxidize SO<sub>2</sub> to sulfate.<sup>25</sup> While hydroxyl radical (•OH) is often considered the dominant oxidant for aqSOA formation,<sup>26</sup> triplets can be an important oxidant in fog and cloud water, in part because their concentrations are typically 10 – 100 times higher than •OH.<sup>27</sup> Moreover, triplet concentrations appear to be enhanced by a few orders of magnitude in aerosol water,<sup>28</sup> indicating a potentially major role in aqSOA formation in ALW.

Simple phenols react with triplets with rate constants near diffusion-controlled, and also react rapidly with •OH,<sup>16,19,29</sup> giving aqueous lifetimes of a few hours, comparable to gas-phase lifetimes.<sup>14,19</sup> These phenol-triplet reactions also efficiently form aqSOA, with mass yields in the range of 70 – 120%.<sup>16,19,30</sup> Compared with •OH oxidation in the gas phase, aqueous reactions in cloud/fog drops can dominate the formation of phenolic SOA.<sup>16,19</sup>

While a number of studies have investigated aqSOA formation under cloud and fog water conditions, less is known about SOA formation in ALW.<sup>31-33</sup> ALW is ubiquitous, with a mass often equivalent to (or

greater than) the dry particle mass,<sup>34</sup> but the amount of particle water (typically 1 – 100  $\mu\text{g m}^{-3}$ ) is orders of magnitude lower than that of fog/cloud drops.<sup>5,35</sup> Because of this, ALW contains very high concentrations of organic and inorganic species, which might affect reaction kinetics, including for aqSOA formation.<sup>31,36–38</sup>

The low water content of ALW leads to very limited partitioning of simple phenols to particle water; e.g., less than 0.001% of syringol will partition into the water phase for an ALW content of 100  $\mu\text{g m}^{-3}$ , an approximate upper bound for a wintertime aerosol in California’s Central Valley.<sup>38</sup> In contrast, highly substituted phenols have much higher  $K_H$  values and might be significant sources of aqSOA in ALW. For example, for the six BB phenols in Figure 2.1,<sup>9–11,39–41</sup> Henry’s law constants range from  $10^6$  to  $10^9$   $\text{M atm}^{-1}$  at 278 K,<sup>15</sup> corresponding to aqueous fractions of 2 to 58% for an ALW content of 100  $\mu\text{g m}^{-3}$ . In addition, the highly substituted phenols measured by Schauer *et al.* are abundant, together accounting for roughly 30 – 45% of total phenols emitted from wood burning.<sup>10</sup> Thus highly substituted phenols should be the dominant phenols in ALW, present at much higher levels than simple phenols. Despite this, the reactions of highly substituted phenols with triplet excited states to make aqSOA have not been examined and it is unclear whether the high solute concentrations in ALW affect these kinetics.

To assess the potential significance of these six highly substituted phenols as sources of aqSOA in ALW, we measure their rate constants with the triplet state of 3,4-dimethoxybenzaldehyde (DMB), which is present in biomass burning particles<sup>42</sup> and has a reactivity similar to ambient triplets in fog and PM in regions of significant wood combustion.<sup>27,28</sup> We also examine the impacts of molar concentrations of salts and a cellulose-derived sugar, and trace amounts of transition metal ions, on the triplet kinetics. We then determine SOA mass yields from these reactions and develop a quantitative structure-activity relationship between phenol oxidation potentials and second-order rate constants with the DMB triplet state. Finally, we calculate the gas- and aqueous-SOA formation rates for three model phenols to investigate their significance as sources of aqSOA and the dependence of this chemistry on liquid water content.



## 2.2. Materials and Methods

### 2.2.1. Chemicals and Solutions

Chemicals were used as received. 3,4-dimethoxybenzaldehyde (DMB) (99%), 4-hydroxy-3-methoxyphenylacetone (GA) (96%), 2-(4-hydroxyphenyl)ethanol (TYR) (98%), vanillyl alcohol (VAL) ( $\geq 98\%$ ), *trans*-ferulic acid (FA) (99%), syringic acid (SyrAcid) ( $\geq 95\%$ ), 2-nitrobenzaldehyde (2-NB) (98%), galactose ( $\geq 98\%$ ), ammonium sulfate ( $\geq 99\%$ ), ammonium nitrate ( $\geq 99\%$ ), Copper(II) sulfate pentahydrate ( $\geq 98\%$ ), Iron(III) chloride ( $\geq 97\%$ ), and sodium chloride ( $\geq 99\%$ ) were from Sigma-Aldrich. (3,5-Dimethoxy-4-hydroxyphenyl)acetone (syringyl acetone, SA) (82%) was synthesized by Carbosynth LLC. Sodium borate (ACS grade) and sulfuric acid (trace metal grade) were from Fisher Scientific. All chemical solutions were prepared using air-saturated ultrapure water (Milli-Q water) from a Milli-Q Advantage A10 system (Millipore;  $\geq 18.2$  M $\Omega$  cm) with an upstream Barnstead activated carbon cartridge.

Kinetic solutions contained 5 – 100  $\mu$ M of one phenol (ArOH), 10  $\mu$ M DMB, and either sulfuric acid or sodium borate to adjust pH to 2 or 5, respectively. In this work, we use the abbreviation “PhOH” to represent the compound phenol (C<sub>6</sub>H<sub>5</sub>OH), and the terms “phenol(s)” and “ArOH” to represent phenols more generally.

### 2.2.2. Solution Illumination and Chemical Analysis

Air-saturated solutions were illuminated in a stirred, airtight quartz cell (2-cm path length) (Spectrocell) at 20 °C. Samples were illuminated with a 1000 W Xenon arc lamp with a water filter, an AM1.0 air mass filter (AM1D-3L, Sciencetech), and a 295-nm long-pass filter (20CGA-295, Thorlabs) to simulate tropospheric sunlight. Dark control samples were wrapped in aluminum foil and kept in the same photoreactor chamber at 20 °C.

During illumination, aliquots were periodically removed from the illuminated and dark cells to measure concentrations of ArOH and DMB with HPLC (Supporting Information Table S2.1). Each

experiment day the photon flux was determined by measuring the photolysis rate constant ( $j_{2\text{NB,exp}}$ ) of a 10  $\mu\text{M}$  2-nitrobenzaldehyde (2NB) solution in a quartz cell identical to that used to illuminate the phenol solution.

### 2.2.3. Kinetic Analysis

The full description of the kinetic analysis is in Smith *et al.*<sup>19</sup> and only an abbreviated version is given here. The measured pseudo-first-order rate constant for phenol loss ( $k'_{\text{Light}}$ ) was determined as the negative of the slope from a linear fitting of  $\ln([\text{ArOH}]_t/[\text{ArOH}]_0)$  versus illumination time, where  $[\text{ArOH}]$  is the concentration of phenol (at time zero or time  $t$ ). Values of  $k'_{\text{Light}}$  were normalized to sunlight conditions at midday on the winter solstice at Davis (solar zenith =  $62^\circ$ ;  $j_{2\text{NB,win}} = 0.0070 \text{ s}^{-1}$ )<sup>43</sup> and corrected for internal light screening:

$$k'_{\text{ArOH}} = \left[ \frac{k'_{\text{Light}}}{S_\lambda \times j_{2\text{NB,exp}}} \right] \times j_{2\text{NB,win}} \quad (2.1)$$

where  $k'_{\text{ArOH}}$  is the normalized first-order rate constant,  $S_\lambda$  is the internal light screening factor, and  $j_{2\text{NB,exp}}$  is the measured rate constant of 2NB loss. Protonated  $^3\text{DMB}^*$  (HT) has a  $\text{p}K_a$  of 3.3 and a higher reactivity than its neutral form (T).<sup>19</sup> Therefore, we performed kinetic experiments at pH 2 (where 95% of  $^3\text{DMB}^*$  is in the protonated form and the apparent first-order rate constant for phenol loss ( $k'_{\text{ArOH}}$ ) is essentially  $k'_{\text{HT}}$ ) and pH 5 (where the neutral form represents 98% of  $^3\text{DMB}^*$  and  $k'_{\text{ArOH}}$  is equal to  $k'_T$ ).

As described in Smith *et al.*,<sup>19</sup> the rate constant of phenol loss is a function of the triplet source and sinks:

$$k'_{\text{ArOH}} =$$

$$\frac{1}{\left( \frac{k_{\text{O}_2+^3\text{DMB}^*}[\text{O}_2] + k'_{^3\text{DMB}^*}}{j_{\text{hv,abs}}\Phi_{\text{ISC}}[\text{DMB}] \times k_{\text{ArOH}+^3\text{DMB}^*}} + \frac{k_{\text{ArOH}+^3\text{DMB}^*} + k_Q}{j_{\text{hv,abs}}\Phi_{\text{ISC}}[\text{DMB}] \times k_{\text{ArOH}+^3\text{DMB}^*}} [\text{ArOH}] \right)} \quad (2.2)$$

Here,  $k_{O_2+{}^3DMB^*}$  is the bimolecular rate constant for reaction of  ${}^3DMB^*$  with dissolved  $O_2$ ,  $k'_{{}^3DMB^*}$  is the first-order rate constant for relaxation of  ${}^3DMB^*$  to the ground state,  $j_{hv,abs}$  is the rate constant for light absorption by DMB under Davis winter solstice conditions,  $\Phi_{ISC}$  is the intersystem crossing quantum yield,  $[DMB]$  is the concentration of DMB,  $k_{ArOH+{}^3DMB^*}$  is the second-order rate constant for ArOH reacting with  ${}^3DMB^*$ , and  $k_Q$  is the second-order rate constant for quenching of  ${}^3DMB^*$  by ArOH without loss of ArOH. Equation 2.2 can be simplified and inverted to:

$$\frac{1}{k'_{ArOH}} = a + b[ArOH] \quad (2.3)$$

To determine  $k_{ArOH+{}^3DMB^*}$ , we fitted our data of  $k'_{ArOH}$  versus  $[ArOH]$  to this equation to obtain values of  $a$  and  $b$ , and then used measured or estimated values for the other parameters in Eq. 2 (see Table S2.2) to calculate  $k_{ArOH+{}^3DMB^*}$ .

To test if phenols undergo significant direct photodegradation, solutions containing 5 – 100  $\mu\text{M}$  of one phenol were illuminated in the absence of DMB. For the three phenols with direct photodegradation (FA, SyrAcid, SA), we corrected their first-order rate constants with  ${}^3DMB^*$  by determining the rate constants for photodecay and subtracting these contributions from the triplet results (Section S2.1).

#### 2.2.4.SOA Mass Yields ( $Y_{SOA}$ )

aqSOA mass yields were determined by illuminating a solution containing 100  $\mu\text{M}$  phenol and 10  $\mu\text{M}$  DMB at pH 5 until approximately 88% of the phenol had reacted (i.e., until three half-lives was reached). For phenols with direct photodegradation, we instead used 50  $\mu\text{M}$  phenol and 10  $\mu\text{M}$  DMB. Aliquots were taken at time zero and at one, two, and three phenol half-lives (i.e.  $t_{1/2}$ ,  $2t_{1/2}$ , and  $3t_{1/2}$ ) and were analyzed by HPLC and High Resolution Time-of-Flight Aerosol Mass Spectrometry (HR-ToF-AMS).<sup>17,30,44</sup> Prior to AMS analysis, samples were spiked with known amounts of ammonium sulfate as an internal standard and were atomized using a constant output atomizer (TSI, Model 3076) with argon as the carrier gas. The

resulting aerosol was then dried in a diffusion drier before being sampled in the AMS. The evaporation of semi-volatile compounds during the aerosolization and drying process will not introduce significant biases in aqSOA mass yield analysis based on previous studies.<sup>17,30</sup> Mass spectra up to  $m/z$  400 were acquired. Each sample was run twice on AMS and data were analyzed using the standard analysis software (SQUIRREL v1.62F and PIKA v1.22F).<sup>17,30</sup> The SOA mass concentration was calculated from the measured organic mass after subtracting the contribution from the unevaporated phenol precursor. The aqSOA mass yield in each sample was calculated by:

$$Y_{SOA} = \frac{SOA \text{ mass formed}}{\text{mass of phenol reacted}} \quad (2.4)$$

More details are provided in the Supporting Information Section S2.2.

### **2.2.5. Oxidation Potentials**

We determined oxidation potentials for the loss of one electron for the six phenols studied here (Figure 2.1) as well as for PhOH, guaiacol, syringol, catechol, hydroquinone, and resorcinol. Values were both measured by cyclic voltammetry (CV) and computed using Gaussian; details are in Supporting Information Section S2.3.

## **2.3. Results and Discussions**

### **2.3.1. Oxidation Kinetics of Phenols by the Triplet Excited State of DMB**

To determine the second-order rate constant for a phenol with  $^3\text{DMB}^*$ , we measure the first-order phenol decay rate constant ( $k'_{\text{ArOH}}$ ) as a function of initial phenol concentration at pH 2 and 5. In illuminated samples, all phenols follow pseudo-first-order decay (e.g., Figure S2.2) and the loss of DMB is insignificant (less than 5%). In dark controls there is no significant loss of phenol or DMB. GA, TYR, and VAL show negligible direct photodegradation over our illumination periods, while direct photodegradation of FA, SA,

and SyrAcid contributes 3% – 34% of the phenol loss measured in the presence of DMB; we correct for this loss in our calculations of the triplet rate constants (Section S2.1). In addition, *trans*-FA undergoes photoisomerization to form *cis*-FA, reaching a photostationary state of the two isomers within 10 min of illumination (see Section S2.4 of the Supporting Information). As shown in Figure S2.2, GA decay at 5 °C is not statistically different from that at 20 °C, indicating no significant temperature dependence of the triplet-phenol reactions, consistent with past work.<sup>19</sup>

The apparent first-order decay rate constant of phenols with <sup>3</sup>DMB\* ( $k'_{\text{ArOH}}$ ), which is the product of the second-order rate constant for phenol with <sup>3</sup>DMB\* ( $k_{\text{ArOH}+\text{3DMB}^*}$ ) and [<sup>3</sup>DMB\*], decreases with increasing initial phenol concentration (Figure S2.5). This is because a higher phenol concentration increases the sink for <sup>3</sup>DMB\*, reducing the triplet steady-state concentration. Thus  $1/k'_{\text{ArOH}}$  increases with increasing phenol concentration. Equation 2.3 is used to fit these data (Figure S2.5) to obtain the regression parameters (Table S2.3), and then  $k_{\text{ArOH}+\text{3DMB}^*}$  is derived from Equation 2.2 with parameters shown in Table S2.2.

Measured second-order rate constants for reactions of phenols with <sup>3</sup>DMB\* are shown in Figure 2.2 and Table S2.4. The rate constants are all rapid, especially at pH 2 where values of  $k_{\text{ArOH}+\text{HT}}$  are in the range of  $(2.6 - 4.6) \times 10^9 \text{ M}^{-1} \text{ s}^{-1}$ . At pH 5, corresponding values of  $k_{\text{ArOH}+\text{T}}$  are 1.6 to 5.4 times lower and more variable among phenols, with a range of  $(0.29 - 2.7) \times 10^9 \text{ M}^{-1} \text{ s}^{-1}$ , showing that the protonated form of <sup>3</sup>DMB\* ( $\text{p}K_{\text{a}} 3.3$ ) is more reactive than its neutral form.<sup>19,20</sup> TYR (a derivative of PhOH) has the slowest rate constant with <sup>3</sup>DMB\*, while SA (a derivative of syringol, i.e., 2,6-dimethoxyphenol) has the highest rate constant among our six phenols. These results are consistent with previous findings that methoxy substitution enhances rate constants by donating electron density to the aromatic ring, activating the phenol.<sup>19,45</sup>

Phenolic hydroxyl groups typically have  $\text{p}K_{\text{a}}$  values around 10.<sup>46</sup> Therefore, for the phenols we studied (Figure 2.1), there is no significant deprotonation of the phenolic hydrogen and the compounds are

in the neutral form at both pH 2 and pH 5. However, FA and SyrAcid also have carboxylic acid groups, which have  $pK_a$  values of 4.6 and 4.2, respectively.<sup>47</sup> At pH 2, the mole fractions for the neutral forms of FA (HFA) and SyrAcid (SyrCOOH) are greater than 99%. However, at pH 5, FA and SyrAcid will mostly dissociate so that the neutral forms are minor and more than 70% of each species is present as the conjugate base ( $FA^-$  or  $SyrCOO^-$ ). Therefore, the apparent first-order reaction rate constants of FA and SyrAcid with  $^3DMB^*$  at pH 5 represent the reactivity of a mixture of the neutral and ion (carboxylate) forms of the phenols. Through these first-order rate constants, we calculate the second-order rate constants for the neutral and ion forms (Section S2.5). At pH 5, the rate constants of the  $FA^-$  isomers are statistically indistinguishable from zero ( $0.31 (\pm 0.36) \times 10^9 \text{ M}^{-1}\text{s}^{-1}$  for *trans*-FA and  $0.29 (\pm 0.36) \times 10^9 \text{ M}^{-1}\text{s}^{-1}$  for *cis*-FA), while the rate constant for HFA is rapid,  $2.1 (\pm 0.54) \times 10^9 \text{ M}^{-1}\text{s}^{-1}$  for both isomers. For syringic acid the reactivities of the neutral and carboxylate forms at pH 5 are statistically indistinguishable:  $2.2 (\pm 0.64) \times 10^9 \text{ M}^{-1}\text{s}^{-1}$  for  $SyrCOO^-$  and  $1.8 (\pm 0.44) \times 10^9 \text{ M}^{-1}\text{s}^{-1}$  for SyrCOOH.

We also use the fitted regression parameter ‘ $b$ ’ in Equation 2.3 to determine the fraction of phenol interacting with  $^3DMB^*$  that leads to reaction (i.e., oxidation of phenol to form products) rather than quenching  $^3DMB^*$  without phenol loss:

$$f_{reaction} = \frac{k_{ArOH+^3DMB^*}}{k_{ArOH+^3DMB^*} + k_Q} = \frac{1}{b \times j_{hv,DMB} \Phi_{ISC}[DMB]} \quad (2.5)$$

Values of  $k_Q$  are calculated from parameters ‘ $a$ ’ and ‘ $b$ ’ and are shown in Table S2.4. For most of our six phenols,  $k_Q$  has the same order of magnitude as  $k_{ArOH+^3DMB^*}$ , which is consistent with past work on methylphenols and methoxyphenols with other triplets.<sup>16,48</sup> The range of  $f_{reaction}$  values for our phenols is 0.20 – 0.88 at pH 2 and 0.09 – 0.98 at pH 5 (Table S2.4). For all of the phenols except for SA,  $f_{reaction}$  at pH 2 is higher than that at pH 5, by an average factor of 2.9. For TYR at pH 5, which has a slow rate constant of oxidation by  $^3DMB^*$ , the reaction fraction is only 0.09, i.e., 91% of the TYR -  $^3DMB^*$  interaction leads to  $^3DMB^*$  quenching but not TYR loss. This result is similar to other research, which observed that PhOH

(C<sub>6</sub>H<sub>5</sub>OH) at pH 8 has an oxidation rate about ten times lower than the quenching rate with triplet.<sup>48</sup> There are at least two mechanisms by which the <sup>3</sup>DMB\*-phenol interaction could lead to no phenol loss. One possibility is that the triplet oxidizes the phenol to make a phenoxy radical, but then this radical is reduced (e.g., by superoxide or hydroperoxyl radical) to regenerate the parent phenol, resulting in no apparent reaction.<sup>48,49</sup> In the case of FA, where  $f_{\text{reaction}}$  is low ( $\leq 0.20$ ) we suspect that another mechanism is important: energy transfer from <sup>3</sup>DMB\* resulting in reversible isomerization of FA. This is what occurs between triplets and sorbic acid,<sup>50</sup> with the resulting isomerization used as a probe to quantify triplet concentrations.<sup>50,51</sup>

### 2.3.2.aqSOA Mass Yields

Aqueous triplet reactions of simple phenols (e.g., PhOH, guaiacol, and syringol) efficiently form low-volatility products, with significant aqSOA yields.<sup>16,19,30</sup> Here we investigate whether triplet reactions with highly-substituted phenols (Figure 2.1) also produce significant amounts of aqSOA, by illuminating solutions containing a phenol and DMB and measuring the aqSOA mass with AMS.

Figure S2.6 shows the SOA mass yields at one, two, and three half-lives for each phenol, i.e., after 50%, 75%, and 88% of the initial phenol has reacted. For a given compound, the yields are typically very similar at all three time points and between duplicates, so for each phenol we calculated the average mass yield from all six data points, except for FA, where an outlier was removed. As shown in Figure 2.3, aqSOA mass yields are generally high, in the range of 59% – 99%, and with an overall average ( $\pm 1 \sigma$ ) of 83 ( $\pm 14$ )%. This result is comparable to the results in Smith *et al.*, where aqSOA mass yields from PhOH, guaiacol and syringol reacting with <sup>3</sup>DMB\* are near 100%.<sup>19</sup> These aqueous yields are significantly higher than  $Y_{\text{SOA}}$  values from gaseous phenol reactions with •OH, which are in the range of 10 – 50%.<sup>52,53</sup> An early step in the aqueous triplet oxidation of a phenol forms phenoxy radicals, which couple to produce low volatility oligomers,<sup>30,44,48</sup> in contrast to gas-phase reactions with •OH, which favor fragmentation of aromatic rings to form more volatile products.<sup>30,52</sup>

### 2.3.3. Effect of Solutes

Unlike relatively dilute cloud or fog drops, particle water typically contains very high concentrations of inorganic and organic solutes, with ionic strengths typically of several molar.<sup>38,54,55</sup> The high ionic strength in ALW might affect triplet kinetics, based on past work showing that seawater concentrations of halides inhibit electron transfer of triplet excited states of natural organic matter.<sup>56,57</sup> However, the effect of ALW-relevant solutes on triplet kinetics has been largely overlooked. Ammonium nitrate, ammonium sulfate, and sodium chloride are common salts in atmospheric aerosols, as are cellulose-derived sugars from biomass burning such as levoglucosan and galactose (a hydrolyzed isomer of levoglucosan).<sup>58</sup> Also, transition metal ions, Fe(III) and Cu(II), can be important drivers of atmospheric aqueous chemistry through redox cycling.<sup>59</sup> Dissolved Fe concentrations vary from  $10^{-9}$  to  $10^{-4}$   $\mu\text{M}$  in cloud/fog water, while copper concentrations are generally 10 times lower.<sup>60</sup> Their concentrations are enhanced in aerosol water but little is known of their effects on triplet kinetics. To study the impacts of these solutes and metals on triplet kinetics, we illuminated solutions containing 10  $\mu\text{M}$  GA (the model phenol), 10  $\mu\text{M}$  DMB, and varying concentrations of one solute or metal, and determined the pseudo-first-order rate constant of GA decay ( $k'_{\text{GA}}$ ). The ratio of the GA decay rate constant with solute addition to the rate constant without solute (i.e., the ratio  $k'_{\text{GA,solute}}/k'_{\text{GA,0}}$ ) was then calculated.

As shown in Figure 2.4, 0.5 M ammonium nitrate increases the rate constant for GA loss significantly, by a factor of over 20 compared with no  $\text{NH}_4\text{NO}_3$  (after correction for light screening by ammonium nitrate). The DMB loss rate also increases with higher concentrations of  $\text{NH}_4\text{NO}_3$  (Figure S2.7). These impacts are because  $\text{NO}_3^-$  photolysis forms  $\bullet\text{OH}$ ,<sup>61,62</sup> which reacts with GA and DMB. To determine if ionic strength makes any contribution to the enhanced decay rate constant in the presence of salts, we next used ammonium sulfate and sodium chloride, which don't undergo photolysis to form reactive species. We used 2 M of each solute to mimic the aqueous phase of aerosols under high humidity condition.<sup>38</sup>



As shown in Figure 2.4, a high concentration of ammonium sulfate or sodium chloride has only a small, and statistically insignificant, impact on triplet kinetics. There is a tendency that 2 M of these salts increases the rate constant for GA loss, which might be due to the high salt concentration decreasing the solubility of dissolved oxygen.<sup>63</sup> Since oxygen is the dominant scavenger for <sup>3</sup>DMB\* in these solutions, decreasing the dissolved O<sub>2</sub> concentration will increase the steady-state concentration of <sup>3</sup>DMB\*, resulting in a higher GA decay rate. For example, 2 M NaCl decreases O<sub>2</sub> solubility by around 40%,<sup>64</sup> which is roughly consistent with the increased  $k'_{\text{GA}}$  at pH 2. Zhou *et al.* found that acetosyringone direct photodegradation increased by a factor of roughly six in the presence of 2 M NaClO<sub>4</sub>.<sup>37</sup> If GA direct photodegradation was enhanced by a similar factor in our (NH<sub>4</sub>)<sub>2</sub>SO<sub>4</sub> and NaCl solutions, it would still be a minor sink, contributing less than 5% of total GA decay in the presence of <sup>3</sup>DMB\*, indicating that GA direct photodegradation does not affect our results significantly. Addition of 0.9 M galactose also causes no significant change to the rate constant for GA decay. Figure S2.8 shows the dependence of  $k'_{\text{GA}}$  on the concentration of galactose. The consistency of these rate constants indicates that galactose reacts, at most, only very slowly with <sup>3</sup>DMB\*; otherwise, high concentrations of galactose would suppress the <sup>3</sup>DMB\* concentration, leading to a slower GA decay. From our kinetic data in Figure 2.4 we can estimate an upper-bound for the rate constant of galactose with <sup>3</sup>DMB\*, by assuming that we cannot discern a 2 $\sigma$  decrease in the average  $k'_{\text{GA}}$  at the highest galactose concentration (0.9 M). Applying this assumption to our data gives a value for  $k_{\text{galactose}+\text{DMB}^*}$  of  $\leq 1 \times 10^5 \text{ M}^{-1} \text{ s}^{-1}$  at pH 2 and 5 and suggests that cellulose-derived sugars are insignificant sinks for triplets in the ALW of biomass-burning particles.

Adding Fe(III) increases the overall decay rate of GA because photolysis of iron complexes Fe(OH)<sup>2+</sup> and FeCl<sup>2+</sup> forms •OH and Cl•, which react with GA.<sup>65-67</sup> Figure S2.9 shows GA decay in the presence of Fe(III) during illumination and the contribution of Fe chemistry. After subtracting the contribution of photolysis of Fe(III), the GA decay rate by <sup>3</sup>DMB\* is not statistically different in the presence of Fe(III) (Figure 2.4). In contrast, Cu(II) strongly inhibits the decay of GA (Figure 2.4). Pan *et al.* observed the same inhibition by Cu(II) on the decay of phenolic compounds by triplets.<sup>68,69</sup> They

proposed that Cu(II) is photochemically reduced to Cu(I),<sup>70</sup> which reacts with phenoxyl radicals to regenerate the parent phenol, slowing phenol decay.<sup>68</sup> As shown in Figure 2.4, inhibition of GA loss by Cu(II) is more significant at pH 5 than at pH 2, likely because of the acid-base speciation of HO<sub>2</sub><sup>•</sup> and its conjugate base <sup>•</sup>O<sub>2</sub><sup>-</sup>. HO<sub>2</sub><sup>•</sup> has a pKa of 4.8,<sup>71</sup> so at pH 2 HO<sub>2</sub><sup>•</sup> is the dominant form, but at pH 5 <sup>•</sup>O<sub>2</sub><sup>-</sup> dominates. Both of these O<sub>2</sub>(-I) species reduce Cu(II) to Cu(I), but the reaction with <sup>•</sup>O<sub>2</sub><sup>-</sup> is around 80 times faster,<sup>72</sup> so we expect a higher Cu(I) concentration at pH 5 compared to pH 2, leading to stronger inhibition of phenol decay.

#### 2.3.4. Quantitative Structure-Activity Relationships

Since biomass burning emits over 50 phenolic compounds,<sup>9,10,73</sup> we would like to develop a quantitative structure-activity relationship (QSAR) to predict rate constants for phenols reacting with triplets. Following promising research on QSARs between reactant oxidation potentials ( $E_{OX}$ ) and their rate constants with triplets,<sup>74-76</sup> we pursued a similar approach for phenols with the triplet state of DMB. While there are some measurements of phenol oxidation potentials,<sup>77-79</sup> there are no values for the six phenols we studied here (Figure 2.1). Therefore we both measured and computed  $E_{OX}$  values for our six phenols as well as for the six phenols whose rate constants with <sup>3</sup>DMB\* were measured by Smith et al.<sup>16,19</sup>

Oxidation potentials of phenols determined in this work are shown in Table S2.5.  $E_{OX}$  values measured by cyclic voltammetry at pH 5 are lower than that at pH 2, as expected,<sup>79</sup> while computed  $E_{OX}$  values are higher than measured values, consistent with the finding of other groups.<sup>78,80</sup> The correlation between our measured and computed  $E_{OX}$  values is modest ( $r^2 = 0.34$ ; Figure S2.10), but our measured values are well correlated with values from the literature ( $r^2 = 0.99$ ; Figure S2.10).

As seen in Figure 2.5, oxidation potentials correlate well with the log of the second-order rate constants with the DMB triplet: as the oxidation potential increases (i.e., the phenol is more difficult to oxidize), the rate constant generally decreases. Based on  $R^2$  values, modeled oxidation potentials perform

better than measured values in the QSAR. For the QSAR based on measured  $E_{OX}$  values at pH 2, most of the phenols are close to the regression line (Figure 2.5B), but there are two notable outliers, hydroquinone and catechol. The data in the corresponding QSAR at pH 5 are much more scattered. While all of our QSARs are approximately linear in this log-linear space, at lower  $E_{OX}$  values  $k_{ArOH+3DMB^*}$  will plateau as it approaches the diffusion-controlled limit.<sup>48</sup>

## 2.4. Atmospheric Implications

Our research group recently showed that concentrations of triplets and singlet molecular oxygen increase by orders of magnitude moving from cloud/fog drops to the more concentrated conditions in aerosol liquid water, while aqueous hydroxyl radical concentrations decrease.<sup>28</sup> To understand how these changing condensed-phase oxidant conditions alter the formation of SOA from biomass-burning phenols, here we estimate initial rates of SOA formation from three model phenols - syringol (SYR), guaiacyl acetone (GA) and syringyl acetone (SA) - across a range of liquid water contents. In our calculations we assume Henry's law partitioning of the phenols, with  $K_H$  values at 278 K of  $2.5 \times 10^4 \text{ M atm}^{-1}$  (SYR),  $9.1 \times 10^6 \text{ M atm}^{-1}$  (GA), and  $6.1 \times 10^8 \text{ M atm}^{-1}$  (SA).<sup>13,15</sup> We consider reactions with gas-phase  $\bullet\text{OH}$  (at a constant  $1 \times 10^6 \text{ molecules cm}^{-3}$ ) and aqueous-phase  $^3\text{C}^*$ ,  $^1\text{O}_2^*$ , and  $\bullet\text{OH}$ , using oxidant concentrations as a function of liquid water content from Figure 2.5 of Kaur *et al.*<sup>28</sup> For oxidizing triplet concentrations we use the geometric mean of the two estimates in Kaur *et al.* Rate constants and SOA mass yields applied in the SOA formation rate calculation are listed in Table S2.8. We assume an initial particulate matter concentration of  $10 \mu\text{g m}^{-3}$ -air and that each phenol has an initial total (gas + aqueous) concentration of  $5 \mu\text{g m}^{-3}$ -air. Details of the calculations are in SI Section S2.6.

The top row of Figure 2.6 shows initial SOA formation rates from SYR, GA and SA reacting with each oxidant as a function of LWC from cloud/fog condition ( $0.33 \text{ g m}^{-3}$ ) to aerosol liquid water ( $10 \mu\text{g m}^{-3}$ ), while the bottom row shows the contribution of each oxidant to aqSOA formation. We start by

considering syringol, which has the lowest Henry's law constant of the three phenols here. Under the cloud/fog condition, only about 20% of SYR is present in the aqueous phase (Figure 6A), but the SOA formation rate from aqueous reactions is comparable to that from the gas-phase reaction, and  $\bullet\text{OH}$  is the dominant oxidant in both phases (Figure 6D). When moving to the drier ALW conditions, the fraction of SYR in the aqueous phase decreases rapidly, causing the aqueous  $\bullet\text{OH}$ -mediated aqSOA formation rate to drop quickly. Formation of aqSOA by  $^3\text{C}^*$  and  $^1\text{O}_2^*$  are initially less sensitive to the decrease in LWC – a result of increasing oxidant concentrations – but they cannot compete with gas-phase  $\bullet\text{OH}$  since so little SYR is in the aqueous phase.

The picture is quite different for GA, which has a Henry's law constant that is nearly 400 times higher than SYR. Most GA is in the aqueous phase under cloud/fog conditions, while a negligible amount is aqueous under ALW conditions (Figure 6B). Initially, the decrease in LWC from cloud/fog conditions increases the aqSOA formation rate - even though the aqueous fraction of GA is decreasing - because of the increase in  $^3\text{C}^*$  and  $^1\text{O}_2^*$  concentrations. But the aqueous formation of SOA peaks at an LWC of approximately  $1 \text{ mg m}^{-3}$ , and under particle water conditions ( $100 \mu\text{g m}^{-3}$  and less) gas-phase  $\bullet\text{OH}$  becomes the major source of SOA from GA.

The final phenol we consider is syringyl acetone, whose Henry's law constant is roughly 70 times higher than that of GA. Because of this, SA is essentially completely partitioned to the aqueous phase under cloud/fog conditions and even significantly partitioned to the aqueous phase ( $\sim 10\%$ ) at an ALW content of  $10 \mu\text{g m}^{-3}$  (Figure 6C). Coupled with the high  $^3\text{C}^*$  and  $^1\text{O}_2^*$  concentrations under ALW conditions, the result is that aqueous reactions dominate SOA formation throughout the entire range of liquid water contents (Figure 6F). Furthermore, the increase in aqueous oxidant concentrations with decreasing LWC causes the aqSOA formation rate from SA to increase by approximately a factor of 30 as liquid water content drops by a factor of roughly 3000 from cloud/fog conditions to  $100 \mu\text{g m}^{-3}$  (Figure 2.6C). While

the rate of aqSOA formation then falls as LWC continues to drop, the rate at an ALW of  $10 \mu\text{g m}^{-3}$  is still around 10 times higher than under cloud conditions.

For all three phenols, the contributions of the aqueous oxidants shift as liquid water content decreases from cloud/fog to ALW conditions (Figure 2.6, bottom row). In the dilute aqueous phase for all three phenols, aqueous  $\bullet\text{OH}$  accounts for roughly 90% of aqSOA formation,  $^3\text{C}^*$  contributes roughly 10%, and  $^1\text{O}_2^*$  is negligible. Moving toward more concentrated ALW conditions, the aqueous  $\bullet\text{OH}$  concentration decreases by a factor of around 6, while  $^1\text{O}_2^*$  and  $^3\text{C}^*$  concentrations initially increase nearly proportionally with particle mass/water ratio and then plateau.<sup>28</sup> Thus the  $\bullet\text{OH}$  contribution to aqSOA formation rate decreases as LWC drops, while  $^1\text{O}_2^*$  and  $^3\text{C}^*$  become more significant, dominating phenolic aqSOA formation under ALW conditions. As described above, aqueous  $^1\text{O}_2^*$  and  $^3\text{C}^*$  compete with the rising influence of gas-phase  $\bullet\text{OH}$  as LWC decreases, with the relative importance of aqueous and gaseous reactions depending on the Henry's law constant of the phenol. Our simple calculations suggest that for phenols with low to moderate  $K_H$  values, gas-phase oxidation dominates across all LWC values at a fairly constant rate. In contrast, for phenols with high  $K_H$  (above approximately  $10^7 \text{ M atm}^{-1}$ ), aqueous-phase reactions generally dominate SOA formation and the rate is sensitive to LWC. Overall, our calculations indicate that reactions of phenols with high  $K_H$  values can be important pathways of SOA formation in aerosol liquid water, with this chemistry largely driven by  $^3\text{C}^*$  and  $^1\text{O}_2^*$ .

## 2.5. Acknowledgment

This work was funded by National Science Foundation grant (AGS-1649212), the California Agricultural Experiment Station (Projects CA-D-LAW-6403-RR and CA-D-ETX-2102-H), and a Jastro Shields Research Award and Donald G. Crosby Fellowship from UC Davis to L.M.

## 2.6. Figures

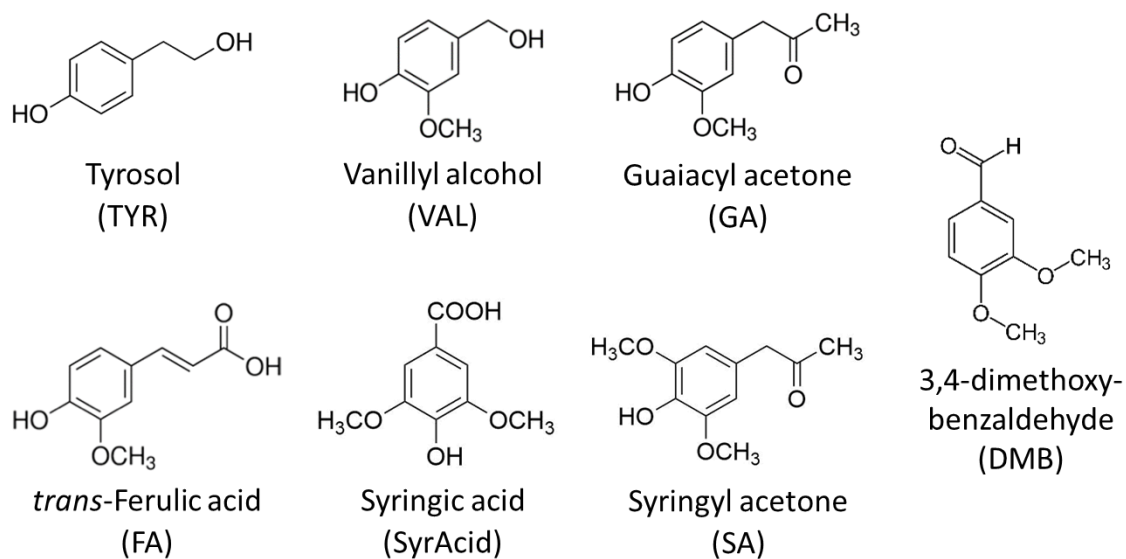


**Figure 2.1.** Chemical structures of phenols used in this study. The structure of the triplet precursor DMB is also shown.

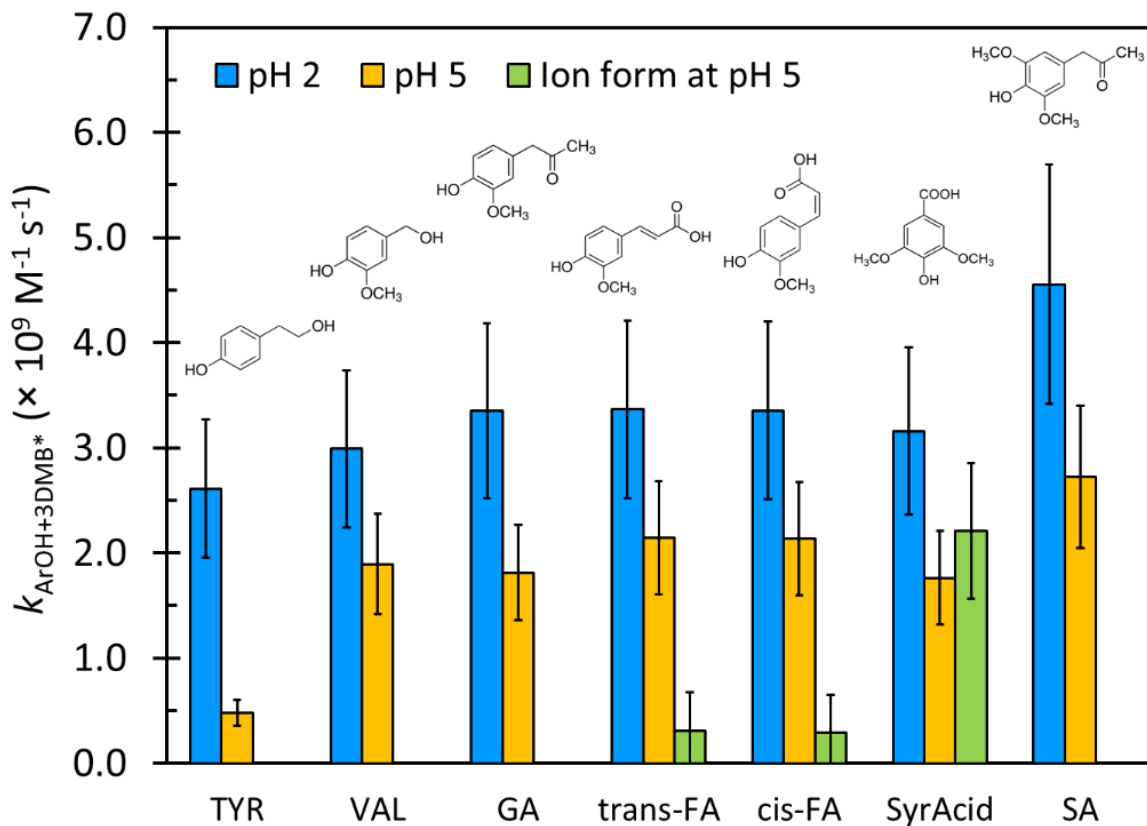


**Figure 2.2.** Second-order rate constants for phenols reacting with  $^3\text{DMB}^*$  at pH 2 and 5. The carboxylic acid groups in FA and SyrAcid ( $\text{pK}_a = 4.6$  and  $4.2$ , respectively) are partially deprotonated at pH 5: the yellow bars represent kinetics for the neutral form while the green bars are for the carboxylate form. Error bars represent  $\pm 1$  standard error propagated from linear regression. Data are listed in Table S2.4.

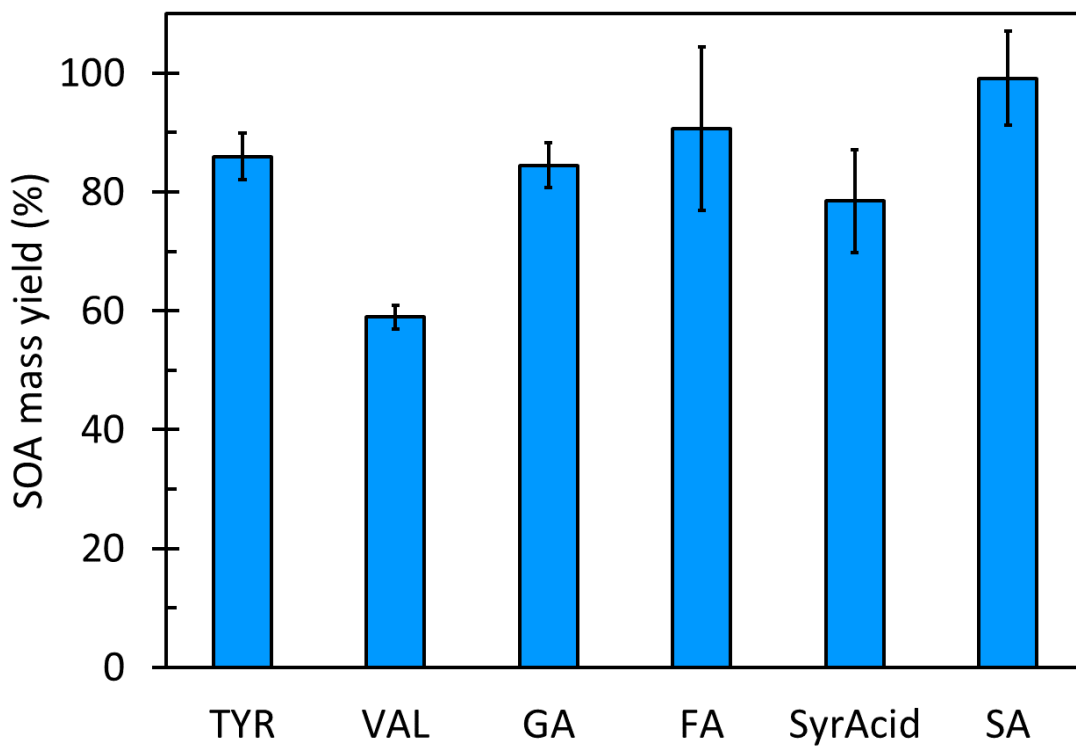


**Figure 2.3.** Aqueous SOA mass yields ( $Y_{\text{SOA}}$ ) from phenol oxidized by the DMB triplet state at pH 5. Error bars are  $\pm 1$  standard deviation, calculated from replicate samples at different times during the reaction, from one to three half-lives. The SA yield is statistically higher ( $p < 0.05$ ) than those of the other compounds except for FA, while the VAL yield is statistically lower than all other values.



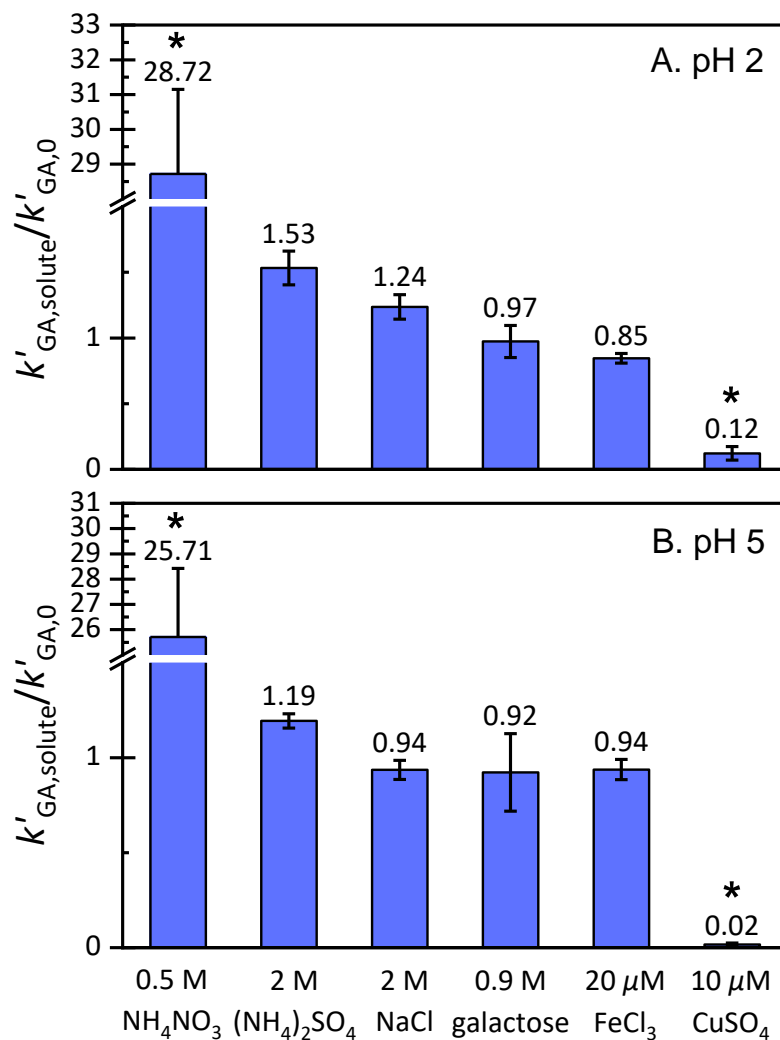


**Figure 2.4.** Effect of different solutes on the first-order rate constant of GA decay ( $k'_{GA}$ ) at pH 2 (panel A) and pH 5 (panel B): values are shown as the ratio of the GA loss rate constant with solute to the rate constant without solute, with both experiments performed on the same day. Solutions contained 10  $\mu\text{M}$  DMB, 10  $\mu\text{M}$  GA,  $\text{H}_2\text{SO}_4$  to adjust the pH, and the listed concentration of solute. All experiments were performed in duplicate. Error bars represent  $\pm 1$  standard deviation. Asterisks represent a ratio that is statistically different from unity ( $p < 0.05$ ) with t tests. For solutions containing  $\text{FeCl}_3$ , we removed the portion of GA loss due to Fe chemistry to examine whether iron alters DMB-phenol kinetics; see Figure S2.9 for details.

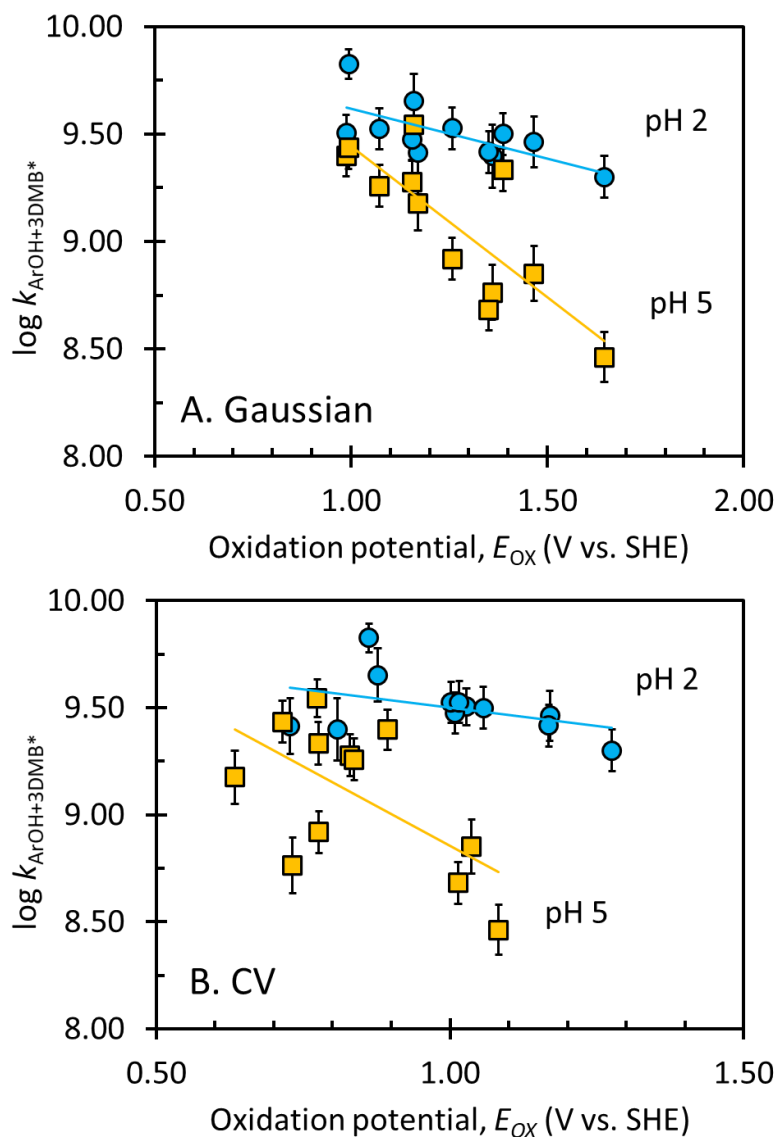


**Figure 2.5.** Correlation between measured bimolecular rate constants for phenols with the DMB triplet state and computed or measured one-electron oxidation potentials of phenols. Panel A shows QSARs based on oxidation potentials calculated by Gaussian:  $\log(k_{\text{ArOH}+3\text{DMB}^*}) = -0.46E_{\text{OX}} + 10.1$  ( $r^2 = 0.47$ ) at pH 2 and  $\log(k_{\text{ArOH}+3\text{DMB}^*}) = -1.41E_{\text{OX}} + 10.8$  ( $r^2 = 0.66$ ) at pH 5. Panel B shows QSARs based on oxidation potentials measured by cyclic voltammetry:  $\log(k_{\text{ArOH}+3\text{DMB}^*}) = -0.34E_{\text{OX}} + 9.84$  ( $r^2 = 0.16$ ) at pH 2 and  $\log(k_{\text{ArOH}+3\text{DMB}^*}) = -1.48E_{\text{OX}} + 10.3$  ( $r^2 = 0.36$ ) at pH 5). Error bars are  $\pm 1$  standard error of  $k_{\text{ArOH}+3\text{DMB}^*}$ .

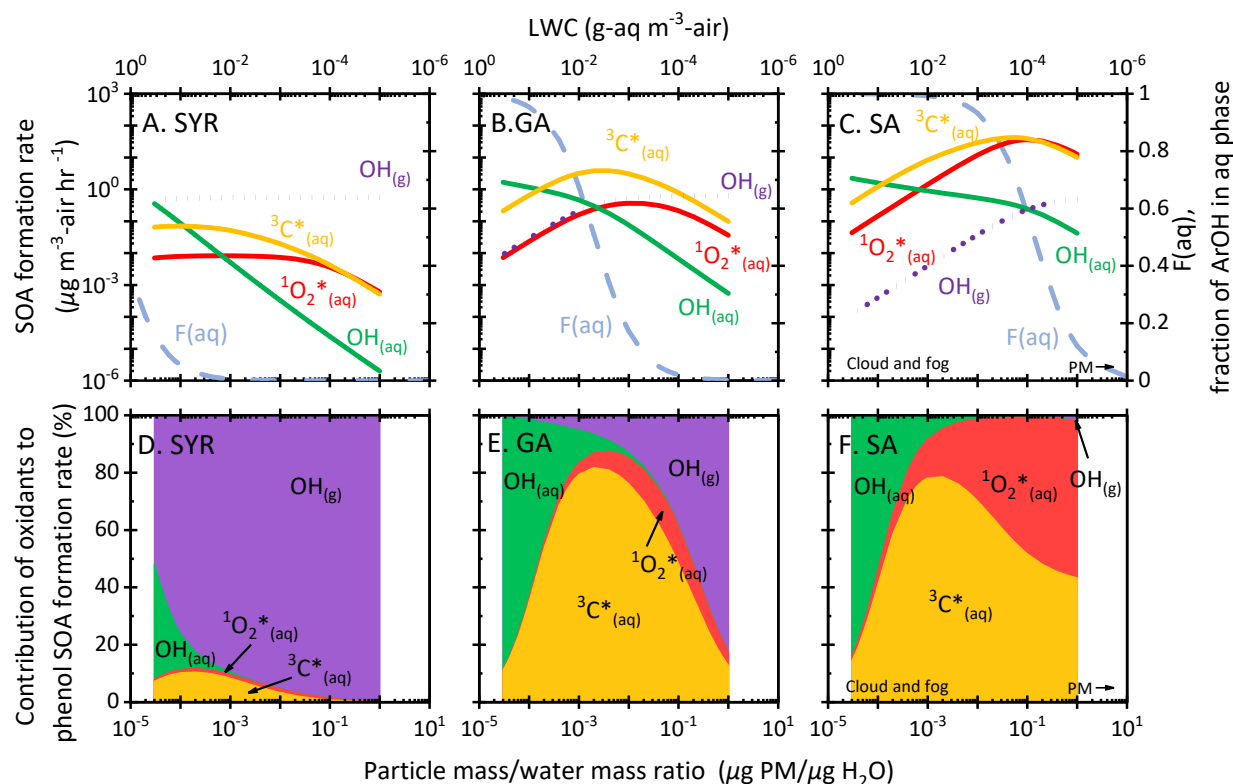


**Figure 2.6.** The top row (panels A-C) shows initial SOA formation rates from gas and aqueous reactions of syringol ( $K_H = 2.5 \times 10^4 \text{ M atm}^{-1}$  at 278 K), guaiacyl acetone ( $K_H = 9.1 \times 10^6 \text{ M atm}^{-1}$ ), and syringyl acetone ( $K_H = 6.1 \times 10^8 \text{ M atm}^{-1}$ ) as a function of liquid water content (top axis; assuming a PM concentration of  $10 \mu\text{g m}^{-3}$ ) and particle mass/water mass ratio (bottom axis). The dotted line is the rate of SOA formation from gas-phase  $\bullet\text{OH}$  with each phenol, while solid lines represent aqSOA formation rates for a given phenol with  ${}^3\text{C}^*$ ,  ${}^1\text{O}_2^*$ , and  $\bullet\text{OH}$ ; see SI Section S2.6 for calculations. Aqueous oxidant concentrations vary with LWC:  $[\bullet\text{OH}] = (0.8 - 5) \times 10^{-15} \text{ M}^{-1}\text{s}^{-1}$ ,  $[{}^3\text{C}^*] = (0.008 - 2) \times 10^{-12} \text{ M}^{-1}\text{s}^{-1}$ ,  $[{}^1\text{O}_2^*] = (0.0007 - 1) \times 10^{-10} \text{ M}^{-1}\text{s}^{-1}$ . The blue dashed line is the fraction of phenol in the aqueous phase,  $F_{(aq)}$ . The bottom row (panels D-F) shows the corresponding contribution of each oxidant to SOA formation from that phenol.

## 2.7. Supporting Information

**Table S2.1:** HPLC methods used to quantify ArOH concentrations. All methods had a flow rate of 0.6 mL min<sup>-1</sup>.

Compound	Eluent <sup>a</sup> (Vol:Vol)	Detection wavelength (nm)
TYR	20%:80% ACN <sup>b</sup> : H <sub>2</sub> O	280
VAL	20%:80% ACN: H <sub>2</sub> O	280
GA	20%:80% ACN: H <sub>2</sub> O	280
FA	20%:80% ACN: 2% acetic acid in H <sub>2</sub> O	320
SyrAcid	20%:80% ACN: 2% acetic acid in H <sub>2</sub> O	280
SA	15%:85% ACN: H <sub>2</sub> O	280

<sup>a</sup> HPLC instrumentation: Shimadzu LC-10AT pump, ThermoScientific BetaBasic-18 C<sub>18</sub> column (250 × 3mm, 5 μm bead), and Shimadzu-10AT UV-Vis detector

<sup>b</sup> ACN = acetonitrile

**Table S2.2:** Measured or estimated values of parameters in Equation 2.2. Uncertainties represent ± 1 standard error.

Parameters	Values	Reference
$\Phi_{\text{ISC}}$	0.095 (± 0.017)	This work (Section S2.7) Smith <i>et al.</i> (2015) <sup>16</sup>
Rate of <sup>3</sup> DMB* formation <sup>a</sup> ( $j_{\text{hv,DMB}}\Phi_{\text{ISC}}[\text{DMB}], \mu\text{M min}^{-1}$ )	4.9 (± 0.98)	Smith <i>et al.</i> (2015) <sup>16</sup>
$k_{\text{O}_2+3\text{DMB}^*}$ (M <sup>-1</sup> s <sup>-1</sup> )	$2.8 (\pm 0.4) \times 10^9$	Kaur <i>et al.</i> (2018) <sup>28</sup>
[O <sub>2</sub> ] (μM) <sup>b</sup>	284	Rounds <i>et al.</i> (2006) <sup>81</sup>

<sup>a</sup> Rate of <sup>3</sup>DMB\* formation in a 10 μM DMB solution illuminated with the equivalent of midday, winter solstice sunlight at Davis (i.e.  $j_{2\text{NB}} = 0.007 \text{ s}^{-1}$ ). The rate was calculated with the new value of  $\Phi_{\text{ISC}}$ .

<sup>b</sup> Value at 298 K.

## Section S2.1: Direct photodegradation of phenols

Some phenols with carbonyl or other chromophoric substituents absorb sunlight and undergo rapid direct photodecay.<sup>82,83</sup> To test if this occurs for the phenols employed in this study over the time of our experiments with <sup>3</sup>DMB\*, we illuminated a solution containing 5-100  $\mu$ M of one phenol at pH 2 and 5 without addition of DMB, and measured the direct photodegradation rate constant ( $j_{\text{ArOH}}$ ).

We found no significant direct photodegradation of TYR, VAL, and GA, consistent with their very low rates of sunlight absorption. However, FA, SA and SyrAcid do absorb sunlight significantly and undergo photodegradation; as described in the main text, we correct our triplet results for the direct photodecay of these three phenols. Figure S2.1 shows their direct photodegradation rate constants as a function of initial phenol concentrations. For FA, the rate constant of photodegradation doesn't change with FA concentration (after correction for internal light screening) and has an average value of  $2.4 (\pm 0.6) \times 10^{-4} \text{ min}^{-1}$  at pH 2 and  $4.3 (\pm 1.1) \times 10^{-4} \text{ min}^{-1}$  at pH 5. Based on these values, direct photodegradation of FA is minor in our <sup>3</sup>DMB\* experiments, accounting for 6% or less of total FA decay in the presence of DMB.

For SyrAcid, photodegradation is initially very slow but then accelerates with illumination time, not following first-order decay. These kinetics suggest SyrAcid photodecay forms compounds that initiate the decay of SyrAcid via pathways other than direct photodecay (e.g. by producing an efficient photosensitizer). The  $j_{\text{SyrAcid}}$  values shown here are for the initial stage of the photodegradation. Rate constants are independent of concentration, with average  $j$  values of  $0.36 (\pm 0.19) \times 10^{-3} \text{ min}^{-1}$  at pH 2 and  $2.7 (\pm 0.7) \times 10^{-3} \text{ min}^{-1}$  at pH 5. Over the illumination duration of our <sup>3</sup>DMB\* experiments, SyrAcid photodegradation is slow at pH 2, contributing less than 5% of total SyrAcid decay in the illuminated solution containing DMB. At pH 5, direct photodecay of SyrAcid accounts for about 15 to 30 % of decay in the triplet experiments. In the case of SA, the photolysis rate constant generally increases with SA concentration (Figure S2.1). At pH 2,  $j_{\text{SA}}$  ranges from  $2.0 \times 10^{-3} \text{ min}^{-1}$  to  $12.5 \times 10^{-3} \text{ min}^{-1}$  and from  $0.5 \times 10^{-3} \text{ min}^{-1}$  to  $3.9$

$\times 10^{-3} \text{ min}^{-1}$  at pH 5. Direct photodecay of SA contributes 3%~34% of total SA loss measured in the presence of  $^3\text{DMB}^*$ .

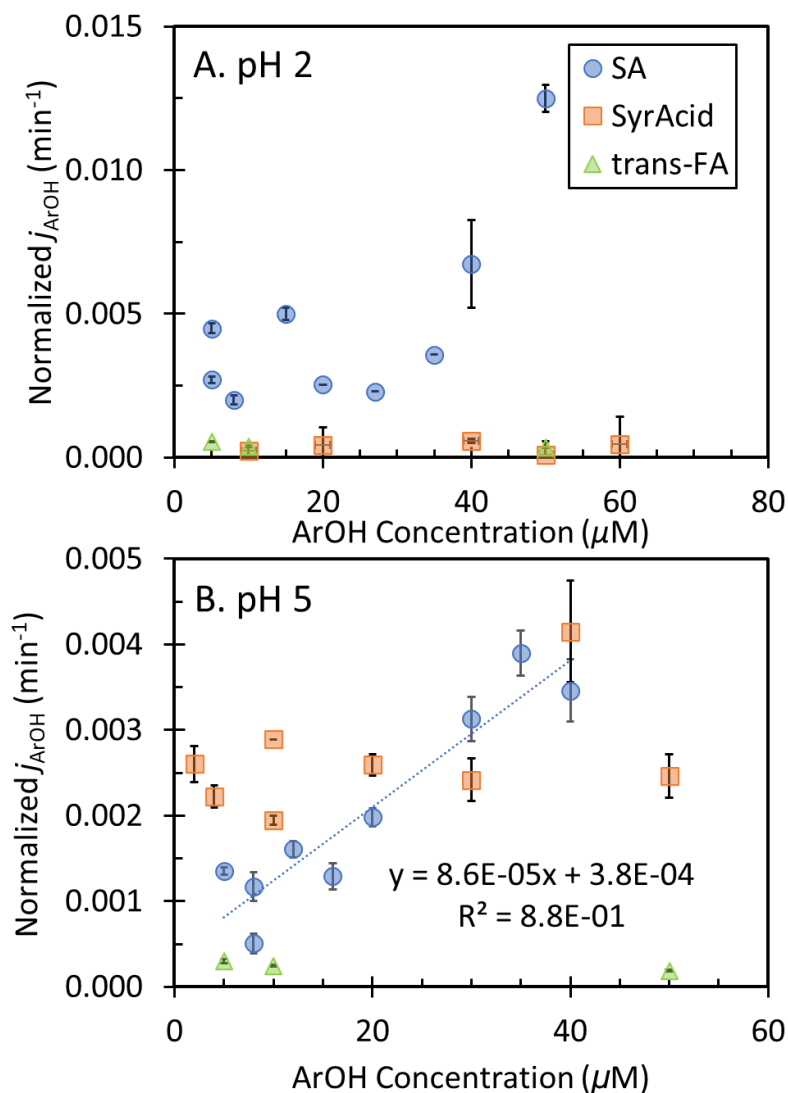


**Figure S2.1:** Summary of the normalized first-order direct photodegradation rate constants for *trans*-FA (green triangle), SA (blue circle), and SyrAcid (orange square) at different initial phenol concentrations at pH 2 (Panel A) and pH 5 (Panel B). *cis*-FA has the same degradation rate constant as *trans*-FA. Error bars represent  $\pm 1$  standard error propagated from standard errors in linear fitting to obtain the slope and  $j_{2\text{NB}}$ . Dotted line represents fitted regression to the  $j_{\text{SA}}$  data at pH 5.

## Section S2.2: Phenolic aqSOA mass yields determination

Ammonium sulfate (AS) is used as an internal standard for aqSOA quantification,<sup>17,30,44,84</sup> under the assumption that sulfate is quantitatively extracted and measured by the AMS (a reasonable assumption given that the ammonium sulfate used is water soluble and non-refractory).<sup>85</sup> Thus, knowing the solution concentration of sulfate, we can use the AMS-measured concentration of ammonium sulfate in aerosols ( $AS_{AMS}$ ;  $\mu\text{g m}^{-3}$ ) to convert the AMS-measured aqSOA mass concentration ( $Org_{AMS}$ ;  $\mu\text{g m}^{-3}$ ) to solution concentration ( $\text{mg L}^{-1}$ ). The aqSOA yield is then given by:

$$SOA\ yield = \frac{[Org]_t - [Org]_0}{[phenol]_t - [phenol]_0} = \frac{[Org_{AMS}]_t \times \frac{[AS]_t}{[AS_{AMS}]_t} - [Org_{AMS}]_0 \times \frac{[AS]_0}{[AS_{AMS}]_0}}{[phenol]_t - [phenol]_0} \quad (S2.1)$$

where [Org], [AS], and [phenol] refer to the solution concentrations ( $\text{mg L}^{-1}$ ) of aqSOA, sulfate, and the phenol under consideration, respectively. The subscripts t and 0 denote the irradiation time. As each sample was spiked to the same concentration of AS,  $[AS]_t = [AS]_0$ . The phenol concentrations were determined by HPLC.

A collection efficiency (CE) of 1 was used in this study for AMS data processing. By using sulfate as an internal standard, the reported liquid aqSOA mass concentration is independent of CE and no correction is required. The reasons are 1) sulfate is expected to be quantitatively measured by the AMS<sup>85</sup> and 2) the aqSOA and sulfate are expected to be internally mixed in the aerosol generated from the reaction solutions.

### Section S2.3: Phenol oxidation potentials determination

Cyclic voltammetry (CV) was performed using a three-electrode BASi EC Epsilon potentiostat consisting of a 3-mm glassy carbon working electrode, an Ag/AgCl 3 M KCl reference electrode, and a 0.5 mm diameter platinum wire (BASi) counter electrode. Before each set of measurements, the working electrode was polished with 0.05  $\mu\text{m}$  alumina polish. Cyclic voltammograms were recorded between -500 to 1200mV, with scan speeds of 50, 100, and 200 mV/s. Measurements were performed in deoxygenated pH 2 (0.2 M NaCl + 0.01 M HCl) and pH 5 (0.1 M potassium hydrogen phthalate + 0.04 M NaOH) buffer solutions with 0.25 mM of phenol. Since all phenols presented irreversible voltammograms, we report values of anodic peak potentials ( $E_p$ ) obtained directly from the voltammograms from the first scan (scan rate of 50 mV/s).<sup>78</sup> Potentials were corrected from the Ag/AgCl reference electrode to standard hydrogen electrode (SHE) by adding 209 mV.<sup>86</sup>

Phenol oxidation potentials (for  $\text{ArOH} \rightarrow \text{ArOH}^{\bullet+} + e^-$ ) were also calculated using Gaussian 09 software with procedures described previously.<sup>74,87</sup> Geometry optimization of phenols and phenoxy radical cations were performed using uB3LYP functionals and 6-31+G(d,p) basis set.<sup>74,88-91</sup> Solvation energies were approximated with solvent mode density (SMD) continuum model for water.<sup>92</sup>

The free energy of the reaction ( $\Delta G^{\circ}_{\text{ox}}$ ) was calculated by the difference in Gibbs free energy of the reactant and products, and was converted to one-electron oxidation potential ( $E_{\text{OX}}$ ) using:

$$E_{\text{OX}} = -\left(\frac{-\Delta G^{\circ}_{\text{ox}}}{nF} + \text{SHE}\right) \quad (\text{S2.2})$$

where  $n$  is the number of electrons (1 here),  $F$  is Faraday's constant (96485.3365 C mol<sup>-1</sup>), and SHE is the potential of the standard hydrogen electrode (4.28 V).<sup>93</sup>



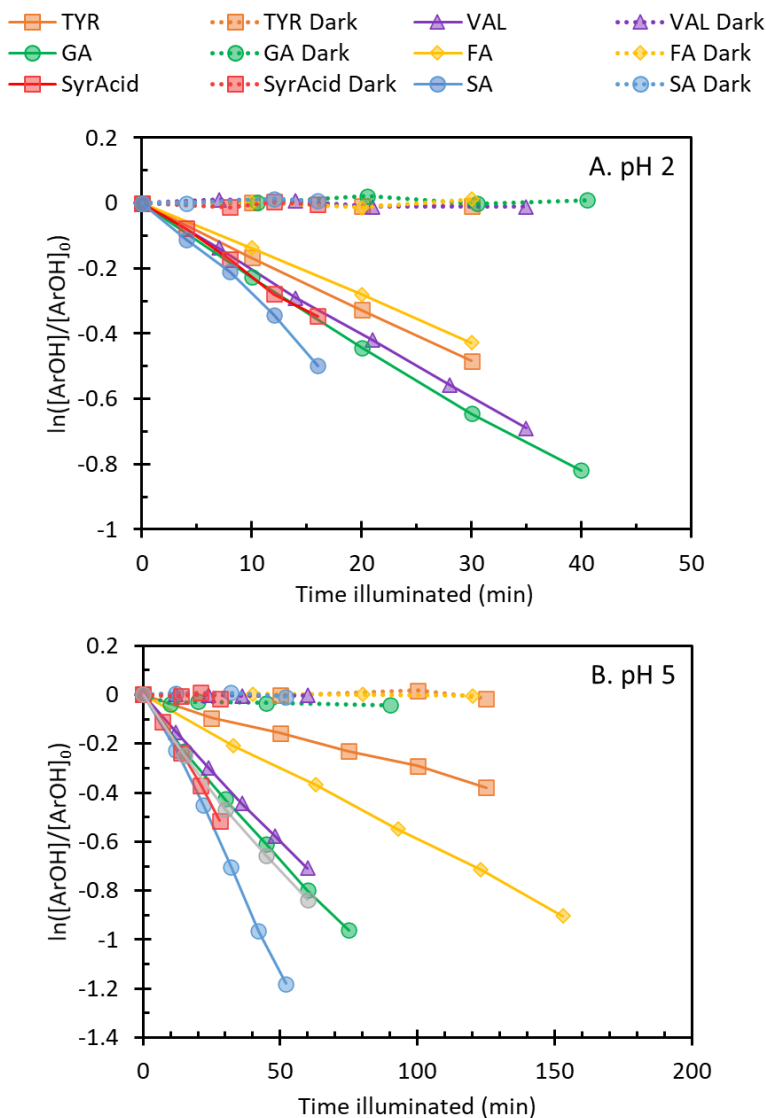


**Figure S2.2:** Representative plots of the aqueous oxidation of six phenols by the triplet excited state of DMB at pH 2 (Panel A) and pH 5 (Panel B) at 20 °C. Results shown here are for solutions containing 10  $\mu$ M ArOH and 10  $\mu$ M DMB. Solid lines represent the illuminated samples; dashed lines represent dark controls. The grey circles and corresponding line in the Panel B are data from the pH 5 oxidation of GA by  $^3DMB^*$  at 5 °C. To examine the temperature effect on triplet kinetic, experiments of GA decay by  $^3DMB^*$  at 5 and 20 °C were performed in duplicate. GA decay rates are not statistically different at two temperatures by a t test ( $p < 0.05$ ), indicating no significant impact of temperature on triplet kinetics, as seen previously for phenol ( $C_6H_5OH$ ) with triplet DMB.<sup>19</sup>

#### Section S2.4: Photoisomerization of ferulic acid

Ferulic acid isolated from plants usually exists as the *trans* isomer,<sup>94</sup> but during illumination it undergoes *cis-trans* isomerization to form a mixture of both isomers,<sup>95,96</sup> which can be separated by HPLC. The rate of FA photoisomerization is more rapid than that of reaction with <sup>3</sup>DMB\*: under our illumination conditions, 10  $\mu$ M FA reaches an isomeric photostationary state within 3 min (Figure S2.3). In experiments of FA reacting with <sup>3</sup>DMB\*, we removed aliquots for FA analysis at intervals greater than 10 min, thus photoisomerization should be at steady state. In our triplet experiments with FA, we first prepared a pH-adjusted solution containing *trans*-FA and illuminated it for 10 minutes to achieve photoisomerization steady state. Next, we added DMB and illuminated to determine the decay rate constant of FA by <sup>3</sup>DMB\*. At a given pH value, *trans*-FA and *cis*-FA show essentially the same first-order decay rate, as shown in Figure S2.4.

The *cis/trans* ratio in the photostationary state varies with pH. At pH 2,  $[cis]/[trans]$  is about 0.5, while at pH 5,  $[cis]/[trans]$  is around 6, which is similar to results from Kahnt *et al.*<sup>95</sup> We found that the presence of DMB did not affect the  $[cis]/[trans]$  ratio in illuminated solution at either pH. The rate constant for 10  $\mu$ M *trans*-FA isomerization can be determined by illuminating *trans*-FA solution, and then determining how the *trans*-FA and *cis*-FA concentrations change with time. The rate constant of a reversible reaction can be calculated using:<sup>97</sup>

$$-(j_{trans \rightarrow cis} + \frac{j_{trans \rightarrow cis}}{K_{eq}})t = \ln \left( \frac{\frac{[cis]_t}{K_{eq}} - [trans]_t}{\frac{[cis]_0}{K_{eq}} - [trans]_0} \right) = \ln \left( \frac{C_t^*}{C_0^*} \right) \quad (S2.3)$$

where  $j_{trans \rightarrow cis}$  is the first-order rate constant of photoisomerization from *trans*-FA to *cis*-FA;  $K_{eq}$  is the equilibrium constant of photoisomerization, i.e., the  $[cis]/[trans]$  ratio at the photostationary state;  $t$  is illumination time; and  $[cis]$  and  $[trans]$  are concentrations of the two isomers at a given time. The first-order rate constant of photoisomerization from *cis*-FA to *trans*-FA can be calculated using:<sup>97</sup>

$$j_{cis \rightarrow trans} = \frac{j_{trans \rightarrow cis}}{K_{eq}} \quad (S2.4)$$

Using the data in the Figure S2.3, we calculated  $C_t^*$  (i.e.,  $\frac{[cis]_t}{K_{eq}} - [trans]_t$ ) at each time point and then obtained  $j_{trans \rightarrow cis}$  from the slope of a linear fitting between  $\ln\left(\frac{C_t^*}{C_0^*}\right)$  and time.  $j$  values were normalized to the sunlight condition of the midday on winter solstice at Davis (i.e.  $j_{2NB} = 0.007 \text{ s}^{-1}$ ). At pH 2,  $j_{trans \rightarrow cis}$  is  $0.23 \text{ s}^{-1}$  while  $j_{cis \rightarrow trans}$  is  $0.46 \text{ s}^{-1}$ . At pH 5,  $j_{trans \rightarrow cis}$  is  $0.031 \text{ s}^{-1}$  which is around six times faster than  $j_{cis \rightarrow trans}$  ( $0.005 \text{ s}^{-1}$ ).

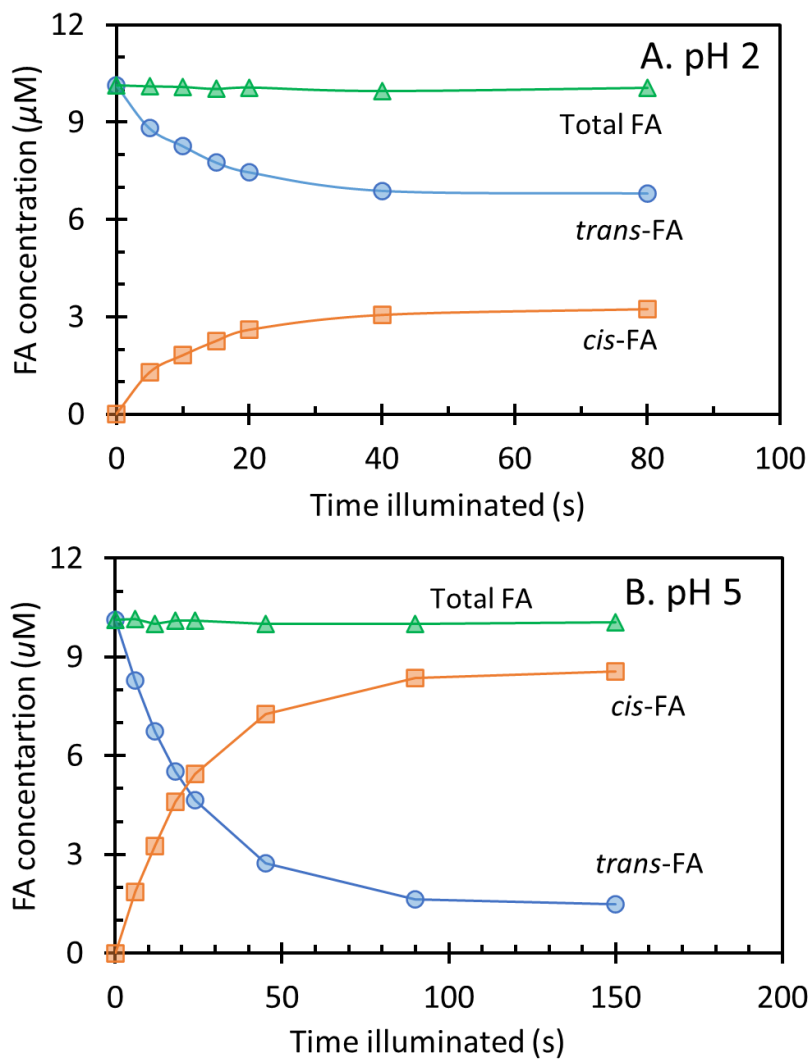


**Figure S2.3:** Changes in the concentrations of *trans*-FA (blue circles), *cis*-FA (orange squares), and total FA (*trans*-FA + *cis*-FA, green triangles) with illumination time during photoisomerization. The results shown here are for pH-adjusted solutions containing 10  $\mu\text{M}$  FA and no DMB.

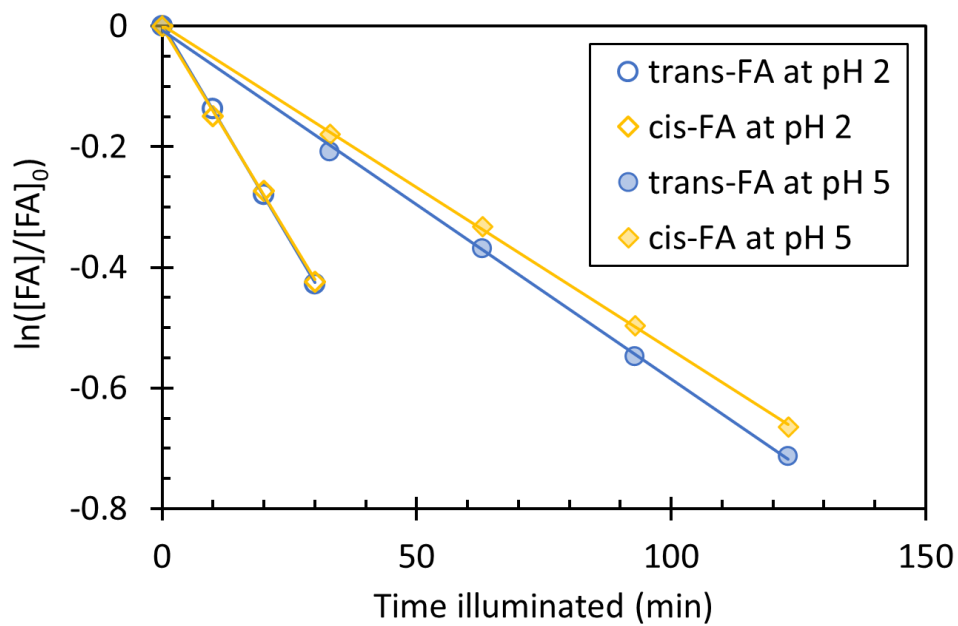


**Figure S2.4:** Representative plot of *trans*-FA (blue circle) and *cis*-FA (yellow diamond) decay with illumination time when reacting with  $^3\text{DMB}^*$  at pH 2 (open symbols) and pH 5 (filled symbols). Initial solutions contained  $10\ \mu\text{M}$  total FA and  $10\ \mu\text{M}$  DMB. Solid lines represent fitted regressions to the data.

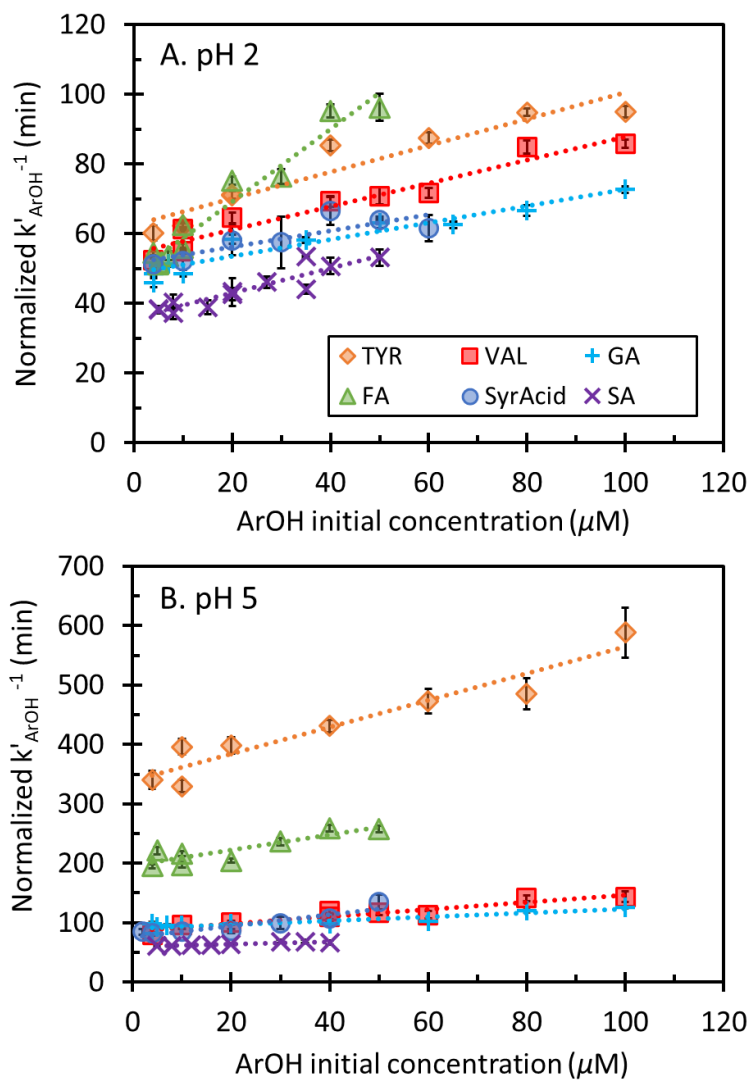


**Figure S2.5:** Inverse of the phenol first-order decay rate constant as a function of the initial phenol concentration at pH 2 (panel A) and pH 5 (panel B). Dotted lines represent fitted regressions to the data. Error bars on points represent  $\pm 1$  standard error propagated from the error of  $k'_{\text{ArOH}}$  (and  $j_{\text{ArOH}}$  for FA, SyrAcid, and SA).

**Table S2.3:** Regression parameters derived from plots of  $k'_{\text{ArOH}^{-1}}$  versus ArOH initial concentration

	pH 2			pH 5		
	y-intercept <sup>a</sup> (min)	Slope <sup>a</sup> (min $\mu\text{M}^{-1}$ )	R <sup>2</sup>	y-intercept <sup>a</sup> (min)	Slope <sup>a</sup> (min $\mu\text{M}^{-1}$ )	R <sup>2</sup>
TYR	62.48 ( $\pm$ 2.56)	0.38 ( $\pm$ 0.05)	0.91	339.2 ( $\pm$ 14.5)	2.25 ( $\pm$ 0.28)	0.92
VAL	54.53 ( $\pm$ 1.75)	0.33 ( $\pm$ 0.03)	0.93	86.16 ( $\pm$ 3.96)	0.61 ( $\pm$ 0.07)	0.91
GA	48.70 ( $\pm$ 1.12)	0.24 ( $\pm$ 0.02)	0.92	89.99 ( $\pm$ 2.58)	0.33 ( $\pm$ 0.05)	0.82
<i>trans</i> -FA	48.40 ( $\pm$ 1.94)	1.03 ( $\pm$ 0.08)	0.95	195.9 ( $\pm$ 7.59)	1.35 ( $\pm$ 0.30)	0.78
<i>cis</i> -FA	48.63 ( $\pm$ 2.14)	1.17 ( $\pm$ 0.09)	0.95	200.1 ( $\pm$ 11.7)	2.44 ( $\pm$ 0.44)	0.83
SyrAcid	51.63 ( $\pm$ 2.39)	0.23 ( $\pm$ 0.07)	0.71	75.89 ( $\pm$ 5.08)	0.95 ( $\pm$ 0.18)	0.85
SA	35.82 ( $\pm$ 1.27)	0.36 ( $\pm$ 0.05)	0.85	59.92 ( $\pm$ 0.94)	0.21 ( $\pm$ 0.04)	0.83

<sup>a</sup>Regression parameters were determined by fitting the data in Figure S2.5 using Equation 2.3.

**Table S2.4:** Second-order rate constants of phenols with <sup>3</sup>DMB\* at pH 2 and pH 5

	pH 2			pH 5		
	$k_{\text{ArOH}+\text{DMB}}^{\text{a}}$ ( $10^9 \text{ M}^{-1} \text{ s}^{-1}$ )	$k_{\text{Q}}^{\text{b}}$ ( $10^9 \text{ M}^{-1} \text{ s}^{-1}$ )	$f_{\text{reaction}}^{\text{c}}$	$k_{\text{ArOH}+\text{DMB}}$ ( $10^9 \text{ M}^{-1} \text{ s}^{-1}$ )	$k_{\text{Q}}$ ( $10^9 \text{ M}^{-1} \text{ s}^{-1}$ )	$f_{\text{reaction}}$
TYR	2.6 ( $\pm$ 0.66)	2.2 ( $\pm$ 1.8)	0.54 ( $\pm$ 0.13)	0.48 ( $\pm$ 0.12)	4.8 ( $\pm$ 1.8)	0.09 ( $\pm$ 0.02)
VAL	3.0 ( $\pm$ 0.75)	1.9 ( $\pm$ 1.8)	0.62 ( $\pm$ 0.14)	1.9 ( $\pm$ 0.48)	3.7 ( $\pm$ 2.0)	0.34 ( $\pm$ 0.08)
GA	3.3 ( $\pm$ 0.83)	0.58 ( $\pm$ 1.6)	0.85 ( $\pm$ 0.19)	1.8 ( $\pm$ 0.45)	1.1 ( $\pm$ 1.1)	0.61 ( $\pm$ 0.16)
<i>trans</i> -FA	3.4 ( $\pm$ 0.85)	14 ( $\pm$ 5.7)	0.20 ( $\pm$ 0.04)	0.83 ( $\pm$ 0.21) <sup>d</sup>	4.6 ( $\pm$ 2.1)	0.16 ( $\pm$ 0.05)
<i>cis</i> -FA	3.4 ( $\pm$ 0.84)	16 ( $\pm$ 6.4)	0.18 ( $\pm$ 0.04)	0.82 ( $\pm$ 0.21) <sup>d</sup>	8.9 ( $\pm$ 3.6)	0.08 ( $\pm$ 0.02)
SyrAcid	3.2 ( $\pm$ 0.80)	0.41 ( $\pm$ 1.7)	0.88 ( $\pm$ 0.31)	2.1 ( $\pm$ 0.55) <sup>d</sup>	7.8 ( $\pm$ 3.8)	0.22 ( $\pm$ 0.06)
SA	4.5 ( $\pm$ 1.1)	3.4 ( $\pm$ 3.0)	0.57 ( $\pm$ 0.14)	2.7 ( $\pm$ 0.68)	0.07 ( $\pm$ 1.2)	0.98 ( $\pm$ 0.26)

<sup>a</sup> Rate constant for reaction, calculated using Equation 2.2 and y-intercept values in Table S2.3. Listed uncertainties (in parentheses) are  $\pm$  1 standard error propagated from the standard errors in regression fittings, intersystem crossing quantum yield, and light absorption rate of DMB.

<sup>b</sup> Rate constant for non-reactive triplet quenching, calculated using  $k_{\text{Q}} = \frac{k_{\text{ArOH}+\text{3DMB}^*}}{f_{\text{reaction}}} - k_{\text{ArOH}+\text{3DMB}^*}$ . Uncertainties in parentheses are  $\pm$  1 standard error propagated from standard errors of  $k_{\text{ArOH}+\text{3DMB}^*}$  and  $f_{\text{reaction}}$ .

<sup>c</sup> Fraction of ArOH-<sup>3</sup>DMB\* interactions that result in chemical reaction (i.e., loss of ArOH), calculated using Equation 7 and the value of the slope in Table S2.3. Errors represents 1 standard error, propagated from the standard errors in regression fittings, intersystem crossing quantum yield, and light absorption rate of DMB.

<sup>d</sup> Apparent second-order rate constant at pH 5, i.e. the rate constant of the mixture of the ion (carboxylate) and neutral forms of the phenol. The calculation details on the rate constants of neutral and ion forms with <sup>3</sup>DMB\* at pH 5 are shown in Section S2.5. The resulting rate constants are:  $k_{\text{HFA}+\text{3DMB}^*} = 2.2 (\pm 0.45) \times 10^9 \text{ M}^{-1} \text{ s}^{-1}$ ,  $k_{\text{FA}+\text{3DMB}^*} = 0.31 (\pm 0.36) \times 10^9 \text{ M}^{-1} \text{ s}^{-1}$ ,  $k_{\text{SyrCOOH}+\text{3DMB}^*} = 1.8 (\pm 0.44) \times 10^9 \text{ M}^{-1} \text{ s}^{-1}$ , and  $k_{\text{SyrCOOH}+\text{3DMB}^*} = 2.2 (\pm 0.64) \times 10^9 \text{ M}^{-1} \text{ s}^{-1}$ .

**Section S2.5:** Determination of  $k_{ArOH+{}^3DMB^*}$  for the neutral and ion (carboxylate) forms of FA and SyrAcid at pH 5

FA and SyrAcid have carboxylic acid groups (with  $pK_a$  values of 4.6 and 4.2, respectively)<sup>47</sup> that at pH 5 will partially deprotonate to form carboxylate ions. Therefore, the apparent reaction rate constants of FA and SyrAcid with  ${}^3DMB^*$  at pH 5 represent the reactivity of a mixture of the neutral and carboxylate forms of the phenols:

$$k_{ArOH+T} = \alpha_{PhCOOH} \times k_{PhCOOH+T} + \alpha_{PhCOO^-} \times k_{PhCOO^-+T} \quad (S2.5)$$

where PhCOOH represents the neutral form, PhCOO<sup>-</sup> is the carboxylate (i.e., ion) form,  $k_{PhCOOH+T}$  and  $k_{PhCOO^-+T}$  values are the second-order rate constants for each form with the neutral DMB triplet state (T), and  $\alpha$  represents the mole fraction of each phenol species. For our other phenols with the base structure of guaiacol (2-methoxyphenol), the ratios of the second-order rate constants at pH 5 to those at pH 2, where the DMB triplet is protonated, (i.e.  $k_{ArOH+T}/k_{ArOH+HT}$ ) have an average ( $\pm 1 \sigma$ ) value of 0.63 ( $\pm 0.11$ ). Therefore, we assume that FA, which also has the base structure of guaiacol, has the same ratio for its neutral form in order to estimate the value of  $k_{HFA+T}$ . We can then use this value, along with the mole fractions, in Equation S2.5 to determine the rate constant for the carboxylate form of FA,  $k_{FA+T}$ . For syringic acid, which has a base structure of syringol (2,6-dimethoxyphenol), we use a similar assumption and the average ( $\pm 1 \sigma$ ) ratio of  $k_{ArOH+T}/k_{ArOH+HT}$  for phenols based on syringol of 0.57 ( $\pm 0.07$ ). Using this method, we calculated rate constants for the neutral and ion forms of FA and SyrAcid with  ${}^3DMB^*$ ; values are shown in the footnote of Table S2.4.



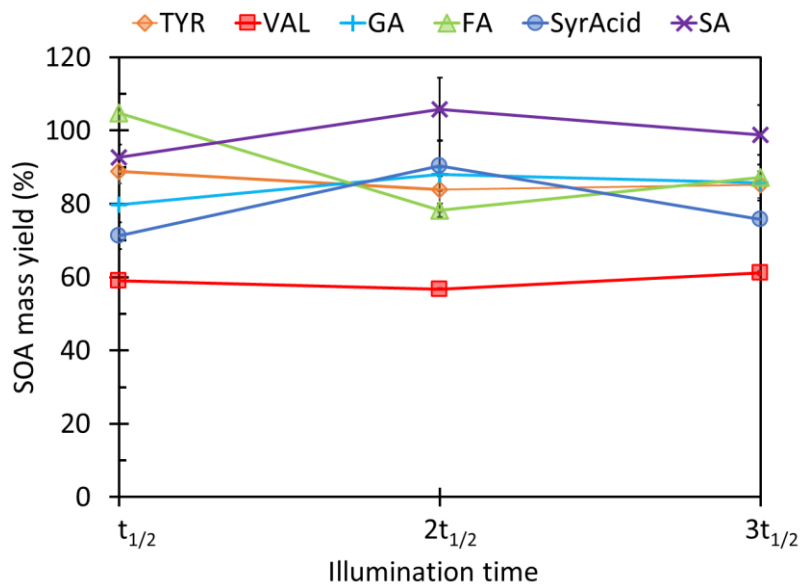


**Figure S2.6:** Time series of SOA mass yields during illumination, plotted at one, two, three half-lives of each phenol. Error bars are standard deviations of  $Y_{\text{SOA}}$  at each half-life from duplicate samples (except for FA at  $3t_{1/2}$ , where an outlier was removed and only one sample was available). In the calculation of the mean  $Y_{\text{SOA}}$  value for a given phenol shown in Figure 2.3,  $Y_{\text{SOA}}$  values at one, two, and three half-lives are used.

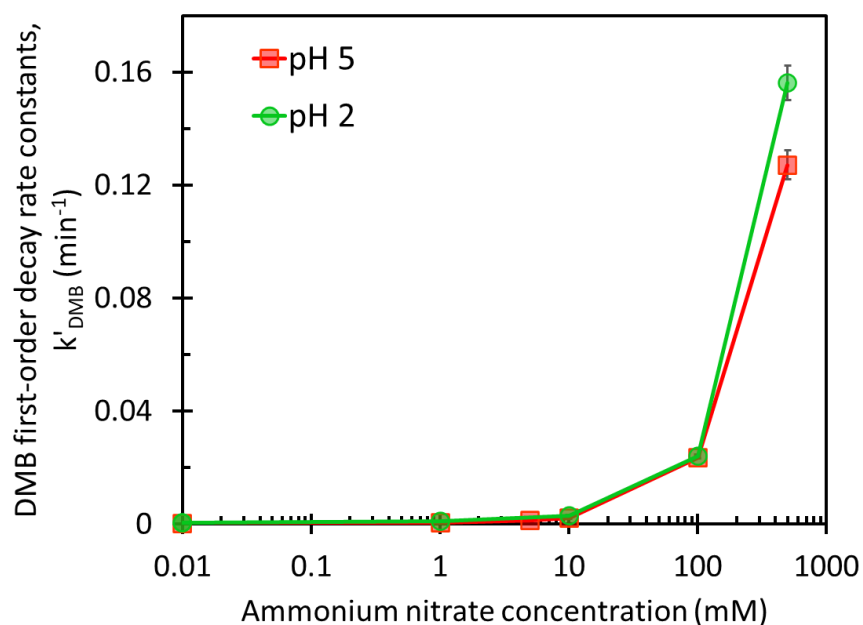


**Figure S2.7:** The dependence of the first-order rate constant of DMB decay on the concentration of ammonium nitrate at pH 5 and 2 after correcting for light screening due to nitrate. Since a zero value cannot be plotted on the logarithmic x-axis, we plot results for no added solutes (i.e., 0 mM ammonium nitrate) at a concentration of 0.01 mM. Error bars represent  $\pm 1$  standard error in  $k'_{\text{DMB}}$  determined from the linear regression fits. Data are not corrected for light screening by nitrate.

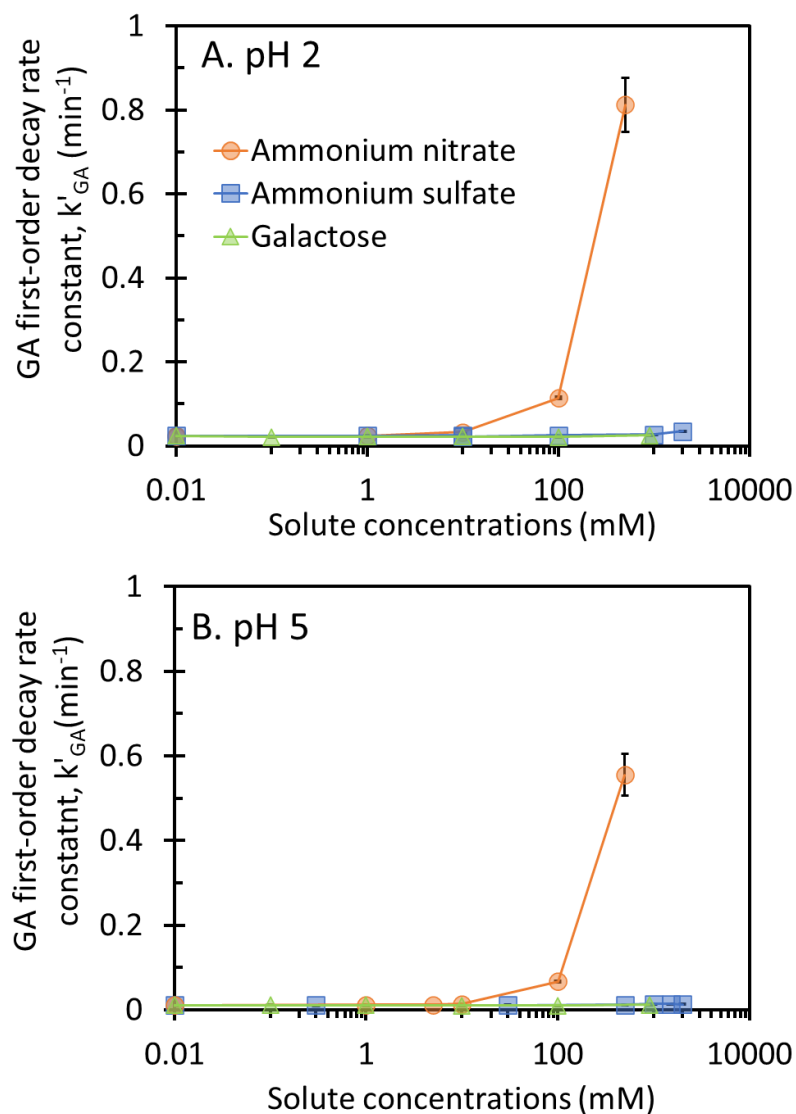


**Figure S2.8:** Dependence of the first-order rate constant of GA decay on the concentration of ammonium nitrate (orange circles), ammonium sulfate (blue squares), and galactose (green triangles) after correcting for light screening by nitrate. Since a zero value cannot be plotted on the logarithmic x-axis, we plot results for no added solutes at a solute concentration of 0.01 mM. Error bars represent  $\pm 1$  standard error in  $k'_{GA}$  from linear regression fits. The light screening factors for solutions containing 0, 1, 10, 100, and 500 mM nitrate are 0.85 (due to DMB light absorption), 0.84, 0.79, 0.45, and 0.15, respectively. A screening factor of 1 represents no screening, while smaller values indicate increasingly larger screenings.

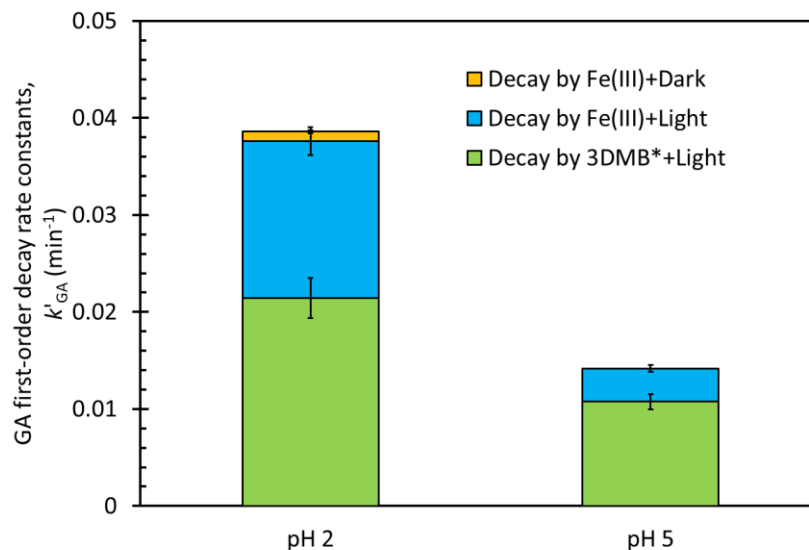


**Figure S2.9.** Decay of GA by <sup>3</sup>DMB\* in the presence of Fe(III). The whole bars represent the total decay rates of GA in illuminated solutions containing both 20  $\mu\text{M}$  FeCl<sub>3</sub> and 10  $\mu\text{M}$  DMB. The yellow portion of the pH 2 bar is the dark decay of GA by Fe(III) in a solution with no DMB; the dark loss of GA in the presence of iron at pH 5 is negligible. The blue bars represent the decay rates of GA measured in illuminated solution containing 20  $\mu\text{M}$  FeCl<sub>3</sub> but no DMB. The green bars are the decay rates of GA by <sup>3</sup>DMB\* after subtraction of its decay by Fe(III) under illumination and in the dark. Error bars represent  $\pm 1$  standard error in  $k'_{\text{GA}}$  from linear regression fits.

**Table S2.5:** Oxidation potentials ( $E_{\text{ox}}$ ) computed by Gaussian 09 and measured using cyclic voltammetry (CV). All data in Volts vs. SHE.

Compounds	Gaussian 09	Cyclic voltammetry		Suatoni <i>et al.</i> <sup>77</sup>	Pavitt <i>et al.</i> <sup>78</sup>
		pH 2	pH 5	pH 5.6	pH 5.6
Phenol	1.65	1.28	1.08	0.874	0.997
Guaiacol	0.99	1.03	0.89	0.697	0.774
Syringol	1.16	0.88	0.77	0.620	0.635
Catechol	1.36	0.81	0.73		0.582
Resorcinol	1.47	1.17	1.04		0.945
Hydroquinone	1.17	0.73	0.63		0.509
TYR	1.35	1.17	1.01		
VAL	1.16	1.01	0.83		
GA	1.07	1.00	0.84		
FA	1.26	1.02	0.78		
SyrAcid	1.39	1.06	0.78		
SA	0.99	0.86	0.72		

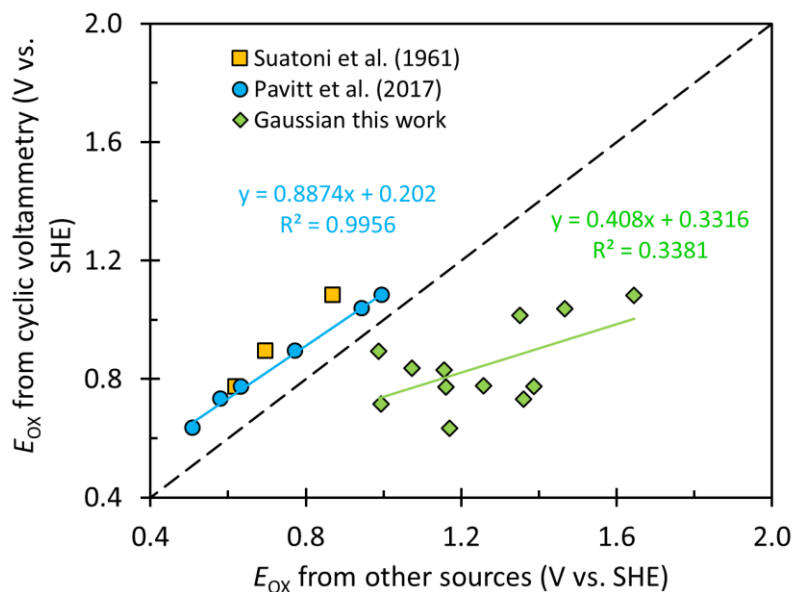


**Figure S2.10:** Comparison of our oxidation potentials measured using cyclic voltammetry with our computed values obtained from Gaussian and measured values from the literature. Since the oxidation potentials from Suatoni *et al.* and Pavitt *et al.* were measured at pH 5.6,<sup>77,78</sup> our CV values measured at pH 5 were used here for comparison. The solid green line represents the linear regression between our values of  $E_{\text{ox}}$  from CV and from Gaussian, with regression function next to it. The dashed line is the 1:1 line.

## Section S2.6: Calculation of SOA formation rates from syringol, guaiacyl acetone, and syringyl acetone

To examine how gas- and aqueous-phase formation of SOA from phenols depends on liquid water content (LWC), we calculated SOA formation rates for syringol (SYR), guaiacyl acetone (GA) and syringyl acetone (SA) in a simple steady-state box model. We varied the LWC from  $0.3 \text{ g m}^{-3}$  (representing a thick fog or cloud) to  $1 \text{ } \mu\text{g m}^{-3}$  (representing a particle water condition) and assumed a temperature of 278 K, Henry's law partitioning for the phenols, a particulate matter concentration of  $10 \text{ } \mu\text{g m}^{-3}$ , an initial concentration of an individual phenol of  $5 \text{ } \mu\text{g m}^{-3}$ , and an aqueous pH of 5. At each LWC value we calculated the corresponding particle mass/water mass ratio and then used the corresponding measured/estimated steady-state aqueous oxidant concentrations ( $\bullet\text{OH}$ ,  $^3\text{C}^*$ ,  $^1\text{O}_2^*$ ) from Kaur *et al.*<sup>28</sup>; for the triplet concentration at a given LWC we used the geometric mean value of the two estimates of Kaur *et al.* In the gas phase we considered ozone (30 ppbv) and  $\bullet\text{OH}$  ( $1 \times 10^6 \text{ molecule cm}^{-3}$ ). Because rate constants of ozone with phenols are quite slow,<sup>98</sup>  $\text{O}_3$  was a negligible sink and we do not show its results. As shown in Table S2.6, bimolecular rate constants of phenols with each oxidant ( $k_{\text{ArOH+Ox}}$ ) at pH 5, and the corresponding SOA mass yields ( $Y_{\text{SOA}}$ ), were obtained from literature when available. When there were no data available, we used data from phenols with a similar structure. Since no  $Y_{\text{SOA}}$  data are available for phenols reacting with  $^1\text{O}_2^*_{(\text{aq})}$ , we assume this value to be 1, consistent with the high yields from other aqueous reactions (Table S2.6). For each oxidant we would expect higher SOA mass yields at 5 °C compared to 20 °C, because there would be less evaporation of semi-volatile organics. However, we cannot experimentally assess the temperature effect on aqSOA mass yields, we use the value of  $Y_{\text{SOA}}$  at 20 °C in these calculations. We do not include the impact of copper on phenol oxidation kinetics or aqSOA formation since this effect is poorly understood and requires more study.

To calculate the initial SOA formation rate, first we calculated the concentrations of phenols in the gas and aqueous phases as a function of liquid water content. The Henry's law constants ( $K_{\text{H}}$ ) of SYR (2.5

$\times 10^4$  M/atm), GA ( $9.1 \times 10^6$  M/atm), and SA ( $6.1 \times 10^8$  M/atm) at 278 K were calculated from measured  $K_H$  at 298 K and the enthalpy of dissolution ( $\Delta H_{sol}$ ):<sup>13,15,35</sup>

$$K_{H,278K} = K_{H,298K} \times \exp\left(\frac{\Delta H_{sol}}{R} \times \left(\frac{1}{298\text{ K}} - \frac{1}{278\text{ K}}\right)\right) \quad (\text{S2.6})$$

Since there is no available  $\Delta H_{sol}$  value for SA, we assume it has the same value as SYR. We calculate  $F(\text{aq})$ , the fraction of each phenol present in the aqueous phase, using:<sup>35</sup>

$$F(\text{aq}) = \frac{1}{1 + \frac{1}{T \times R \times LWC \times K_H}} \quad (\text{S2.7})$$

where LWC is in dimensionless units (L-aq / L-air),  $T$  is the temperature (278 K) and  $R$  is the gas constant ( $0.08206$  L-air atm mol<sup>-1</sup> K<sup>-1</sup>).

The concentration of the phenol in each phase was calculated with:

$$[ArOH]_{aq} = [ArOH]_{tot} \times F(aq) \quad (\text{S2.8})$$

$$[ArOH]_{gas} = [ArOH]_{tot} \times (1 - F(aq)) \quad (\text{S2.9})$$

The initial rate of SOA formation from one phenol reacting with an oxidant was then calculated with:

$$R_{SOA(aq),ox} = k_{ArOH+ox} \times [ArOH]_{aq} \times [Ox]_{aq} \times Y_{SOA(aq),ox} \quad (\text{S2.10})$$

The gas-phase SOA formation rate was calculated with an analogous form of this equation.

**Table S2.6:** Gas- and aqueous-phase reaction rate constants and SOA mass yields for SYR, GA, and SA with the major oxidants

Compounds		Syringol	Syringyl acetone	Guaiacyl acetone
Gas-phase rate constants, $k_{ArOH+Ox(g)}$ ( $\text{cm}^3 \text{ molec}^{-1} \text{ s}^{-1}$ )	$\bullet\text{OH}_{(g)}$	9.66E-11	9.66E-11 <sup>b</sup>	7.53E-11 <sup>c</sup>
	Ref.	(Lauraguais <i>et al.</i> , 2012) <sup>53</sup>		(Coeur-Tourneur <i>et al.</i> , 2010) <sup>99</sup>
Gaseous reaction SOA mass yield, $Y_{SOA(g)}$	$\bullet\text{OH}_{(g)}$	0.32	0.32 <sup>b</sup>	0.47 <sup>c</sup>
	Ref.	(Yee <i>et al.</i> , 2013) <sup>52</sup>		
Aqueous-phase rate constants, $k_{ArOH+Ox(aq)}$ ( $\text{M}^{-1} \text{ s}^{-1}$ )	$\bullet\text{OH}_{(aq)}$	2.0E+10	2.0E+10 <sup>b</sup>	1.6E+10 <sup>c</sup>
	Ref.	(Smith <i>et al.</i> , 2015) <sup>16</sup>		
	$^1\text{O}_2^*_{(aq)}$	3.6E+07	3.6E+07 <sup>b</sup>	6.0E+06 <sup>c</sup>
	Ref.	(Tratnyek and Hoigne, 1991) <sup>100</sup>		
	$^3\text{C}^*_{(aq)}$ <sup>a</sup>	3.5E+09	2.7E+09	1.8E+09
	Ref.	(Smith <i>et al.</i> , 2015) <sup>16</sup>	This work	This work
Aqueous reaction SOA mass yields, $Y_{SOA(aq)}$	$\bullet\text{OH}_{(aq)}$	1.14	1.14 <sup>b</sup>	1.09 <sup>c</sup>
	Ref.	(Smith <i>et al.</i> , 2014) <sup>19</sup>		
	$^1\text{O}_2^*_{(aq)}$	1 <sup>d</sup>	1 <sup>d</sup>	1 <sup>d</sup>
	Ref.	-	-	-
	$^3\text{C}^*_{(aq)}$ <sup>a</sup>	0.83	0.99	0.85
	Ref.	(Smith <i>et al.</i> , 2014) <sup>19</sup>	This work	This work

<sup>a</sup> For triplet excited states we use  $^3\text{DMB}^*$  as the model triplet.

<sup>b</sup> Since literature data is not available for SA, we used the values from syringol.

<sup>c</sup> Since literature data is not available for GA, we used values from guaiacol.

<sup>d</sup> No literature data is available for the SOA mass yield from phenols with  $^1\text{O}_2^*$ , so we assumed a value of 1, consistent with the high yields for the other two aqueous oxidants.



## Section S2.7: Determination of intersystem crossing quantum yield

Smith *et al.*<sup>16</sup> determined the intersystem crossing (ISC) quantum yield for DMB ( $\Phi_{\text{ISC}}$ ), and explained the method in their supplemental information. Because their quantum yield has a relatively large uncertainty (with a relative standard deviation of 30%), which contributes to a large uncertainty in the derived second-order rate constants, we used their method to make additional measurements of  $\Phi_{\text{ISC}}$  and reduce its uncertainty. Briefly, we illuminated solutions containing 5 – 200  $\mu\text{M}$  SYR and 10  $\mu\text{M}$  DMB at pH 5 in a monochromatic illumination system using light of 313 nm to measure the SYR loss rate. Next, we did a linear fitting of the inverse of the rate of SYR loss ( $R_{\text{SYR,L,exp}}^{-1}$ ) versus the inverse of the initial SYR concentration to obtain the rate of SYR loss at infinite concentration ( $R_{\text{ArOH,L},\infty}$ ), which is the inverse of the y-intercept from the linear fitting. This rate is equal to the rate of triplet excited state formation ( $R_{3\text{C}^*,\text{F}}$ ) times the fraction of triplet interacting with phenols that leads to the decay of phenols ( $f_{\text{reaction}}$ ). We use SYR as the model phenol because its value of  $f_{\text{reaction}}$  is essentially 1. Therefore,  $R_{\text{ArOH,L},\infty}$  essentially equals the formation rate of the triplet excited state, allowing us to determine the ISC quantum yield using:

$$\Phi_{\text{ISC}} = \frac{R_{\text{ArOH,L},\infty}}{2.303 \times \varepsilon_{313,\text{DMB}} \times l \times I'_{313} \times [\text{DMB}]} \quad (\text{S2.11})$$

where  $\varepsilon_{313,\text{DMB}}$  is the molar absorptivity of DMB at 313 nm,  $l$  is the cell pathlength, and  $I'_{313}$  is the actinic flux at 313 nm. This actinic flux was determined from  $j_{2\text{NB}}$ , the decay rate constant of the actinometer 2-nitrobenzaldehyde (2-NB), which was measured on each experiment day. Results of our two new sets of experiments for the determination of  $R_{\text{ArOH,L},\infty}$  are shown in Figure S2.11. With Equation S2.11, we calculated  $\Phi_{\text{ISC}}$  values of  $0.087 \pm 0.007$  and  $0.092 \pm 0.011$ . As shown in Table S2.7, we combined these data with results from Smith *et al.* to determine an average ( $\pm 1\sigma$ ) value of  $\Phi_{\text{ISC}}$  of  $0.095 \pm 0.017$ . This new average is very similar to the previously used value ( $0.10 \pm 0.03$ ) but has a smaller uncertainty.

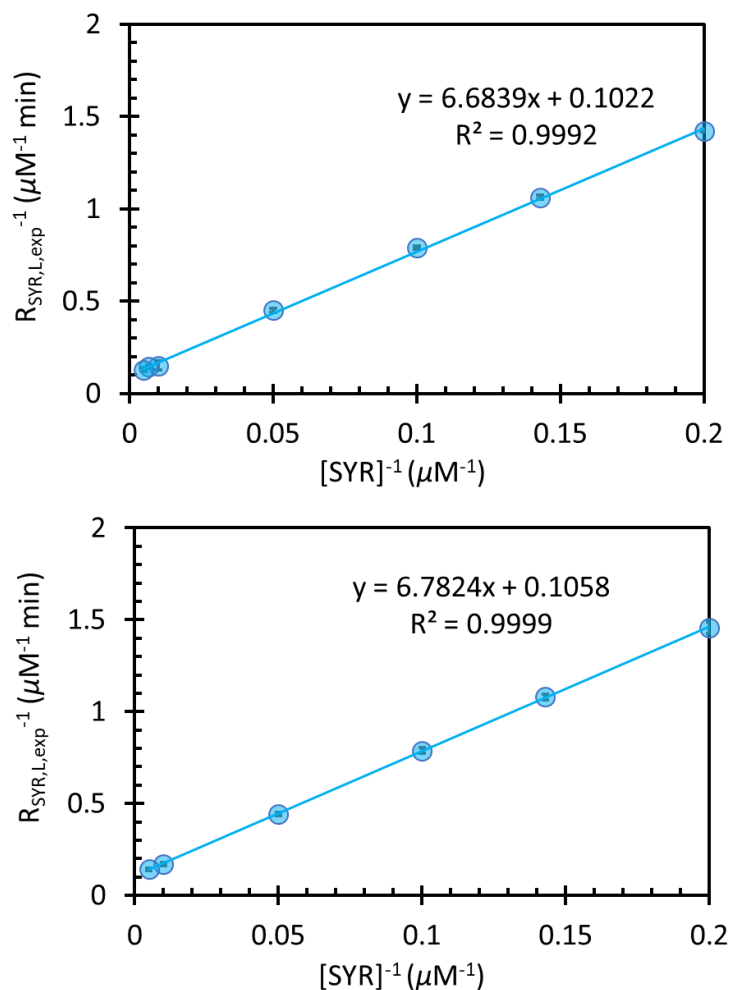


**Figure S2.11:** Experimental results of the decay of SYR reacting with  $^3\text{DMB}^*$  at 313 nm: the inverse of SYR loss rate versus the inverse of SYR initial concentration for two sets of independent experiments. The y-intercept is the inverse of the SYR loss rate at infinite SYR concentration. Error bars (which are smaller than the symbols) represent  $\pm 1$  standard error, propagated from standard errors in the linear fittings used to obtain  $R_{\text{SYR,L,exp}}$ .

**Table S2.7:** Summary of the quantum yield of  $^3\text{DMB}^*$  intersystem crossing

	$\Phi_{\text{ISC}}$
Smith <i>et al.</i> <sup>16</sup>	0.12 ( $\pm 0.01$ ) <sup>a</sup>
	0.08 ( $\pm 0.01$ ) <sup>a</sup>
This work	0.087 ( $\pm 0.007$ ) <sup>a</sup>
	0.092 ( $\pm 0.011$ ) <sup>a</sup>
Mean ( $\pm \sigma$ )	0.095 ( $\pm 0.017$ ) <sup>b</sup>

<sup>a</sup>Standard error propagated from errors in  $R_{\text{SYR,L},\infty}$ ,  $\epsilon_{313,\text{DMB}}$ , and  $I'_{313}$ .

<sup>b</sup>Standard deviation of  $\Phi_{\text{ISC}}$  determined as the average of all four experiments.

## 2.8. References

- (1) Sommers, W. T.; Loehman, R. A.; Hardy, C. C. Wildland fire emissions, carbon, and climate: science overview and knowledge needs. *For. Ecol. Manag.* **2014**, *317*, 1–8.
- (2) Pöschl, U. Atmospheric aerosols: composition, transformation, climate and health effects. *Angew. Chem. Int. Ed. Engl.* **2005**, *44*, 7520–7540.
- (3) Hallquist, M.; Wenger, J. C.; Baltensperger, U.; Rudich, Y.; Simpson, D.; Claeys, M.; Dommen, J.; Donahue, N. M.; George, C.; Goldstein, A. H.; et al. The formation, properties and impact of secondary organic aerosol: current and emerging issues. *Atmos. Chem. Phys.* **2009**, *9*, 5155–5236.
- (4) Ervens, B.; Turpin, B. J.; Weber, R. J. Secondary organic aerosol formation in cloud droplets and aqueous particles (aqSOA): a review of laboratory, field and model studies. *Atmos. Chem. Phys.* **2011**, *11*, 11069–11102.
- (5) McNeill, V. F. Aqueous organic chemistry in the atmosphere: sources and chemical processing of organic aerosols. *Environ. Sci. Technol.* **2015**, *49*, 1237–1244.
- (6) Herrmann, H.; Schaefer, T.; Tilgner, A.; Styler, S. A.; Weller, C.; Teich, M.; Otto, T. Tropospheric aqueous-phase chemistry: kinetics, mechanisms, and its coupling to a changing gas phase. *Chem. Rev.* **2015**, *115*, 4259–4334.
- (7) Bond, T. C.; Streets, D. G.; Yarber, K. F.; Nelson, S. M.; Woo, J.; Klimont, Z. A technology-based global inventory of black and organic carbon emissions from combustion. *J. Geophys. Res. Atmos.* **2004**, *109*.
- (8) Bruns, E. A.; El Haddad, I.; Slowik, J. G.; Kilic, D.; Klein, F.; Baltensperger, U.; Prévôt, A. S. H. Identification of significant precursor gases of secondary organic aerosols from residential wood combustion. *Sci. Rep.* **2016**, *6*, 27881.
- (9) Oros, D. R.; Simoneit, B. R. . Identification and emission factors of molecular tracers in organic aerosols from biomass burning Part 1. Temperate climate conifers. *Applied Geochemistry* **2001**, *16*, 1513–1544.
- (10) Schauer, J. J.; Kleeman, M. J.; Cass, G. R.; Simoneit, B. R. Measurement of emissions from air pollution sources. 3. C1-C29 organic compounds from fireplace combustion of wood. *Environ. Sci. Technol.* **2001**, *35*, 1716–1728.
- (11) Simoneit, B. R. . Biomass burning — a review of organic tracers for smoke from incomplete combustion. *Applied Geochemistry* **2002**, *17*, 129–162.
- (12) Andreae, M. O. Emission of trace gases and aerosols from biomass burning – an updated assessment. *Atmos. Chem. Phys.* **2019**, *19*, 8523–8546.
- (13) Sagebiel, J. C.; Seiber, J. N.; Woodrow, J. E. Comparison of headspace and gas-stripping methods for determining the Henry’s law constant (H) for organic compounds of low to intermediate H. *Chemosphere* **1992**, *25*, 1763–1768.
- (14) Feigenbrugel, V.; Le Calvé, S.; Mirabel, P.; Louis, F. Henry’s law constant measurements for phenol, o-, m-, and p-cresol as a function of temperature. *Atmospheric Environment* **2004**, *38*, 5577–5588.
- (15) McFall, A. S.; Johnson, A. W.; Anastasio, C. Air-Water Partitioning of Biomass-Burning Phenols and the Effects of Temperature and Salinity. *Environ. Sci. Technol.* **2020**, *54*, 3823–3830.
- (16) Smith, J. D.; Kinney, H.; Anastasio, C. Aqueous benzene-diols react with an organic triplet excited state and hydroxyl radical to form secondary organic aerosol. *Phys. Chem. Chem. Phys.* **2015**, *17*, 10227–10237.

- (17) Sun, Y. L.; Zhang, Q.; Anastasio, C.; Sun, J. Insights into secondary organic aerosol formed via aqueous-phase reactions of phenolic compounds based on high resolution mass spectrometry. *Atmos. Chem. Phys.* **2010**, *10*, 4809–4822.
- (18) Vione, D.; Maurino, V.; Minero, C.; Duncianu, M.; Olariu, R.-I.; Arsene, C.; Sarakha, M.; Mailhot, G. Assessing the transformation kinetics of 2-and 4-nitrophenol in the atmospheric aqueous phase. Implications for the distribution of both nitroisomers in the atmosphere. *Atmospheric Environment* **2009**, *43*, 2321–2327.
- (19) Smith, J. D.; Sio, V.; Yu, L.; Zhang, Q.; Anastasio, C. Secondary organic aerosol production from aqueous reactions of atmospheric phenols with an organic triplet excited state. *Environ. Sci. Technol.* **2014**, *48*, 1049–1057.
- (20) Anastasio, C.; Faust, B. C.; Rao, C. J. Aromatic carbonyl compounds as aqueous-phase photochemical sources of hydrogen peroxide in acidic sulfate aerosols, fogs, and clouds. 1. Non-phenolic methoxybenzaldehydes and methoxyacetophenones with reductants (phenols). *Environ. Sci. Technol.* **1996**, *31*, 218–232.
- (21) Rossignol, S.; Aregahegn, K. Z.; Tinel, L.; Fine, L.; Nozière, B.; George, C. Glyoxal induced atmospheric photosensitized chemistry leading to organic aerosol growth. *Environ. Sci. Technol.* **2014**, *48*, 3218–3227.
- (22) Aregahegn, K. Z.; Nozière, B.; George, C. Organic aerosol formation photo-enhanced by the formation of secondary photosensitizers in aerosols. *Faraday Discuss* **2013**, *165*, 123–134.
- (23) Mekić, M.; Liu, J.; Zhou, W.; Loisel, G.; Cai, J.; He, T.; Jiang, B.; Yu, Z.; Lazarou, Y. G.; Li, X.; et al. Formation of highly oxygenated multifunctional compounds from cross-reactions of carbonyl compounds in the atmospheric aqueous phase. *Atmos. Environ.* **2019**, *219*, 117046.
- (24) Xia, S.-S.; Eugene, A. J.; Guzman, M. I. Cross photoreaction of glyoxylic and pyruvic acids in model aqueous aerosol. *J. Phys. Chem. A* **2018**, *122*, 6457–6466.
- (25) Wang, X.; Gemayel, R.; Hayeck, N.; Perrier, S.; Charbonnel, N.; Xu, C.; Chen, H.; Zhu, C.; Zhang, L.; Wang, L.; et al. Atmospheric photosensitization: A new pathway for sulfate formation. *Environ. Sci. Technol.* **2020**, *54*, 3114–3120.
- (26) Herrmann, H.; Hoffmann, D.; Schaefer, T.; Brüner, P.; Tilgner, A. Tropospheric aqueous-phase free-radical chemistry: radical sources, spectra, reaction kinetics and prediction tools. *ChemPhysChem* **2010**, *11*, 3796–3822.
- (27) Kaur, R.; Anastasio, C. First measurements of organic triplet excited states in atmospheric waters. *Environ. Sci. Technol.* **2018**, *52*, 5218–5226.
- (28) Kaur, R.; Labins, J. R.; Helbock, S. S.; Jiang, W.; Bein, K. J.; Zhang, Q.; Anastasio, C. Photooxidants from brown carbon and other chromophores in illuminated particle extracts. *Atmos. Chem. Phys.* **2019**, *19*, 6579–6594.
- (29) Buxton, G. V.; Greenstock, C. L.; Helman, W. P.; Ross, A. B. Critical Review of rate constants for reactions of hydrated electrons, hydrogen atoms and hydroxyl radicals ( $\bullet\text{OH}/\bullet\text{O}^-$  in Aqueous Solution). *J. Phys. Chem. Ref. Data* **1988**, *17*, 513–886.
- (30) Yu, L.; Smith, J.; Laskin, A.; Anastasio, C.; Laskin, J.; Zhang, Q. Chemical characterization of SOA formed from aqueous-phase reactions of phenols with the triplet excited state of carbonyl and hydroxyl radical. *Atmos. Chem. Phys.* **2014**, *14*, 13801–13816.
- (31) Herrmann, H. Kinetics of aqueous phase reactions relevant for atmospheric chemistry. *Chem. Rev.* **2003**, *103*, 4691–4716.

- (32) Volkamer, R.; San Martini, F.; Molina, L. T.; Salcedo, D.; Jimenez, J. L.; Molina, M. J. A missing sink for gas-phase glyoxal in Mexico City: Formation of secondary organic aerosol. *Geophys. Res. Lett.* **2007**, *34*.
- (33) Faust, J. A.; Wong, J. P. S.; Lee, A. K. Y.; Abbatt, J. P. D. Role of Aerosol Liquid Water in Secondary Organic Aerosol Formation from Volatile Organic Compounds. *Environ. Sci. Technol.* **2017**, *51*, 1405–1413.
- (34) Nguyen, T. K. V.; Zhang, Q.; Jimenez, J. L.; Pike, M.; Carlton, A. G. Liquid water: ubiquitous contributor to aerosol mass. *Environ. Sci. Technol. Lett.* **2016**, *3*, 257–263.
- (35) Seinfeld, J. H.; Pandis, S. N. *Atmospheric Chemistry And Physics: From Air Pollution To Climate Change*; 3rd ed.; Wiley: Hoboken, New Jersey, 2016; p. 1152.
- (36) Mekic, M.; Brigante, M.; Vione, D.; Gligorovski, S. Exploring the ionic strength effects on the photochemical degradation of pyruvic acid in atmospheric deliquescent aerosol particles. *Atmos. Environ.* **2018**, *185*, 237–242.
- (37) Zhou, W.; Mekic, M.; Liu, J.; Loisel, G.; Jin, B.; Vione, D.; Gligorovski, S. Ionic strength effects on the photochemical degradation of acetosyringone in atmospheric deliquescent aerosol particles. *Atmos. Environ.* **2019**, *198*, 83–88.
- (38) Parworth, C. L.; Young, D. E.; Kim, H.; Zhang, X.; Cappa, C. D.; Collier, S.; Zhang, Q. Wintertime water-soluble aerosol composition and particle water content in Fresno, California. *J. Geophys. Res. Atmos.* **2017**, *122*, 3155–3170.
- (39) Oros, D. R.; Simoneit, B. R. Identification and emission factors of molecular tracers in organic aerosols from biomass burning Part 2. Deciduous trees. *Applied Geochemistry* **2001**, *16*, 1545–1565.
- (40) Zangrando, R.; Barbaro, E.; Zennaro, P.; Rossi, S.; Kehrwald, N. M.; Gabrieli, J.; Barbante, C.; Gambaro, A. Molecular markers of biomass burning in Arctic aerosols. *Environ. Sci. Technol.* **2013**, *47*, 8565–8574.
- (41) Hoffmann, D.; Iinuma, Y.; Herrmann, H. Development of a method for fast analysis of phenolic molecular markers in biomass burning particles using high performance liquid chromatography/atmospheric pressure chemical ionisation mass spectrometry. *J. Chromatogr. A* **2007**, *1143*, 168–175.
- (42) Fleming, L. T.; Lin, P.; Roberts, J. M.; Selimovic, V.; Yokelson, R.; Laskin, J.; Laskin, A.; Nizkorodov, S. A. Molecular composition and photochemical lifetimes of brown carbon chromophores in biomass burning organic aerosol. *Atmos. Chem. Phys.* **2020**, *20*, 1105–1129.
- (43) Anastasio, C.; McGregor, K. G. Chemistry of fog waters in California's Central Valley: 1. In situ photoformation of hydroxyl radical and singlet molecular oxygen. *Atmos. Environ.* **2001**, *35*, 1079–1089.
- (44) Jiang, W.; Misovich, M. H.; Anusha Priyadarshani Silva; McFall, A.; Anastasio, C.; Zhang, Q. Photosensitized Reactions of a Phenolic Carbonyl from Wood Combustion in the Aqueous Phase – Chemical Evolution and Light Absorption Properties of AqSOA. *Environ. Sci. Technol.* **2021**.
- (45) Canonica, S.; Hoigné, J. Enhanced oxidation of methoxy phenols at micromolar concentration photosensitized by dissolved natural organic material. *Chemosphere* **1995**, *30*, 2365–2374.
- (46) Ragnar, M.; Lindgren, C. T.; Nilvebrant, N.-O. pK<sub>a</sub> -Values of Guaiacyl and Syringyl Phenols Related to Lignin. *Journal of Wood Chemistry and Technology* **2000**, *20*, 277–305.
- (47) Erdemgil, F. Z.; Şanlı, S.; Şanlı, N.; Özkan, G.; Barbosa, J.; Guiteras, J.; Beltran, J. L. Determination of pK<sub>a</sub> values of some hydroxylated benzoic acids in methanol–water binary mixtures by LC methodology and potentiometry. *Talanta* **2007**, *72*, 489–496.

- (48) Canonica, S.; Hellrung, B.; Wirz, J. Oxidation of phenols by triplet aromatic ketones in aqueous solution. *The Journal of Physical Chemistry A* **2000**, *104*, 1226–1232.
- (49) Jonsson, M.; Lind, J.; Reitberger, T.; Eriksen, T. E.; Merenyi, G. Free radical combination reactions involving phenoxy radicals. *The Journal of Physical Chemistry* **1993**, *97*, 8229–8233.
- (50) Grebel, J. E.; Pignatello, J. J.; Mitch, W. A. Sorbic acid as a quantitative probe for the formation, scavenging and steady-state concentrations of the triplet-excited state of organic compounds. *Water Res.* **2011**, *45*, 6535–6544.
- (51) Schmitt, M.; Moor, K. J.; Erickson, P. R.; McNeill, K. Sorbic acid as a triplet probe: reactivity of oxidizing triplets in dissolved organic matter by direct observation of aromatic amine oxidation. *Environ. Sci. Technol.* **2019**, *53*, 8087–8096.
- (52) Yee, L. D.; Kautzman, K. E.; Loza, C. L.; Schilling, K. A.; Coggon, M. M.; Chhabra, P. S.; Chan, M. N.; Chan, A. W. H.; Hersey, S. P.; Crouse, J. D.; et al. Secondary organic aerosol formation from biomass burning intermediates: phenol and methoxyphenols. *Atmos. Chem. Phys.* **2013**, *13*, 8019–8043.
- (53) Lauraguais, A.; Coeur-Tourneur, C.; Cassez, A.; Seydi, A. Rate constant and secondary organic aerosol yields for the gas-phase reaction of hydroxyl radicals with syringol (2, 6-dimethoxyphenol). *Atmos. Environ.* **2012**, *55*, 43–48.
- (54) Tang, I. N.; Munkelwitz, H. R. Water activities, densities, and refractive indices of aqueous sulfates and sodium nitrate droplets of atmospheric importance. *J. Geophys. Res. Atmos.* **1994**, *99*, 18801–18808.
- (55) Sareen, N.; Schwier, A. N.; Shapiro, E. L.; Mitroo, D.; McNeill, V. F. Secondary organic material formed by methylglyoxal in aqueous aerosol mimics. *Atmos. Chem. Phys.* **2010**, *10*, 997–1016.
- (56) Parker, K. M.; Pignatello, J. J.; Mitch, W. A. Influence of ionic strength on triplet-state natural organic matter loss by energy transfer and electron transfer pathways. *Environ. Sci. Technol.* **2013**, *47*, 10987–10994.
- (57) Grebel, J. E.; Pignatello, J. J.; Mitch, W. A. Impact of halide ions on natural organic matter-sensitized photolysis of 17 $\beta$ -estradiol in saline waters. *Environ. Sci. Technol.* **2012**, *46*, 7128–7134.
- (58) Simoneit, B. R.; Schauer, J. J.; Nolte, C. G.; Oros, D. R.; Elias, V. O.; Fraser, M. P.; Rogge, W. F.; Cass, G. R. Levoglucosan, a tracer for cellulose in biomass burning and atmospheric particles. *Atmospheric Environment* **1999**, *33*, 173–182.
- (59) Mao, J.; Fan, S.; Jacob, D. J.; Travis, K. R. Radical loss in the atmosphere from Cu-Fe redox coupling in aerosols. *Atmos. Chem. Phys.* **2013**, *13*, 509–519.
- (60) Deguillaume, L.; Leriche, M.; Desboeufs, K.; Mailhot, G.; George, C.; Chaumerliac, N. Transition metals in atmospheric liquid phases: sources, reactivity, and sensitive parameters. *Chem. Rev.* **2005**, *105*, 3388–3431.
- (61) Brezonik, P. L.; Fulkerson-Brekken, J. Nitrate-Induced Photolysis in Natural Waters: Controls on Concentrations of Hydroxyl Radical Photo-Intermediates by Natural Scavenging Agents. *Environ. Sci. Technol.* **1998**, *32*, 3004–3010.
- (62) Chu, L.; Anastasio, C. Quantum Yields of Hydroxyl Radical and Nitrogen Dioxide from the Photolysis of Nitrate on Ice. *J. Phys. Chem. A* **2003**, *107*, 9594–9602.
- (63) Ming, G.; Zhenhao, D. Prediction of oxygen solubility in pure water and brines up to high temperatures and pressures. *Geochim. Cosmochim. Acta* **2010**, *74*, 5631–5640.
- (64) Millero, F. J.; Huang, F.; Laferiere, A. L. The solubility of oxygen in the major sea salts and their mixtures at 25 C. *Geochim. Cosmochim. Acta* **2002**, *66*, 2349–2359.

- (65) Feng, W.; Nansheng, D. Photochemistry of hydrolytic iron (III) species and photoinduced degradation of organic compounds. A minireview. *Chemosphere* **2000**, *41*, 1137–1147.
- (66) Pang, H.; Zhang, Q.; Wang, H.; Cai, D.; Ma, Y.; Li, L.; Li, K.; Lu, X.; Chen, H.; Yang, X.; et al. Photochemical Aging of Guaiacol by Fe(III)-Oxalate Complexes in Atmospheric Aqueous Phase. *Environ. Sci. Technol.* **2019**, *53*, 127–136.
- (67) Khanra, S.; Minero, C.; Maurino, V.; Pelizzetti, E.; Dutta, B. K.; Vione, D. Phenol transformation induced by UVA photolysis of the complex FeCl<sub>2</sub><sup>+</sup>. *Environ Chem Lett* **2008**, *6*, 29–34.
- (68) Pan, Y.; Garg, S.; Waite, T. D.; Yang, X. Copper Inhibition of Triplet-Induced Reactions Involving Natural Organic Matter. *Environ. Sci. Technol.* **2018**, *52*, 2742–2750.
- (69) Pan, Y.; Ruan, X.; Garg, S.; Waite, T. D.; Lei, Y.; Yang, X. Copper Inhibition of Triplet-Sensitized Phototransformation of Phenolic and Amine Contaminants. *Environ. Sci. Technol.* **2020**, *54*, 9980–9989.
- (70) Buerge-Weirich, D.; Sulzberger, B. Formation of Cu(I) in Estuarine and Marine Waters: Application of a New Solid-Phase Extraction Method To Measure Cu(I). *Environ. Sci. Technol.* **2004**, *38*, 1843–1848.
- (71) Bielski, B. H. J.; Cabelli, D. E.; Arudi, R. L.; Ross, A. B. Reactivity of HO<sub>2</sub>/O<sub>2</sub><sup>-</sup> radicals in aqueous solution. *J. Phys. Chem. Ref. Data* **1985**, *14*, 1041–1100.
- (72) Rabani, J.; Klug-Roth, D.; Lilie, J. Pulse radiolytic investigations of the catalyzed disproportionation of peroxy radicals. Aqueous cupric ions. *J. Phys. Chem.* **1973**, *77*, 1169–1175.
- (73) Chan, L. K.; Nguyen, K. Q.; Karim, N.; Yang, Y.; Rice, R. H.; He, G.; Denison, M. S.; Nguyen, T. B. Relationship between the molecular composition, visible light absorption, and health-related properties of smoldering woodsmoke aerosols. *Atmos. Chem. Phys.* **2020**, *20*, 539–559.
- (74) Kaur, R.; Hudson, B. M.; Draper, J.; Tantillo, D. J.; Anastasio, C. Aqueous reactions of organic triplet excited states'' with atmospheric alkenes. *Atmos. Chem. Phys.* **2019**, *19*, 5021–5032.
- (75) Arnold, W. A. One electron oxidation potential as a predictor of rate constants of N-containing compounds with carbonate radical and triplet excited state organic matter. *Environ. Sci. Process. Impacts* **2014**, *16*, 832–838.
- (76) Arnold, W. A.; Oueis, Y.; O'Connor, M.; Rinaman, J. E.; Taggart, M. G.; McCarthy, R. E.; Foster, K. A.; Latch, D. E. QSARs for phenols and phenolates: oxidation potential as a predictor of reaction rate constants with photochemically produced oxidants. *Environmental Science: Processes & Impacts* **2017**, *19*, 324–338.
- (77) Suatoni, J. C.; Snyder, R. E.; Clark, R. O. Voltammetric studies of phenol and aniline ring substitution. *Anal. Chem.* **1961**, *33*, 1894–1897.
- (78) Pavitt, A. S.; Bylaska, E. J.; Tratnyek, P. G. Oxidation potentials of phenols and anilines: correlation analysis of electrochemical and theoretical values. *Environ. Sci. Process. Impacts* **2017**, *19*, 339–349.
- (79) Li, C.; Hoffman, M. Z. One-Electron Redox Potentials of Phenols in Aqueous Solution. *J. Phys. Chem. B* **1999**, *103*, 6653–6656.
- (80) Winget, P.; Cramer, C. J.; Truhlar, D. G. Computation of equilibrium oxidation and reduction potentials for reversible and dissociative electron-transfer reactions in solution. *Theor. Chem. Acc.* **2004**, *112*.
- (81) *Chapter A6. section 6.2. dissolved oxygen*; 2006.
- (82) Smith, J. D.; Kinney, H.; Anastasio, C. Phenolic carbonyls undergo rapid aqueous photodegradation to form low-volatility, light-absorbing products. *Atmos. Environ.* **2016**, *126*, 36–44.



- (83) Dallin, E.; Wan, P.; Krogh, E.; Gill, C.; Moore, R. M. New pH-dependent photosubstitution pathways of syringic acid in aqueous solution: Relevance in environmental photochemistry. *J. Photochem. Photobiol. A* **2009**, *207*, 297–305.
- (84) Huang, D. D.; Zhang, Q.; Cheung, H. H. Y.; Yu, L.; Zhou, S.; Anastasio, C.; Smith, J. D.; Chan, C. K. Formation and Evolution of aqSOA from Aqueous-Phase Reactions of Phenolic Carbonyls: Comparison between Ammonium Sulfate and Ammonium Nitrate Solutions. *Environ. Sci. Technol.* **2018**, *52*, 9215–9224.
- (85) Daellenbach, K. R.; Bozzetti, C.; Křepelová, A.; Canonaco, F.; Wolf, R.; Zotter, P.; Fermo, P.; Crippa, M.; Slowik, J. G.; Sosedova, Y.; et al. Characterization and source apportionment of organic aerosol using offline aerosol mass spectrometry. *Atmos. Meas. Tech.* **2016**, *9*, 23–39.
- (86) *Handbook of Electrochemistry*; Elsevier, 2007.
- (87) M. J. Frisch, G. W. T.; M. A. Robb, J. R. C.; G. A. Petersson, H. N.; A. F. Izmaylov, J. B.; M. Ehara, K. T.; Y. Honda, O. K.; J. E. Peralta, F. O.; K. N. Kudin, V. N. S.; K. Raghavachari, A. R.; M. Cossi, N. R.; et al. Gaussian 09, Revision E.01. *Gaussian, Inc.*, **2013**.
- (88) Lee, C.; Yang, W.; Parr, R. G. Development of the Colle-Salvetti correlation-energy formula into a functional of the electron density. *Phys. Rev. B, Condens. Matter* **1988**, *37*, 785–789.
- (89) Stephens, P. J.; Devlin, F. J.; Chabalowski, C. F.; Frisch, M. J. Ab Initio Calculation of Vibrational Absorption and Circular Dichroism Spectra Using Density Functional Force Fields. *J. Phys. Chem.* **1994**, *98*, 11623–11627.
- (90) Tirado-Rives, J.; Jorgensen, W. L. Performance of B3LYP density functional methods for a large set of organic molecules. *J. Chem. Theory Comput.* **2008**, *4*, 297–306.
- (91) Becke, A. D. Density-functional thermochemistry. I. The effect of the exchange-only gradient correction. *J. Chem. Phys.* **1992**, *96*, 2155–2160.
- (92) Marenich, A. V.; Cramer, C. J.; Truhlar, D. G. Universal solvation model based on the generalized born approximation with asymmetric descreening. *Journal of chemical theory and computation* **2009**, *5*, 2447–2464.
- (93) Tripkovic, V.; Björketun, M. E.; Skúlason, E.; Rossmeisl, J. Standard hydrogen electrode and potential of zero charge in density functional calculations. *Phys. Rev. B* **2011**, *84*, 115452.
- (94) Graf, E. Antioxidant potential of ferulic acid. *Free Radic. Biol. Med.* **1992**, *13*, 435–448.
- (95) Kahnt, G. Trans-cis-equilibrium of hydroxycinnamic acids during irradiation of aqueous solutions at different pH. *Phytochemistry* **1967**, *6*, 755–758.
- (96) Changelnet-Barret, P.; Plaza, P.; Martin, M. M. Primary events in the photoactive yellow protein chromophore in solution. *Chem. Phys. Lett.* **2001**, *336*, 439–444.
- (97) Benjamin, M. M.; Lawler, D. F. *Water Quality Engineering: Physical / Chemical Treatment Processes*; 1st ed.; Wiley, 2013; p. 912.
- (98) Zein, A. E.; Coeur, C.; Obeid, E.; Lauraguais, A.; Fagniez, T. Reaction Kinetics of Catechol (1,2-Benzenediol) and Guaiacol (2-Methoxyphenol) with Ozone. *J. Phys. Chem. A* **2015**, *119*, 6759–6765.
- (99) Coeur-Tourneur, C.; Cassez, A.; Wenger, J. C. Rate coefficients for the gas-phase reaction of hydroxyl radicals with 2-methoxyphenol (guaiacol) and related compounds. *J. Phys. Chem. A* **2010**, *114*, 11645–11650.
- (100) Tratnyek, P. G.; Hoigne, J. Oxidation of substituted phenols in the environment: a QSAR analysis of rate constants for reaction with singlet oxygen. *Environ. Sci. Technol.* **1991**, *25*, 1596–1604.

## Chapter 3: An Evaluation of Probes to Measure Oxidizing Organic Triplet Excited States in Aerosol Liquid Water

### ABSTRACT

Oxidizing triplet excited states of organic matter ( $^3\text{C}^*$ ) drive numerous reactions in fog/cloud waters and aerosol liquid water (ALW). Quantifying oxidizing triplet concentrations in ALW is difficult because degradation of  $^3\text{C}^*$  probes can be inhibited by dissolved organic matter (DOM) and copper ion, leading to an underestimate of triplet concentrations. In addition, an ideal triplet probe reacts slowly with singlet molecular oxygen ( $^1\text{O}_2^*$ ), whose concentrations are also high in ALW. Our overarching goal is to find a triplet probe that has low inhibition by DOM and Cu(II), and low sensitivity to  $^1\text{O}_2^*$ . To this end, we tested 12 potential probes from a variety of compound classes. Some probes, including 2,4,6-trimethylphenol, are strongly inhibited by DOM, while others react rapidly with  $^1\text{O}_2^*$ . One of the probe candidates, (phenylthiol)acetic acid (PTA), seems well suited for ALW conditions, with mild inhibition and fast rate constants with triplets, but it also has weaknesses, including a pH-dependent reactivity with triplets. We evaluated the performance of both PTA and syringol (SYR) as triplet probes in several aqueous extracts of particulate matter extracts. While PTA is less sensitive to inhibition than SYR, it results in lower triplet concentrations, possibly because it is less sensitive to weakly oxidizing triplets.

### 3.1. Introduction

Chromophoric dissolved organic matter (DOM) in natural aquatic systems absorbs light to form oxidizing triplet excited states ( $^3\text{DOM}^*$  or  $^3\text{C}^*$ ), which react with numerous environmental contaminants.<sup>1-3</sup> Triplets are also important in atmospheric waters, including cloud/fog drops and aerosol liquid water (ALW), where they react with organics to form aqueous secondary organic aerosol (aqSOA),<sup>4-6</sup> and oxidize sulfite and organosulfur compounds to sulfate.<sup>7-9</sup> Triplets also produce other oxidants, including hydroxyl

radical ( $\bullet\text{OH}$ ), singlet molecular oxygen ( $^1\text{O}_2^*$ ), and hydrogen peroxide ( $\text{HOOH}$ ).<sup>10-13</sup> While hydroxyl radical is generally the only oxidant considered in models of fog/cloud chemistry,  $^3\text{C}^*$  can be equally important as a sink for certain organics since triplet concentrations can be 10 – 100 times higher than  $\bullet\text{OH}$ .<sup>14,15</sup> In addition,  $^3\text{C}^*$  concentrations are even higher – by a few orders of magnitude – in ALW, where they appear to play a significant role in aqSOA formation.<sup>16,17</sup> Therefore, knowing triplet steady-state concentrations is important to understand chemistry in particle water. However, this goal is complicated since triplets represent a complex mixture with a wide range of reactivities.<sup>1,18</sup>

There are two general types of probes for  $^3\text{DOM}^*$  quantification: energy transfer and electron transfer. The first type takes advantage of the fact that triplets can transfer energy to dienes, resulting in their isomerization.<sup>13,18-20</sup> Monitoring the isomerization of a probe like sorbic acid and its derivatives is commonly used to quantify triplet concentrations.<sup>19,20</sup> This method quantifies triplets that contains high triplet energy ( $E_T \geq 250 \text{ kJ mol}^{-1}$ ). The other type of probe is electron transfer, where the oxidation of a probe such as 2,4,6-trimethylphenol (TMP) or 2,6-dimethoxyphenol (syringol or SYR) by  $^3\text{C}^*$  is monitored to determine the triplet steady-state concentration.<sup>14,16,21,22</sup> Since our long-term goal is to understand the contributions of triplets in driving chemistry in particle water, our interest is on oxidizing triplets and so we focus here on electron transfer probes.

One complication with electron transfer probes is that DOM is both a photosensitizer forming triplets, but also an antioxidant that can inhibit triplet-induced oxidation.<sup>23-27</sup> For example, when compounds containing phenol or aniline moieties react with a triplet, they donate an electron and form an intermediate phenoxyl or aniline radical,<sup>28</sup> which can be reduced by DOM to regenerate the parent compound. This inhibition of the decay of phenol/aniline probes by DOM leads to an underestimate of the triplet concentration. Similarly, nanomolar concentrations of Cu(II) inhibit the net decay of phenols and anilines by  $^3\text{C}^*$ .<sup>17,29,30</sup> While these reactions of DOM and Cu(II) with oxidized products of phenols and anilines are

environmentally relevant, they complicate proper determination of triplet concentrations by probes and should be avoided or corrected.

An ideal electron-transfer probe would be resistant to regeneration by DOM after oxidation. Electron-rich phenols like TMP are resistant to inhibition by DOM under surface water conditions (i.e., up to DOM concentrations of approximately  $6 \text{ mg C L}^{-1}$ ).<sup>23,24,31,32</sup> *N*-cyclopropylanilines were developed as DOM-regeneration-resistant triplet probes, where the oxidized intermediate undergoes rapid and irreversible ring-opening, avoiding reduction by aquatic DOM.<sup>33</sup> but it is unclear whether these probes work in concentrated aqueous extracts of particles. In addition to higher DOM levels,<sup>34–37</sup> aerosol liquid water tends to have much lower pH values ( $\leq 5$ )<sup>38–41</sup> and much higher dissolved copper,<sup>42–45</sup> compared to surface waters. Additionally, biomass-burning influenced aerosols can contain high concentrations of phenols, potent antioxidants that increase probe inhibition.<sup>46–48</sup> In addition,  $^1\text{O}_2^*$  in ALW appears to be a competitive photooxidant with  $^3\text{C}^*$ , with a typical  $^1\text{O}_2^*/^3\text{C}^*$  concentration ratio range of 10 – 100.<sup>49</sup> Therefore, a triplet probe for PM extracts should react quickly with  $^3\text{C}^*$  but slowly with  $^1\text{O}_2^*$ .

In this study we evaluate the suitability of 12 triplet probes under aqueous particle extract conditions. We examine the susceptibility of the probes for inhibition, including by a lab mixture of Cu(II) and syringol (a biomass-burning phenol) as well as in particle extracts. To gauge the specificity of the probe for triplets, we also measure the rate constants for probes with singlet oxygen and a model atmospheric triplet. Based on our results, we identify a good candidate probe for triplets in atmospheric particle extracts and compare its performance to syringol, a phenol probe that we have used in the past, in several illuminated particle extracts.

## 3.2. Materials and Methods

### 3.2.1. Chemicals, Illuminations, and Kinetic Analysis

Details on chemicals, illuminations, and the determination of first-order rate constants for probe loss ( $k'_{\text{Light}}$ ) are in Section S3.1 of the Supplemental Information.

### 3.2.2. Relative Rate Method

We determined second-order rate constants of probe (target) compounds reacting with the triplet state of 3,4-dimethoxybenzaldehyde (DMB) using a relative rate method with methyl jasmonate (MeJA) as the reference compound and simulated sunlight.<sup>50</sup> For singlet oxygen rate constants, we used a relative rate method with furfuryl alcohol (FFA) as the reference and 549 nm illumination.<sup>50–52</sup> Solutions containing 20  $\mu\text{M}$  target compound, 20  $\mu\text{M}$  reference compound, and 100  $\mu\text{M}$  DMB (triplet precursor) or 20  $\mu\text{M}$  Rose Bengal ( $^1\text{O}_2^*$  precursor) were prepared and adjusted to pH 4.2, a typical value for ALW in California's Central Valley during winter.<sup>39</sup> We took aliquots at certain reaction times to determine first-order decay rate constants of the reference ( $k'_{\text{ref}}$ ) and target compounds ( $k'_{\text{target}}$ ). The bimolecular rate constant of target compound reacting with  $^3\text{DMB}^*$  or  $^1\text{O}_2^*$  ( $k_{\text{target+Ox}}$ ) was then determined from

$$k_{\text{target+Ox}} = \frac{k'_{\text{target}}}{k'_{\text{ref}}} \times k_{\text{ref+Ox}} \quad (3.1)$$

where  $k_{\text{ref+Ox}}$  is the second-order rate constant for the reference compound reacting with  $^3\text{DMB}^*$  ( $k_{\text{MeJA+}^3\text{DMB}^*} = 4.1 (\pm 1) \times 10^8 \text{ M}^{-1} \text{ s}^{-1}$ ) or  $^1\text{O}_2^*$  ( $k_{\text{FFA+}^1\text{O}_2^*} = 1.0 (\pm 0.1) \times 10^8 \text{ M}^{-1} \text{ s}^{-1}$ ).<sup>50,51</sup>

### 3.2.3. Inhibition Factors

We quantified inhibition of triplet probe oxidation by aqueous particulate matter extracts (PME; see SI Section S3.2 for particle collection and extraction details), Suwanee River Fulvic Acid, or a mixture of

SYR and CuSO<sub>4</sub> (at a molar ratio of 70:1, we refer it to SYR+Cu solution) as a mimic of PME with high antioxidant activity. 10 μM probe and a photosensitizer (15 μM benzophenone (BP) or 80 μM DMB) were spiked into either Milli-Q water, SYR+Cu solution or PME at pH 4.2. Solutions were illuminated and the first-order rate constant of probe decay was determined. The photodegradation of probe compound in PME or SYR+Cu solution without photosensitizer was also measured. The inhibition factor (IF) for probe oxidation was calculated using

$$IF = \frac{k'_{Sens,DOM} - k'_{DOM}}{k'_{Sens}} \quad (3.2)$$

where:  $k'_{Sens,DOM}$  is the first-order decay rate constant of target compound in a solution containing photosensitizer and either PME or SYR+Cu;  $k'_{DOM}$  is the target compound decay rate constant in either PME or SYR+Cu solution without photosensitizer, and  $k'_{Sens}$  is the target compound decay rate constant with the photosensitizer in Milli-Q water. All  $k'$  values were corrected for internal light screening in the cuvette or the tube due to absorption by DOM in PME or by the triplet photosensitizer with screening factors ( $S_\lambda$ ), which were calculated with equation 2 in Smith et al.<sup>53</sup> For probe compounds that undergo direct photodegradation, we subtracted this contribution in the probe decay. For compounds without direct photodegradation, the decay in SYR+Cu solution is zero (i.e.  $k'_{DOM} = 0$ ).

### 3.2.4. Quantifying Oxidizing Triplet Excited States of Organic Matter in PM Extracts

We determined concentrations of photogenerated •OH and <sup>1</sup>O<sub>2</sub>\* in PME as described in SI Section S3.3 and in Kaur et al.<sup>16</sup> For oxidizing triplets, we spiked 10 μM of triplet probe in PME, illuminated the solution, and measured the first-order decay rate constant  $k'_{P,exp}$ .  $k'$  values were normalized to sunlight conditions at midday on the winter solstice at Davis (solar zenith = 62°;  $j_{2NB,win} = 0.0070 \text{ s}^{-1}$ ) and corrected for internal light screening:

$$k'_{P,norm} = \left[ \frac{k'_{P,exp}}{S_{\lambda} \times j_{2NB,exp}} \right] \times j_{2NB,win} \quad (3.3)$$

The contributions of  $\bullet\text{OH}$  and  $^1\text{O}_2^*$  to probe decay were subtracted from  $k'_{P,norm}$  to obtain  $k'_{P,3C^*}$ , the first-order rate constant for probe loss due to triplets. We assume that  $^3\text{C}^*$  in PME has the same average reactivity as  $^3\text{DMB}^*$ ,<sup>16,54</sup> so the  $^3\text{C}^*$  concentration in a PME can be estimated with

$$[^3\text{C}^*] = \frac{k'_{P,3C^*}}{k_{P+3DMB^*}} \quad (3.4)$$

where  $k'_{P+3DMB^*}$  is the second-order rate constant of probe with  $^3\text{DMB}^*$ .

### 3.3. Results and Discussion

#### 3.3.1. Inhibition Effects on Triplet Probes in an Aerosol Water Mimic

There are at least two ways in which DOM and other sample components can alter the oxidation of probes by triplet excited states: (1) regenerate the oxidized probe back to the parent form, which is an artifact that leads to an underestimate of the  $^3\text{C}^*$  concentration, and (2) react directly with triplets to suppress their steady-state concentration, which is not an artifact but instead reflects what occurs in the environment.<sup>55</sup> To quantify these pathways, we measure inhibition factors (*IF*, equation 3.2) in solutions containing a triplet precursor, triplet probe, and syringol and  $\text{CuSO}_4$  as a lab mimic of particle water. SYR is a surrogate for ALW phenols, which are one of the DOM groups that inhibit triplet-induced oxidation,<sup>25,56</sup> while Cu(II) is also present in atmospheric waters and inhibits the oxidation of phenols and anilines.<sup>29,30,43</sup> The *IF* quantifies how much SYR and Cu(II) inhibit net probe oxidation: a value of 1 indicates no inhibition, while an *IF* of 0 means that probe oxidation is fully suppressed. Since high concentrations of SYR can also suppress triplet concentrations, we also measure *IF* for furfuryl alcohol (FFA). FFA is a probe for singlet oxygen,<sup>57</sup> whose concentration will be proportional,<sup>57</sup> to the triplet concentration, which can be used to evaluate the suppression effect.<sup>1</sup> While Cu(II) can also quench  $^3\text{C}^*$ ,<sup>29</sup> since its concentration is much lower

than SYR, its suppression of triplet concentrations in our *IF* experiments is negligible. To distinguish between triplet suppression and inhibition of probe oxidation, we define a corrected inhibition factor for the probe:

$$IF_{P,corr} = \frac{IF_P}{IF_{FFA}} \quad (3.5)$$

This corrected *IF*, which quantifies inhibition of probe oxidation by removing the influence of reduced triplet concentrations, is derived in SI Section S3.4.

We start by performing inhibition experiments with oxidizing triplet probes representing four different organic classes: 2,4,6-trimethyl phenol (TMP), methyl jasmonate (MeJA), *N*-cyclopropylaniline (CAN), and (phenylthio)acetic acid (PTA) (Figure 3.1). To examine the inhibition effect, we measured the pseudo first-order rate constants of the probe decay by the triplet excited state of BP (<sup>3</sup>BP\*) in Milli-Q water and, separately, in SYR+Cu solution at pH 4.2. An example of the decays of TMP and MeJA in illuminated solution containing BP is in Figure S3.1.

Figure 3.1 shows the *IF* (Panel A) and *IF*<sub>P,corr</sub> (Panel B) values for FFA and the four probes in the presence of 70 μM SYR and 1 μM Cu(II). The *IF*<sub>FFA</sub> of 0.66 (± 0.02) indicates that this concentration of syringol quenches roughly 34% of <sup>3</sup>BP\* in air-saturated solutions. Assuming SYR has the same second-order rate constant with <sup>3</sup>BP\* as does TMP (5 × 10<sup>9</sup> M<sup>-1</sup> s<sup>-1</sup>),<sup>58</sup> 70 μM SYR would quench 30% of <sup>3</sup>BP\*, essentially the same as the measured *IF*, indicating that *IF*<sub>FFA</sub> can quantify the suppression of triplet concentrations. As shown in Figure 3.1, the *IF*<sub>MeJA</sub> of 0.71 (± 0.05) is not significantly different from *IF*<sub>FFA</sub>, showing that MeJA oxidation by <sup>3</sup>BP\* is not inhibited by SYR+Cu. This is also shown by the *IF*<sub>MeJA,corr</sub> value of 1.08 (± 0.08), which indicates *IF*<sub>P,corr</sub> describes inhibition of oxidation and not suppression of triplet concentration. Since oxidation of organic sulfur is not affected by phenol or natural organic matter,<sup>8</sup> sulfides such as (phenylthio)acetic acid might be robust triplet probes. The *IF*<sub>PTA,corr</sub> value of 0.69 (± 0.04) shows



that PTA decay is mildly inhibited by SYR+Cu. The resistance of PTA to inhibition is likely because its intermediate sulfur radical cation undergoes rapid and irreversible decarboxylation, preventing it from reduction to its original form.<sup>59</sup>

Both CAN and TMP show resistance to inhibition under surface water conditions. However, in SYR+Cu solution their corrected  $IF$  values are smaller than 0.1, indicating that their oxidation by  $^3BP^*$  is almost fully inhibited. In contrast, they are not inhibited by up to 20 mg C L<sup>-1</sup> of Suwannee River fulvic acid (SRFA),<sup>23,33</sup> indicating that our ALW mimic of SYR and Cu(II) is a more stringent test condition. Since Pan et al.<sup>29</sup> found that nanomolar concentrations of Cu(II) can decrease TMP decay, we also measured  $IF$  with SYR but not Cu(II). As shown in Figure S3.2,  $IF_{TMP,corr}$  of 0.51( $\pm$ 0.04) with 70  $\mu$ M SYR indicates that syringol itself can inhibit TMP decay by  $^3C^*$ , but as not significantly as Cu(II). This is consistent with the fact that SYR has a lower redox potential than TMP and so can reduce the TMP phenoxyl radical cation back to TMP.<sup>60-62</sup>

Since we use SYR as the mimic of atmospheric water DOM, we cannot examine  $IF_{SYR}$  with this mimic. Instead, we measure  $IF_{SYR}$  in a particle water extract (PME) with  $^3BP^*$ . As shown in Figure S3.3, we first started with methyl jasmonate and found that  $IF_{MeJA,corr}$  is not significantly different from 1, consistent with Figure 3.1. In contrast,  $IF_{P,corr}$  values for SYR and TMP are 0.04 ( $\pm$  0.04) and 0.01 ( $\pm$  0.05), indicating that oxidation of SYR and TMP by  $^3BP^*$  is strongly inhibited by DOM in particle extracts. Since TMP, SYR, and CAN are strongly impacted by simulated ALW conditions, we searched for a new triplet probe that is more resistant to inhibition by DOM.

### 3.3.2. Screening Potential Triplet Probes

An ideal triplet probe for aerosol liquid water would not be inhibited by DOM (i.e.,  $IF_{P,corr} \sim 1$ ) and would react rapidly with  $^3C^*$  but slowly with  $^1O_2^*$ . The rate constant with  $^1O_2^*$  is important because estimated  $^1O_2^*$  concentrations in ambient particle water are roughly 10 – 100 times higher than  $^3C^*$ .<sup>16</sup> We

explored inhibition and singlet oxygen reactivity for 12 potential probes in five different organic classes that have been shown to react with  $^3\text{C}^*:$ <sup>1</sup> sulfide, alkene, amine, phenol, and aniline. For each probe, we measured rate constants with  $^1\text{O}_2^*$  and  $^3\text{DMB}^*$  at pH 4.2; we employ DMB as the triplet precursor because it has been detected in biomass-burning particles and its triplet state has a reactivity similar to ambient triplets in fog waters and particle water extracts.<sup>14,16,54</sup> We also calculated the fraction of probe reacting with  $^3\text{C}^*$  in a concentrated PME (i.e., a PM mass/liquid water mass ratio of  $4 \times 10^{-3} \mu\text{g PM}/\mu\text{g H}_2\text{O}$ ) to assess probe selectivity, using the estimated  $\bullet\text{OH}$ ,  $^3\text{C}^*$ , and  $^1\text{O}_2^*$  concentrations of  $1.7 \times 10^{-15}$ ,  $4.1 \times 10^{-13}$ , and  $8.5 \times 10^{-12}$  M, respectively.<sup>16</sup> We measured the *IF* of each probe at pH 4.2 using  $^3\text{BP}^*$  as the triplet and SYR+Cu as the mimic of reducing species in ALW. For compounds that absorb sunlight, we also measured direct photolysis rate constants. Structures for each probe are in Table S3.1, while Table 3.1 lists the results of our tests, which are summarized below.

PTA reacts rapidly with the DMB triplet at pH 4.2 ( $k_{\text{PTA}+3\text{DMB}^*} = 2.2 \times 10^9 \text{ M}^{-1} \text{ s}^{-1}$ ) and is significantly less reactive with  $^1\text{O}_2^*$ , with a rate constant ratio  $k_{\text{PTA}+3\text{DMB}^*}/k_{\text{PTA}+1\text{O}_2^*}$  of 284 ( $\pm 71$ ). At this high ratio,  $^3\text{C}^*$  account for 90% of PTA oxidation in PME, indicating the probe has good triplet selectivity. Though it undergoes direct photodegradation, this rate is almost negligible (i.e., roughly 50 times slower) compared with its decay rate by triplets in PME. Also, PTA shows only mild inhibition (described earlier), indicating it is a promising probe. We also examined three PTA analogs, (phenylthio)acetyl chloride, 2-(phenylthio)ethanol, and *S*-phenyl thioacetate. However, the first one rapidly hydrolyzes in water to form PTA and hydrochloric acid, while the other two react slowly with  $^3\text{DMB}^*$  ( $k < 10^8 \text{ M}^{-1} \text{ s}^{-1}$ ) and 2-(phenylthiol)ethanol exhibits a low *IF* value (0.14); based on its slow kinetics, we did not measure *IF* for *S*-phenyl thioacetate.

Alkenes appear to be a promising triplet probe class since methyl jasmonate (an alkene) showed very little inhibition by DOM and SYR+Cu, as described above. However, four of the six alkenes we tested, including MeJA, have low values of  $k_{\text{probe}+3\text{DMB}^*}/k_{\text{probe}+1\text{O}_2^*}$ , indicating relatively poor selectivity towards

$^3\text{C}^*$ . For the remaining two alkenes, other issues reduce their effectiveness as triplet probes. Terpineol (TPN), like MeJA, has a corrected  $IF$  near one, indicating its decay is essentially not inhibited by SYR+Cu, but it reacts relatively slowly with the DMB triplet (which was difficult to measure; see SI Section S3.5) and thus has low specificity for triplets in particle water. Oxidation of the other alkene, pulegone, is inhibited by SYR+Cu ( $IF_{\text{corrected}} = 0.30$ ), which is not ideal but could work. However, after performing our tests we found in the literature that the reaction between alkenes and  $^3\text{C}^*$  is not solely (or perhaps even predominantly) electron transfer, but also includes photoaddition with no electron transfer.<sup>63,64</sup> Due to this, alkenes might not be a suitable probe to quantify oxidizing triplets because they might capture a greater pool of  $^3\text{C}^*$ . This might also explain why alkenes show only a modest correlation between rate constants with  $^3\text{BP}^*$  and modeled one-electron oxidation potentials.<sup>49</sup>

We next examined atenolol as a potential probe because some amines are resistant to regeneration by phenol when oxidized by  $^3\text{C}^*$  and show no inhibition by Cu(II).<sup>26,29</sup> We measured  $IF_{\text{corrected,ANL}}$  of 0.86 ( $\pm 0.05$ ), indicating minor inhibition by SYR+Cu, but, its  $^3\text{C}^*/^1\text{O}_2^*$  rate constant ratio is low (55 ( $\pm 16$ )), indicating modest selectivity towards triplets in particle extracts. Our next class of probes were the *N*-cyclopropylanilines, which were developed by Pflug et al. as triplet probes that are resistant to inhibition by SRFA at pH 7 and up to 20 mg C L<sup>-1</sup>.<sup>33</sup> However, in pH 4.2 solutions containing 70  $\mu\text{M}$  SYR and 1  $\mu\text{M}$  Cu(II) our two candidates, CAN and DCCAN, show low  $IF_{\text{P,corr}}$  values (0.04 and 0.14, respectively), indicating their decay by  $^3\text{BP}^*$  is heavily inhibited. Moreover, the probes absorb sunlight (290 – 310 nm) and undergo appreciable direct photodegradation in our studies; while Pflug et al. used UVA radiation (350 – 400 nm), our illumination system more closely simulates sunlight and includes wavelengths as low as 290 nm.<sup>15,33</sup> We also had difficulty determining the CAN rate constant with  $^3\text{DMB}^*$ , obtaining a rate constant higher than 10<sup>10</sup> M<sup>-1</sup> s<sup>-1</sup>, the diffusion-controlled limit. This impossibly high rate constant suggests there might be an unknown oxidant reacting with CAN in our illuminated solutions. Based on these results, CAN and DCCAN are poor choices for a  $^3\text{C}^*$  probe under aerosol liquid water conditions. Lastly, the phenol

probes (SYR and TMP) show strong inhibition by both PM matter extracts and SYR+Cu, as mentioned above, while TMP also has a modest  ${}^3\text{C}^*/{}^1\text{O}_2^*$  rate constant ratio.

### 3.3.3. Kinetic Study on PTA

Based on our results shown in Table 3.1, PTA appears to be the best choice for a triplet probe under particle extract conditions: it has a high  $k_{\text{probe}+3\text{DMB}^*}/k_{\text{probe}+1\text{O}_2^*}$  ratio and is only mildly inhibited by syringol and Cu(II). Therefore, we further investigated PTA as the triplet probe. One disadvantage of PTA is that it is an acid, so its reactivity with triplets might vary with solution acidity. To explore this, we first determined the  $\text{pK}_a$  of PTA based on light absorbance measurements, finding a value of 3.56 ( $\pm 0.02$ ) (Figure S3.5). To explore the pH dependence of PTA reactivity with  ${}^3\text{DMB}^*$ , we measured pseudo first-order rate constants of PTA decay with  ${}^3\text{DMB}^*$  at different pH (Figure 3.2). The decay of PTA peaks at pH 3.5, and is roughly 5 times lower at pH 2 and 5. At pH values above 6, the decay rate is very low, approaching zero. This trend of decay rate constant is likely due to the different reactivities of the neutral and deprotonated forms of PTA. In addition, protonated  ${}^3\text{DMB}^*$  has a  $\text{pK}_a$  value of 3.3, with the protonated form having generally higher reactivity with phenols.<sup>65</sup> The measured first-order rate constant  $k'_{\text{PTA}}$  is the mole-fraction weighted reactivity of the protonated and deprotonated forms of  ${}^3\text{DMB}^*$  (HT and T, respectively) with the neutral and deprotonated forms of PTA (HPTA and  $\text{PTA}^-$ , respectively):

$$k'_{\text{PTA}} = a * \alpha_{\text{HT}}\alpha_{\text{HPTA}} + b * \alpha_{\text{T}}\alpha_{\text{HPTA}} + c * \alpha_{\text{HT}}\alpha_{\text{PTA}^-} + d * \alpha_{\text{T}}\alpha_{\text{PTA}^-} \quad (3.6)$$

where  $\alpha$  is the mole fraction of each acid/base form of  ${}^3\text{DMB}^*$  or PTA (a function of pH), and  $a$ ,  $b$ ,  $c$ , and  $d$  represent the reactivity of each combination of  ${}^3\text{DMB}^*$  and PTA forms. To fit our data to this equation, initially we applied all parameters in the fitting. However, we found that  $b$  and  $c$  are not independent, while the value of  $d$  should be very low since  $k'_{\text{PTA}}$  values are essentially zero at higher pH. Thus in our second iteration we set parameters  $b$  and  $d$  to zero, but this resulted in a negative value of  $a$ , which is unreasonable (Figure. S3.6). We then set  $a$ ,  $b$ , and  $d$  to zero, resulting in an equation that fits the data reasonably well

(Figure 3.2), and gives a  $c$  value of  $0.046 \text{ min}^{-1}$ . This shows that the deprotonated form of PTA is more reactive than the neutral form with  $^3\text{DMB}^*$ , possibly because the sulfur radical of the PTA anion has a shorter lifetime,<sup>59</sup> leading to faster decarboxylation. Both forms of PTA seem to exhibit poor reactivity towards neutral  $^3\text{DMB}^*$ . Overall, the strong pH dependence of the PTA- $^3\text{DMB}^*$  reaction, and the associated very low reactivity at high and low pH, is a weakness, but the probe works reasonably well under mildly acidic conditions, which are common for aerosol liquid water at our location in winter.<sup>39</sup> We also examined the pH dependence of PTA reacting with  $^3\text{BP}^*$  (Figure S3.7); here the rate constant increases with increasing pH, plateauing around pH 4, which also suggests that the deprotonated form of PTA is more reactive.

To investigate the PTA reactivity with  $\bullet\text{OH}$  and the sensitivity to triplets with different energies, we determined the bimolecular rate constants of PTA with  $\bullet\text{OH}$  and two other triplets, 3'-methoxyacetophenone ( $^3\text{MAP}^*$ ) and 2-acetonaphthone ( $^3\text{2AN}^*$ ) at pH 4.2. The rate constants are shown in Table S3.2, while the triplet energies and reduction potentials are in Table S3.3. The rate constant of PTA with  $^3\text{MAP}^*$  is  $3.1 (\pm 0.4) \times 10^9 \text{ M}^{-1} \text{ s}^{-1}$ , which is statistically the same as with  $^3\text{DMB}^*$  (Table 3.1). However, the rate constant with  $^3\text{2AN}^*$ , a weaker triplet, is around 100 times lower, at  $2.4 (\pm 0.2) \times 10^7 \text{ M}^{-1} \text{ s}^{-1}$ . In contrast, for SYR at pH 5 the rate constant with  $^3\text{2AN}^*$  is only 2 times lower than the value with  $^3\text{DMB}^*$  (Figure S3.8).<sup>14</sup> This apparent low reactivity of PTA with weakly oxidizing triplets complicates determining triplet concentrations in environmental samples, where the relative amounts of different energy triplets is unknown. However, measuring triplets with both PTA and SYR might allow determination of both highly and weakly oxidizing triplets.

### 3.3.4. Dependence of $IF_{\text{PTA}}$ on SYR+Cu concentrations and EDC

Previous studies showed that increasing DOM concentration increases inhibition of  $^3\text{C}^*$ -induced oxidation, leading to a decreasing probe degradation rate.<sup>24</sup> To investigate the effect of DOM concentration

on PTA decay by  $^3\text{C}^*$ , we measured the inhibition factors of PTA and FFA as a function of SYR+Cu concentrations (at a fixed molar ratio of 70:1) with DMB as the triplet precursor. We also investigated the relationship between  $IF$  and electron donating capacity (EDC), which is correlated with the antioxidant capacity, phenolic content, and inhibition efficiency of DOM.<sup>66–69</sup> Moreover, Leresche et al. found that phenol and DOM quenching of an aromatic amine radical cation increases with EDC.<sup>27</sup> We determined EDC using a method modified from Walpen et al.<sup>70</sup> and Yuan et al.<sup>71</sup>, as described in SI Section S3.6. Our goal was to develop a relationship between  $IF$  and EDC so that we could predict  $IF_{\text{PTA}}$  in solutions using EDC, which is much simpler to measure.

Figure 3.3 shows inhibition factors for PTA and FFA, and  $IF_{\text{PTA,corr}}$ , as a function of SYR concentration in solutions with triplet DMB:  $IF$  and  $IF_{\text{P,corr}}$  both decrease with increasing SYR and Cu(II). With 420  $\mu\text{M}$  SYR and 6  $\mu\text{M}$  Cu(II),  $IF_{\text{FFA}}$  is 0.44 ( $\pm 0.03$ ), indicating that more than half of  $^3\text{DMB}^*$  is quenched by SYR+Cu. At this concentration,  $IF_{\text{PTA}}$  is 0.23 ( $\pm 0.01$ ), showing the high inhibition, corresponding to a corrected  $IF$  of 0.53 ( $\pm 0.04$ ). We employed a kinetic model from Wenk et al. to fit the data (Scheme S1 in SI).<sup>24</sup> In this model, the intermediate from probe oxidation can either undergo further irreversible oxidation to form products (with a first-order rate constant  $k_{\text{ox}}$ ), or be reduced by DOM to regenerate the parent probe (with second-order rate constant  $k_{\text{red,DOM}}$ ). Therefore, the inverse of  $IF_{\text{PTA,corr}}$  can be expressed by:

$$\frac{1}{IF_{\text{PTA,corr}}} = 1 + \frac{k_{\text{red,DOM}}}{k_{\text{ox}}} [\text{SYR}] \quad (3.7)$$

Figure 3.3B shows this fitting for our PTA data. The linear regression has a slope of 0.0021  $\mu\text{M}^{-1}$ , while the inverse of this is  $[\text{SYR}]_{1/2}$ , i.e., the SYR concentration that causes  $IF_{\text{PTA,corr}}$  to equal 0.5. This concentration is 480  $\mu\text{M}$ , a fairly high value that shows the resistance of PTA to inhibition; in contrast, based on the  $IF_{\text{FFA}}$  data, it only takes around 150  $\mu\text{M}$  SYR to quench half of the DMB triplets (Fig. 3B). Figure S3.10 shows the dependence of  $IF_{\text{PTA}}$  and  $IF_{\text{FFA}}$  on SYR using benzophenone as the triplet precursor.

Compared with the DMB results,  $IF$  for both FFA and PTA are lower with  $^3BP^*$ , likely because  $^3BP^*$  is a more reactive triplet that is more rapidly quenched by SYR. However,  $IF_{PTA,corr}$  with  $^3BP^*$  does not behave in the same way as it does with  $^3DMB^*$ , with the former showing an odd minimum at 70  $\mu M$  SYR and a value approaching unity at higher SYR and Cu(II) concentrations.

To investigate the relationship between inhibition and EDC, we fit a linear regression to the measured  $IF_{FFA}$  and  $IF_{PTA,corr}$  as a function of EDC in SYR+Cu solutions, particle water extracts, and SRFA at pH 4.2 (Figure 3.4). The  $y$ -intercept is set to 1, because at zero EDC there should be no inhibition (i.e.,  $IF = 1$ ). We have expressed the  $x$ -axis as EDC ( $mmol e^- g_C^{-1}$ ) times DOC ( $mg C L^{-1}$ ) with units of  $mmol e^- L^{-1}$  so that we can quantify the total amount of electrons that DOM can donate in a solution. As shown in Figure 3.4,  $IF_{FFA}$  values decrease with increasing EDC $\times$ DOC, consistent with the idea that higher DOC corresponds to more triplet quenching. The SRFA result is an outlier, with an  $IF_{FFA}$  value close to 2, suggesting that the interaction of DOM and  $^3DMB^*$  forms species that react with FFA, accelerating its decay.<sup>24</sup> Other than that,  $IF_{FFA}$  correlates well with EDC ( $R^2 = 0.59$ ).  $IF_{PTA,corr}$  shows a good correlation with EDC in the SYR+Cu solutions, but the relationship is poor for the SRFA and PME solutions, suggesting relationship is not robust across different samples.

### 3.4. Determination of [ $^3C^*$ ] in PME using PTA as the triplet probe

For our last experiments, we used PTA and SYR to evaluate probe inhibition and determine triplet concentrations in four aqueous extracts of fine particles. PMEs were prepared from  $PM_{2.5}$  samples collected in Davis, CA, with DOC ranging from 9.9 to 105  $mg C L^{-1}$ . Sample details are provided in Table S3.4: PME1 is from a sample collected on a clear summer day; PME2 and PME3 are extracted from winter samples with residential wood burning; and PME4 represents air that was heavily impacted by summer wildfires.

As shown in Figure 3.5A,  $IF_{\text{FFA}}$  in the PMEs is 1 or greater, indicating  $^3\text{DMB}^*$  is not significantly quenched by DOM. In contrast, based on the rate constants of aquatic DOM quenching  $^3\text{C}^*$  determined by Wenk et al.,<sup>55</sup> we would expect DOM to quench 13 – 30% of triplets at a DOC concentration of 105 mg C L<sup>-1</sup>. Therefore, the high  $IF_{\text{FFA}}$  might be attributed to the formation of reactive species from the interaction between  $^3\text{DMB}^*$  and DOM. In PME1 with low DOC (9.9 mg C L<sup>-1</sup>), the  $IF_{\text{SYR,corr}}$  and  $IF_{\text{PTA,corr}}$  both are around 0.76, indicating neither is heavily impacted by DOM in this relatively dilute PME. For PME2 and PME3, which have moderate DOC (64 and 69 mg C L<sup>-1</sup>), corrected  $IF$  values for SYR are 0.50 ( $\pm$  0.11) and 0.16 ( $\pm$  0.03), respectively, and for PTA are 1.3 ( $\pm$  0.3) and 0.97 ( $\pm$  0.09). Thus, while SYR decay by  $^3\text{DMB}^*$  is significantly inhibited by DOM, PTA essentially is not. For PME4, the extract from the wildfire particles, corrected  $IF$  values for SYR and PTA are 0.31 ( $\pm$  0.04) and 0.59 ( $\pm$  0.08), respectively. Thus both probes are inhibited in this sample (though PTA is less affected), possibly because of abundant antioxidant phenols, which are present in biomass-burning aerosols<sup>72,73</sup>. This is consistent with the high EDC value of PME4. However, there is no consistent trend of  $IF$  values with DOC, though we expected that the extent of inhibition would increase with DOC.

We next determined triplet concentrations in the four PM extracts based on SYR and PTA data. We also measured  $\bullet\text{OH}$  and  $^1\text{O}_2^*$  concentrations so that we could subtract their contributions to SYR and PTA decay in PME (Table S3.5).  $\bullet\text{OH}$  accounts for 5% – 22% of SYR decay and 7% – 28% of PTA decay, while  $^1\text{O}_2^*$  contributes 9% – 17% and 4% – 9%, respectively. Based on our past work,<sup>14,16</sup> we assume that  $^3\text{C}^*$  in PME have similar reactivity as  $^3\text{DMB}^*$  and use the second-order rate constants of each probe with  $^3\text{DMB}^*$  to calculate the  $^3\text{C}^*$  concentration from each set of probe data. We then correct each triplet concentration for inhibition using<sup>31,74</sup>

$$[{}^3\text{C}^*]_{P,corr} = \frac{[{}^3\text{C}^*]_P}{IF_{P,corr}} \quad (3.8)$$



Note that when  $IF_{P,corr}$  is greater than 1, which indicates no inhibition, we do not make a correction for the  $^3C^*$  concentration. As Figure 3.5B shows, for uncorrected  $^3C^*$  concentrations, PTA-derived  $[^3C^*]$  ranges from  $(0.02 - 2) \times 10^{-13}$  M, while SYR-derived  $[^3C^*]$  are in the range of  $(0.07 - 2) \times 10^{-13}$  M, with  $[^3C^*]_{PTA}/[^3C^*]_{SYR}$  ratios of 0.32 to 2.3. Based on the properties of these two probes (Table 3.1), we expected that uncorrected triplet concentrations would be higher based on PTA decays (since this probe is less susceptible to inhibition), but this expectation is only true for PME2 and PME3. With  $IF$  correction,  $[^3C^*]_{P,corr}$  increases by factors of 1 – 1.7 for PTA and 1.5 – 6.2 for SYR, respectively, compared with uncorrected values. We also expected that correcting for inhibition would yield similar  $[^3C^*]$  for the two probes. However, we only observe this in PME2, while for the other three samples the triplet concentration from  $IF$ -corrected PTA data is lower than the concentration from  $IF$ -corrected SYR data. The range of  $[^3C^*]_{PTA,corr}/[^3C^*]_{SYR,corr}$  is 0.27 – 0.91 with a mean value of 0.45. This suggests that PTA is missing weakly oxidizing triplets that are captured by SYR, consistent with the large difference in SYR and PTA rate constants with the weakly oxidizing 2-acetonaphthone triplet (Figure S3.8 and Table S3.3). PME4, the wildfire samples, has the lowest value of  $[^3C^*]_{PTA,corr}/[^3C^*]_{SYR,corr}$ , suggesting that  $^3C^*$  in PME4 are lower reactivity than those in other samples. This is consistent with the observation that highly aromatic DOM, such as in wildfire particles,<sup>75</sup> might show a lower triplet reactivity.<sup>24</sup>

Our results in the particle extracts show that PTA is less sensitive to inhibition to DOM than is SYR, as planned, but we have also found that PTA has some disadvantages. For one, the  $^3C^*$  concentration obtained by PTA is lower than that from SYR after  $IF$  correction, suggesting PTA is “missing” low-energy triplets that can oxidize SYR. In addition, the PTA reactivity with triplets depends on pH, which reduces its utility. As for SYR, it suffers more from inhibition but captures more of the total pool of oxidizing  $^3C^*$ . Furthermore, while we can correct triplet concentrations using measured inhibition factors in each sample, the corrected  $[^3C^*]$  are as divergent between the two probes as are the uncorrected values, possibly because

of the inability of PTA to “see” weakly oxidizing triplets. Applying both triplet probes will allow us to obtain a comprehensive understanding of  $^3\text{C}^*$  concentration as well as reactivity.

### **3.5. Acknowledgements**

This work was funded by the National Science Foundation grant (AGS-1649212), the California Agricultural Experiment Station (CA-D-LAW-6403-RR) and a Jastro-Shields Research Award and Donald G. Crosby Fellowship to L.M. We thank Keith J. Bein for loan of, and assistance with, a  $\text{PM}_{2.5}$  high-volume sampler and Wenqing Jiang, Christopher Niedek, and Qi Zhang for DOC and ions analysis of our PM extracts.

### 3.7. Figures

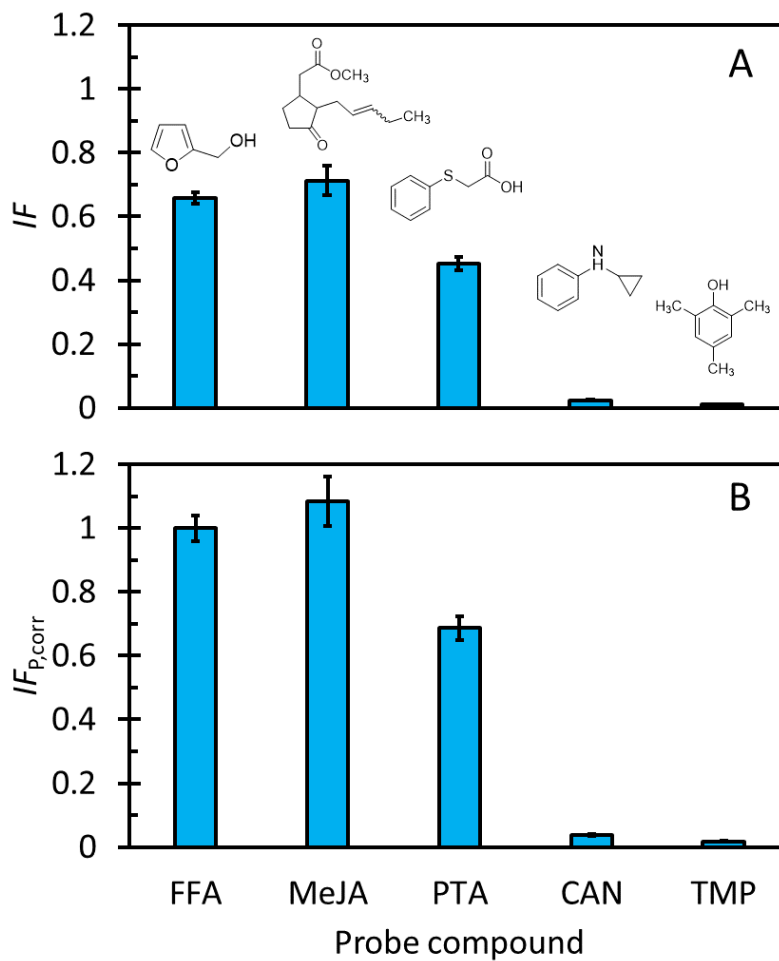


**Figure 3.1.** Inhibition factor (Panel A) and the corrected inhibition factors (Panel B; equation 3.5) for triplet probes reacting with  ${}^3BP^*$  in solutions containing  $70 \mu M$  SYR and  $1 \mu M$  Cu(II). Error bars represent  $\pm 1$  standard error propagated from linear regressions.

**Table 3.1. Information on potential probe compounds (P)<sup>a</sup>**

Class	Compound	$k_{P+3DMB^*}$ (M <sup>-1</sup> s <sup>-1</sup> )	$k_{P+1O2^*}$ (M <sup>-1</sup> s <sup>-1</sup> )	$k_{P+3DMB^*}/k_{P+1O2^*}$	% ( $k'_{3C^*}$ ) in PME <sup>b</sup>	$IF^c$	$IF_{P,corr}^d$	$j$ (s <sup>-1</sup> ) <sup>e</sup>
Sulfide	(Phenylthio)acetic acid (PTA)	$2.5 (\pm 0.6) \times 10^{9f}$	$8.8 (\pm 0.6) \times 10^6$	284 ( $\pm 71$ )	90	0.45 ( $\pm 0.02$ )	0.69 ( $\pm 0.04$ )	$1.0 (\pm 0.1) \times 10^{-5}$
	Methyl jasmonate (MeJA)	$4.1 (\pm 1.0) \times 10^8$	$6.0 (\pm 0.7) \times 10^6$	68 ( $\pm 18$ )	67	0.71 ( $\pm 0.05$ )	1.08 ( $\pm 0.08$ )	n/a <sup>g</sup>
	Terpineol (TPN)	$2.1 (\pm 0.2) \times 10^8$	$1.7 (\pm 0.1) \times 10^6$	121 ( $\pm 16$ )	64	0.65 ( $\pm 0.01$ )	0.99 ( $\pm 0.03$ )	n/a
Alkene	Pulegone	$4.7 (\pm 1.2) \times 10^9$	$3.7 (\pm 0.4) \times 10^7$	128 ( $\pm 37$ )	85	0.25 ( $\pm 0.02$ )	0.30 ( $\pm 0.03$ )	$1.4 (\pm 0.3) \times 10^{-6}$
	<i>cis</i> -3-Hexenyl acetate	$2.7 (\pm 0.7) \times 10^8$	$6.2 (\pm 1.4) \times 10^6$	44 ( $\pm 15$ )	57	ND <sup>h</sup>	ND	n/a
	Prenyl acetate	$1.5 (\pm 0.4) \times 10^8$	$1.0 (\pm 0.2) \times 10^7$	15 ( $\pm 5$ )	34	0.61 ( $\pm 0.06$ )	0.93 ( $\pm 0.09$ )	n/a
	Linalool	$1.7 (\pm 0.4) \times 10^9$	$1.5 (\pm 0.2) \times 10^8$	11 ( $\pm 3$ )	35	ND	ND	n/a
Amine	Atenolol (ANL)	$1.0 (\pm 0.3) \times 10^8$	$1.8 (\pm 0.2) \times 10^6$	55 ( $\pm 16$ )	46	0.56 ( $\pm 0.03$ )	0.86 ( $\pm 0.05$ )	n/a
Anilines	<i>N</i> -cyclopropylaniline (CAN)	n/a <sup>i</sup>	$2.8 (\pm 0.6) \times 10^9$	n/a	n/a	0.03 ( $\pm 0.01$ )	0.04 ( $\pm 0.01$ )	$5.2 (\pm 0.8) \times 10^{-4}$
	3,5-dichloro- <i>N</i> -cyclopropylaniline (DCCAN)	$1.5 (\pm 0.2) \times 10^{10}$	$6.0 (\pm 1.1) \times 10^8$	24 ( $\pm 5$ )	54	0.09 ( $\pm 0.01$ )	0.14 ( $\pm 0.01$ )	$2.4 (\pm 0.1) \times 10^{-4}$
Phenols	Syringol (SYR)	$3.9 (\pm 0.7) \times 10^{9j}$	$3.6 (\pm 0.7) \times 10^{7k}$	107 ( $\pm 29$ )	82	n/a	n/a	$<3.6 \times 10^{-6l}$
	2,4,6-trimethylphenol (TMP)	$2.4 (\pm 0.4) \times 10^9$	$6.2 (\pm 1.0) \times 10^{7k}$	39 ( $\pm 9$ )	64	0.01 ( $\pm 0.01$ )	0.02 ( $\pm 0.01$ )	n/a

<sup>a</sup>Errors in parentheses are 1 standard error.

<sup>b</sup>Percentage of probe decay due to triplet reaction in a concentrated particle extract, calculated at an extract particle mass/water mass ratio of  $4 \times 10^{-3}$   $\mu\text{g PM}/\mu\text{g H}_2\text{O}$  based on results from Kaur et al.,<sup>16</sup> where  $\bullet\text{OH}$ ,  $^3\text{C}^*$ , and  $^1\text{O}_2^*$  concentrations were  $1.7 \times 10^{-15}$ ,  $4.1 \times 10^{-13}$ , and  $8.5 \times 10^{-12}$  M, respectively.

<sup>c</sup>Inhibition factor in solutions containing 70  $\mu\text{M}$  SYR and 1  $\mu\text{M}$  Cu(II). We used 15  $\mu\text{M}$  BP as the triplet precursor, except for pulegone, where we used 80  $\mu\text{M}$  DMB.

<sup>d</sup> $IF_{corrected}$  is calculated with equation 3.5 and  $IF_{FFA}$  values., which are 0.66 with 15  $\mu\text{M}$  BP and 0.83 with 80  $\mu\text{M}$  DMB.

<sup>e</sup>The direct photolysis rate constants are determined at pH 4.2 and normalized to sunlight conditions at midday on the winter solstice at Davis (solar zenith = 62°;  $j_{2NB,win} = 0.0070$  s<sup>-1</sup>).

<sup>f</sup>The rate constant is determined with the direct measurement method, see details in Figure S3.8.

<sup>g</sup>Not applicable.

<sup>h</sup>Not determined.

<sup>i</sup>The rate constant of CAN measured with the relative rate method ( $>10^{11} \text{ M}^{-1} \text{ s}^{-1}$ ) is much higher than the diffusion-controlled rate constant (approximately  $10^{10} \text{ M}^{-1} \text{ s}^{-1}$ ), indicating a problem. One possibility is that an oxidant other than <sup>3</sup>DMB\* is responsible for most of the probe loss.

<sup>j</sup>From Smith et al.<sup>76</sup>

<sup>k</sup>From Tratnyek et al.<sup>77</sup>

<sup>l</sup>From Kaur et al.<sup>14</sup>

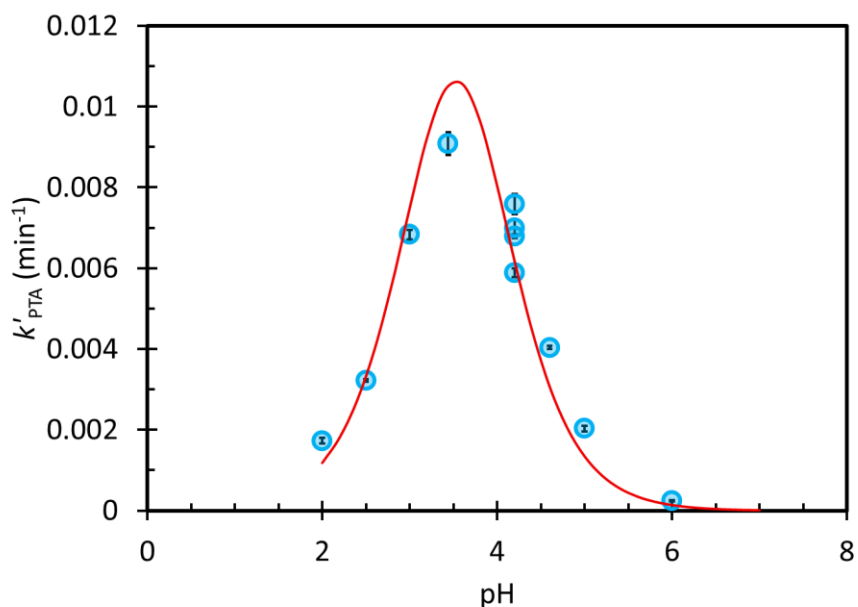


**Figure 3.2.** Influence of pH on the first-order PTA decay rate constant due to the DMB triplet; rate constants are corrected for direct photodegradation and are normalized to a  $j_{2\text{NB}}$  value of  $0.007 \text{ s}^{-1}$ . Solutions contained  $10 \mu\text{M}$  DMB,  $10 \mu\text{M}$  PTA, and either  $\text{H}_2\text{SO}_4$  or  $\text{NaOH}$  for pH adjustment and were maintained at  $20 \text{ }^\circ\text{C}$ . The red line is the regression fit to eq 6, with  $\text{p}K_a$  values of  ${}^3\text{DMB}^*$  and PTA of 3.5 and 3.56, respectively,<sup>65</sup> and values of  $a$ ,  $b$ , and  $d$  set as zero. The resulting fitted value of  $c$  is  $0.046 \text{ min}^{-1}$ . Error bars represent  $\pm 1 \text{ SE}$ , propagated from the linear regressions and  $j_{2\text{NB}}$ .

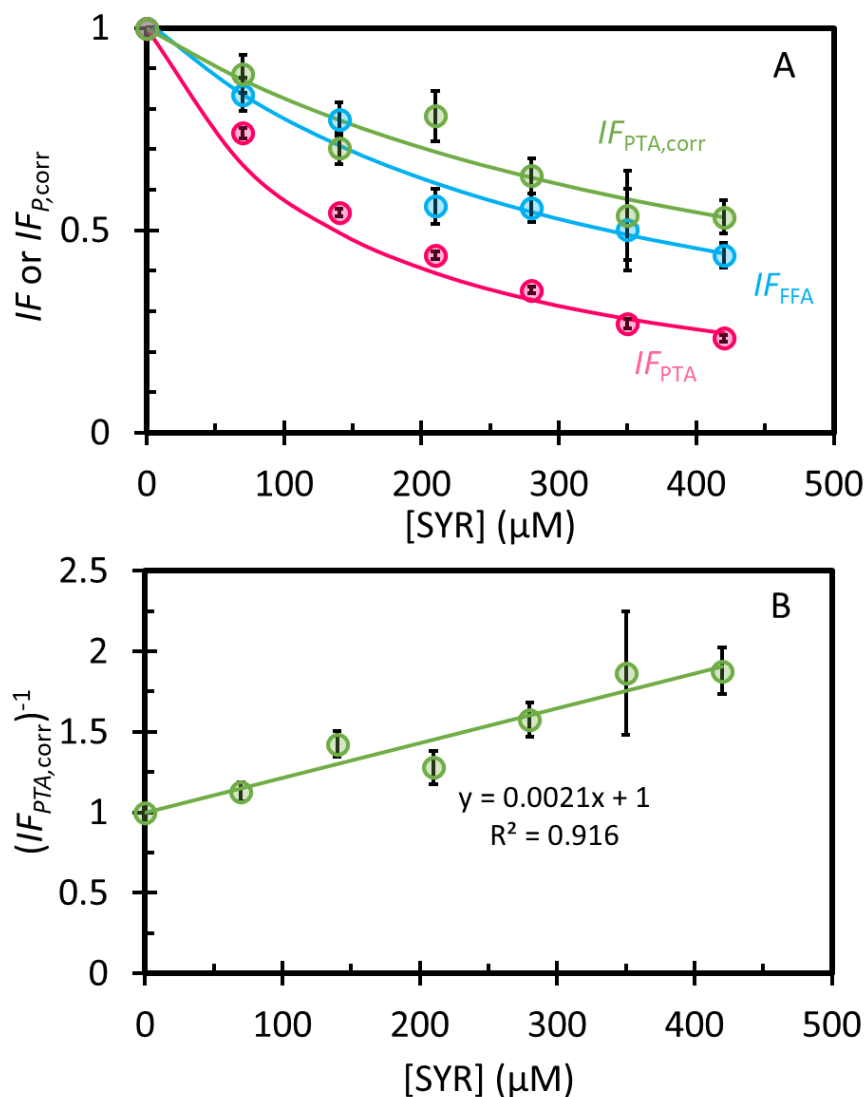


**Figure 3.3.** (A) Inhibition factors of FFA (blue) and PTA (red), and the corrected inhibition factor of PTA (green) as a function of SYR concentration with 80  $\mu M$  DMB as the triplet precursor in solution at pH 4.2; solutions also contain Cu(II) at a molar ratio of SYR/Cu(II) of 70:1. The solid lines represent linear regression fits between the inverse of IF values versus the SYR concentration. (B) The inverse of  $IF_{corrected,PTA}$  (from Panel A) as a function of SYR concentration. For both panels, error bars represent  $\pm 1$  SE, propagated from the linear regressions.

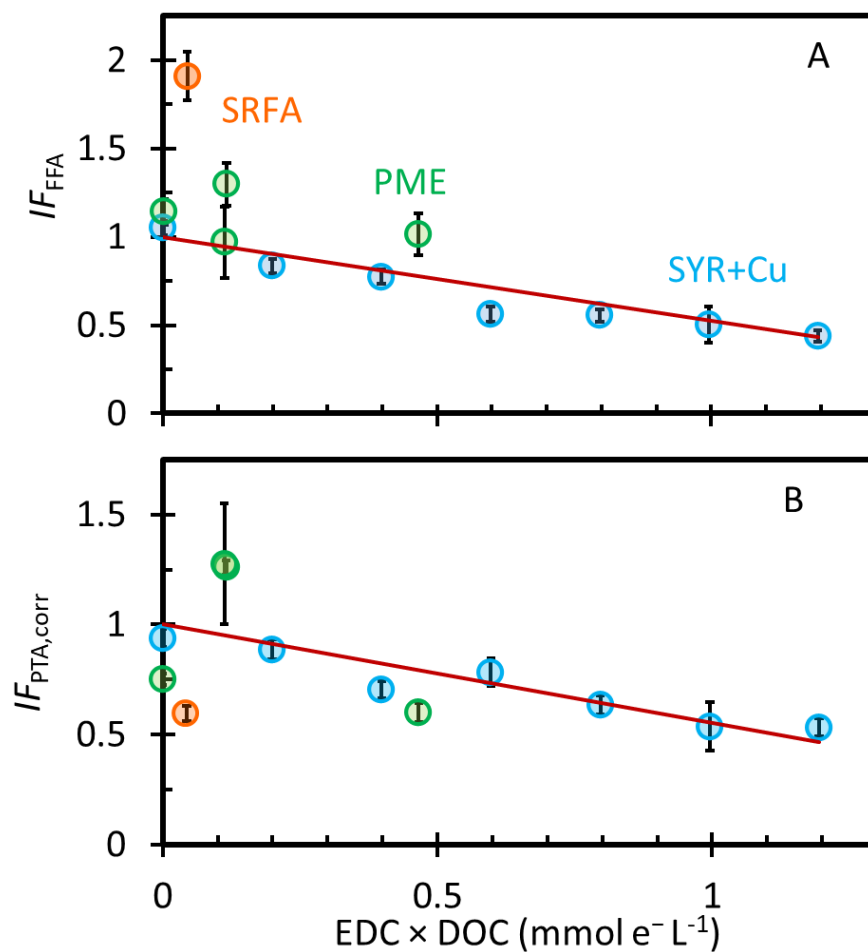


**Figure 3.4.** The inhibition factor of FFA (Panel A) and corrected inhibition factor of PTA (Panel B) as a function of the product of electron donating capacity (EDC) with dissolved organic carbon (DOC) in SRFA (orange), PME (green), and SYR+Cu (blue) solutions with 80  $\mu\text{M}$  DMB as the triplet precursor at pH 4.2. Error bars represent  $\pm 1$  SE, propagated from the linear regressions of the FFA and/or PTA decay plots. Data are available in Table S3.3. Red lines represent the linear regressions of all data points.



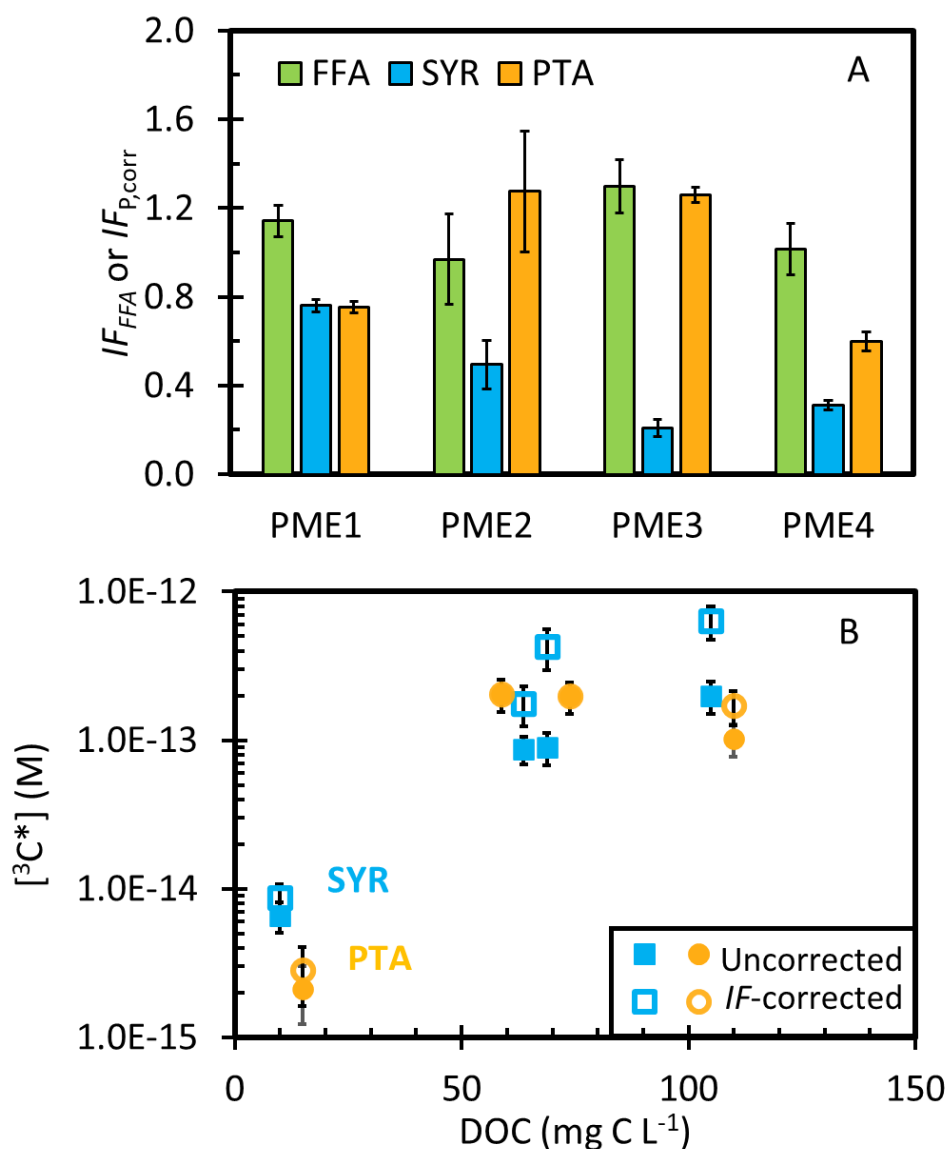


**Figure 3.5.** (A) Inhibition factors of FFA and corrected inhibition factors of SYR and PTA in particle extracts with 80  $\mu$ M DMB as the triplet precursor. (B) Raw (solid symbols) and inhibition-corrected (open symbols) concentrations of  $^3C^*$  determined from SYR (blue squares) and PTA (yellow circles) as a function of dissolved organic carbon concentration. To separate the SYR and PTA results, we add 5  $mg\ C\ L^{-1}$  to the DOC concentration for each PTA-derived value. To separate the PME2 and PME3 results, we subtract 5  $mg\ C\ L^{-1}$  from the former. The uncorrected and *IF*-corrected  $^3C^*$  derived by PTA values were overlapped for PME2 and PME3. Error bars represent  $\pm 1$  SE, propagated from the regressions of probe decay and second-order rate constants.

### 3.8. Supporting Information

#### Section S3.1. Chemicals, Illuminations, and Kinetic Analysis

All chemicals were used as received. Methyl jasmonate (95%), furfuryl alcohol (FFA, 98%), linalool (97%), *cis*-3-Hexenyl acetate ( $\geq 98\%$ ), prenyl acetate ( $\geq 98\%$ ), atenolol ( $\geq 98\%$ ), (phenylthio)acetic acid (PTA, 96%), pulegone ( $\geq 98.5\%$ ), syringol (SYR, 99%), benzophenone (BP, 99%),  $\alpha$ -terpineol ( $\geq 96\%$ ), 3,4-dimethoxybenzaldehyde (DMB, 99%), Rose Bengal (95%), 2,4,6-trimethylphenol (97%), and 2,2'-azino-bis(3-ethylbenzothiazoline-6-sulfonic acid) diammonium salt (ABTS,  $\geq 98\%$ ) were from Millipore Sigma. N-cyclopropylaniline (97%) was from Acrotein and 3,5-dichloro-N-cyclopropylaniline (95%) was from EnamineStore. Suwannee River Fulvic Acid (SRFA) was obtained from the International Humic Substances Society. All chemical solutions were prepared using air-saturated ultrapure water (Milli-Q water) from a Milli-Q Advantage A10 system (Millipore;  $\geq 18.2 \text{ M}\Omega \text{ cm}$ ) with an upstream Barnstead activated carbon cartridge.

Solutions were pipetted either into a silicone-plugged GE 021 quartz tube (5 mm inner diameter, 1.0 mL volume) or a 1-cm quartz cuvette (5 mL, Spectrocell), then illuminated at 20 °C with a 1000 W xenon arc lamp with a water filter, an AM1.0 air mass filter (AM1D-3L, Sciencetech), and a 295 nm long-pass filter (20CGA-295, Thorlabs) to simulate tropospheric sunlight. Dark control samples were wrapped in aluminum foil and kept in the photoreactor chamber. During illumination, aliquots were collected from the illuminated and dark cells at specific time intervals to measure concentrations of probes with high-performance liquid chromatography (HPLC, Shimadzu LC-20AB pump, Thermo Scientific Accucore XL C18 column (50  $\times$  3 mm, 4  $\mu\text{m}$  bead), and Shimadzu-M20A UV-Vis detector).

The measured pseudo-first-order rate constant for probe loss ( $k'_{\text{Light}}$ ) was determined as the negative of the slope from a linear regression of  $\ln([\text{probe}]_t/[\text{probe}]_0)$  versus illumination time ( $t$ ), where  $[\text{probe}]_0$  is

the concentration of probe compound at time zero. The photon flux of the photoreactor was determined on each experiment day by measuring the photolysis rate constant of a 10  $\mu\text{M}$  2-nitrobenzaldehyde (2NB) solution in the same type of container as samples.<sup>78</sup>

### Section S3.2. Particle collection and extraction method

Particles were collected on the roof of Ghausi Hall on the UC Davis campus in December 2019, January 2020, and August 2020. In August 2020, there were several wildfires around Davis and air quality was heavily impacted. PM<sub>2.5</sub> was collected on Teflon-coated borosilicate glass microfiber filters (Pall Corporation, EmFab™ filters, 8 in. × 10 in., pre-cleaned by gently shaking in Milli-Q water and then drying at 100 °C) by a high-volume sampler equipped with a PM<sub>10</sub> inlet (Graseby Andersen) and two offset, slotted impactor plates (Tisch Environmental, Inc., 230 series) to remove particles greater than 2.5 μm. The airflow rate was maintained at 40 (±1) cfm. Particles were either collected for 24 hr or a week. Upon collection, samples were wrapped in aluminum foil (baked previously at 500 °C for 8 hr) and stored at -20 °C. To prepare particulate matter extracts (PMEs), filters were cut into 2 cm × 2 cm pieces, which were each placed in individual 20-mL amber glass vials and extracted with 1.0 mL Milli-Q water by shaking for 4 hr in the dark. The extracts from the same filter were combined, filtered (0.22 μm PTFE; Pall corporation), and adjusted to pH 4.2 using sulfuric acid to mimic the acidity of particle water.<sup>39</sup> PME samples were flash-frozen in liquid nitrogen immediately after preparation and were later thawed on the day of the experiment. Dissolved organic carbon (DOC) and major ion concentrations were measured by a Shimadzu TOC-VCPH analyzer and Metrohm ion chromatographs (881 Compact IC Pro) equipped with conductivity detectors, respectively. PME sample information is provided in Table S3.5.

### Section S3.3. Determination of hydroxyl radical ( $\bullet\text{OH}$ ) and singlet oxygen ( $^1\text{O}_2^*$ ) concentrations in PME

Details about determining  $\bullet\text{OH}$  and  $^1\text{O}_2^*$  concentrations are provided in Anastasio et al.<sup>79</sup> and Kaur et al.<sup>14</sup> and are only discussed briefly here. To determine  $\bullet\text{OH}$  concentrations in PME, we spiked pH-unadjusted 10  $\mu\text{M}$  benzoic acid (BA) into PME and illuminated it in a quartz tube, taking aliquots occasionally to measure benzoic acid concentrations by HPLC in order to determine the pseudo-first order decay rate constant for BA loss. The  $\bullet\text{OH}$  concentration was determined and normalized to sunlight conditions at midday on the winter solstice at Davis (solar zenith =  $62^\circ$ ;  $j_{2\text{NB},\text{win}} = 0.0070 \text{ s}^{-1}$ ) and corrected for internal light screening by equation S3.1:

$$[\bullet\text{OH}] = \left[ \frac{k'_{\text{BA}}}{k_{\text{BA}+\bullet\text{OH}} \times S_\lambda \times j_{2\text{NB},\text{exp}}} \right] \times j_{2\text{NB},\text{win}} \quad (\text{S3.1})$$

where  $k'_{\text{BA}}$  is the measured first-order decay rate constant of BA,  $k_{\text{BA}+\bullet\text{OH}}$  is the second-order rate constant of BA reacting with  $\bullet\text{OH}$  at pH 4.2 ( $5.1 \times 10^9 \text{ M}^{-1} \text{ s}^{-1}$ ),<sup>80,81</sup>  $S_\lambda$  is the internal light screening factor in an individual sample (determined based on the wavelength range 280 – 364 nm), and  $j_{2\text{NB},\text{exp}}$  is the photolysis rate constant of 2-nitrobenzaldehyde (2NB) measured on the experiment day.

To determine  $^1\text{O}_2^*$  concentrations, we used FFA as a probe and heavy water ( $\text{D}_2\text{O}$ ) as a diagnostic tool.<sup>79</sup> We prepared two solutions for each sample: one where 0.5 mL of PME was diluted with 0.5 mL  $\text{H}_2\text{O}$  and one diluted with 0.5 mL deuterium oxide ( $\text{D}_2\text{O}$ ). We spiked 10  $\mu\text{M}$  FFA into both solutions and determined the loss rate constants of FFA during illumination. The  $^1\text{O}_2^*$  concentration in the undiluted sample was determined from the difference of FFA loss rate constants in  $\text{H}_2\text{O}$  and  $\text{D}_2\text{O}$  using equation 14 in Kaur and Anastasio.<sup>15</sup>  $^1\text{O}_2^*$  concentrations were normalized by light screening factors of PME and to Davis winter sunlight, analogous to equation S3.1.

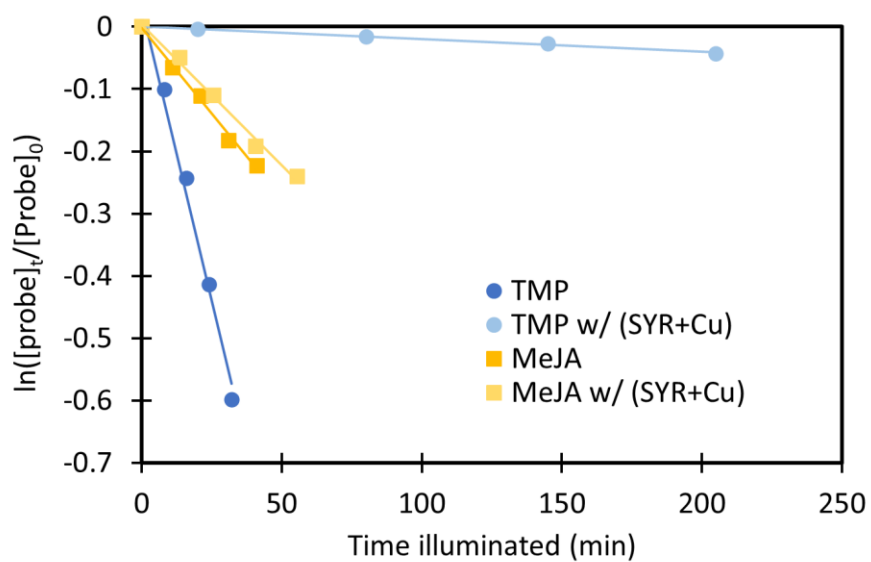
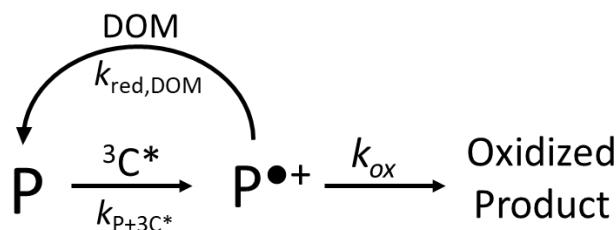


**Figure S3.1.** Representative plot of decay of TMP and MeJA by the triplet excited state of BP with and without SYR+Cu at pH 4.2. Results shown are for solutions containing 10  $\mu\text{M}$  TMP or MeJA, 15  $\mu\text{M}$  BP, and with or without 70  $\mu\text{M}$  SYR and 1  $\mu\text{M}$  Cu(II).

### Section S3.4: Derivation of equation 3.5

Scheme S3.1 shows the kinetic model for reaction of a probe (P) with a triplet state ( ${}^3\text{C}^*$ ) and the potential inhibition of net probe loss by DOM, as derived by Canonica et al. and Wenk et al.<sup>23,24</sup>



**Scheme S3.1**

The probe (P) is oxidized by  ${}^3\text{C}^*$  with a rate constant  $k_{P+3C^*}$  to form the intermediate radical cation ( $\text{P}^{\bullet+}$ ). The intermediate can either undergo further oxidation to form oxidized product with first-order rate constant  $k_{ox}$ , or be reduced by DOM back to P with a second-order rate constant  $k_{red,DOM}$ .

In addition to regenerating oxidized probe, DOM can also reduce net probe loss by acting as a sink for triplets, decreasing the steady-state concentration of  ${}^3\text{C}^*$ . We can quantify this suppression of triplet concentration by DOM with the inhibition factor for FFA loss ( $IF_{FFA}$ ). Since the  ${}^1\text{O}_2^*$  concentration is proportional to  ${}^3\text{C}^*$ ,  $IF_{FFA}$  can be expressed as

$$IF_{FFA} = \frac{[{}^3\text{C}^*]_{DOM}}{[{}^3\text{C}^*]_0} \quad (\text{S3.2})$$

where  $[{}^3\text{C}^*]_{DOM}$  is the triplet concentration in the presence of DOM (or SYR+Cu), and  $[{}^3\text{C}^*]_0$  is the triplet concentration without DOM or SYR+Cu.

In the absence of DOM or SYR+Cu, the pseudo-first-order decay rate constant of triplet probe by  ${}^3\text{C}^*$  can be expressed as:

$$k'_{p,0} = k_{P+3C^*} [{}^3\text{C}^*]_0 \quad (\text{S3.3})$$

In the presence of DOM or SYR+Cu, the decay rate of the probe by  ${}^3\text{C}^*$  can be expressed with the equation below from Wenk et al.:<sup>24</sup>

$$k'_{p,DOM} = k_{P+3C^*} [{}^3\text{C}^*]_{DOM} \left( \frac{k_{ox}}{k_{ox} + k_{red,DOM}[DOM]} \right) \quad (\text{S3.4})$$

where the factor in parentheses represents the fraction of  $\text{P}^{\bullet+}$  that is oxidized to stable product rather than reduced back to P. Based on this, the inhibition factor for the probe ( $IF_P$ ), can be expressed as a function of  $IF_{FFA}$ :

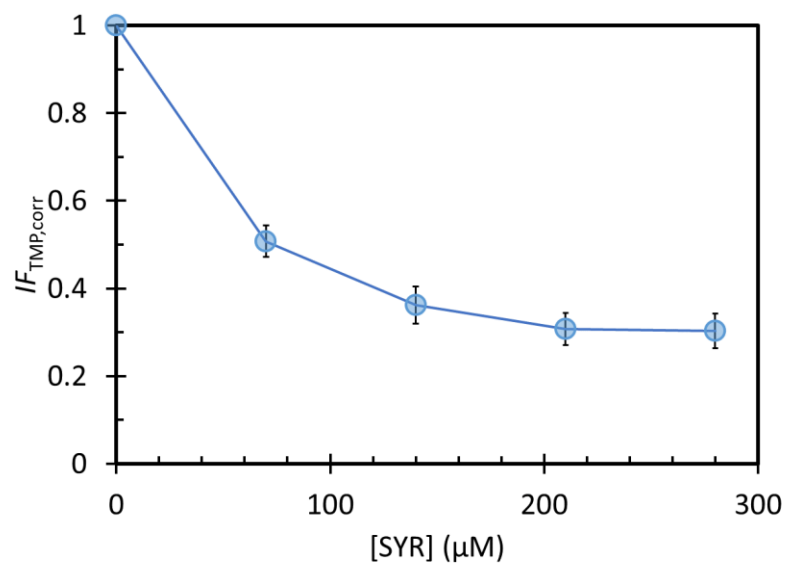
$$IF_P = \frac{k'_{p,DOM}}{k'_{p,0}} = \frac{k_{P+3C^*} [{}^3\text{C}^*]_{DOM} \left( \frac{k_{ox}}{k_{ox} + k_{red,DOM}[DOM]} \right)}{k_{P+3C^*} [{}^3\text{C}^*]_0} = IF_{FFA} \left( \frac{k_{ox}}{k_{ox} + k_{red,DOM}[DOM]} \right) \quad (\text{S3.5})$$

The inhibition factor  $IF_P$  includes both of the impacts of DOM on probe loss, i.e., the decrease in  ${}^3\text{C}^*$  concentrations and regeneration of oxidized probe back to its original state. We define  $IF_{P,corr}$  as the corrected inhibition factor, which only expresses the inhibition effect of DOM on  $\text{P}^{\bullet+}$ :

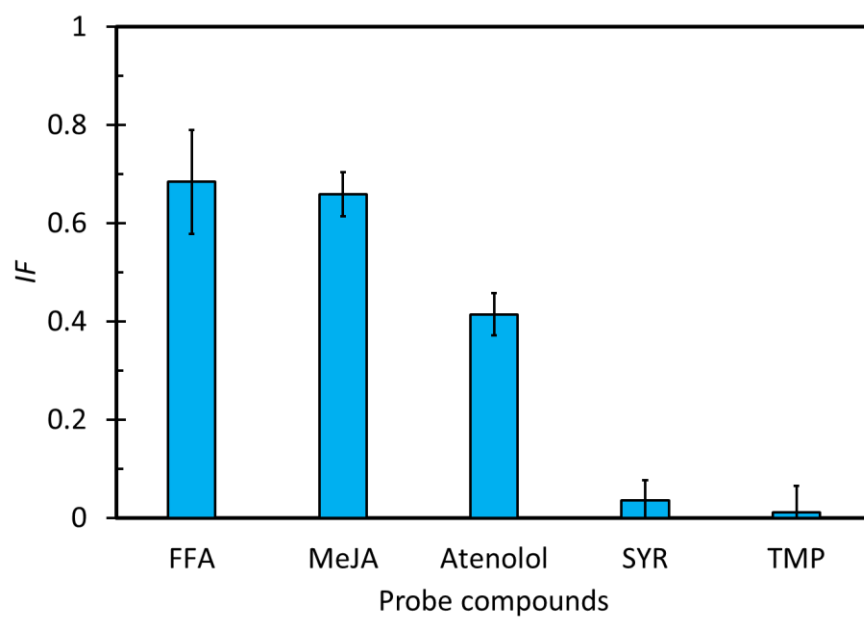
$$IF_{P,corr} = \left( \frac{k_{ox}}{k_{ox} + k_{red,DOM}[DOM]} \right) = \frac{IF_P}{IF_{FFA}} \quad (\text{S3.6})$$

When  $IF_{FFA}$  or  $IF_P$  greater than 1, this indicates that the impact of DOM in  ${}^3\text{C}^*$  concentration decrease is negligible. Under this condition, there is no need for  $IF$  correction, and  $IF_{P,corr} = IF_P$ .



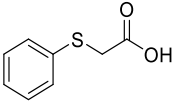
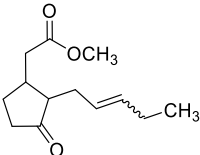
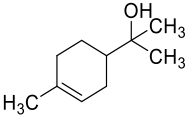
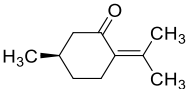
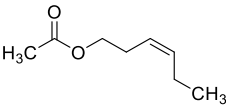
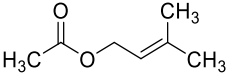
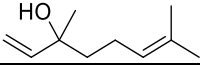
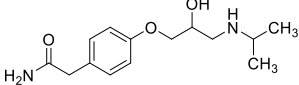
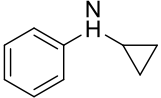
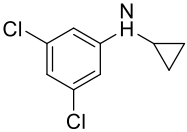
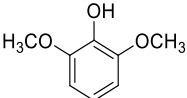
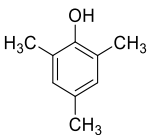


**Figure S3.2.** Influence of SYR on the decay of TMP by  $^3\text{BP}^*$ , shown as the corrected inhibition factor of TMP. Solutions contained 10  $\mu\text{M}$  TMP, 15  $\mu\text{M}$  BP, and 0 to 280  $\mu\text{M}$  syringol. No Cu(II) was added.



**Figure S3.3.** Inhibition factors of probe compounds in PME5 with 15  $\mu$ M BP as the triplet precursor. Data are shown in Table S3.3. Error bars represent  $\pm 1$  standard error propagated from the linear regression.

**Table S3.1.** The structures of probe compounds in Table 3.1

Classes	Compounds	Structure
Sulfide	(Phenylthio)acetic acid (PTA)	
	Methyl jasmonate (MeJA)	
	Terpineol (TPN)	
Alkenes	Pulegone	
	<i>cis</i> -3-Hexenyl acetate	
	Prenyl acetate	
	Linalool	
Amine	Atenolol (ANL)	
	<i>N</i> -cyclopropylaniline (CAN)	
Anilines	3,5-dichloro- <i>N</i> -cyclopropylaniline (DCCAN)	
	Syringol (SYR)	
Phenols	2,4,6-trimethylphenol (TMP)	

### Section S3.5. Determination of the second-order rate constant of TPN with <sup>3</sup>DMB\*

The photochemical reaction between a carbonyl compound and an alkene can form an oxetane through the Paternò-Büchi reaction.<sup>63,64</sup> This is a photocycloaddition between an excited carbonyl compound (singlet or triplet state) and an alkene. The mechanism can either form a diradical intermediate or an exciplex from charge-transfer complexes. The latter involves intermolecular electron transfer to form a radical-ion pair, which is observed only for very electron-rich alkenes.<sup>82</sup> The mechanistic pathway depends on the difference in redox potentials between the alkene and the singlet or triplet state of the carbonyl compound.<sup>83</sup> If the redox potential of alkene is smaller, electron transfer might proceed. Therefore, the reaction between alkene and triplets does not necessarily involve electron transfer, complicating the use of alkenes to determine concentrations of oxidizing triplets. Consequently, alkenes do not appear to be appropriate as probes for oxidizing triplets, although alkene decay is not inhibited by DOM, which is likely a consequence of the irreversible formation of oxetane.

Prior to understanding the importance of the Paternò-Büchi reaction, we worked to assess alkenes as oxidizing triplet probes because of their resistance to inhibition. We encountered difficulty determining the bimolecular rate constant of  $\alpha$ -terpineol with <sup>3</sup>DMB\*. As shown in Figure S3.4, our measured values are different with different methods. The red triangles represent rate constants obtained with a direct measurement technique described in Smith et al. and Ma et al.<sup>17,76</sup> The values of the rate constant vary by a factor of 2.5 between the two measurements. Also, when using a relative rate method, the TPN concentration appears to affect the TPN rate constant: rate constants determined with 10  $\mu$ M TPN are about 4 times lower than those measured with 20  $\mu$ M TPN.

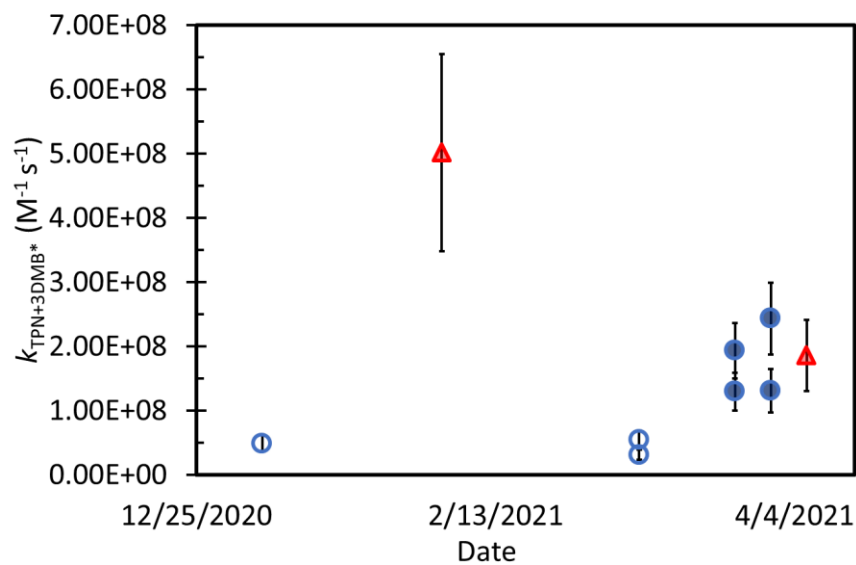


**Figure S3.4.** Measured second-order rate constants of TPN reacting with  $^3\text{DMB}^*$  at pH 2 with two different experimental methods. The red triangles represent values obtained with a direct measurement method.<sup>65</sup> The open blue circles represent values from a relative rate method using 10  $\mu\text{M}$  TPN, while the solid blue circles represent the values obtained using 20  $\mu\text{M}$  TPN.

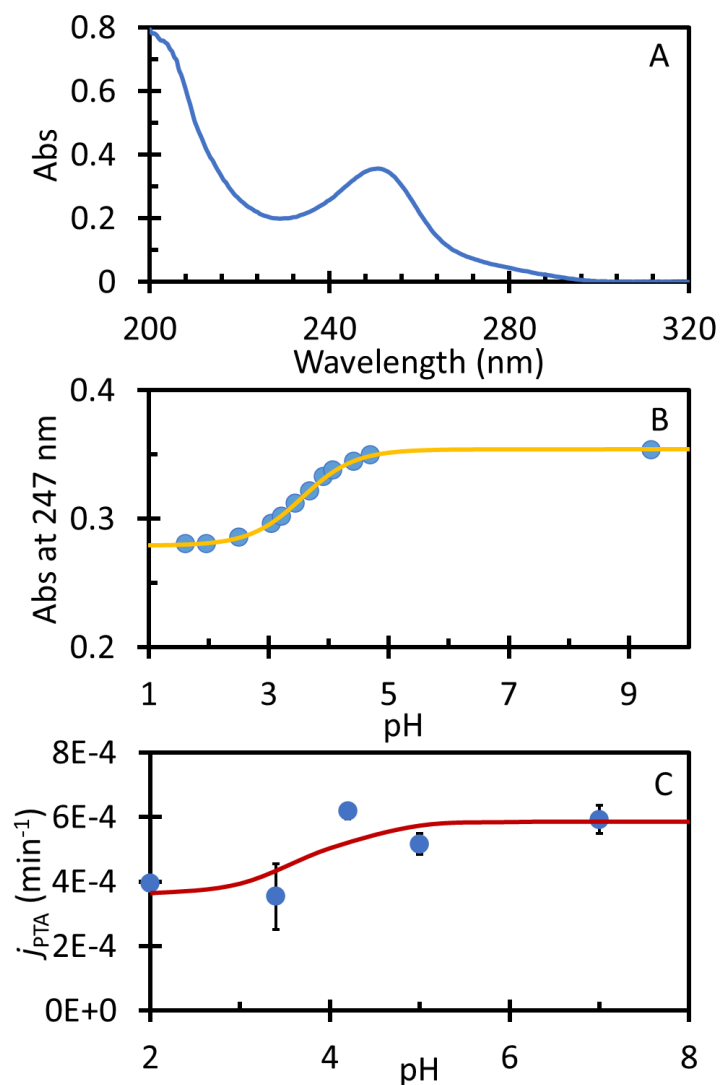


**Figure S3.5.** (A) Absorption spectrum of 50  $\mu\text{M}$  PTA at pH 4.2 in a 1-cm cuvette. (B) The absorbance of 50  $\mu\text{M}$  PTA solution at 247 nm as a function of pH in a 1-cm cuvette. Data are fitted with the equation  $Abs_{TOT} = Abs_{SHPTA} + \frac{Abs_{SPTA} - Abs_{SHPTA}}{1 + \frac{[H^+]}{K_a}}$  to obtain  $pK_a$ ,  $Abs_{SPTA}$  and  $Abs_{SHPTA}$  values, where  $Abs_{TOT}$  is the absorbance of a 50  $\mu\text{M}$  PTA solution (in a 1-cm cell) at 247 nm at different pH values,  $Abs_{SHPTA}$  and  $Abs_{SPTA}$  are the absorbance values of the protonated and deprotonated forms of PTA, respectively. From the fitting,  $pK_a = 3.56 (\pm 0.02)$ ,  $Abs_{SHPTA} = 0.28 (\pm 0.01)$  and  $Abs_{SPTA} = 0.35 (\pm 0.01)$ . (C) Winter solstice-normalized direct photodegradation rate constant of PTA as a function of pH. Data are fitted with the equation  $j_{TOT} = j_{HPTA} + \frac{j_{PTA} - j_{HPTA}}{1 + \frac{[H^+]}{K_a}}$  to  $j_{HPTA}$  and  $j_{PTA}$  values, which are direct photodegradation rate constants of protonated and deprotonated forms of PTA, respectively. From the fitting,  $j_{HPTA} = 3.5 (\pm 0.7) \times 10^{-4} \text{ min}^{-1}$  and  $j_{PTA} = 5.8 (\pm 0.5) \times 10^{-4} \text{ min}^{-1}$ .

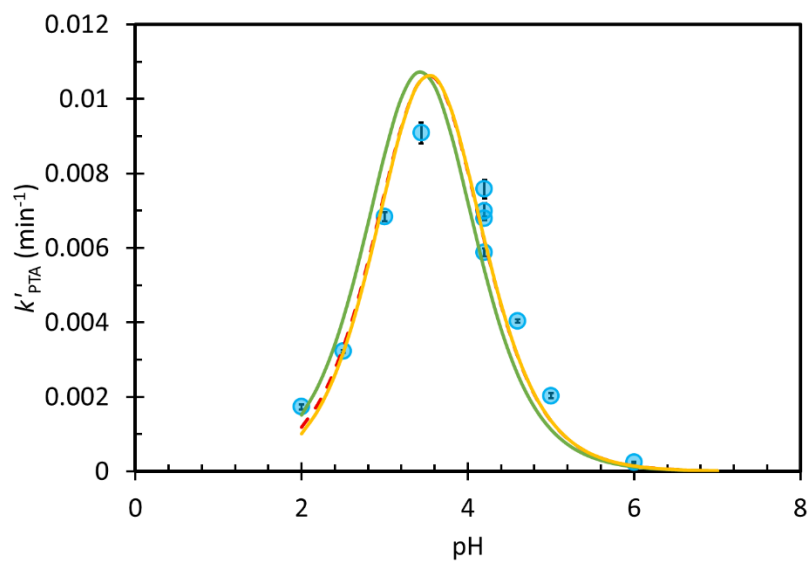


**Figure S3.6.** Dependence of the measured first-order PTA decay rate constant on pH for illuminated solutions containing 10  $\mu\text{M}$  DMB and 10  $\mu\text{M}$  PTA at 20  $^{\circ}\text{C}$ . The red dashed line is the regression in Figure 3.2. The green solid line represents the regression fit to eq 6 using 3.3 as the  $\text{p}K_{\text{a}}$  of  $^3\text{DMB}^*$ , with  $a$ ,  $b$ , and  $d$  set as zero and the fitted  $c$  value of  $0.059 \text{ min}^{-1}$ . The yellow solid line represents the regression fit with  $b$  and  $d$  set to zero, with fitted  $a$  and  $c$  values of  $-1.9 \times 10^{-4} \text{ min}^{-1}$  and  $0.046 \text{ min}^{-1}$ , respectively.

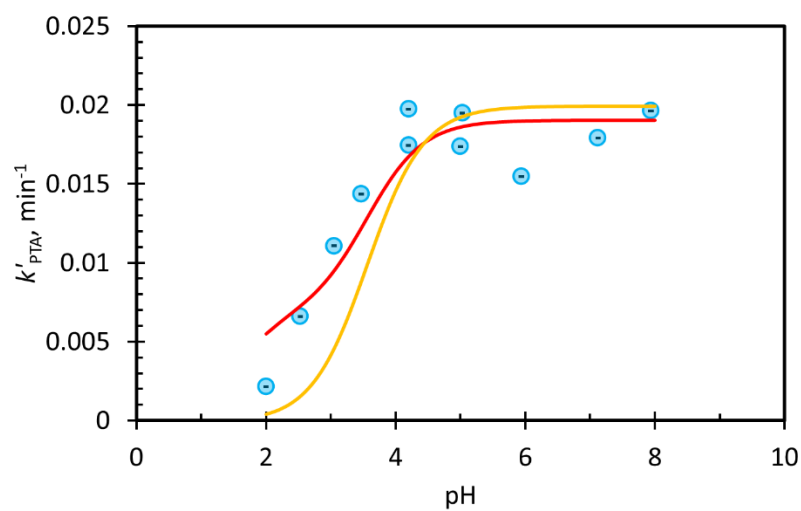


**Figure S3.7.** pH dependence of the first-order PTA decay rate constant for illuminated solutions containing 15  $\mu\text{M}$  BP and 10  $\mu\text{M}$  PTA at 20  $^{\circ}\text{C}$ . The red line is the regression fitted to a BP-analog of eq 6, with  $a$  and  $c$  set to zero and fitted  $b$  and  $d$  values of 0.0069  $\text{min}^{-1}$  and 0.19  $\text{min}^{-1}$ , respectively. The yellow line represents the regression fit with  $a$ ,  $b$ , and  $c$  set as zero and a fitted  $d$  value of 0.020  $\text{min}^{-1}$ . We used the  $^3\text{BP}^*$   $pK_a$  of 1.5 in all regression fits.<sup>84</sup>



**Table S3.2.** Second-order rate constants of PTA reacting with triplet excited states, singlet oxygen, and hydroxyl radical.

	Rate constant at pH 4.2 (M <sup>-1</sup> s <sup>-1</sup> )	Method (Reference compound)	Reference compound rate constant	Reference for reference compound rate constant
$k_{\text{PTA}+3\text{BP}^*}$	$5.0 (\pm 0.9) \times 10^9$	Relative (TMP)	$5.1 (\pm 0.9) \times 10^9$	Canonica et al. <sup>58</sup>
$k_{\text{PTA}+3\text{DMB}^*}$	$2.5 (\pm 0.6) \times 10^9$	Direct <sup>a</sup>	-	
$k_{\text{PTA}+3\text{MAP}^*}$	$3.1 (\pm 0.4) \times 10^9$	Relative (TMP)	$2.6 (\pm 0.3) \times 10^9$	Canonica et al. <sup>58</sup>
$k_{\text{PTA}+2\text{AN}^*}$	$2.4 (\pm 0.2) \times 10^7$	Relative (TMP)	$7.2 (\pm 0.1) \times 10^8$	Canonica et al. <sup>58</sup>
$k_{\text{PTA}+1\text{O}_2^*}$	$8.8 (\pm 0.6) \times 10^6$	Relative (FFA)	$1.0 (\pm 0.1) \times 10^8$	Appiani et al. <sup>51</sup>
$k_{\text{PTA}+\text{OH}^*}$	$10.3 (\pm 0.6) \times 10^9$	Relative (Benzene)	$7.7 (\pm 0.4) \times 10^9$	Kochany et al. <sup>85</sup>

<sup>a</sup> See Figure S3.9

**Table S3.3.** Characteristic of model triplet species

Model Triplet	$E_T$ (kJ mol <sup>-1</sup> ) <sup>a</sup>	$E_0^*({}^3\text{C}^*/\text{C}^{\bullet-})$ (V) <sup>b</sup>
2-acetonaphthone ( <sup>3</sup> 2AN*)	249	1.10
3-methoxyacetophenone ( <sup>3</sup> 3MAP*)	303	1.64
3,4-dimethoxybenzaldehyde ( <sup>3</sup> DMB*)	268	-
Benzophenone ( <sup>3</sup> BP*)	288	1.67

All values are from Canonica et al. and Felber et al.<sup>58,86</sup>

<sup>a</sup> Triplet state energy ( $T_1 \rightarrow S_0$ ).

<sup>b</sup> One-electron reduction potential for the triplet/triplet radical anion pair.

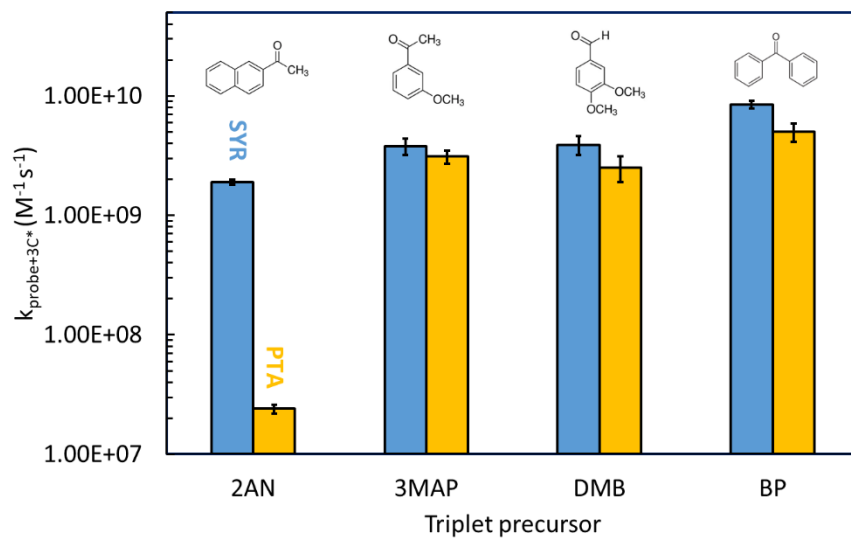


**Figure S3.8.** Bimolecular rate constants for syringol (blue) and (phenolthio)acetic acid (yellow) with the triplet excited states of four model organics. Structures show the ground state of each photosensitizer.

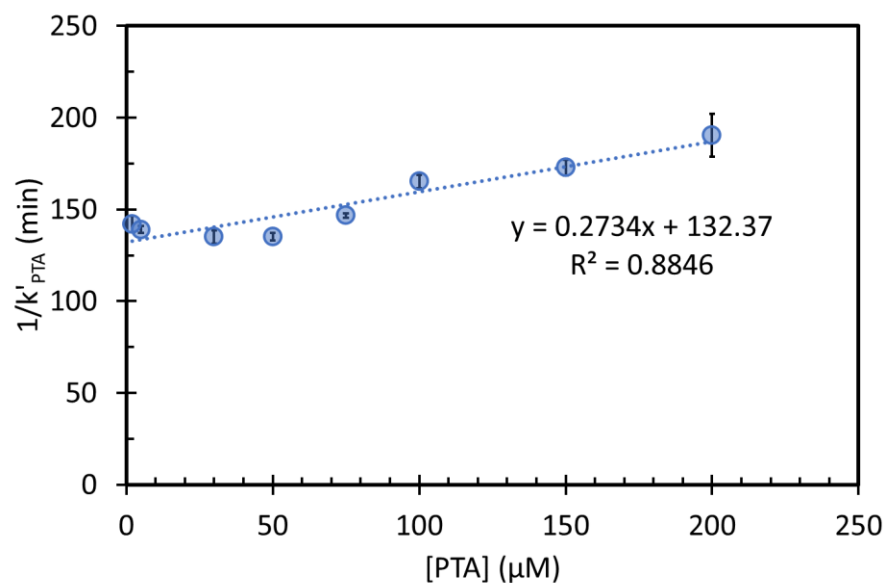


**Figure S3.9.** Inverse of the PTA first-order decay rate constant with  $^3\text{DMB}^*$  as a function of initial PTA concentration at pH 4.2. The dotted line is a linear regression fit to the data. Error bars on points represent  $\pm 1$  standard error propagated from the errors of  $k'_{\text{PTA}}$  and  $j_{\text{PTA}}$ . Details of the method to determine  $k_{\text{PTA}+^3\text{DMB}^*}$  are provided in Smith et al. and Ma et al.<sup>17,65</sup>

### Section S3.6. Electron Donating Capacity (EDC) Determination

We adapted the EDC method from Walpen et al. and Yuan et al.<sup>70,71</sup>, using a 0.10 mM ABTS (2,2'-azino-bis(3-ethylbenzothiazoline-6-sulfonic acid) solution prepared with acetate buffer (0.05 M) to maintain pH at 4.2. We prepared a 10 mM NaClO solution by diluting concentrated sodium hypochlorite solution using the molar absorption coefficient of hypochlorite ( $\epsilon(292 \text{ nm}) = 359 \text{ M}^{-1}\text{cm}^{-1}$  at pH 11).<sup>87</sup> The ABTS<sup>•+</sup> solution was prepared by adding 10 mM NaClO to ABTS solution to oxidize around 70% of the ABTS to ABTS<sup>•+</sup>, and then shaking for 10 min. To determine EDC for PME, 200  $\mu\text{L}$  PME (for extracts with high DOC) or 1 ml PME (for extracts with low DOC) was spiked into 5.0 mL of ABTS<sup>•+</sup> solution. After spiking, we shook the solution for 5 min and then let it stand for 10 min. The absorbance of the solution at 728 nm was measured by a UV-Vis spectrophotometer to determine the ABTS<sup>•+</sup> concentration (using a molar absorption coefficient  $\epsilon = 14000 \text{ M}^{-1} \text{ cm}^{-1}$  at 728 nm)<sup>88</sup> and EDC was determined from a standard curve prepared using Trolox.

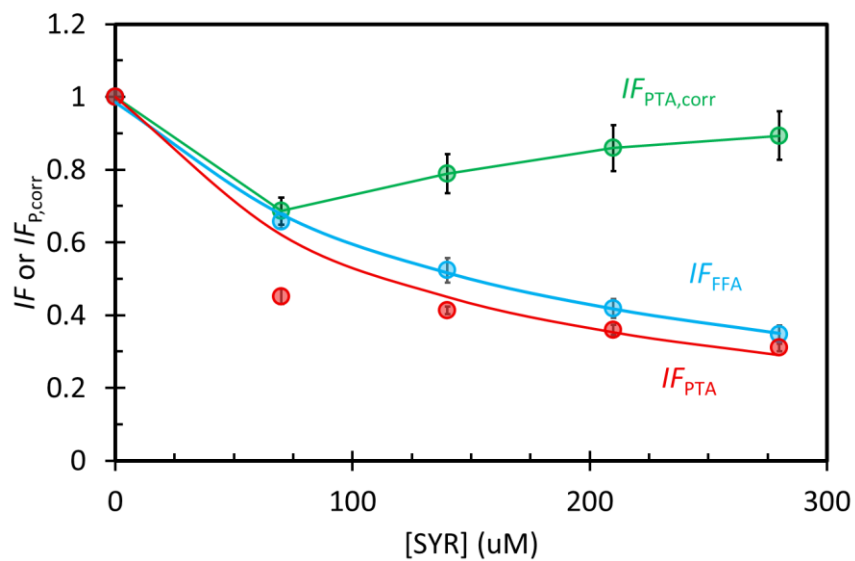


**Figure S3.10.** Inhibition factors of FFA (blue) and PTA (red), and the corrected inhibition factor of PTA (green), as a function of SYR concentration with 15  $\mu$ M BP as the triplet precursor in SYR+Cu solution at pH 4.2. The red and blue lines represent the linear regression between the inverse of IF values versus the SYR concentration. Error bars represent  $\pm 1$  SE, propagated from the linear regression.

**Table S3.4.** Summary of inhibition factors of probes with different DOM

	PME1	PME2	PME3	PME4	PME5 <sup>b</sup>	SRFA	SRFA	70 $\mu$ M SYR + 1 $\mu$ M Cu(II)	140 $\mu$ M SYR + 2 $\mu$ M Cu(II)	210 $\mu$ M SYR + 3 $\mu$ M Cu(II)	280 $\mu$ M SYR + 4 $\mu$ M Cu(II)	350 $\mu$ M SYR + 5 $\mu$ M Cu(II)	420 $\mu$ M SYR + 6 $\mu$ M Cu(II)	
DOC (mg C L <sup>-1</sup> )	9.9	63.7	68.8	104.9	27.8	25.8	51.5	6.7	13.4	20.2	26.9	33.6	40.3	
EDC (mmol e <sup>-</sup> gc <sup>-1</sup> )	< LOD <sup>a</sup>	1.8 ( $\pm$ 0.1)	1.7 ( $\pm$ 0.2)	4.4 ( $\pm$ 0.1)	-	1.7 ( $\pm$ 0.1)	1.7 ( $\pm$ 0.1)	36	28	28	27	29	29	
EDC $\times$ DOC (mmol e <sup>-</sup> L <sup>-1</sup> )	< LOD	0.11 ( $\pm$ 0.01)	0.12 ( $\pm$ 0.01)	0.47 ( $\pm$ 0.01)	-	0.04 ( $\pm$ 0.01)	0.08 ( $\pm$ 0.02)	0.25	0.38	0.56	0.73	0.96	1.16	
<i>IF</i> w/ 80 $\mu$ M DMB	FFA	1.10 ( $\pm$ 0.07)	1.00 ( $\pm$ 0.20)	1.30 ( $\pm$ 0.12)	1.00 ( $\pm$ 0.12)	-	1.91 ( $\pm$ 0.14)	-	0.83 ( $\pm$ 0.04)	0.77 ( $\pm$ 0.04)	0.56 ( $\pm$ 0.04)	0.55 ( $\pm$ 0.04)	0.50 ( $\pm$ 0.10)	0.44 ( $\pm$ 0.03)
	SYR	0.76 ( $\pm$ 0.03)	0.48 ( $\pm$ 0.03)	0.21 ( $\pm$ 0.04)	0.31 ( $\pm$ 0.02)	-	1.17 ( $\pm$ 0.10)	-	-	-	-	-	-	
	PTA	0.75 ( $\pm$ 0.03)	1.24 ( $\pm$ 0.06)	1.26 ( $\pm$ 0.03)	0.60 ( $\pm$ 0.04)	-	0.59 ( $\pm$ 0.03)	-	0.74 ( $\pm$ 0.01)	0.54 ( $\pm$ 0.01)	0.44 ( $\pm$ 0.01)	0.35 ( $\pm$ 0.01)	0.27 ( $\pm$ 0.01)	0.23 ( $\pm$ 0.01)
<i>IF</i> w/ 15 $\mu$ M BP	FFA	-	-	-	-	0.68 ( $\pm$ 0.10)	-	0.71 ( $\pm$ 0.32)	0.66 ( $\pm$ 0.02)	0.52 ( $\pm$ 0.03)	0.42 ( $\pm$ 0.03)	0.35 ( $\pm$ 0.02)	-	-
	SYR	-	-	-	-	0.03 ( $\pm$ 0.04)	-	0.61 ( $\pm$ 0.11)	-	-	-	-	-	-
	PTA	-	-	-	-	-	-	-	0.45 ( $\pm$ 0.02)	0.41 ( $\pm$ 0.01)	0.36 ( $\pm$ 0.01)	0.31 ( $\pm$ 0.10)	-	-
	TMP	-	-	-	-	0.01 ( $\pm$ 0.05)	-	-	0.01 ( $\pm$ 0.01)	-	-	-	-	-
	Aten- olol	-	-	-	-	0.41 ( $\pm$ 0.04)	-	-	-	-	-	-	-	-
	MeJA	-	-	-	-	0.66 ( $\pm$ 0.04)	-	0.47 ( $\pm$ 0.02)	0.71 ( $\pm$ 0.05)	0.49 ( $\pm$ 0.01)	0.41 ( $\pm$ 0.01)	-	-	-
	TPN	-	-	-	-	-	-	-	0.65 ( $\pm$ 0.01)	0.49 ( $\pm$ 0.01)	0.43 ( $\pm$ 0.01)	0.35 ( $\pm$ 0.01)	-	-

Errors (in parentheses) represent one standard error propagated from the error of linear regression.

<sup>a</sup> Below detection limit.

<sup>b</sup> PME5 was used to determine *IF* values with BP but was not characterized for photooxidant concentrations.

**Table S3.5. Information on PME samples**

Sample ID	PME1	PME2	PME3	PME4	PME5 <sup>g</sup>
Collection dates	08/04/20 - 08/21/20	01/03/20 - 01/10/20	12/17/19 - 12/24/19	08/24/20 - 08/25/20	01/10/16 - 01/12/16
Collection time (hr)	24	168 (one week)	168 (one week)	24	28
Daily PM <sub>2.5</sub> concentration (µg m <sup>-3</sup> -air) <sup>a</sup>	6.9	9.0	10	50	5.9
Average mass of PM extracted (µg) <sup>b</sup>	79 (±14)	620 (±53)	540 (±35)	311 (±21)	132 (±11)
PM mass/water ratio (10 <sup>-4</sup> µg PM/µg H <sub>2</sub> O)	0.79 (±0.14)	6.2 (±0.5)	5.4 (±0.4)	3.1 (±0.2)	1.3 (±0.1)
α <sub>300</sub> (cm <sup>-1</sup> ) <sup>c</sup>	0.020	0.553	0.723	1.524	0.33
AAE (300-450) <sup>d</sup>	6.7	7.7	7.4	7.4	6.2
DOC (mg C L <sup>-1</sup> )	9.9	63.7	68.8	104.9	27.8
EDC (mmol e <sup>-</sup> L <sup>-1</sup> )	< LOD <sup>e</sup>	0.11 (±0.01)	0.12 (±0.01)	0.47 (±0.01)	-
[ <sup>1</sup> O <sub>2</sub> *] (10 <sup>-12</sup> M)	0.080 (±0.003)	2.3 (±0.1)	2.5 (±0.2)	3.0 (±0.2)	-
[*OH] (10 <sup>-15</sup> M)	0.22 (±0.11)	5.8 (±0.5)	4.8 (±0.5)	1.5 (±1.1)	-
IF <sub>FFA</sub> <sup>f</sup>	1.10 (±0.07)	0.97 (±0.20)	1.30 (±0.12)	1.00 (±0.12)	-
IF <sub>SYR</sub> <sup>f</sup>	0.76 (±0.03)	0.48 (±0.03)	0.21 (±0.04)	0.31 (±0.02)	-
IF <sub>SYR,corr</sub>	0.76 (±0.03)	0.48 (±0.03)	0.21 (±0.04)	0.31 (±0.02)	-
IF <sub>PTA</sub> <sup>f</sup>	0.75 (±0.03)	1.24 (±0.06)	1.26 (±0.03)	0.60 (±0.04)	-
IF <sub>PTA,corr</sub>	0.75 (±0.03)	1.24 (±0.06)	1.26 (±0.03)	0.60 (±0.04)	-
[ <sup>3</sup> C*] <sub>SYR</sub> (10 <sup>-14</sup> M)	0.66 (±0.15)	8.7 (±1.8)	9.0 (±2.2)	20 (±5)	-
[ <sup>3</sup> C*] <sub>SYR,corr</sub> (10 <sup>-14</sup> M)	0.87 (±0.20)	18 (±5)	43 (±13)	63 (±16)	-
[ <sup>3</sup> C*] <sub>PTA</sub> (10 <sup>-14</sup> M)	0.21 (±0.09)	21 (±5)	20 (±5)	10 (±3)	-
[ <sup>3</sup> C*] <sub>PTA,corr</sub> (10 <sup>-14</sup> M)	0.28 (±0.12)	21 (±5)	20 (±5)	17 (±4)	-

<sup>a</sup> Daily PM<sub>2.5</sub> concentration for each sampling period measured at the UC Davis sampling site by the California Air Resources as reported on the iADAM online database (California Air Resources Board, 2019 –2020)

<sup>b</sup> The average (± 1σ) mass of PM extracted from each 2 cm × 2 cm filter square.

<sup>c</sup> Base-10 absorbance coefficient of the extract (in cm<sup>-1</sup>) at 300 nm.

<sup>d</sup> Absorption Angstrom Exponent (AAE) describes the dependence of absorbance on wavelength from 300 nm to 450 nm and is calculated with equation:  $AAE = [\log(Abs_{300}) - \log(Abs_{450})] / \log(300/450)$ , where  $Abs_{450}$  and  $Abs_{300}$  are the absorbances at 450 and 300 nm, respectively.

<sup>e</sup> Below detection limit.

<sup>f</sup> *IF* values shown in this table were measured with 80  $\mu$ M DMB.

<sup>g</sup> PME5 was prepared using a particle filter collected by Kaur et al.<sup>16</sup> PME5 was used to determine *IF* values with BP but was not characterized for photooxidant concentrations.



### 3.9. References

- (1) McNeill, K.; Canonica, S. Triplet state dissolved organic matter in aquatic photochemistry: reaction mechanisms, substrate scope, and photophysical properties. *Environ. Sci. Process. Impacts* **2016**, *18*, 1381–1399.
- (2) Remucal, C. K. The role of indirect photochemical degradation in the environmental fate of pesticides: a review. *Environ. Sci. Process. Impacts* **2014**, *16*, 628–653.
- (3) Challis, J. K.; Hanson, M. L.; Friesen, K. J.; Wong, C. S. A critical assessment of the photodegradation of pharmaceuticals in aquatic environments: defining our current understanding and identifying knowledge gaps. *Environ. Sci. Process. Impacts* **2014**, *16*, 672–696.
- (4) Aregahegn, K. Z.; Nozière, B.; George, C. Organic aerosol formation photo-enhanced by the formation of secondary photosensitizers in aerosols. *Faraday Discuss* **2013**, *165*, 123–134.
- (5) González Palacios, L.; Corral Arroyo, P.; Aregahegn, K. Z.; Steimer, S. S.; Bartels-Rausch, T.; Nozière, B.; George, C.; Ammann, M.; Volkamer, R. Heterogeneous photochemistry of imidazole-2-carboxaldehyde: HO<sub>2</sub> radical formation and aerosol growth. *Atmos. Chem. Phys.* **2016**, *16*, 11823–11836.
- (6) Rossignol, S.; Aregahegn, K. Z.; Tinel, L.; Fine, L.; Nozière, B.; George, C. Glyoxal induced atmospheric photosensitized chemistry leading to organic aerosol growth. *Environ. Sci. Technol.* **2014**, *48*, 3218–3227.
- (7) Wang, X.; Gemayel, R.; Hayeck, N.; Perrier, S.; Charbonnel, N.; Xu, C.; Chen, H.; Zhu, C.; Zhang, L.; Wang, L.; et al. Atmospheric photosensitization: A new pathway for sulfate formation. *Environ. Sci. Technol.* **2020**, *54*, 3114–3120.
- (8) Ossola, R.; Clerc, B.; McNeill, K. Mechanistic Insights into Dissolved Organic Sulfur Photomineralization through the Study of Cysteine Sulfinic Acid. *Environ. Sci. Technol.* **2020**, *54*, 13066–13076.
- (9) Ossola, R.; Tolu, J.; Clerc, B.; Erickson, P. R.; Winkel, L. H. E.; McNeill, K. Photochemical Production of Sulfate and Methanesulfonic Acid from Dissolved Organic Sulfur. *Environ. Sci. Technol.* **2019**, *53*, 13191–13200.
- (10) Anastasio, C.; Faust, B. C.; Rao, C. J. Aromatic carbonyl compounds as aqueous-phase photochemical sources of hydrogen peroxide in acidic sulfate aerosols, fogs, and clouds. 1. Non-phenolic methoxybenzaldehydes and methoxyacetophenones with reductants (phenols). *Environ. Sci. Technol.* **1996**, *31*, 218–232.
- (11) Corral Arroyo, P.; Bartels-Rausch, T.; Alpert, P. A.; Dumas, S.; Perrier, S.; George, C.; Ammann, M. Particle-Phase Photosensitized Radical Production and Aerosol Aging. *Environ. Sci. Technol.* **2018**, *52*, 7680–7688.
- (12) Zepp, R. G.; Wolfe, N. L.; Baughman, G. L.; Hollis, R. C. Singlet oxygen in natural waters. *Nature* **1977**, *267*, 421.
- (13) Zepp, R. G.; Schlotzhauer, P. F.; Sink, R. M. Photosensitized transformations involving electronic energy transfer in natural waters: role of humic substances. *Environ. Sci. Technol.* **1985**, *19*, 74–81.
- (14) Kaur, R.; Anastasio, C. First measurements of organic triplet excited states in atmospheric waters. *Environ. Sci. Technol.* **2018**, *52*, 5218–5226.
- (15) Kaur, R.; Anastasio, C. Light absorption and the photoformation of hydroxyl radical and singlet oxygen in fog waters. *Atmos. Environ.* **2017**, *164*, 387–397.

- (16) Kaur, R.; Labins, J. R.; Helbock, S. S.; Jiang, W.; Bein, K. J.; Zhang, Q.; Anastasio, C. Photooxidants from brown carbon and other chromophores in illuminated particle extracts. *Atmos. Chem. Phys.* **2019**, *19*, 6579–6594.
- (17) Ma, L.; Guzman, C.; Niedek, C.; Tran, T.; Zhang, Q.; Anastasio, C. Kinetics and Mass Yields of Aqueous Secondary Organic Aerosol from Highly Substituted Phenols Reacting with a Triplet Excited State. *Environ. Sci. Technol.* **2021**, *55*, 5772–5781.
- (18) Schmitt, M.; Moor, K. J.; Erickson, P. R.; McNeill, K. Sorbic acid as a triplet probe: reactivity of oxidizing triplets in dissolved organic matter by direct observation of aromatic amine oxidation. *Environ. Sci. Technol.* **2019**, *53*, 8087–8096.
- (19) Grebel, J. E.; Pignatello, J. J.; Mitch, W. A. Sorbic acid as a quantitative probe for the formation, scavenging and steady-state concentrations of the triplet-excited state of organic compounds. *Water Res.* **2011**, *45*, 6535–6544.
- (20) Zhou, H.; Yan, S.; Ma, J.; Lian, L.; Song, W. Development of Novel Chemical Probes for Examining Triplet Natural Organic Matter under Solar Illumination. *Environ. Sci. Technol.* **2017**, *51*, 11066–11074.
- (21) Rosario-Ortiz, F. L.; Canonica, S. Probe compounds to assess the photochemical activity of dissolved organic matter. *Environ. Sci. Technol.* **2016**, *50*, 12532–12547.
- (22) Maizel, A. C.; Remucal, C. K. The effect of probe choice and solution conditions on the apparent photoreactivity of dissolved organic matter. *Environ. Sci. Process. Impacts* **2017**, *19*, 1040–1050.
- (23) Canonica, S.; Laubscher, H.-U. Inhibitory effect of dissolved organic matter on triplet-induced oxidation of aquatic contaminants. *Photochem. Photobiol. Sci.* **2008**, *7*, 547.
- (24) Wenk, J.; von Gunten, U.; Canonica, S. Effect of dissolved organic matter on the transformation of contaminants induced by excited triplet states and the hydroxyl radical. *Environ. Sci. Technol.* **2011**, *45*, 1334–1340.
- (25) Wenk, J.; Canonica, S. Phenolic Antioxidants Inhibit the Triplet-Induced Transformation of Anilines and Sulfonamide Antibiotics in Aqueous Solution. *Environ. Sci. Technol.* **2012**, *46*, 5455–5462.
- (26) Leresche, F.; von Gunten, U.; Canonica, S. Probing the Photosensitizing and Inhibitory Effects of Dissolved Organic Matter by Using N,N-dimethyl-4-cyanoaniline (DMABN). *Environ. Sci. Technol.* **2016**, *50*, 10997–11007.
- (27) Leresche, F.; Ludvíková, L.; Heger, D.; von Gunten, U.; Canonica, S. Quenching of an aniline radical cation by dissolved organic matter and phenols: A laser flash photolysis study. *Environ. Sci. Technol.* **2020**, *54*, 15057–15065.
- (28) Weinberg, D. R.; Gagliardi, C. J.; Hull, J. F.; Murphy, C. F.; Kent, C. A.; Westlake, B. C.; Paul, A.; Ess, D. H.; McCafferty, D. G.; Meyer, T. J. Proton-Coupled Electron Transfer. *Chem. Rev.* **2012**, *112*, 4016–4093.
- (29) Pan, Y.; Garg, S.; Waite, T. D.; Yang, X. Copper Inhibition of Triplet-Induced Reactions Involving Natural Organic Matter. *Environ. Sci. Technol.* **2018**, *52*, 2742–2750.
- (30) Pan, Y.; Ruan, X.; Garg, S.; Waite, T. D.; Lei, Y.; Yang, X. Copper Inhibition of Triplet-Sensitized Phototransformation of Phenolic and Amine Contaminants. *Environ. Sci. Technol.* **2020**, *54*, 9980–9989.
- (31) McCabe, A. J.; Arnold, W. A. Reactivity of Triplet Excited States of Dissolved Natural Organic Matter in Stormflow from Mixed-Use Watersheds. *Environ. Sci. Technol.* **2017**, *51*, 9718–9728.

- (32) Bodhipaksha, L. C.; Sharpless, C. M.; Chin, Y.-P.; Sander, M.; Langston, W. K.; MacKay, A. A. Triplet photochemistry of effluent and natural organic matter in whole water and isolates from effluent-receiving rivers. *Environ. Sci. Technol.* **2015**, *49*, 3453–3463.
- (33) Pflug, N. C.; Schmitt, M.; McNeill, K. Development of N-Cyclopropylanilines to Probe the Oxidative Properties of Triplet-State Photosensitizers. *Environ. Sci. Technol.* **2019**, *53*, 4813–4822.
- (34) Leenheer, J. A.; Croué, J.-P. Peer reviewed: characterizing aquatic dissolved organic matter. *Environ. Sci. Technol.* **2003**, *37*, 18A–26A.
- (35) Ervens, B.; Turpin, B. J.; Weber, R. J. Secondary organic aerosol formation in cloud droplets and aqueous particles (aqSOA): a review of laboratory, field and model studies. *Atmos. Chem. Phys.* **2011**, *11*, 11069–11102.
- (36) McNeill, V. F. Aqueous organic chemistry in the atmosphere: sources and chemical processing of organic aerosols. *Environ. Sci. Technol.* **2015**, *49*, 1237–1244.
- (37) Ervens, B. Progress and problems in modeling chemical processing in cloud droplets and wet aerosol particles. In *Multiphase environmental chemistry in the atmosphere*; Hunt, S. W.; Laskin, A.; Nizkorodov, S. A., Eds.; ACS Symposium Series; American Chemical Society: Washington, DC, 2018; Vol. 1299, pp. 327–345.
- (38) Pye, H. O. T.; Nenes, A.; Alexander, B.; Ault, A. P.; Barth, M. C.; Clegg, S. L.; Collett Jr., J. L.; Fahey, K. M.; Hennigan, C. J.; Herrmann, H.; et al. The acidity of atmospheric particles and clouds. *Atmos. Chem. Phys.* **2020**, *20*, 4809–4888.
- (39) Parworth, C. L.; Young, D. E.; Kim, H.; Zhang, X.; Cappa, C. D.; Collier, S.; Zhang, Q. Wintertime water-soluble aerosol composition and particle water content in Fresno, California. *J. Geophys. Res. Atmos.* **2017**, *122*, 3155–3170.
- (40) Graber, E. R.; Rudich, Y. Atmospheric HULIS: How humic-like are they? A comprehensive and critical review. *Atmos. Chem. Phys.* **2006**, *6*, 729–753.
- (41) Tilgner, A.; Schaefer, T.; Alexander, B.; Barth, M.; Collett Jr., J. L.; Fahey, K. M.; Nenes, A.; Pye, H. O. T.; Herrmann, H.; McNeill, V. F. Acidity and the multiphase chemistry of atmospheric aqueous particles and clouds. *Atmos. Chem. Phys.* **2021**, *21*, 13483–13536.
- (42) Buerge-Weirich, D.; Sulzberger, B. Formation of Cu(I) in Estuarine and Marine Waters: Application of a New Solid-Phase Extraction Method To Measure Cu(I). *Environ. Sci. Technol.* **2004**, *38*, 1843–1848.
- (43) Deguillaume, L.; Leriche, M.; Desboeufs, K.; Mailhot, G.; George, C.; Chaumerliac, N. Transition metals in atmospheric liquid phases: sources, reactivity, and sensitive parameters. *Chem. Rev.* **2005**, *105*, 3388–3431.
- (44) Tapparo, A.; Di Marco, V.; Badocco, D.; D’Aronco, S.; Soldà, L.; Pastore, P.; Mahon, B. M.; Kalberer, M.; Giorio, C. Formation of metal-organic ligand complexes affects solubility of metals in airborne particles at an urban site in the Po valley. *Chemosphere* **2020**, *241*, 125025.
- (45) Gen, M.; Zhang, R.; Li, Y.; Chan, C. K. Multiphase Photochemistry of Iron-Chloride Containing Particles as a Source of Aqueous Chlorine Radicals and Its Effect on Sulfate Production. *Environ. Sci. Technol.* **2020**, *54*, 9862–9871.
- (46) Sannigrahi, P.; Sullivan, A. P.; Weber, R. J.; Ingall, E. D. Characterization of water-soluble organic carbon in urban atmospheric aerosols using solid-state <sup>13</sup>C NMR spectroscopy. *Environ. Sci. Technol.* **2006**, *40*, 666–672.

- (47) Duarte, R. M. B. O.; Santos, E. B. H.; Pio, C. A.; Duarte, A. C. Comparison of structural features of water-soluble organic matter from atmospheric aerosols with those of aquatic humic substances. *Atmos. Environ.* **2007**, *41*, 8100–8113.
- (48) Huo, Y.; Guo, Z.; Li, Q.; Wu, D.; Ding, X.; Liu, A.; Huang, D.; Qiu, G.; Wu, M.; Zhao, Z.; et al. Chemical Fingerprinting of HULIS in Particulate Matters Emitted from Residential Coal and Biomass Combustion. *Environ. Sci. Technol.* **2021**, *55*, 3593–3603.
- (49) Kaur, R.; Hudson, B. M.; Draper, J.; Tantillo, D. J.; Anastasio, C. Aqueous reactions of organic triplet excited states with atmospheric alkenes. *Atmos. Chem. Phys.* **2019**, *19*, 5021–5032.
- (50) Richards-Henderson, N. K.; Pham, A. T.; Kirk, B. B.; Anastasio, C. Secondary organic aerosol from aqueous reactions of green leaf volatiles with organic triplet excited states and singlet molecular oxygen. *Environ. Sci. Technol.* **2015**, *49*, 268–276.
- (51) Appiani, E.; Ossola, R.; Latch, D. E.; Erickson, P. R.; McNeill, K. Aqueous singlet oxygen reaction kinetics of furfuryl alcohol: effect of temperature, pH, and salt content. *Environ. Sci.: Processes Impacts* **2017**, *19*, 507–516.
- (52) Bower, J. P.; Anastasio, C. Measuring a 10,000-fold enhancement of singlet molecular oxygen ( $^1O_2$ ) concentration on illuminated ice relative to the corresponding liquid solution. *Atmos. Environ.* **2013**, *75*, 188–195.
- (53) Smith, J. D.; Kinney, H.; Anastasio, C. Phenolic carbonyls undergo rapid aqueous photodegradation to form low-volatility, light-absorbing products. *Atmos. Environ.* **2016**, *126*, 36–44.
- (54) Fleming, L. T.; Lin, P.; Roberts, J. M.; Selimovic, V.; Yokelson, R.; Laskin, J.; Laskin, A.; Nizkorodov, S. A. Molecular composition and photochemical lifetimes of brown carbon chromophores in biomass burning organic aerosol. *Atmos. Chem. Phys.* **2020**, *20*, 1105–1129.
- (55) Wenk, J.; Eustis, S. N.; McNeill, K.; Canonica, S. Quenching of excited triplet states by dissolved natural organic matter. *Environ. Sci. Technol.* **2013**, *47*, 12802–12810.
- (56) Rice-Evans, C. A.; Miller, N. J.; Paganga, G. Structure-antioxidant activity relationships of flavonoids and phenolic acids. *Free Radic. Biol. Med.* **1996**, *20*, 933–956.
- (57) Haag, W. R.; Hoigne, J.; Gassman, E.; Braun, A. Singlet oxygen in surface waters — Part I: Furfuryl alcohol as a trapping agent. *Chemosphere* **1984**, *13*, 631–640.
- (58) Canonica, S.; Hellrung, B.; Wirz, J. Oxidation of phenols by triplet aromatic ketones in aqueous solution. *The Journal of Physical Chemistry A* **2000**, *104*, 1226–1232.
- (59) Korzeniowska-Sobczuk, A.; Hug, G. L.; Carmichael, I.; Bobrowski, K. Spectral, Kinetics, and Theoretical Studies of Radical Cations Derived from Thioanisole and Its Carboxylic Derivative. *J. Phys. Chem. A* **2002**, *106*, 9251–9260.
- (60) Pavitt, A. S.; Bylaska, E. J.; Tratnyek, P. G. Oxidation potentials of phenols and anilines: correlation analysis of electrochemical and theoretical values. *Environ. Sci. Process. Impacts* **2017**, *19*, 339–349.
- (61) Ohkatsu, Y.; Suzuki, F. Synergism between Phenolic Antioxidants in Autoxidation. *J. Jpn. Petrol. Inst.* **2011**, *54*, 22–29.
- (62) Jørgensen, L. V.; Madsen, H. L.; Thomsen, M. K.; Dragsted, L. O.; Skibsted, L. H. Regeneration of phenolic antioxidants from phenoxyl radicals: an ESR and electrochemical study of antioxidant hierarchy. *Free Radic. Res.* **1999**, *30*, 207–220.

- (63) Fréneau, M.; Hoffmann, N. The Paternò-Büchi reaction—Mechanisms and application to organic synthesis. *J. Photochem. Photobiol. C* **2017**, *33*, 83–108.
- (64) D’Auria, M. The Paternò-Büchi reaction - a comprehensive review. *Photochem Photobiol Sci* **2019**, *18*, 2297–2362.
- (65) Smith, J. D.; Sio, V.; Yu, L.; Zhang, Q.; Anastasio, C. Secondary organic aerosol production from aqueous reactions of atmospheric phenols with an organic triplet excited state. *Environ. Sci. Technol.* **2014**, *48*, 1049–1057.
- (66) Re, R.; Pellegrini, N.; Proteggente, A.; Pannala, A.; Yang, M.; Rice-Evans, C. Antioxidant activity applying an improved ABTS radical cation decolorization assay. *Free Radic. Biol. Med.* **1999**, *26*, 1231–1237.
- (67) Pellegrini, N.; Del Rio, D.; Colombi, B.; Bianchi, M.; Brighenti, F. Application of the 2,2’-azinobis(3-ethylbenzothiazoline-6-sulfonic acid) radical cation assay to a flow injection system for the evaluation of antioxidant activity of some pure compounds and beverages. *J. Agric. Food Chem.* **2003**, *51*, 260–264.
- (68) Aeschbacher, M.; Graf, C.; Schwarzenbach, R. P.; Sander, M. Antioxidant properties of humic substances. *Environ. Sci. Technol.* **2012**, *46*, 4916–4925.
- (69) Wenk, J.; Aeschbacher, M.; Sander, M.; von Gunten, U.; Canonica, S. Photosensitizing and Inhibitory Effects of Ozonated Dissolved Organic Matter on Triplet-Induced Contaminant Transformation. *Environ. Sci. Technol.* **2015**, *49*, 8541–8549.
- (70) Walpen, N.; Houska, J.; Salhi, E.; Sander, M.; von Gunten, U. Quantification of the electron donating capacity and UV absorbance of dissolved organic matter during ozonation of secondary wastewater effluent by an assay and an automated analyzer. *Water Res.* **2020**, *185*, 116235.
- (71) Yuan, Y.; Zhang, H.; Wei, Y.; Si, Y.; Li, G.; Zhang, F. Onsite quantifying electron donating capacity of dissolved organic matter. *Sci. Total Environ.* **2019**, *662*, 57–64.
- (72) Akherati, A.; He, Y.; Coggon, M. M.; Koss, A. R.; Hodshire, A. L.; Sekimoto, K.; Warneke, C.; de Gouw, J.; Yee, L.; Seinfeld, J. H.; et al. Oxygenated Aromatic Compounds are Important Precursors of Secondary Organic Aerosol in Biomass-Burning Emissions. *Environ. Sci. Technol.* **2020**, *54*, 8568–8579.
- (73) Bruns, E. A.; El Haddad, I.; Slowik, J. G.; Kilic, D.; Klein, F.; Baltensperger, U.; Prévôt, A. S. H. Identification of significant precursor gases of secondary organic aerosols from residential wood combustion. *Sci. Rep.* **2016**, *6*, 27881.
- (74) McCabe, A. J.; Arnold, W. A. Multiple linear regression models to predict the formation efficiency of triplet excited states of dissolved organic matter in temperate wetlands. *Limnol. Oceanogr.* **2018**, *63*, 1992–2014.
- (75) Liang, Y.; Jen, C. N.; Weber, R. J.; Misztal, P. K.; Goldstein, A. H. Chemical composition of PM<sub>2.5</sub> in October 2017 Northern California wildfire plumes. *Atmos. Chem. Phys.* **2021**, *21*, 5719–5737.
- (76) Smith, J. D.; Kinney, H.; Anastasio, C. Aqueous benzene-diols react with an organic triplet excited state and hydroxyl radical to form secondary organic aerosol. *Phys. Chem. Chem. Phys.* **2015**, *17*, 10227–10237.
- (77) Tratnyek, P. G.; Hoigne, J. Oxidation of substituted phenols in the environment: a QSAR analysis of rate constants for reaction with singlet oxygen. *Environ. Sci. Technol.* **1991**, *25*, 1596–1604.
- (78) Galbavy, E. S.; Ram, K.; Anastasio, C. 2-Nitrobenzaldehyde as a chemical actinometer for solution and ice photochemistry. *J. Photochem. Photobiol. A* **2010**, *209*, 186–192.

- (79) Anastasio, C.; McGregor, K. G. Chemistry of fog waters in California's Central Valley: 1. In situ photoformation of hydroxyl radical and singlet molecular oxygen. *Atmos. Environ.* **2001**, *35*, 1079–1089.
- (80) Ashton, L.; Buxton, G. V.; Stuart, C. R. Temperature dependence of the rate of reaction of OH with some aromatic compounds in aqueous solution. Evidence for the formation of a  $\pi$ -complex intermediate? *J. Chem. Soc., Faraday Trans.* **1995**, *91*, 1631–1633.
- (81) Wander, R.; Neta, P.; Dorfman, L. M. Pulse radiolysis studies. XII. Kinetics and spectra of the cyclohexadienyl radicals in aqueous benzoic acid solution. *J. Phys. Chem.* **1968**, *72*, 2946–2949.
- (82) Gersdorf, J.; Mattay, J.; Goerner, H. Radical cations. 3. Photoreactions of biacetyl, benzophenone, and benzil with electron-rich alkenes. *J. Am. Chem. Soc.* **1987**, *109*, 1203–1209.
- (83) Eckert, G.; Goetz, M. Photoinduced Electron-Transfer Reactions of Aryl Olefins. 1. Investigation of the Paterno-Buechi Reaction between Quinones and Anetholes in Polar Solvents. *J. Am. Chem. Soc.* **1994**, *116*, 11999–12009.
- (84) Rayner, D. M.; Wyatt, P. A. H. Laser study of the protonation equilibrium of triplet benzophenone. *J. Chem. Soc., Faraday Trans. 2* **1974**, *70*, 945.
- (85) Kochany, J.; Bolton, J. R. Mechanism of photodegradation of aqueous organic pollutants. 2. Measurement of the primary rate constants for reaction of hydroxyl radicals with benzene and some halobenzenes using an EPR spin-trapping method following the photolysis of hydrogen peroxide. *Environ. Sci. Technol.* **1992**, *26*, 262–265.
- (86) Felber, T.; Schaefer, T.; He, L.; Herrmann, H. Aromatic carbonyl and nitro compounds as photosensitizers and their photophysical properties in the tropospheric aqueous phase. *J. Phys. Chem. A* **2021**, *125*, 5078–5095.
- (87) Wang, D.; Bolton, J. R.; Hofmann, R. Medium pressure UV combined with chlorine advanced oxidation for trichloroethylene destruction in a model water. *Water Res.* **2012**, *46*, 4677–4686.
- (88) Walpen, N.; Schroth, M. H.; Sander, M. Quantification of Phenolic Antioxidant Moieties in Dissolved Organic Matter by Flow-Injection Analysis with Electrochemical Detection. *Environ. Sci. Technol.* **2016**, *50*, 6423–6432.

## Chapter 4: Predicting Photooxidant Concentrations in Aerosol Liquid Water Based on Laboratory Extracts of Ambient Particles

### ABSTRACT

Aerosol liquid water (ALW) is a unique medium for the formation of secondary organic aerosol, but the chemistry in ALW is poorly understood. For example, little is known of photooxidant concentrations - including hydroxyl radical ( $\bullet\text{OH}$ ), singlet molecular oxygen ( $^1\text{O}_2^*$ ), and oxidizing triplet excited states of organic matter ( $^3\text{C}^*$ ) - even though they likely drive much of ALW chemistry. Due to the very limited water content of particles, it is difficult to quantify oxidant concentrations in ALW directly. To predict these values, we measured photooxidant concentrations in illuminated aqueous particle extracts as a function of dilution and used the resulting oxidant kinetics to extrapolate to ALW conditions. Extracts were prepared from winter (WIN) and summer (SUM) particles from Davis, California. Both periods were influenced by biomass burning, with dissolved organic carbon (DOC) in the extracts ranging from 10 to 495 mg C L<sup>-1</sup>. In winter samples, the  $\bullet\text{OH}$  concentration is independent of particle mass concentration, with an average value of  $5.0 (\pm 2.2) \times 10^{-15}$  M, while in summer  $\bullet\text{OH}$  increases with DOC in the range  $(0.4 - 7.7) \times 10^{-15}$  M. In both winter and summer samples,  $^3\text{C}^*$  concentrations increase rapidly with particle mass concentrations in the extracts, and then plateau under more concentrated conditions, with a range of  $(0.2 - 7) \times 10^{-13}$  M. WIN and SUM have the same range of  $^1\text{O}_2^*$  concentrations,  $(0.2 - 8.5) \times 10^{-12}$  M, but in WIN, the  $^1\text{O}_2^*$  concentration increases linearly with DOC, while in SUM  $^1\text{O}_2^*$  approaches a plateau.

By extrapolating the relationship of oxidant formation rates and sinks with particle mass concentration to the much more concentrated condition of aerosol liquid water (and including mass transport of  $\bullet\text{OH}$  from the gas phase), we predict  $\bullet\text{OH}$  concentrations in ALW on the order of  $10^{-14}$  M, similar to those in fog/cloud waters. In contrast, predicted concentrations of  $^3\text{C}^*$  and  $^1\text{O}_2^*$  in ALW are approximately 10 - 100 times higher than in cloud/fogs, with values of  $(4 - 9) \times 10^{-13}$  M and  $(1 - 18) \times 10^{-12}$  M, respectively. Although  $\bullet\text{OH}$  is often considered the main sink for organic compounds in the aqueous

phase, the much higher concentrations of  $^3\text{C}^*$  and  $^1\text{O}_2^*$  in aerosol liquid water suggest these photooxidants will be more important sinks for many organics in particle water.

#### 4.1. Introduction

The chemical processing of organic compounds in cloud/fog water and aerosol liquid water is an important source and sink of secondary organic aerosol (SOA) (Ervens et al., 2011; Gilardoni et al., 2016; Lim et al., 2010; McNeill, 2015). Aerosol liquid water (ALW), i.e., the liquid-phase water on airborne particles, is both much less abundant (in terms of liquid water content) and contains much higher concentrations of solutes compared to clouds and fogs. ALW appears to be an efficient and important medium for the production of aqueous SOA (aqSOA) (Ervens and Volkamer, 2010; Faust et al., 2017; Volkamer et al., 2007; Wu et al., 2018; Zhang et al., 2011) and ALW chemistry is often different from that in more dilute cloud and fog drops (Ervens, 2018; Mekic et al., 2018; Zhou et al., 2019). For example reactions in ALW can more efficiently produce high molecular-weight compounds like oligomers and brown carbon (De Haan et al., 2020; Lim et al., 2010; Renard et al., 2014; Tan et al., 2012; Xia et al., 2018). Modeled rates of aqSOA formation in ALW vary enormously, likely because reactant concentrations and chemical processes in particle water are poorly understood (Ervens and Volkamer, 2010; Ervens, 2018; Lin et al., 2014; Washenfelder et al., 2011).

A key driver of ALW reactivity is likely the concentrations of photochemically-generated oxidants (Herrmann et al., 2015; Lim et al., 2010). Common aqueous photooxidants include hydroxyl radical ( $^{\bullet}\text{OH}$ ), oxidizing triplet excited states of organic compounds ( $^3\text{C}^*$ ), and singlet molecular oxygen ( $^1\text{O}_2^*$ ) (Kaur et al., 2019).  $^{\bullet}\text{OH}$  is the most widely studied oxidant due to its ubiquity and high reactivity: it reacts with most organics with near diffusion-controlled rate constants (Herrmann et al., 2015). The main sources of aqueous  $^{\bullet}\text{OH}$  include mass transfer from the gas-phase, the photo-Fenton reaction, and photolysis of nitrate, nitrite, and other species (Anastasio and McGregor, 2001; Arakaki and Faust, 1998; Badali et al., 2015; Herrmann et al., 2010; Tilgner and Herrmann, 2018), while the main sinks of  $^{\bullet}\text{OH}$  are dissolved organic compounds



(Anastasio and Newberg, 2007; Arakaki et al., 2013). Based on lab studies of clouds, fogs, and aqueous particle extracts, concentrations of •OH in atmospheric waters (with the inclusion of calculated rates of gas-to-particle partitioning of •OH) are typically  $10^{-16}$ - $10^{-15}$  M (Anastasio and McGregor, 2001; Anastasio and Newberg, 2007; Arakaki et al., 2013; Faust and Allen, 1993; Kaur et al., 2019; Zhou et al., 2008). In contrast, modeled •OH concentrations in aqueous aerosol are generally  $10^{-13}$  to  $10^{-12}$  M (Ervens et al., 2014; Tilgner and Herrmann, 2018; Tilgner et al., 2013), but these are likely overestimates because of missing •OH sinks (Arakaki et al., 2013).

Oxidizing triplet excited states of organic matter are formed when organic chromophores (i.e., brown carbon) absorb sunlight (McNeill and Canonica, 2016). Oxidizing triplets can transform numerous atmospheric species, including converting phenols and biogenic volatile compounds to aqSOA, and oxidizing sulfite to sulfate (González Palacios et al., 2016; Monge et al., 2012; Rossignol et al., 2014; Smith et al., 2014; Wang et al., 2020). Previous studies show that  $^3C^*$  can be an important oxidant in atmospheric and surface waters, with a concentration of  $10^{-15}$ - $10^{-13}$  M (Kaur and Anastasio, 2018; Kaur et al., 2019; McNeill and Canonica, 2016). In comparison, triplet concentrations in ALW are expected to be higher because the production rate of  $^3C^*$  increases with dissolved organic carbon (Cannonica and Freiburghaus, 2001; McCabe and Arnold, 2017), although organic compounds can also be important sinks for  $^3C^*$ , suppressing its steady-state concentration (Gemayel et al., 2021; Wenk et al., 2013). This dual effect of organic compounds makes it difficult to predict  $^3C^*$  in ALW. Kaur et al. (2019) estimated a concentration of oxidizing  $^3C^*$  in ALW of  $10^{-13}$  to  $10^{-11}$  M based on measurements in dilute particle extracts, while Tilgner et al. (2021) estimated the  $^3C^*$  ALW concentration as  $10^{-11}$  M.

Most or all of atmospheric triplets (i.e., both oxidizing and non-oxidizing triplets) also transfer energy to dissolved oxygen to form another important photooxidant, singlet molecular oxygen.  $^1O_2^*$  concentrations in fog/cloud drops and dilute extracts of ambient particles and lab SOA are higher than •OH and  $^3C^*$ , typically  $10^{-14}$  to  $10^{-12}$  M (Anastasio and McGregor, 2001; Faust and Allen, 1992; Kaur and Anastasio, 2017;

Kaur et al., 2019; Li et al., 2019; Manfrin et al., 2019). Though  $^1\text{O}_2^*$  is generally less reactive than  $\bullet\text{OH}$  and  $^3\text{C}^*$ , it can react quickly with electron-rich compounds and can be a competitive oxidant because of its high concentration. Kaur et al. (2019) estimated  $^1\text{O}_2^*$  might be as high as  $10^{-10}$  M under ALW conditions due to increased  $^3\text{C}^*$  concentrations, which would make it an important oxidant in particle water (Ma et al., 2021).

Due to its limited water content, it is difficult to study chemistry in ALW directly. To get around this problem, Kaur et al. (2019) measured  $\bullet\text{OH}$ ,  $^3\text{C}^*$ , and  $^1\text{O}_2^*$  kinetics as a function of dilution in extracts of a single PM sample and extrapolated the results to aqueous aerosol conditions. However, there are large uncertainties with this extrapolation since the PM extracts were approximately 1000 times more dilute than ALW conditions. In addition, these authors only examined a sample collected during winter and did not correct their triplet results for probe inhibition by organic compounds. To revisit this approach and, we hope, reduce uncertainty, here we apply the same method but with higher dissolved organic matter concentrations in particle extracts and with correction for triplet probe inhibition. Moreover, in this work we study both a winter PM sample as well as summer wildfire particles to explore differences in oxidant kinetics.

## 4.2. Experimental Methods

### 4.2.1. Chemicals

Furfuryl alcohol (FFA, 98%), benzoic acid (BA,  $\geq 99.5\%$ ), *p*-hydroxybenzoic acid (*p*HBA, 99%), (phenylthiol)acetic acid (PTA, 96%), syringol (SYR, 99%), 3,4-dimethoxybenzaldehyde (DMB, 99%), deuterium oxide (99.9% D-atom) were received from Millipore Sigma. All chemical solutions and particulate matter extracts were prepared using air-saturated ultrapure water (Milli-Q water) from a Milli-Q Advantage A10 system (Millipore;  $\geq 18.2$  M $\Omega$  cm) with an upstream cartridge to remove organics.

#### 4.2.2. Particle Collection and Extraction

Fine particles (PM<sub>2.5</sub>) were collected on the roof of Ghausi Hall on the campus of the University of California, Davis in February and August 2020. Davis air quality in winter is often impacted by residential wood combustion, while the August 2020 samples were impacted by Northern California wildfires. PM<sub>2.5</sub> was collected using a high-volume sampler equipped with a PM<sub>10</sub> inlet (Graseby Andersen) and two offset, slotted impactor plates (Tisch Environmental, Inc., 230 series). Particles were collected onto Teflon-coated borosilicate glass microfiber filters (Pall Corporation, EmFab™ filters, 8 in. × 10 in., pre-cleaned by gently shaking in Milli-Q water for 8 h and then drying at 100 °C). During sampling, the airflow rate was maintained at 68 (±2) m<sup>3</sup> per hour. Particles were either collected for 24 h or up to a week; see Table S4.1 for details. Upon collection, each sample was wrapped in aluminum foil (baked previously at 500 °C for 8 h), sealed in a Ziploc bag, and frozen at -20 °C. Field blanks were obtained in an identical manner as samples, including loading the clean filters into the sampler and turning on the pump for 2 min.

To prepare particulate matter extracts (PMEs), filters were cut into 2 cm × 2 cm squares on the day of extraction. Each square was placed in an individual, sealed, 20-mL amber glass vial and extracted with Milli-Q water by shaking for 4 h in the dark. The extracts from the same filter sample were combined, filtered (0.22 μm PTFE; Pall), and adjusted to pH 4.2 with sulfuric acid or sodium hydroxide to mimic the acidity of winter particle water in the Central Valley of California (Parworth et al., 2017). The pH of each extract was measured by a pH microelectrode (MI-414 series, protected tip; Microelectrodes, Inc.) The UV-Vis spectrum of each PME was measured in a 1-cm cuvette immediately after pH adjustment with a Shimadzu UV-2501PC spectrophotometer. PMEs were divided into 4-mL HDPE bottles and flash-frozen in liquid nitrogen immediately after preparation and were later thawed on the day of experiments. Filter squares were weighed by a microbalance (Sartorius M2P) before and after extraction to determine the PM mass extracted. Dissolved organic carbon (DOC) and major ion concentrations (Table S4.2) in PMEs were

measured by a Shimadzu TOC-VCPH analyzer and Metrohm ion chromatographs (881 Compact IC Pro) equipped with conductivity detectors, respectively.

To investigate the relationship between particle dilution and oxidant concentration, filter squares from the same sample were extracted with five different volumes of Milli-Q water: 10, 2, 0.7, 0.4, and 0.3 mL. To obtain enough filter squares for this dilution series, for both the winter (WIN) and summer (SUM) sample we combined extracts from 180 filter squares cut from three sheets of filter that were collected on consecutive days. The same number of squares were cut from each of the three filters in a given sample. We use “PME-water volume” (e.g., WIN-0.7) to denote the sample and extraction volume. Because it is difficult to extract squares with only 0.4 or 0.3 mL of Milli-Q, for these dilutions we extracted each filter square with 1 mL of Milli-Q and then used a rotary evaporator (Buchi Rotavapor R-110; temperature set to no higher than 65 °C) to remove water until we obtained the equivalent of a 0.4 or 0.3 mL extract. We define the concentration factor (CF) as the inverse of the volume used for extraction. For example, WIN-10 has a concentration factor of 0.1.

#### **4.2.3. Sample Illumination and Chemical Analysis**

We illuminated samples with light from a 1000 W xenon arc lamp passed through a water filter, an AM1.0 air mass filter (AM1D-3L, Sciencetech), and a 295 nm long-pass filter (20CGA-295, Thorlabs) to simulate tropospheric sunlight (Kaur and Anastasio, 2017). We first transferred the extract into a silicone-plugged GE 021 quartz tube (5 mm inner diameter, 1.0 mL volume) and then spiked it with the photooxidant probe and mixed it. The entire tube was illuminated at 20 °C and was not stirred. Dark control samples were wrapped in aluminum foil and kept in the same photoreactor chamber. During illumination, approximately 150  $\mu$ L aliquots were removed from the illuminated and dark tubes at specific time intervals to measure concentrations of probes with high-performance liquid chromatography (HPLC, Shimadzu LC-20AB pump, Thermo Scientific Accucore XL C18 column (50  $\times$  3 mm, 4  $\mu$ m bead), and Shimadzu-M20A UV-Vis detector). The photon flux on each experiment day was determined by measuring the photolysis

rate constant of a 10  $\mu\text{M}$  2-nitrobenzaldehyde (2NB) solution in the same type of container as samples (Galbavy et al., 2010).

#### 4.2.4. Photooxidant Measurements

Details about determining photooxidant concentrations are provided in past papers (Anastasio and McGregor, 2001; Kaur and Anastasio, 2017; Kaur et al., 2019) and are only discussed briefly here.

##### 4.2.4.1. Hydroxyl radical ( $\bullet\text{OH}$ )

The production rate, rate constant for loss, and steady-state concentration of  $\bullet\text{OH}$  were quantified using benzoic acid (BA) and a competition kinetic technique. A stock solution of benzoic acid/benzoate was prepared and adjusted to pH 4.2. For each sample, four 1.0-mL aliquots of PME were spiked with different concentrations (100 – 1200  $\mu\text{M}$ ) of BA, keeping PME dilution by the addition of probe to less than 10%. During each PME illumination we monitored the formation of *p*-hydroxybenzoic acid (*p*-HBA), which is formed from BA oxidation by  $\bullet\text{OH}$ , by HPLC. The initial rate of *p*-HBA formation was determined from a regression between concentration and illumination time, using either a linear regression or three-parameter exponential fit

$$[p\text{-HBA}]_t = [p\text{-HBA}]_0 + a(1 - e^{-bt}) \quad (4.1)$$

where  $[p\text{-HBA}]_t$  and  $[p\text{-HBA}]_0$  are the concentrations at illumination times  $t$  and zero, respectively, and  $a$  and  $b$  are regression fit parameters. For exponential kinetic data the initial formation rate of *p*-HBA,  $R_{P,EXP}$ , was calculated with

$$R_{P,EXP} = a \times b \quad (4.2)$$

This rate was normalized to sunlight conditions at midday on the winter solstice at Davis (solar zenith = 62°;  $j_{2NB,win} = 0.0070 \text{ s}^{-1}$  (Anastasio and McGregor, 2001)), and corrected for internal light screening due to sample absorption, using

$$R_{P,norm} = \left[ \frac{R_{P,EXP}}{S_{\lambda} \times j_{2NB,EXP}} \right] \times j_{2NB,win} \quad (4.3)$$

where  $S_{\lambda}$  is the internal light screening factor in an individual sample (Table S4.1) and  $j_{2NB,exp}$  is the photolysis rate constant of 2NB measured on the experiment day.

We then fitted  $1/R_{P,norm}$  versus  $1/[BA]$  with a linear regression and used the slope and y-intercept to calculate the initial production rate of  $\bullet\text{OH}$  ( $P_{OH}$ ), the pseudo first-order rate constant of  $\bullet\text{OH}$  loss by natural sinks ( $k'_{OH}$ ), and the steady-state  $\bullet\text{OH}$  concentration

$$P_{OH} = \frac{1}{y - \text{intercept} \times Y_{pHBA}} \quad (4.4)$$

$$k'_{OH} = k_{BA+\bullet OH} \left( \frac{\text{slope}}{y - \text{intercept}} \right) \quad (4.5)$$

$$[\bullet OH] = \frac{1}{k_{BA+\bullet OH} \times \text{slope} \times Y_{p-HBA}} \quad (4.6)$$

Here  $Y_{p-HBA}$  (0.18) is the yield of *p*-HBA from the reaction of BA with  $\bullet\text{OH}$  (Anastasio and McGregor, 2001) and  $k_{BA+\bullet OH}$  is the second-order rate constant of BA reacting with  $\bullet\text{OH}$  at pH 4.2 ( $5.1 \times 10^9 \text{ M}^{-1} \text{ s}^{-1}$ ) (Ashton et al., 1995; Wander et al., 1968).  $\bullet\text{OH}$  measurements are in Table S4.3.

#### 4.2.4.2. Oxidizing triplet excited states of organic matter ( $^3\text{C}^*$ )

Triplets were measured employing syringol (SYR) and (phenylthio)acetic acid (PTA) as probes (Kaur and Anastasio, 2018; Ma et al., 2022). SYR captures both weakly and strongly oxidizing triplets, but

its decay can be inhibited by dissolved organic matter (DOM) in PME (Canonica and Laubscher, 2008; Ma et al., 2022; Wenk and Canonica, 2012; Wenk et al., 2015). In contrast, PTA is less sensitive to inhibition by DOM, but it only reacts appreciably with strongly oxidizing triplets (Ma et al., 2022). Two 1.0 mL aliquots of PME were either spiked with 10  $\mu\text{M}$  of SYR or PTA, and then were illuminated to determine the pseudo-first order rate constants for loss of each probe ( $k'_{P,EXP}$ ). Next,  $k'_{P,EXP}$  values were normalized to Davis winter sunlight conditions and corrected for light screening using an equation analogous to Eq. 4.3 to obtain rate constant  $k'_P$ . The contributions of direct photodegradation,  $\bullet\text{OH}$ , and  $^1\text{O}_2^*$  to probe decay were then subtracted to determine the rate constant for loss of probe due to triplets,  $k'_{P,3C^*}$

$$k'_{P,3C^*} = k'_P - (j_P + k_{P+OH}[\bullet\text{OH}] + k_{P+1O2^*}[^1\text{O}_2^*]) \quad (4.7)$$

Here  $j_P$  is the probe direct photodegradation rate constant under Davis winter sunlight, and  $k_{P+OH}$  and  $k_{P+1O2^*}$  are the bimolecular rate constants of probe reacting with  $\bullet\text{OH}$  and  $^1\text{O}_2^*$ , respectively (Table S4.4).  $\bullet\text{OH}$  accounts for 2% - 35% and 3% - 17% of the decay of SYR and PTA, respectively, while  $^1\text{O}_2^*$  accounts for 3% - 45% and 2% - 10% for SYR and PTA (Tables S4.5 and S4.6). Since “triplets” in PMEs represent the excited states of a complex mixture of brown carbon, there is no single value for the second-order rate constant of  $^3\text{C}^*$  reacting with probes ( $k_{P+3C^*}$ ). To estimate triplet concentrations, we assume that  $^3\text{C}^*$  in PME have the same average reactivity as  $^3\text{DMB}^*$  (Fleming et al., 2020; Kaur and Anastasio, 2018; Kaur et al., 2019). Unlike our past work (Kaur et al., 2019), we corrected for DOM inhibiting the decays of SYR and PTA, which can cause an underestimate of  $^3\text{C}^*$  concentrations. To do this, we measured the inhibition factor ( $IF$ ) in each sample (Canonica and Laubscher, 2008; Ma et al., 2022; Wenk et al., 2011) and used it to correct the  $^3\text{C}^*$  concentration. Details about inhibition factor measurements and [ $^3\text{C}^*$ ] corrections are in Supplemental Section S4.1. The  $^3\text{C}^*$  concentration after inhibition correction is

$$[^3\text{C}^*]_P = \frac{k'_{P,3C^*}}{k_{P+3DMB^*} \times IF_{P,corr}} \quad (4.8)$$

where  $k_{P+3DMB^*}$  is the second-order rate constant of probe with  $^3DMB^*$  (Table S4.4), and  $IF_{P,corr}$  is the inhibition factor of the probe (Table S4.7).  $^3C^*$  concentrations in the main text are values after  $IF$  correction.

#### 4.2.4.3. Singlet molecular oxygen ( $^1O_2^*$ )

We used FFA as a probe to determine  $^1O_2^*$  concentrations (Anastasio and McGregor, 2001; Haag et al., 1984). 1.0 mL of PME sample was divided into two 0.5 mL aliquots, and then one was diluted with 0.5 mL  $H_2O$  while the other was diluted with 0.5 mL deuterium oxide ( $D_2O$ ). 10  $\mu M$  FFA was spiked into each solution and then both were illuminated. The pseudo-first-order rate constant of FFA loss in  $H_2O$ - and  $D_2O$ -diluted PME ( $k'_{FFA,H_2O}$  and  $k'_{FFA,D_2O}$ ) during illumination was determined as the negative slope of a linear regression between  $\ln([FFA]_t/[FFA]_0)$  versus illumination time ( $t$ ). The  $^1O_2^*$  concentration in the undiluted PME was determined from the difference of FFA loss rates in  $H_2O$  and  $D_2O$  using (Anastasio and McGregor, 2001)

$$[^1O_2^*]_{EXP} = \frac{k'_{FFA,D_2O} - k'_{FFA,H_2O}}{D \times k_{FFA+^1O_2^*} \times \left( \frac{k'_{H_2O}}{k'_{H_2O}\chi_{H_2O} + k'_{D_2O}\chi_{D_2O}} - 1 \right)} \quad (4.9)$$

where  $D$  is the sample dilution factor (i.e., 0.5 for our experiments);  $k_{FFA+^1O_2^*}$  is the second-order rate constant of FFA reacting with  $^1O_2^*$  at 20 °C,  $1.0 (\pm 0.1) \times 10^8 M^{-1} s^{-1}$  (Appiani et al., 2017); and  $\chi_{H_2O}$  and  $\chi_{D_2O}$  are the mole fractions of  $H_2O$  and  $D_2O$  in the  $D_2O$ -diluted solution;  $k'_{H_2O}$  and  $k'_{D_2O}$  are the first-order rate constants for loss of  $^1O_2^*$  in 100%  $H_2O$  ( $2.2 \times 10^5 s^{-1}$ ) and  $D_2O$  ( $1.6 \times 10^4 s^{-1}$ ), respectively (Bilski et al., 1997). Analogous to equation 4.3, we normalized  $^1O_2^*$  concentrations using the light screening factor of each PME and to Davis winter sunlight conditions.  $^1O_2^*$  measurements are in Table S4.8.



## 4.3. Results and Discussions

### 4.3.1. Testing Extractions and Rotary Evaporation

Our winter particle samples were collected in February 2020, when Davis was humid and influenced by residential wood combustion; the average  $PM_{2.5}$  concentration during our sampling was  $9.2 \mu\text{g m}^{-3}$ . The summer particles were collected in August 2020, when severe wildfires were occurring approximately 30 km from Davis and the average  $PM_{2.5}$  was  $54 \mu\text{g m}^{-3}$ . Figure 4.1 shows the dissolved organic carbon (DOC) concentrations and rates of light absorption ( $R_{\text{abs}}$ ) as a function of dilution in the winter (WIN) and summer (SUM) particle extracts. We express dilution as the ratio of particle mass to liquid water mass in our extracts since we can directly measure these quantities and can estimate the ratio for both clouds/fogs and airborne particles. Both DOC and  $R_{\text{abs}}$  are directly proportional to particle mass/water mass ratio, indicating that the extractions of filter squares with varying volumes of water achieved the same extraction efficiency. The DOC of the most concentrated extracts, PME-0.4 and PME-0.3, also follow the linear relationship, showing that the rotary evaporation process used for these dilutions did not lead to significant loss of brown carbon or other organic compounds. As shown in Figure S4.1, UV-Vis spectra of the -0.4 and -0.3 extracts before and after rotovapping are essentially the same, indicating evaporation did not change the BrC composition significantly.

We also examined if rotovapping affects photooxidant concentrations. First, we extracted one filter either with 0.7 mL water/square (PME-NR) or 2 mL water/square followed by rotovapping to the equivalent of 0.7 mL/square (PME-R). In the second test, we diluted a rotovapped sample (WIN-0.3) by a factor of 6.7 with water to obtain an extract equivalent to 2 mL Milli-Q/square (WIN-0.3D); this diluted, rotovapped sample should be equivalent to WIN-2, a not rotovapped sample with the same overall dilution. Figure S4.2 presents photooxidant concentrations in the two tests. In each test, the concentrations are essentially the same in the rotovapped and not rotovapped samples, indicating a negligible effect of rotary evaporating on photooxidant kinetics.

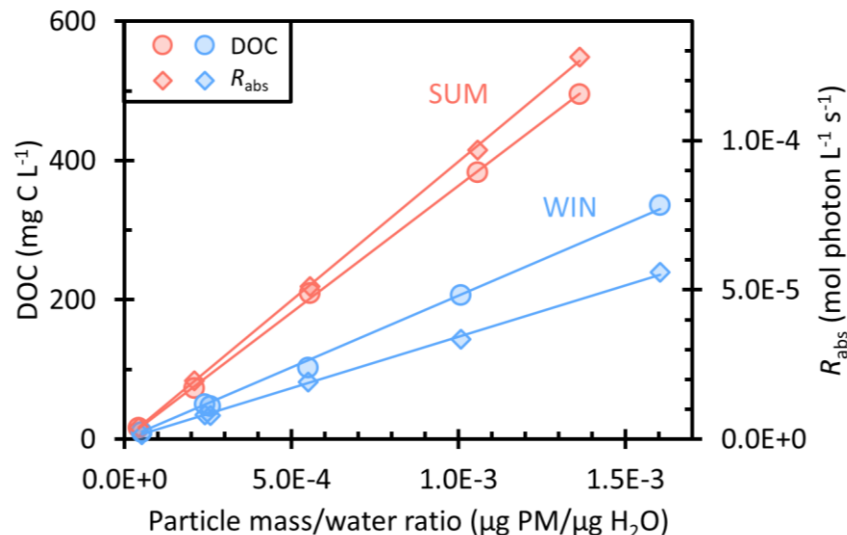


**Figure 4.1.** Dependence of dissolved organic carbon (DOC, circles) and rate of sunlight absorption between 300 – 450 nm ( $R_{\text{abs}}$ , diamonds) on particle mass/water mass ratio (i.e., aqueous particle concentration) in summer (SUM, red) and winter (WIN, blue) particle extracts.

#### 4.3.2. Ions and Light Absorption

Figure 4.1 shows that summer and winter PMEs have DOC in the range of 16 – 495 and 10 – 336 mg C L<sup>-1</sup>, respectively, but WIN has slightly higher particle mass/water ratios,  $(0.05 - 1.6) \times 10^{-3}$  µg PM/µg H<sub>2</sub>O, compared to  $(0.04 - 1.4) \times 10^{-3}$  µg PM/µg H<sub>2</sub>O for SUM. The summer wildfire sample shows a higher average fraction of organic carbon to PM mass,  $0.37 (\pm 0.02)$ , compared to winter  $(0.20 \pm 0.01)$ . The OC/PM ratio in SUM, which represents relatively fresh aerosols from wildfires, is lower than the typical values near 0.5 for biomass burning particles (Reid et al., 2005; Schauer et al., 2001), probably because our water extractions did not solubilize non-polar organic compounds from the particles. The winter sample has lower organic carbon but higher concentrations of ions, including nitrate (NO<sub>3</sub><sup>-</sup>), sulfate (SO<sub>4</sub><sup>2-</sup>), and ammonium (NH<sub>4</sub><sup>+</sup>) (Table S4.2). For example, nitrate concentrations in WIN range from 0.18 – 5.2 mM, contributing to 20 (± 2)% of total extracted PM mass. These concentrations are about five times higher than that in SUM (0.03 – 1.0 mM) at the same concentration factor, which only contributes to 4.2 (± 0.4)% of SUM PM mass. The sulfate accounts for 11 (± 4) % of WIN extracted PM mass, with the concentration (0.03 – 2.3 mM).

around 4 times higher than SUM (0.02 – 0.6 mM).  $\text{NH}_4^+$  has a concentration of 0.20 – 3.6 mM in WIN that is higher than SUM (0.10 – 1.3 mM). Sodium concentrations in both WIN and SUM are high and comparable to ammonium, with ranges of 0.2 – 3.6 mM and 0.1 – 1.7 mM, respectively. Concentrations of potassium, a tracer of biomass burning (Andreae, 1983), are 0.03 – 0.7 mM in both WIN and SUM, with a K/PM mass ratio of 0.02 ( $\pm 0.004$ ), in the range for biomass burning aerosols, 0.02 to 0.05 (Reid et al., 2005; Urban et al., 2012).

For all PMEs, absorbance declines exponentially with wavelength, and WIN and SUM samples have the same absorption Ångström exponent (AAE, 300 – 450 nm) of 7.2, comparable to AEE values (6-8) previously reported in water soluble organic carbon of biomass burning particles (Hecobian et al., 2010; Hoffer et al., 2006; Kaur et al., 2019). The pathlength-normalized absorption coefficient at 300 nm ( $\alpha_{300}$ ) for the summer samples (0.2 – 6.7  $\text{cm}^{-1}$ ) is about 2 times higher than winter samples at the same concentration factor (0.1 – 3.0  $\text{cm}^{-1}$ ). Thus, summer extracts absorb sunlight at approximately twice the rate as winter extracts (Figure 4.1). We also calculated the dissolved organic carbon-normalized mass absorption coefficient ( $\text{MAC}_{\text{DOC}}$ ) of each extract by dividing the absorbance at 300 or 365 nm by the DOC concentration. SUM average  $\text{MAC}_{\text{DOC}}$  values are 3.1 ( $\pm 0.1$ ) and 1.0 ( $\pm 0.1$ )  $\text{m}^2 (\text{g C})^{-1}$  at 300 and 365 nm, respectively, which are approximately 1.5 times higher than the WIN values. This difference is likely driven by the relative abundance of biomass burning organic aerosols (BBOA), because the SUM sample from wildfire is likely dominated by BBOA that contained organic compounds with a higher degree of unsaturation, increasing light absorption (Fleming et al., 2020) while WIN sample has a smaller fraction. Our MAC value for WIN is similar to the average MAC value in previous Davis winter samples (Kaur et al., 2019).

### **4.3.3. Photooxidants in PM Extracts**

In this section we first present our measured oxidant concentrations as a function of particle dilution in the WIN and SUM extracts. We use DOC as the independent variable in our plots because BrC likely

dominates the production of  $^3\text{C}^*$  and  $^1\text{O}_2^*$  and is proportional to concentration factor in each extract series. We then examine how the production rate ( $P_{\text{OX}}$ ) and rate constant for loss ( $k'_{\text{OX}}$ ) for each oxidant vary as a function of dilution. These parameters are related to the steady-state concentration,  $[\text{OX}]$ , by

$$[\text{OX}] = \frac{P_{\text{OX}}}{k'_{\text{OX}}} \quad (4.10)$$

In the next section, we extrapolate these kinetic parameters to aerosol liquid water conditions to predict photooxidant concentrations in ALW.

#### 4.3.3.1. Hydroxyl radical in PM extracts

As shown in Fig. 4.2a, in the WIN dilution series the most dilute sample, WIN-10, has the lowest  $\bullet\text{OH}$  concentration, while in the other dilutions  $[\bullet\text{OH}]$  is noisy but appears independent of DOC. This result, that  $\bullet\text{OH}$  concentration is essentially independent of particle mass concentration, is similar to what Kaur et al. (2019) observed for winter samples (green points in Fig. 4.2), although our  $\bullet\text{OH}$  concentrations are approximately 10 times higher.

Kaur et al. (2019) found that the  $\bullet\text{OH}$  photoproduction rate ( $P_{\text{OH}}$ ) and sink ( $k'_{\text{OH}}$ ) both linearly increase with concentration factor, leading to a roughly constant  $\bullet\text{OH}$  concentration since this is equal to the ratio  $P_{\text{OH}}/k'_{\text{OH}}$  (Eq. 10). To explore this in our samples, we determined  $P_{\text{OH}}$  and  $k'_{\text{OH}}$  in all of the WIN and SUM extracts; we start here by considering the WIN results. As shown in Fig. 4.3(a),  $P_{\text{OH}}$  and  $k'_{\text{OH}}$  both increase linearly with DOC, consistent with the winter PM extract observations of Kaur et al. (2019).  $P_{\text{OH}}$  in WIN ranges from 0.02 to  $4.8 \times 10^{-8} \text{ M s}^{-1}$ , significantly higher than typical values (approximately  $10^{-10} \text{ M s}^{-1}$ ) in cloud and fog waters (Arakaki et al., 2013; Kaur and Anastasio, 2018; Tilgner and Herrmann, 2018). In Davis fog samples, the major source of  $\bullet\text{OH}$  is photolysis of nitrite and nitrate (Anastasio and McGregor, 2001; Kaur and Anastasio, 2017). However, in our winter PM extracts, nitrate accounts for 10 % or less of  $P_{\text{OH}}$  (Table S4.3), while the nitrite contribution is negligible. As for  $\bullet\text{OH}$  sinks in our WIN extracts,  $k'_{\text{OH}}$  is

in the range  $(0.2 - 9.9) \times 10^6 \text{ s}^{-1}$ . The lowest  $k'_{\text{OH}}$  (in WIN-10, the most dilute extract) is comparable to the field blank values (Table S4.3), suggesting that  $[\bullet\text{OH}]$  in WIN-10 may be artificially low because of background contamination. We also calculated the rate constant of organics reacting with  $\bullet\text{OH}$  ( $k_{\text{DOC}+\text{OH}}$ ) for the winter samples; our average WIN value,  $2.4 (\pm 0.7) \times 10^8 \text{ L (mol C)}^{-1} \text{ s}^{-1}$ , is similar to the one determined by Arakaki et al. (2013) for general atmospheric waters,  $3.8 (\pm 1.9) \times 10^8 \text{ L (mol C)}^{-1} \text{ s}^{-1}$ .

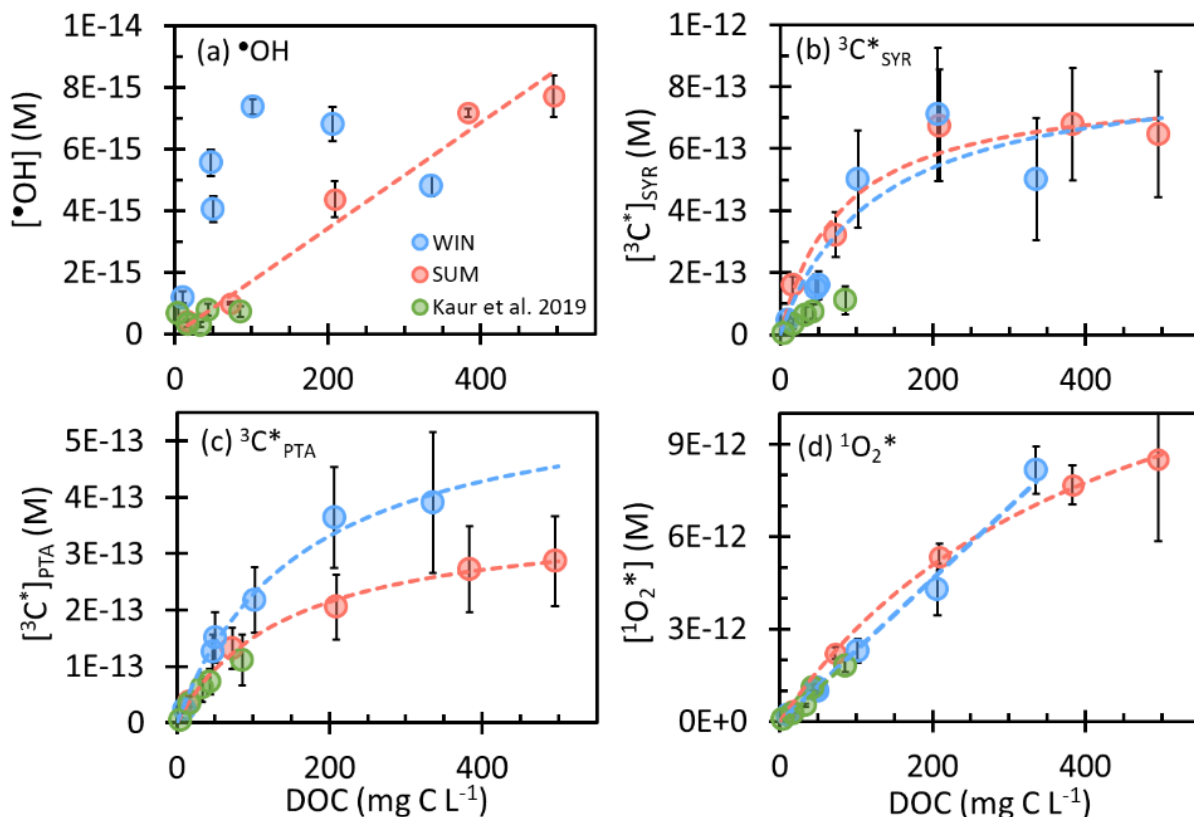


**Figure 4.2.** Steady-state concentrations of (a) hydroxyl radical, oxidizing triplet excited states of brown carbon determined by (b) SYR and (c) PTA, and (d) singlet molecular oxygen in WIN (blue) and SUM (red) samples as a function of dissolved organic carbon. WIN-0.3D results are also included. Previous measurements in Davis winter particle extracts are shown in green (Kaur et al., 2019). Error bars represent  $\pm 1$  standard error propagated from linear regression and uncertainties in rate constants. Dashed lines represent linear or hyperbolic regression fits for WIN and SUM samples.

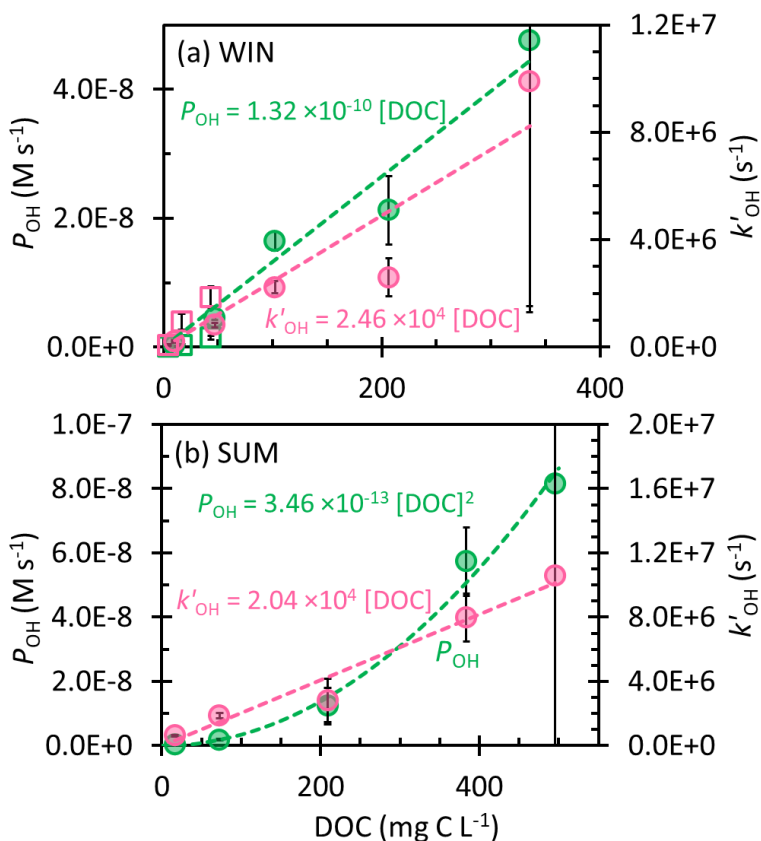


**Figure 4.3.** Dependence of rate of  $\bullet\text{OH}$  photoproduction ( $P_{OH}$ ; green, left y-axis) and rate constant for loss of  $\bullet\text{OH}$  due to natural sinks ( $k'_{OH}$ ; pink, right y-axis) on dissolved organic carbon in (a) winter and (b) summer wildfire samples. Error bars represent  $\pm 1$  standard error propagated from the error in regressions and rate constants; error bars for the 0.3 mL extracts (highest DOC) extend past the plot borders. Dashed lines represent linear regression fits, except the green dashed line in (b) SUM that is derived from the linear regression of  $P_{OH}$  with  $[\text{DOC}]^2$ . Previous measurements in Davis winter particle extracts are shown as open rectangular symbols in panel (a) (Kaur et al., 2019).

Unlike WIN, the  $\bullet\text{OH}$  concentration in the summer samples linearly increases with concentration factor or DOC, in the range  $(0.4 - 7.7) \times 10^{-15} \text{ M}$  (Fig. 4.2a). This indicates that either  $P_{OH}$  or  $k'_{OH}$  does not increase linearly with DOC. As shown in Fig. 4.3b,  $k'_{OH}$  is linear with DOC, but  $P_{OH}$  is proportional to the square of DOC concentration. Our interpretation is that  $\bullet\text{OH}$  production in SUM is a bimolecular reaction rather than a first-order photolysis. The most likely candidate is the photo-Fenton reaction involving soluble iron and hydrogen peroxide (or organic peroxides) (Paulson et al., 2019; Zepp et al., 1992), where the concentrations of both reactants increase with concentration factor, as does [DOC]. Therefore, although

WIN and SUM have roughly similar  $\bullet\text{OH}$  concentrations, they apparently have different mechanisms governing  $\bullet\text{OH}$  formation.  $P_{\text{OH}}$  in SUM is in the range  $(0.03 - 8.2) \times 10^{-8} \text{ M s}^{-1}$ , with the value in SUM-0.3 nearly double that of WIN-0.3. In contrast,  $\bullet\text{OH}$  sinks for the summer and winter samples are similar (Fig. 4.3) and the average  $k_{\text{DOC}+\text{OH}}$  value in SUM is  $2.9 (\pm 1.1) \times 10^8 \text{ L (mol C)}^{-1} \text{ s}^{-1}$ , not significantly different from the WIN value.

#### 4.3.3.2. Oxidizing triplet excited states of organic matter in PM extracts

We determined oxidizing triplet concentrations using two probes. SYR is highly reactive towards both strongly and weakly oxidizing triplets, but its decay by  ${}^3\text{C}^*$  can be inhibited by DOM, leading to an underestimate of  ${}^3\text{C}^*$  concentration (Canonica and Laubscher, 2008; Maizel and Remucal, 2017; Wenk et al., 2011). PTA is less sensitive to weakly oxidizing triplets, but is more resistant to inhibition by DOM (Ma et al., 2022). To correct for probe inhibition, we measured the inhibition factor ( $IF$ ) and used it to correct  ${}^3\text{C}^*$  concentration (Sec. S4.1 and Table S4.7). Inhibition factors of SYR are as low as  $0.13 (\pm 0.03)$  in the most concentrated sample (WIN-0.3), indicating that approximately  $87 (\pm 20) \%$  of SYR decay is inhibited by DOM in this sample, which would lead to a  ${}^3\text{C}^*$  concentration that is  $7.5 (\pm 1.7)$  times lower than the actual value if there was no correction for inhibition. For simplicity, we only show  ${}^3\text{C}^*$  concentrations after inhibition factor correction; uncorrected values are given in the supplement. As for PTA,  $IF$  values are all greater than 0.9, indicating little inhibition.

${}^3\text{C}^*$  concentrations as a function of DOC are in Figure 4.2. With SYR as the triplet probe (Fig. 4.2b), the  $[{}^3\text{C}^*]_{\text{SYR}}$  range is  $(0.5 - 7.1) \times 10^{-13} \text{ M}$  in WIN and  $(1.6 - 6.8) \times 10^{-13} \text{ M}$  in SUM. At the same DOC,  $[{}^3\text{C}^*]_{\text{SYR}}$  values in summer and winter are similar, despite their differences in composition (Table S4.5). Oxidizing triplet concentrations in our samples are generally higher than those from Kaur et al. (2019) (Fig. 4.2c, green points), which can be attributed to higher DOC in our samples and our correction for SYR inhibition. From PTA, the  $[{}^3\text{C}^*]_{\text{PTA}}$  range is  $(0.2 - 3.9) \times 10^{-13} \text{ M}$  in WIN and  $(0.4 - 2.9) \times 10^{-13} \text{ M}$  in SUM, with WIN having higher values than SUM at the same concentration factor (Fig. 4.2c).  $[{}^3\text{C}^*]_{\text{PTA}}$  is lower

than  $[^3\text{C}^*]_{\text{SYR}}$  in every dilution, with average  $[^3\text{C}^*]_{\text{PTA}}/[^3\text{C}^*]_{\text{SYR}}$  of 0.67 ( $\pm 0.22$ ) in WIN and 0.36 ( $\pm 0.09$ ) in SUM. Since PTA appears to only capture highly oxidizing triplets, the ratio of  $[^3\text{C}^*]_{\text{PTA}}/[^3\text{C}^*]_{\text{SYR}}$  should represent the highly oxidizing fraction of the total oxidizing triplet pool (i.e., 67% in WIN and 36% in SUM). Highly oxidizing  $^3\text{C}^*$  typically contain aromatic ketone or carbonyl groups in their precursors, such as 3,4-dimethoxybenzaldehyde, while weakly oxidizing  $^3\text{C}^*$  include polycyclic aromatic structures (e.g. 2-acetonaphthone) (McNeill and Canonica, 2016). Our oxidizing triplet concentrations are approximately 100 times higher than  $[\bullet\text{OH}]$  (Fig. 4.2), indicating the likely importance of  $^3\text{C}^*$  as an oxidant in atmospheric drops and particles.

For both probes, the  $^3\text{C}^*$  concentration initially increases with DOC but then approaches a plateau under more concentrated conditions. Kaur et al. (2019) observed the same trend. Their interpretation was that in dilute solutions  $\text{O}_2$  is the dominant sink for triplets, while under more concentrated conditions DOM becomes the major sink. Therefore,  $^3\text{C}^*$  production and loss are both functions of DOC, as described by

$$[^3\text{C}^*] = \frac{a[\text{DOC}]}{1 + b[\text{DOC}]} \quad (4.11)$$

The dashed lines in Figures 4.2b and 4.2c show the regression fitting results. From the fitted parameter  $b$  (Table S4.9), we can determine  $k_{\text{rxn}+\text{Q},^3\text{C}^*}$  (Eqn. S4.6), the total rate constant of triplet quenching and reaction with DOC. Values from our Fig. 4.2 fittings are  $7.6 (\pm 6.8) \times 10^7 \text{ L (mol C)}^{-1} \text{ s}^{-1}$  for WIN and  $1.2 (\pm 0.5) \times 10^8 \text{ L (mol C)}^{-1} \text{ s}^{-1}$  for SUM (Table S4.10). Kaur et al. (2019) obtained  $9.3 (\pm 1.3) \times 10^7 \text{ L (mol C)}^{-1} \text{ s}^{-1}$  for Davis winter particle extracts, but they didn't correct for SYR inhibition, which should be more significant at higher DOC, leading to an earlier plateau and higher apparent rate constant. Despite this, the three values are not significantly different. Wenk et al. (2013) obtained a range of values of  $(1.3 - 3.9) \times 10^7 \text{ L (mol C)}^{-1} \text{ s}^{-1}$  for surface water DOM quenching and reacting with 2-acetonaphthone and 3-methoxyacetophenone triplets; their lower values imply that atmospheric DOM, at least in our samples, is a more efficient quencher than DOM in surface water.



The equivalent rate constants from our PTA-derived triplet concentrations are  $5.7 (\pm 1.2) \times 10^7$  and  $6.6 (\pm 1.0) \times 10^7 \text{ L (mol C)}^{-1} \text{ s}^{-1}$  for WIN and SUM, respectively. These values are lower than the those obtained using SYR, as reflected by the weaker curvature of the PTA dashed lines (Figure 4.2c) compared to SYR (Figure 4.2b). The similar values of  $k_{\text{rxn}+\text{Q},3\text{C}^*}$  from PTA in WIN and SUM suggest that the quenching rate is insensitive to the particle type. Therefore, the higher  $[\text{}^3\text{C}^*]_{\text{PTA}}$  in WIN compared to SUM at the same DOC level can be attributed to differences in  $\text{}^3\text{C}^*$  production. This is consistent with the differences in apparent quantum yields: the WIN yield of  $1.8 (\pm 0.3)\%$  is more than double the SUM value of  $0.8 (\pm 0.1)\%$  (Table S4.6).

#### 4.3.3.3. Singlet molecular oxygen in PM extracts

The final photooxidant we measured is singlet molecular oxygen. As shown in Fig. 4.2d, winter and summer samples have similar  $\text{}^1\text{O}_2^*$  concentrations, in the range of  $(0.2 - 8.5) \times 10^{-12} \text{ M}$ , with values increasing with DOC. The lowest values, in the most dilute extracts, are comparable to fog water concentrations, while our highest concentrations are approximately four times higher than those in previous Davis winter particle extracts (Anastasio and McGregor, 2001; Kaur and Anastasio, 2017; Kaur et al., 2019).  $\text{}^1\text{O}_2^*$  is the most abundant oxidant in our PMEs, with concentrations roughly 10 times higher than  $\text{}^3\text{C}^*$  and 1000 times higher than  $\bullet\text{OH}$ . In both series of samples, the  $\text{}^1\text{O}_2^*$  concentration increases with DOC, which is consistent with the trend of  $\text{}^1\text{O}_2^*$  in the study of Kaur et al. (2019). Since brown carbon is the source of  $\text{}^1\text{O}_2^*$ , the  $\text{}^1\text{O}_2^*$  production rate increases with DOC. In contrast, in our extracts the dominant sink for  $\text{}^1\text{O}_2^*$  is water, whose concentration is independent of concentration factor. All three sets of samples in Fig. 4.2d exhibit very similar relationships between  $\text{}^1\text{O}_2^*$  and DOC, suggesting DOC concentration might be a good predictor of  $\text{}^1\text{O}_2^*$  concentrations in atmospheric waters. Apparent quantum yields of  $\text{}^1\text{O}_2^*$  are  $3.0 (\pm 0.2)\%$  for WIN and  $2.0 (\pm 0.4)\%$  for SUM, which are in the range of typical values for atmospheric waters (Kaur and Anastasio, 2017; Kaur et al., 2019; Manfrin et al., 2019) and surface waters (Ossola et al., 2020). For WIN,  $\text{}^1\text{O}_2^*$  is linear with DOC throughout the dilution series, but in SUM the singlet oxygen concentration

exhibits a linear relationship at low DOC and then starts to level off in the more concentrated samples (Fig. 4.2d). Kaur et al. (2019) predicted this plateauing under aerosol liquid water conditions as the very high concentration of organics can become the dominant  $^1\text{O}_2^*$  sink. However, a better explanation for this curvature is that the concentration of  $^3\text{C}^*$ , the precursor of  $^1\text{O}_2^*$ , plateaus at high DOC, which makes the production rate of  $^1\text{O}_2^*$  slow. In the summer sample of Figure 4.2d, the curvature of  $^1\text{O}_2^*$  is more likely a consequence of  $^3\text{C}^*$  plateauing, rather than DOC becoming an important  $^1\text{O}_2^*$  sink, because  $^1\text{O}_2^*$  generally has lower reactivity than triplets with most organics. For organics to be an important sink of  $^1\text{O}_2^*$ , the DOC concentration would need to be  $\sim 5000 \text{ mg C L}^{-1}$  (Kaur et al., 2019), which is 10 times higher than the maximum DOC in our extracts. Assuming  $^3\text{C}^*$  is responsible for the  $^1\text{O}_2^*$  curvature in the SUM sample, we can derive a kinetic equation for  $[^1\text{O}_2^*]$  as a function of DOC, taking the plateauing  $^3\text{C}^*$  concentration into consideration. The simplified equation, Eq. S8, is analogous to Eq. 11 and is derived in Sec. S4.2.

This equation gives a good fit to the SUM data, as shown by the red dashed line in Fig. 4.2d. From the parameter  $b$ , we calculate a rate constant for DOC reaction and quenching of  $^1\text{O}_2^*$ -producing triplet states ( $k_{\text{rxn}+\text{Q},^3\text{C}^*}$ ) of  $2.1 (\pm 0.3) \times 10^7 \text{ L (mol C)}^{-1} \text{ s}^{-1}$ . This is lower than the values acquired from  $[^3\text{C}^*]_{\text{SYR}}$  and  $[^3\text{C}^*]_{\text{PTA}}$ , which is reasonable since the  $^1\text{O}_2^*$ -derived value represents the whole triplet pool (i.e., all triplets that can undergo energy transfer with dissolved oxygen) which is a larger pool than oxidizing triplets. Our results indicate that the non-oxidizing, lower-energy triplets have lower reactivity than oxidizing triplets, leading to a lower rate constant for reaction and quenching by DOC, as seen previously by Canonica et al. (2000).

#### 4.3.4. Extrapolating Photooxidant Concentrations to ALW Conditions

In the dilution experiments above, we investigated oxidant kinetics and concentrations as a function of concentration factor, i.e., particle mass/water mass ratio. For the next step, in this section we extrapolate these relationships from our dilute extract conditions (with PM mass/water mass ratios of  $(0.04 - 1.6) \times 10^7$

<sup>3</sup> μg PM/μg H<sub>2</sub>O) to the much more concentrated conditions of aerosol liquid water (up to ~ 1 μg PM/μg H<sub>2</sub>O).

#### 4.3.4.1. Hydroxyl radical in ALW

To estimate [ $\bullet$ OH] for WIN, we apply the linear relationships of  $P_{\text{OH}}$  and  $k'_{\text{OH}}$  with DOC in our extracts (Fig. 4.3a) and ratios of DOC to particle mass/water mass ratio to more concentrated condition. Parameters used for extrapolation are provided in Table S4.11. Extrapolating to an ALW of 1 μg PM/μg H<sub>2</sub>O yields an estimated  $P_{\text{OH}}$  of  $2.7 \times 10^{-5} \text{ M s}^{-1}$ , and  $k'_{\text{OH}}$  of  $5.0 \times 10^9 \text{ s}^{-1}$ . However, since our aqueous experiments do not include  $\bullet$ OH transferred from the gas phase ( $P_{\text{OH,gas}}$ ), we added  $P_{\text{OH,gas}}$  estimated by Kaur et al. (2019) to our extrapolated  $P_{\text{OH}}$  to calculate  $P_{\text{OH,tot}}$ . We then estimate [ $\bullet$ OH] as  $P_{\text{OH,tot}}$  divided by  $k'_{\text{OH}}$  (Eq. 10). Estimating [ $\bullet$ OH] for the SUM sample is more complicated since  $P_{\text{OH}}$  increases with the square of DOC. We simulate the  $\bullet$ OH production rate as a function of DOC by using photo-Fenton reaction rate constants and setting soluble iron and hydrogen peroxide concentrations to fit measured values (Sec. S4.3). We then apply this simple model to predict  $P_{\text{OH}}$  for SUM out to ALW conditions. For  $k'_{\text{OH}}$  in SUM, we use the measured linear dependence on DOC (Fig. 4.3b).

Figure 4.4a shows the predicted hydroxyl radical steady-state concentrations for SUM and WIN across a wide range of liquid water contents, from dilute cloud/fog drops to concentrated aqueous particle conditions. We also include the winter PM  $\bullet$ OH predictions from Kaur et al. (2019) for comparison. [ $\bullet$ OH] for WIN slowly decreases from  $1.1 \times 10^{-14} \text{ M}$  in cloud/fog waters to  $5.5 \times 10^{-15} \text{ M}$  in ALW (1 μg PM/μg H<sub>2</sub>O). Calculated [ $\bullet$ OH] values are higher than measured values, especially under the most dilute conditions, because  $\bullet$ OH from gas-phase mass transfer is included in our extrapolation. The  $\bullet$ OH trend for WIN is consistent with the result of Kaur et al. (2019), but our concentrations are 6 – 12 times higher. This is because WIN has a slope of  $P_{\text{OH}}$  vs. DOC around 4 times higher than that in Kaur et al. (2019), while the slopes for  $k'_{\text{OH}}$  are slightly lower (Fig. 4.3a). For our winter sample under dilute conditions, aqueous processes are as important an  $\bullet$ OH source as is gas-phase transfer (Fig. 4.4b). However, the aqueous

production rate rises more rapidly with PM mass concentration than does gas-phase mass transfer, making aqueous reactions the dominant source of  $\bullet\text{OH}$  under ALW conditions. The slower increase of  $P_{\text{OH,gas}}$  is also responsible for the decreasing  $[\bullet\text{OH}]$  with increasing PM mass concentration.

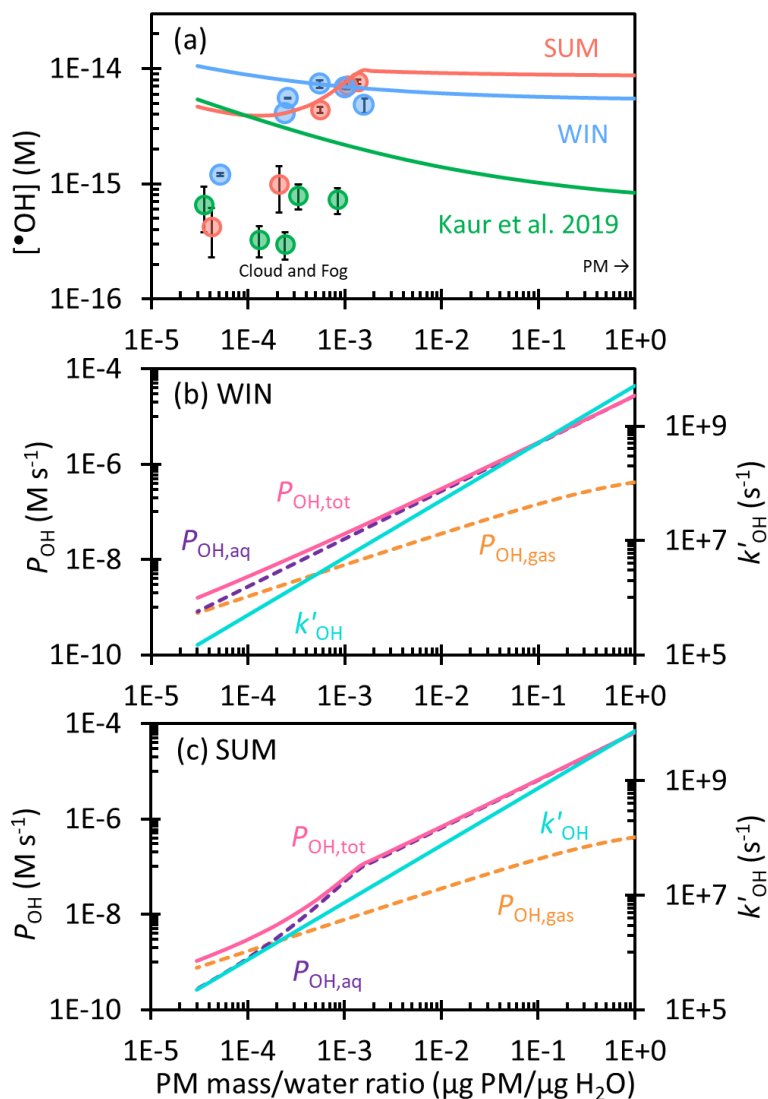


**Figure 4.4.** (a) Dependence of hydroxyl radical concentration on particle mass/water mass ratio in winter (blue) and summer (red) extracts. Solid circles are measured values, while lines are extrapolations to the ambient aqueous aerosol conditions, including contributions from aqueous  $\bullet\text{OH}$  formation and  $\bullet\text{OH}$  mass transport from the gas phase. Previous measurements and extrapolation with Davis winter particle extracts are shown in green (Kaur et al., 2019). (b)&(c) Dependence of hydroxyl radical production rate, including the rate of transport from the gas phase ( $P_{\text{OH,gas}}$ , orange), aqueous reaction ( $P_{\text{OH,aq}}$ , purple), and the total rate

( $P_{\text{OH,tot}} = P_{\text{OH,aq}} + P_{\text{OH,gas}}$ , pink), and the rate constant of  $\bullet\text{OH}$  loss by natural sinks ( $k'_{\text{OH}}$ , blue) on particle mass/water mass ratio for (b) WIN and (c) SUM.

For SUM,  $[\bullet\text{OH}]$  is approximately constant at  $4 \times 10^{-15}$  M under dilute conditions, with  $P_{\text{OH,gas}}$  being the major source of  $\bullet\text{OH}$  (Fig. 4.4b).  $[\bullet\text{OH}]$  then increases to  $1 \times 10^{-14}$  M at  $1 \times 10^{-3}$   $\mu\text{g PM}/\mu\text{g H}_2\text{O}$  as the production rate of aqueous reaction ( $P_{\text{OH,aq}}$ ) increases rapidly and aqueous reactions dominate  $\bullet\text{OH}$  production. When moving to more concentrated conditions,  $[\bullet\text{OH}]$  hits a plateau because we assume the aqueous  $\text{H}_2\text{O}_2$  concentration reaches a maximum due to equilibrium with the gas phase. Thereafter,  $P_{\text{OH,aq}}$  increases linearly, but more slowly, with PM mass/water mass ratio; since  $k'_{\text{OH}}$  also increases linearly with concentration factor,  $[\bullet\text{OH}]$  remains nearly constant at  $9 \times 10^{-15}$  M for conditions of  $1 \mu\text{g PM}/\mu\text{g H}_2\text{O}$ . For both WIN and SUM, our measured  $\bullet\text{OH}$  concentrations in the most concentrated extracts are approximately an order of magnitude higher than in Kaur et al. (2019) and this difference is maintained throughout the predicted  $[\bullet\text{OH}]$  to ambient particle water conditions.

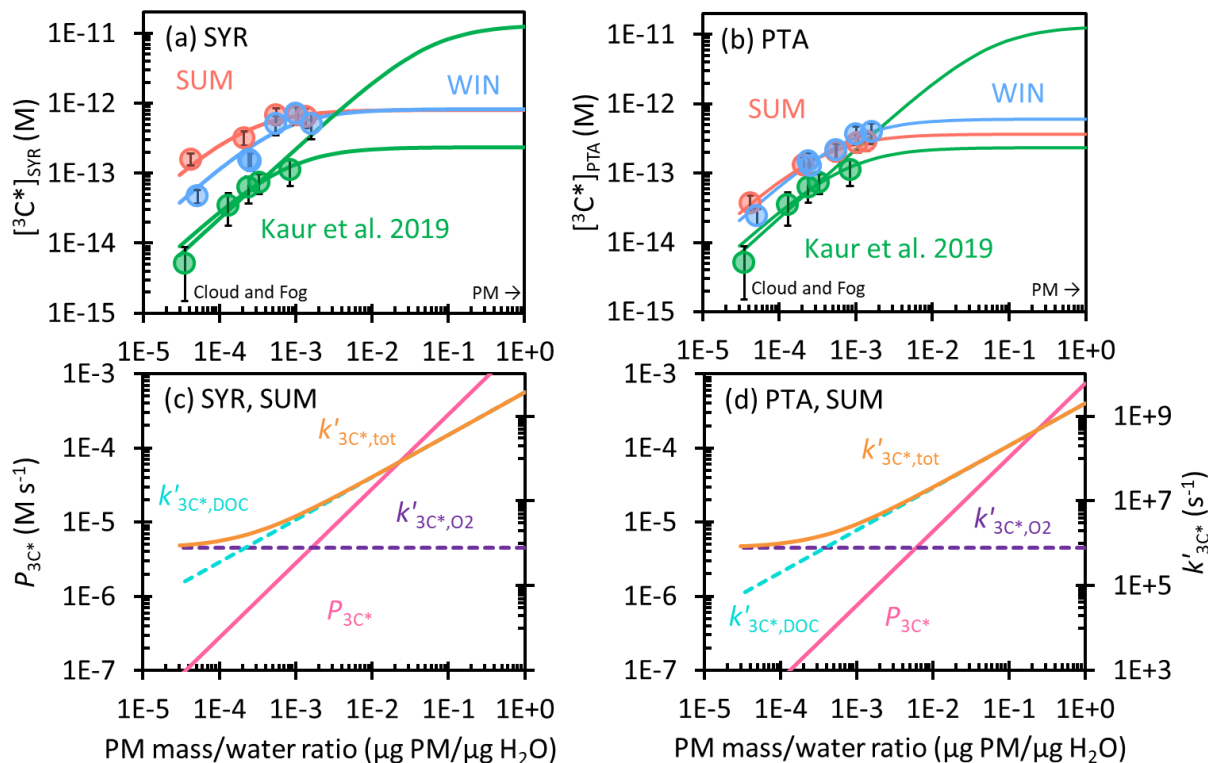


**Figure 4.5.** Top row: Dependence of triplet excited state concentration determined by (a) SYR and (b) PTA on particle mass/water mass ratio in WIN (blue) and SUM (red). Solid circles are measured values in dilution experiments, while lines are extrapolation to ALW conditions. Previous measurements and extrapolations (best fit and high estimate) for Davis winter particle extracts are in green (Kaur et al., 2019). Bottom row: Triplet production rate ( $P_{3C^*}$ , pink) and first-order rate constants for  $^3C^*$  loss, including quenching by oxygen ( $k'_{3C^*,O_2}$ , purple), dissolved organic carbon ( $k'_{3C^*,DOC}$ , blue), and total ( $k'_{3C^*,tot} = k'_{3C^*,O_2} + k'_{3C^*,DOC}$ , orange) determined by (c) SYR and (d) PTA for SUM. Figure S4.4 shows  $P_{3C^*}$  and  $k'_{3C^*}$  for WIN.

#### 4.3.4.2. Oxidizing triplet concentrations in ALW

To predict  $^3C^*$  concentrations in aerosol liquid water, we extrapolated  $^3C^*$  production rate ( $P_{3C^*}$ ) and sinks ( $k'_{3C^*}$ ) to concentrated condition and calculated  $^3C^*$  concentration for SYR and PTA, respectively with Eq.4.10. As shown in Figs. 4.5a and b, measured  $[^3C^*]$  in SUM and WIN are higher than the results in Kaur et al. (2019) at the same particle mass/water ratio. This is attributed to higher ratios of OC/PM in our samples. In all three sets of samples,  $[^3C^*]$  rises rapidly with PM mass/water mass ratio at low DOC, and then reaches or approaches a plateau under aqueous aerosol conditions, as the dominant triplet sink

transitions from dissolved O<sub>2</sub> to DOC. We believe the production rate of <sup>3</sup>C\* linearly increases with particle mass/water mass ratio ( $P_{3C^*}$  in Figs. 4.5c and 4.5d), but the sinks for triplets change, as proposed by Kaur et al. (2019). Under dilute conditions, O<sub>2</sub> is a dominant and constant sink ( $k'_{3C^*,O_2}$ ). Since O<sub>2</sub> concentration in aqueous solution is nearly constant, [<sup>3</sup>C\*] increases with increasing concentration factor. Under more concentrated conditions, organic compounds become the major sink for <sup>3</sup>C\* (Figs 4.5c and d). The ratio of the production rate and sink rate becomes constant at higher DOC, causing [<sup>3</sup>C\*] to plateau. For SYR, WIN and SUM both reach a maximum value of  $8 \times 10^{-13}$  M at 1 μg PM/μg H<sub>2</sub>O (ALW condition). This value is 22 times higher than the concentration under the most dilute conditions in WIN, while it is around 8 times higher than the dilute result in SUM. While SUM starts with a higher [<sup>3</sup>C\*]<sub>SYR</sub> under dilute conditions, it experiences greater curvature than WIN, possibly because its organic compounds are more reactive with oxidizing triplets. For both samples, the ALW prediction for [<sup>3</sup>C\*]<sub>SYR</sub> is near the geometric mean of the two bounding fits of Kaur et al. (2019). For the lower <sup>3</sup>C\* concentrations determined by PTA, SUM and WIN start with essentially the same [<sup>3</sup>C\*]<sub>PTA</sub> at  $3 \times 10^{-5}$  μg PM/μg H<sub>2</sub>O ( $3 \times 10^{-14}$  and  $2 \times 10^{-14}$  M, respectively). SUM exhibits more curvature, as seen for [<sup>3</sup>C\*]<sub>SYR</sub>, leading to a lower [<sup>3</sup>C\*]<sub>PTA</sub> at 1 μg PM/μg H<sub>2</sub>O:  $4 \times 10^{-13}$  M for SUM vs.  $6 \times 10^{-13}$  M for WIN. [<sup>3</sup>C\*]<sub>PTA</sub> increases by factors of 14 and 29 for SUM and WIN, respectively, from the most dilute condition to ALW condition, similar to [<sup>3</sup>C\*]<sub>SYR</sub>.

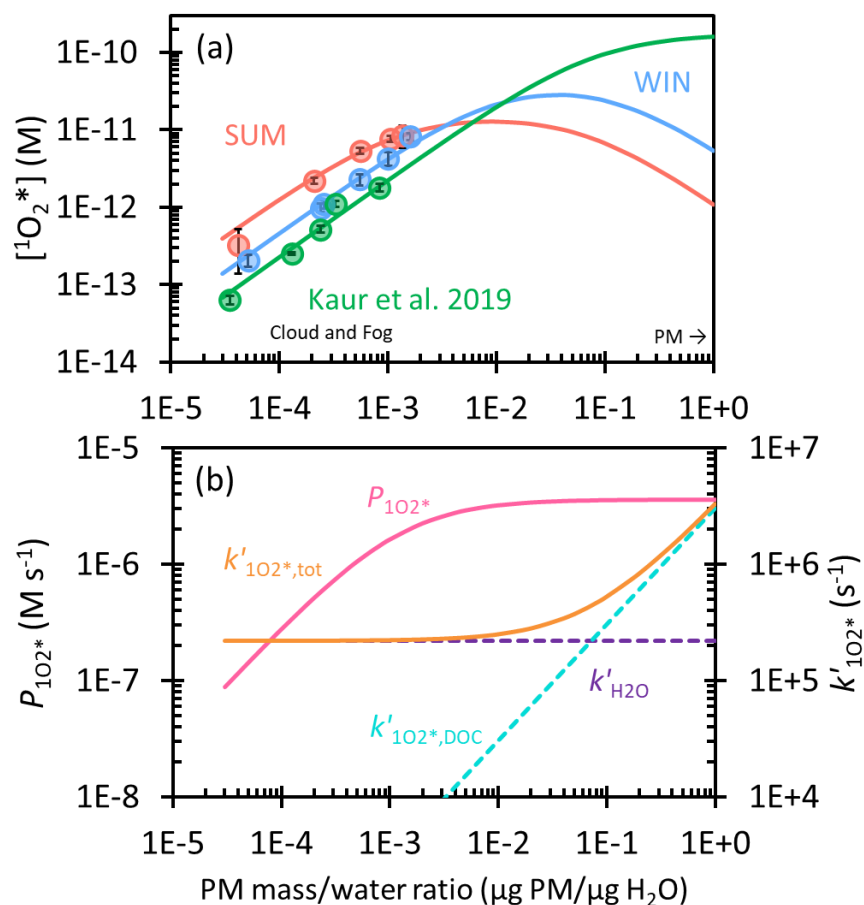


**Figure 4.6.** (a) Dependence of singlet molecular oxygen concentration on particle mass/water mass ratio in winter (blue) and summer (red) samples. Solid circles are measured values in dilution experiments, while lines are extrapolations to ALW conditions. Previous measurements and extrapolation with Davis winter particle extracts are in green (Kaur et al., 2019). (b) Dependence of singlet oxygen production rate ( $P_{1\text{O}_2^*}$ , pink) and the rate constant for  $^1\text{O}_2^*$  loss, including deactivation by water ( $k'_{\text{H}_2\text{O}}$ , purple), quenching by dissolved organic carbon ( $k'_{1\text{O}_2^*,\text{DOC}}$ , blue), and the total sink ( $k'_{1\text{O}_2^*,\text{tot}} = k'_{\text{H}_2\text{O}} + k'_{1\text{O}_2^*,\text{DOC}}$ , orange) on particle mass/water mass ratio for SUM. Figure S4.6 shows  $P_{1\text{O}_2^*}$  and  $k'_{1\text{O}_2^*}$  for the winter samples.

#### 4.3.4.3. Singlet molecular oxygen in ALW

Lastly, we consider the extrapolation of  $^1\text{O}_2^*$  concentrations from our dilute experimental solutions to ALW conditions. To do this, we consider three factors: the production of  $^1\text{O}_2^*$  by  $^3\text{C}^*$  and  $\text{H}_2\text{O}$  and DOM as sinks for singlet oxygen. In terms of  $^1\text{O}_2^*$  sources, the plateauing of  $[^3\text{C}^*]$  at high concentration factors results in a plateauing of the  $^1\text{O}_2^*$  production rate, as evidenced in the curvature of  $[^1\text{O}_2^*]$  in SUM.



To account for this effect, we fit [ $^1\text{O}_2^*$ ] versus DOC using Eq. 11 and calculate the  $^1\text{O}_2^*$  production rate ( $P_{1\text{O}_2^*}$ ) with the fitted parameters (Eq. S11). This process does not work for WIN, however, since it shows no curvature of [ $^1\text{O}_2^*$ ]. So to predict the  $^3\text{C}^*$  effect for this sample, we adjusted the regression parameters so that the fitted line passed through the first 4 data points (Figure S4.5). In terms of modeling DOM as a sink for  $^1\text{O}_2^*$ , this effect does not appear in our lab extracts (due to their relatively low DOC content), but we expect it will happen under more concentrated conditions. To incorporate this effect, we applied the estimated parameter by Kaur et al. (2019), the second order rate constant for loss of  $^1\text{O}_2^*$  by DOC ( $k'_{1\text{O}_2^*,\text{DOC}}$ ), which is  $1 \times 10^5 \text{ L (mol C)}^{-1} \text{ s}^{-1}$  and the sink is calculated as the product of the rate constant and DOC.

The resulting predictions for  $^1\text{O}_2^*$  concentrations, along with the production rate and sink rate constants for the summer sample, are in Figure 4.6. Figure 4.6a shows that our predictions of  $^1\text{O}_2^*$  under ALW conditions are lower than those in Kaur et al. (2019) because we consider the effect of the plateauing  $^3\text{C}^*$  concentration on  $^1\text{O}_2^*$  production, which decreases  $^1\text{O}_2^*$  concentrations under ALW conditions. In Fig. 4.6a, for SUM [ $^1\text{O}_2^*$ ] starts at  $4 \times 10^{-13} \text{ M}$  in dilute drops, peaks at  $1 \times 10^{-11} \text{ M}$  at  $1.0 \times 10^{-2} \mu\text{g PM}/\mu\text{g H}_2\text{O}$ , when  $P_{1\text{O}_2^*}$  plateaus (Fig. 4.6b), and then starts to decrease. This decrease is because the production rate for  $^1\text{O}_2^*$  ( $P_{1\text{O}_2^*}$ ) is constant while the  $^1\text{O}_2^*$  sink ( $k'_{1\text{O}_2^*,\text{DOC}}$ ) increases with particle mass concentration and becomes the dominant  $^1\text{O}_2^*$  sink; the result is a singlet oxygen concentration of  $1 \times 10^{-12} \text{ M}$  at  $1 \mu\text{g PM}/\mu\text{g H}_2\text{O}$ . This concentration is only 1.4 times higher than [ $^3\text{C}^*$ ] $_{\text{SYR}}$  under the same condition (Fig. S4.8). For WIN, [ $^1\text{O}_2^*$ ] starts at  $1 \times 10^{-13} \text{ M}$  in dilute drops, reaches a maximum of  $3 \times 10^{-11} \text{ M}$  at  $4.0 \times 10^{-2} \mu\text{g PM}/\mu\text{g H}_2\text{O}$ , and then decreases to  $5 \times 10^{-12} \text{ M}$ . Under ALW conditions, WIN has a maximum [ $^1\text{O}_2^*$ ] that is 3 times higher than SUM because [ $^1\text{O}_2^*$ ] in WIN presents much less curvature than SUM. Therefore, the plateau of  $P_{1\text{O}_2^*}$  in WIN shows up only under more concentrated conditions compared to SUM (Fig. S4.6).

#### 4.4. Conclusion and Uncertainties

We studied aqueous extracts of winter particles influenced by residential wood combustion and summer wildfire particles and measured concentrations of three photooxidants - hydroxyl radical, oxidizing triplet excited states of organic matter, and singlet molecular oxygen - as a function of particle dilution. The extracts contain high amounts of organic matter, with dissolved organic carbon concentrations ranging from 10 to 495 mg C L<sup>-1</sup>. DOC-normalized mass absorption coefficients at 300 nm are 2.1 (±0.2) m<sup>2</sup> (g C)<sup>-1</sup> in winter and 3.1 (±0.1) m<sup>2</sup> (g C)<sup>-1</sup> in summer, with absorption Ångström exponents of 7.2 for both, indicating significant amounts of brown carbon.

In winter samples, the •OH concentration appears to be independent of concentration factor, while in summer samples it increases with concentration factor. We hypothesize that the different behaviors of •OH is due to different dominant pathways for •OH production. In WIN, the unimolecular reactions such as direct photodegradation of chromophores appears to be the major source, while in SUM bimolecular reactions, such as HOOH plus Fe(II), dominate. In both WIN and SUM, <sup>3</sup>C\* concentrations determined by SYR and PTA initial increase rapidly with concentration factor, and then start to level off or even reach a plateau under more concentrated conditions. <sup>1</sup>O<sub>2</sub>\* concentrations in WIN are linear with DOC, while in SUM it shows curvature (like <sup>3</sup>C\*) in more concentrated extracts.

By extrapolating the relationship between oxidant kinetics and particle mass concentration to the much more concentrated conditions of ambient particle water (1 μg PM/μg H<sub>2</sub>O), photooxidant concentrations are [•OH] = (6 – 9) × 10<sup>-15</sup> M, [<sup>3</sup>C\*] = (4 – 8) × 10<sup>-13</sup> M, and [<sup>1</sup>O<sub>2</sub>\*] = (1 – 5) × 10<sup>-12</sup> M. •OH concentration is not significantly different from that in fog/cloud waters, while [<sup>3</sup>C\*] and [<sup>1</sup>O<sub>2</sub>\*] are 10 – 30 and 3 – 40 times higher than values in the dilute phase (3 × 10<sup>-5</sup> μg PM/μg H<sub>2</sub>O), respectively. The ratio of concentrations of <sup>1</sup>O<sub>2</sub>\*: <sup>3</sup>C\*: •OH in ambient particle is 10<sup>3</sup> – 10<sup>2</sup> : 10<sup>2</sup> : 1, which is lower than the 10<sup>5</sup> : 10<sup>4</sup> – 10<sup>2</sup>: 1 ALW ratio predicted by Kaur et al. (2019). Compared to their work, our predicted ALW concentration of •OH is approximately 10 times higher, <sup>3</sup>C\* is around 5 times higher than their best fit but

more than 10 times lower than their high estimate, and  $^1\text{O}_2^*$  is 30 – 150 times lower (Fig. S4.7). Kaur et al. (2019) discussed the uncertainties to predict  $^1\text{O}_2^*$  and  $^3\text{C}^*$  because of the difficulty to access the interaction between DOC and  $^3\text{C}^*$  or  $^1\text{O}_2^*$ . However, in this work, we were able to better see the DOC-triplet interaction since DOC concentrations in our particle water extracts were up to 5 times higher, enabling us to better see the behavior of  $^1\text{O}_2^*$  and  $^3\text{C}^*$  with DOC. When moving to more concentrated conditions,  $^3\text{C}^*$  concentrations are heavily suppressed due to quenching by DOC, with our plateaus between the two estimates from Kaur et al. (2019). For the first time, we also see the relationship between  $[\text{}^1\text{O}_2^*]$  and DOC start to curve at high DOC (at least in the summer sample), caused by the leveling-off of the  $^3\text{C}^*$  concentration. With this experimental finding, we are able to include this effect in the prediction of  $^1\text{O}_2^*$  concentrations under particle water conditions. The ratio of photooxidant production rates in ALW, which equals to oxidant consumption rate at the steady state, is  $^1\text{O}_2^* : ^3\text{C}^* : \bullet\text{OH}$  is 1: 10:  $10^2$ . Since organic compounds will be the major sink for oxidants in ALW, the highest  $P_{3\text{C}^*}$  indicates that  $^3\text{C}^*$  might be more important in organic compounds oxidation compared to the other two.

Our work is an extension of the study of Kaur et al. (2019), by using particle water extracts with higher DOC, as well as different types of particles (winter and summer wildfire). The difference in particle types can affect the major sources for  $\bullet\text{OH}$  production, while  $[\text{}^1\text{O}_2^*]$  and  $[\text{}^3\text{C}^*]$  are less impacted. However, due to the experimental limitation, the extrapolation we made is still over a very wide range (approximately a factor of 600), bringing significant uncertainties. For example, we did not observe how efficiently organic matters quenching  $^1\text{O}_2^*$ . Therefore, we are unable to accurately account for this effect. In addition, highly concentrated particle extracts brought difficulty in oxidant measurement, especially for  $^3\text{C}^*$ . SYR, as the triplet probe, suffers from a strong inhibition by dissolved organic matter. The correction for  $^3\text{C}^*$  concentration determined by SYR is up to a factor of 7.5 in this work, bringing large uncertainties. High DOC also generates heavy light screening effect, which brought uncertain by correcting this effect as well. To obtain more concentrated particle extracts, will require rotary evaporation or other techniques to remove water but not change the characterization of extracts. Since high particle mass concentrations can lead to

significant light screening, using containers that have very short pathlengths for illumination experiments are recommended.

#### **4.5. Financial Support**

This research has been supported by the National Science Foundation (grants 1649212 and 2220307); the California Agricultural Experiment Station (Projects CA-D-LAW-6403-RR and CA-D-ETX-2102-H); and the University of California, Davis (Donald G. Crosby Graduate Fellowship in Environmental Chemistry and Jastro Shields Research Awards).

## 4.6. Supporting Information

**Table S4.1.** Particle sample collection and PME information

Sample ID <sup>a</sup>	Collection dates <sup>b</sup>	Sampling duration (h)	Average PM <sub>2.5</sub> concentration <sup>d</sup> (μg/m <sup>3</sup> -air)	Particle mass/water ratio <sup>e</sup> (10 <sup>-4</sup> μg PM/μg H <sub>2</sub> O)	α <sub>300</sub> <sup>f</sup> (cm <sup>-1</sup> )	R <sub>abs</sub> (300-450 nm) (10 <sup>-6</sup> mol-photons L <sup>-1</sup> s <sup>-1</sup> ) <sup>g</sup>	AA E <sup>h</sup>	MAC <sub>D</sub> oc (300nm) (m <sup>2</sup> (g C) <sup>-1</sup> ) <sup>i</sup>	MAC <sub>D</sub> oc (365nm) (m <sup>2</sup> (g C) <sup>-1</sup> ) <sup>i</sup>	DOC (mg C L <sup>-1</sup> )	Light screening factor <sup>j</sup>
WIN-10	2/5/20 – 2/28/20	168 <sup>c</sup> (one week)	9.2	0.51 (±0.09)	0.086	1.5	7.58	2.0	0.57	10.1	0.98
WIN-2				2.6 (±0.4)	0.446	7.8	7.28	2.2	0.65	47.2	0.88
WIN-0.7				5.5 (±0.9)	1.089	19	7.23	2.5	0.74	102.1	0.74
WIN-0.4				10 (±1.5)	1.820	33	7.02	2.0	0.63	206.3	0.61
WIN-0.3				16 (±2.4)	3.029	56	7.00	2.1	0.65	335.6	0.48
WIN-0.3D				2.4 (±0.4)	0.452	8.1	7.16	2.1	0.64	50.2	0.88
SUM-10	8/21/20 – 8/24/20	28.8 <sup>c</sup>	54.5	0.42 (±0.07)	0.220	3.9	7.42	3.1	0.96	16.4	0.94
SUM-2				2.1 (±0.4)	1.062	20	7.17	3.4	1.07	72.7	0.74
SUM-0.7				5.5 (±1.3)	2.780	51	7.17	3.1	0.97	208.9	0.50
SUM-0.4				11 (±2.3)	5.147	97	7.05	3.1	0.99	383.4	0.32
SUM-0.3				14 (±2.4)	6.679	128	6.93	3.1	1.01	495.4	0.26
PME-NR <sup>k</sup>	10/6/20 – 10/8/20	48	30.9	6.4 (±0.2)	1.504	22	7.57	1.7	0.40	209.9	0.70
PME-R <sup>l</sup>	6.4 (±0.3)			1.579	23	7.74	1.8	0.44	204.3	0.68	
Field blanks <sup>m</sup>											
FB1	8/4/20	3 min	6.9	0.16 (±0.06)	0.0022	0.017				2.1	1
FB2	1/2/20	3 min	15.6	0.13 (±0.06)	0.0015	0.0013				2.0	1
FB3	10/5/20	3 min	39.6	0.47 (±0.38)	0.0065	0.086				3.0	1

<sup>a</sup> Samples were named as “PME-water volume” (e.g., WIN-0.7) to denote the sample and extraction volume. WIN-0.3D is the WIN-0.3 sample diluted to an equivalent extract volume of 2 mL/square (i.e., to the equivalent dilution of WIN-2).

<sup>b</sup> For the WIN and SUM samples, we collected three separate, consecutive samples during each collection period and then composited them during extraction. Each winter sample was collected for a week, while each summer sample was collected for approximately 24-hr. The 10/6/20-10/8/20 sample was just one filter collected for 48 h.

- <sup>c</sup> The average sampling duration for each filter within a given composite.
- <sup>d</sup> Average PM<sub>2.5</sub> concentration for each sampling period measured at the UC Davis sampling site by the California Air Resources as reported on the iADAM online database (California Air Resources Board, 2019 –2020; <https://www.arb.ca.gov/adam>).
- <sup>e</sup> Particle mass/water mass ratio ( $\pm 1 \sigma$ ) is calculated as the extracted particle mass per filter square (determined as the difference of filter weights before and after extraction) divided by the volume of water used for extraction.
- <sup>f</sup> Base-10 absorbance coefficient of the extract (in cm<sup>-1</sup>) at 300 nm. This is determined as the sample absorbance divided by the cell pathlength.
- <sup>g</sup> Rate of sunlight absorption by PME in the 300-450 nm wavelength range, calculated by equation 2 in Kaur et al. (2019), using the actinic flux at midday on the winter solstice in Davis (photons cm<sup>-2</sup> s<sup>-1</sup> nm<sup>-1</sup>) obtained from the Tropospheric Ultraviolet and Visible (TUV) Radiation Model version 4.1. If we apply the actinic flux at midday on the summer solstice, the rate of light absorption is larger by a factor 1.9.
- <sup>h</sup> AAE, the Angstrom Absorption Exponent, is calculated as the negative slope of a linear regression between ln(absorbance) vs. ln(wavelength) in the 300 – 450 nm wavelength range.
- <sup>i</sup> Mass absorption coefficients at 300 or 365 nm, normalized to dissolved organic carbon, calculated as  $MAC_{DOC,300nm} = \frac{\alpha_{300nm} \times \ln(10) \times 10^6}{[DOC]}$  (Kaur et al., 2019). The contributions of nitrate and nitrite to the total absorbance of PME samples are negligible (< 2 %).
- <sup>j</sup> Light-absorption-weighted internal screening factor, calculated with equation 2 in Smith et al. (2016) using a wavelength range of 280-364 nm. A value of 1 indicates no light screening, while a low value represents a strong screening effect.
- <sup>k</sup> This sample was extracted with 0.7 mL water/square and is not rotovapped.
- <sup>l</sup> This sample was extracted using the same filter as PME-NR, with 2 mL water/square, and then rotovapped to an equivalent extract volume of 0.7 mL/square.
- <sup>m</sup> Field blank samples were extracted with 1.0 mL water/square.

**Table S4.2.** Ion concentrations in PME

Sample ID	[NO <sup>3-</sup> ] ( $\mu$ M)	[NO <sub>2</sub> <sup>-</sup> ] ( $\mu$ M)	[SO <sub>4</sub> <sup>2-</sup> ] ( $\mu$ M) <sup>a</sup>	[Cl <sup>-</sup> ] ( $\mu$ M)	[HCOO <sup>-</sup> ] ( $\mu$ M)	[NH <sub>4</sub> <sup>+</sup> ] ( $\mu$ M)	[Na <sup>+</sup> ] ( $\mu$ M)	[K <sup>+</sup> ] ( $\mu$ M)	[Ca <sup>2+</sup> ] ( $\mu$ M)
WIN-10	179.1	< DL <sup>d</sup>	25.0	5.21	2.65	160.8	196.3	34.0	68.8
WIN-2	793.1	3.49	346.9	29.3	30.3	590.4	612.1	98.4	240.3
WIN-0.7	1535	6.49	538.8	20.5	45.9	1826.7	1238.3	261.4	449.9
WIN-0.4	3215	13.6	1435	89.7	116.4	2558.6	2543.9	457.3	149.4
WIN-0.3	5221	21.3	2347	129.2	193.6	3898.2	3601.5	658.4	1214
WIN-0.3D <sup>b</sup>									
SUM-10	27.4	< DL	21.4	5.21	3.53	100.8	134.2	31.5	50.4
SUM-2	137.6	1.95	90.3	23.4	46.0	208.1	276.0	101.1	98.1
SUM-0.7	325.9	2.49	194.1	64.2	92.8	676.4	607.5	315.8	70.5
SUM-0.4	777.7	< DL	478.0	144.7	145.5	1125	1360	561.3	578.6
SUM-0.3	1018	7.85	618.2	184.2	187.9	1330	1717	676.4	696.7
PME-NR	487.0	8.00	352.7	5.21	3.53	1565	1458	356.5	606.6
PME-R	479.7	8.00	349.1	23.4	46.0	1496	1201	517.0	526.7
Field blanks									
FB1 <sup>c</sup>	3.12	<DL		2458	3.03	0.12	96.0	-0.02	7.01
FB2	4.58	<DL		1.07	2.94	1.42	93.8	5.92	7.02
FB3	1.99	<DL	12.41	0.65	5.54	1.11	124.6	8.88	7.08

<sup>a</sup> The amount of sulfuric acid added to adjust sample pH has been subtracted.

<sup>b</sup> Ion concentrations were not measured in this sample.

<sup>c</sup> This field blank sample was contaminated by the pH electrode filling solution, resulting in extremely high concentrations of Cl<sup>-</sup> and possible other, uncharacterized, contaminants.

<sup>d</sup> Below detection limit.

**Table S4.3.** Hydroxyl radical measurements

Sample ID	$P_{OH}$ ( $10^{-9}$ M $s^{-1}$ ) <sup>a</sup>	$k'_{OH}$ ( $10^6$ $s^{-1}$ ) <sup>b</sup>	$[•OH]$ ( $10^{-15}$ M) <sup>c</sup>	$10^4 \times \Phi_{OH}$ <sup>e</sup>	$k_{DOC+OH}$ ( $10^8$ L (mol-C) <sup>-1</sup> $s^{-1}$ ) <sup>f</sup>	% $P_{OH,NO_3}$ <sup>g</sup>
WIN-10	0.24 ( $\pm$ 0.01)	0.20 ( $\pm$ 0.03)	1.2 ( $\pm$ 0.2)	1.7 ( $\pm$ 0.1)	4.5 ( $\pm$ 0.4)	10.4
WIN-2	4.6 ( $\pm$ 0.4)	8.82 ( $\pm$ 0.09)	5.6 ( $\pm$ 0.4)	5.8 ( $\pm$ 0.5)	3.1 ( $\pm$ 0.3)	2.4
WIN-0.7	16.4 ( $\pm$ 1.5)	2.2 ( $\pm$ 0.2)	7.4 ( $\pm$ 0.2)	8.6 ( $\pm$ 0.8)	1.6 ( $\pm$ 0.8)	1.3
WIN-0.4	21.3 ( $\pm$ 5.3)	2.6 ( $\pm$ 0.7)	6.8 ( $\pm$ 0.5)	6.3 ( $\pm$ 1.6)	2.5 ( $\pm$ 0.5)	2.1
WIN-0.3	47.5 ( $\pm$ 41.2)	9.9 ( $\pm$ 8.6)	4.8 ( $\pm$ 0.3)	8.5 ( $\pm$ 7.4)	2.6 ( $\pm$ 3.1)	1.5
WIN-0.3D	-	-	4.1 ( $\pm$ 0.4)			
SUM-10	0.26 ( $\pm$ 0.01)	0.61 ( $\pm$ 0.06)	0.43 ( $\pm$ 0.01)	0.67 ( $\pm$ 0.03)	2.4 ( $\pm$ 0.4)	1.5
SUM-2	1.8 ( $\pm$ 0.1)	1.9 ( $\pm$ 0.2)	1.0 ( $\pm$ 0.01)	0.94 ( $\pm$ 0.07)	2.1 ( $\pm$ 0.2)	1.0
SUM-0.7	12.3 ( $\pm$ 5.7)	2.8 ( $\pm$ 1.4)	4.4 ( $\pm$ 0.6)	2.4 ( $\pm$ 1.1)	2.6 ( $\pm$ 0.3)	0.4
SUM-0.4	57.3 ( $\pm$ 10.7)	8.0 ( $\pm$ 1.5)	7.2 ( $\pm$ 0.1)	5.9 ( $\pm$ 1.1)	1.5 ( $\pm$ 0.4)	0.2
SUM-0.3	81.5 ( $\pm$ 98.4)	10.6 ( $\pm$ 12.8)	7.7 ( $\pm$ 0.7)	6.4 ( $\pm$ 7.7)	3.5 ( $\pm$ 3.1)	0.2
PME-NR	-	-	4.2 ( $\pm$ 0.3)	-	-	-
PME-R	-	-	4.6 ( $\pm$ 0.8)	-	-	-
Field blanks						
FB1 <sup>h</sup>	-	-	0.57 ( $\pm$ 0.03)	-	-	-
FB2 <sup>i</sup>	0.0011 ( $\pm$ 0.0001)	0.20 ( $\pm$ 0.02)	0.06 ( $\pm$ 0.01)	-	-	5.7
FB3 <sup>i</sup>	0.0008 ( $\pm$ 0.0001)	0.05 ( $\pm$ 0.02)	0.15 ( $\pm$ 0.01)	-	-	3.6

<sup>a</sup> Davis winter solstice-normalized rate of  $\bullet OH$  photoproduction.

<sup>b</sup> Apparent pseudo-first-order rate constant for destruction of  $\bullet OH$  due to natural sinks.

<sup>c</sup> Winter solstice-normalized steady-state concentration of  $\bullet OH$ .

<sup>e</sup> Apparent quantum yield of  $\bullet OH$  during simulated sunlight illumination, calculated as  $\Phi_{OH} = P_{OH}/R_{abs}$

<sup>f</sup> Second-order rate constant of dissolved organic carbon scavenging  $\bullet OH$ , calculated as  $k_{DOC+OH} = k'_{OH}/DOC$

<sup>g</sup> Fraction of nitrate contribution to the  $\bullet OH$  photoproduction rate, calculated as  $(j_{NO_3 \rightarrow OH} \times [NO_3^-]/P_{OH})$  using the aqueous nitrate photolysis rate constant,  $j_{NO_3 \rightarrow OH} = 1.4 \times 10^{-7} s^{-1}$  (Anastasio and McGregor, 2001) and the molar concentration of  $NO_3^-$ . We also calculated the fraction of  $\bullet OH$  production rate due to nitrite: it is negligible, with an average value of 1 %.

<sup>h</sup> This field blank sample was contaminated by the pH electrode.



<sup>i</sup> The  $\bullet\text{OH}$  production rate in field blanks was determined by adding 1.2 mM benzoic acid to 1.0 mL FB sample and monitoring the formation of *p*-hydroxy benzoic acid, assuming that all  $\bullet\text{OH}$  produced reacts with benzoic acid.

**Table S4.4.** Rate constants of SYR and PTA reacting with triplet excited states, singlet oxygen, and hydroxyl radical at pH 4.2

Oxidants	$k_{\text{SYR+Ox}} (\text{M}^{-1} \text{s}^{-1})$	Reference	$k_{\text{PTA+Ox}} (\text{M}^{-1} \text{s}^{-1})$	Reference
$\bullet\text{OH}$	$20 (\pm 4) \times 10^9$	(Smith et al., 2015)	$10.3 (\pm 0.6) \times 10^9$	(Ma et al., 2022)
$^1\text{O}_2^*$	$3.6 (\pm 0.7) \times 10^7$	(Tratnyek and Hoigne, 1991)	$8.8 (\pm 0.6) \times 10^6$	
$^3\text{DMB}^*$	$3.9 (\pm 0.7) \times 10^9$	(Smith et al., 2015)	$2.5 (\pm 0.6) \times 10^9$	
Direct photodegradation	$j_{\text{SYR}} (\text{s}^{-1})$		$j_{\text{PTA}} (\text{s}^{-1})$	
	$< 4.3 \times 10^{-6}$	(Kaur and Anastasio, 2018)	$6.2 (\pm 0.2) \times 10^{-4}$	(Ma et al., 2022)

**Table S4.5.** Syringol loss kinetics and resulting triplet excited state concentrations

Sample ID	$k'_{\text{SYR}}^{\text{a}}$ ( $10^{-2}$ min $^{-1}$ )	$f_{\text{SYR,OH}}^{\text{b}}$	$f_{\text{SYR,1O2}^*}^{\text{c}}$	$f_{\text{SYR,3C}^*}^{\text{d}}$	$[\text{}^3\text{C}^*]_{\text{SYR,uncorr}}^{\text{e}}$ ( $10^{-14}$ M)	$[\text{}^3\text{C}^*]_{\text{SYR}}^{\text{f}}$ ( $10^{-14}$ M)	$k'_{\text{3C}^*,\text{SYR}}^{\text{g}}$ ( $10^6$ s $^{-1}$ )	$P_{\text{3C}^*,\text{SYR}}^{\text{h}}$ ( $10^{-7}$ M s $^{-1}$ )	$10^2 \times \Phi_{\text{3C}^*,\text{SYR}}^{\text{i}}$
WIN-10	0.63 ( $\pm 0.03$ )	0.23 ( $\pm 0.06$ )	0.07 ( $\pm 0.02$ )	0.70 ( $\pm 0.07$ )	1.9 ( $\pm 0.4$ )	4.8 ( $\pm 1.0$ )	0.85	0.40 ( $\pm 0.09$ )	2.8 ( $\pm 0.6$ )
WIN-2	1.9 ( $\pm 0.1$ )	0.35 ( $\pm 0.08$ )	0.13 ( $\pm 0.03$ )	0.52 ( $\pm 0.09$ )	4.2 ( $\pm 1.0$ )	15 ( $\pm 4$ )	1.1	1.6 ( $\pm 0.5$ )	2.1 ( $\pm 0.6$ )
WIN-0.7	3.7 ( $\pm 0.2$ )	0.24 ( $\pm 0.05$ )	0.14 ( $\pm 0.04$ )	0.62 ( $\pm 0.09$ )	9.8 ( $\pm 2.3$ )	50 ( $\pm 16$ )	1.4	7.2 ( $\pm 2.4$ )	3.7 ( $\pm 1.2$ )
WIN-0.4	4.6 ( $\pm 0.2$ )	0.18 ( $\pm 0.04$ )	0.20 ( $\pm 0.06$ )	0.62 ( $\pm 0.08$ )	12 ( $\pm 3$ )	71 ( $\pm 22$ )	2.1	15 ( $\pm 5$ )	4.4 ( $\pm 1.3$ )
WIN-0.3	3.9 ( $\pm 0.2$ )	0.15 ( $\pm 0.03$ )	0.45 ( $\pm 0.10$ )	0.40 ( $\pm 0.11$ )	6.7 ( $\pm 2.3$ )	50 ( $\pm 20$ )	2.9	15 ( $\pm 6$ )	2.6 ( $\pm 1.0$ )
WIN-0.3D	1.7 ( $\pm 0.1$ )	0.28 ( $\pm 0.06$ )	0.12 ( $\pm 0.03$ )	0.60 ( $\pm 0.09$ )	4.5 ( $\pm 1.0$ )	16 ( $\pm 5$ )	1.1	1.8 ( $\pm 0.5$ )	2.2 ( $\pm 0.6$ )
SUM-10	2.2 ( $\pm 0.1$ )	0.02 ( $\pm 0.01$ )	0.03 ( $\pm 0.01$ )	0.95 ( $\pm 0.03$ )	8.9 ( $\pm 1.6$ )	16 ( $\pm 3$ )	0.94	1.5 ( $\pm 0.3$ )	3.8 ( $\pm 0.7$ )
SUM-2	4.5 ( $\pm 0.1$ )	0.03 ( $\pm 0.01$ )	0.10 ( $\pm 0.02$ )	0.87 ( $\pm 0.03$ )	17 ( $\pm 3$ )	32 ( $\pm 7$ )	1.5	4.8 ( $\pm 1.1$ )	2.4 ( $\pm 0.5$ )
SUM-0.7	8.7 ( $\pm 0.3$ )	0.06 ( $\pm 0.01$ )	0.13 ( $\pm 0.03$ )	0.81 ( $\pm 0.04$ )	31 ( $\pm 6$ )	68 ( $\pm 18$ )	2.8	19 ( $\pm 5$ )	3.7 ( $\pm 1.0$ )
SUM-0.4	7.9 ( $\pm 0.1$ )	0.11 ( $\pm 0.02$ )	0.21 ( $\pm 0.04$ )	0.68 ( $\pm 0.05$ )	23 ( $\pm 5$ )	68 ( $\pm 18$ )	4.5	31 ( $\pm 8$ )	3.2 ( $\pm 0.9$ )
SUM-0.3	7.3 ( $\pm 0.1$ )	0.13 ( $\pm 0.03$ )	0.25 ( $\pm 0.09$ )	0.62 ( $\pm 0.10$ )	20 ( $\pm 6$ )	65 ( $\pm 20$ )	5.6	36 ( $\pm 11$ )	2.8 ( $\pm 0.9$ )
PME-NR	10.7 ( $\pm 0.3$ )	0.05 ( $\pm 0.01$ )	0.06 ( $\pm 0.01$ )	0.89 ( $\pm 0.03$ )	41 ( $\pm 8$ )	54 ( $\pm 28$ )	2.0	11 ( $\pm 6$ )	5.0 ( $\pm 2.6$ )
PME-R	11.2 ( $\pm 0.4$ )	0.05 ( $\pm 0.01$ )	0.05 ( $\pm 0.01$ )	0.90 ( $\pm 0.04$ )	43 ( $\pm 8$ )	69 ( $\pm 15$ )	2.0	14 ( $\pm 3$ )	5.9 ( $\pm 1.3$ )
Field blanks									
FB1 <sup>j</sup>	0.031 ( $\pm 0.002$ )	2.20 ( $\pm 1.34$ )	0.11 ( $\pm 0.02$ )	-1.31 ( $\pm 1.34$ )	-0.018 ( $\pm 0.018$ )	-0.32 ( $\pm 0.33$ )			
FB2	0.008 ( $\pm 0.001$ )	0.09 ( $\pm 0.02$ )	0.05 ( $\pm 0.01$ )	0.86 ( $\pm 0.03$ )	0.30 ( $\pm 0.05$ )	0.32 ( $\pm 0.08$ )			
FB3	0.12 ( $\pm 0.01$ )	0.15 ( $\pm 0.04$ )	0.05 ( $\pm 0.01$ )	0.80 ( $\pm 0.06$ )	0.42 ( $\pm 0.08$ )	0.42 ( $\pm 0.08$ )			

<sup>a</sup> Davis winter-solstice-normalized pseudo-first-order rate constant for loss of syringol (SYR)

<sup>b</sup> Fraction of SYR loss due to hydroxyl radical, calculated as  $f_{\text{SYR,OH}} = (k_{\text{SYR+OH}} \times [\text{}^{\bullet}\text{OH}]) / k'_{\text{SYR}}$ . Hydroxyl radical concentrations are in Table S4.5.

<sup>c</sup> Fraction of SYR loss due to singlet oxygen, calculated as  $f_{\text{SYR,1O2}^*} = (k_{\text{SYR+1O2}^*} \times [^1\text{O}_2^*]) / k'_{\text{SYR}}$ . Singlet oxygen concentrations are in Table S4.8.

<sup>d</sup> Fraction of SYR loss due to triplets, calculated as  $f_{\text{SYR,3C}^*} = (1 - f_{\text{SYR,OH}} - f_{\text{SYR,1O2}^*})$ .

<sup>e</sup> Uncorrected triplet steady-state concentration calculated from syringol loss as  $k'_{\text{SYR,3C}^*} / k_{\text{SYR+3DMB}^*}$ .

<sup>f</sup> Triplet concentration after correction for inhibition of SYR loss, calculated as  $[\text{}^3\text{C}^*]_{\text{SYR,uncorr}} / IF_{\text{SYR,corr}}$ .

<sup>g</sup> Apparent pseudo-first-order rate constant for quenching of  $^3\text{C}^*$  due to natural organic sinks and dissolved oxygen, as determined by SYR. This was calculated as  $k'_{\text{3C}^*,\text{SYR}} = k_{\text{rxn+Q,3C}^*} [\text{DOC}] + k_{\text{3C}^*+\text{O}_2} [\text{O}_2]$ , where  $k_{\text{rxn+Q,3C}^*}$  is estimated from the fitting between  $[\text{}^3\text{C}^*]_{\text{SYR}}$  and DOC using equation (4.11) in the main text (see values in Table S4.9), and  $k_{\text{3C}^*+\text{O}_2} = 2.8 (\pm 0.4) \times 10^9 \text{ M}^{-1} \text{ s}^{-1}$  from Kaur et al. (2019).

<sup>h</sup> Production rate of triplets determined by SYR, calculated as  $P_{3C^*,SYR} = [^3C^*]_{SYR} \times k'_{3C^*,SYR}$ .

<sup>i</sup> Apparent quantum yield of  $^3C^*$  determined by SYR during simulated sunlight illumination, calculated as  $\Phi_{3C^*,SYR} = P_{3C^*,SYR}/R_{abs}$ .

<sup>j</sup> This field blank sample was contaminated by filling solution from a pH electrode.

**Table S4.6.** (Phenylthio)acetic acid (PTA) loss kinetics and resulting triplet excited state concentrations

Sample ID	$k'_{\text{PTA}}^{\text{a}}$ ( $10^{-2}$ $\text{min}^{-1}$ )	$f_{\text{PTA,OH}}^{\text{b}}$	$f_{\text{PTA,1O2}}^{\text{c}}$	$f_{\text{PTA,3C}}^{\text{d}}$	$[\text{}^3\text{C}^*]_{\text{PTA,unco}}^{\text{e}}$ ( $10^{-14}$ M)	$[\text{}^3\text{C}^*]_{\text{PT}}^{\text{f}}$ ( $10^{-14}$ M)	$k'_{\text{3C}^*,\text{PT}}^{\text{g}}$ ( $10^6$ s $^{-1}$ )	$P_{\text{3C}^*,\text{PT}}^{\text{h}}$ ( $10^{-7}$ M s $^{-1}$ )	$10^2 \times \Phi_{\text{3C}^*,\text{PT}}^{\text{i}}$	$[\text{}^3\text{C}^*]_{\text{PT}}^{\text{j}}$ / $[\text{}^3\text{C}^*]_{\text{SY}}^{\text{j}}$
WIN-10	0.45 ( $\pm 0.02$ )	0.17 ( $\pm 0.03$ )	0.02 ( $\pm 0.01$ )	0.81 ( $\pm 0.06$ )	2.4 ( $\pm 0.06$ )	2.4 ( $\pm 0.06$ )	0.83	0.20 ( $\pm 0.05$ )	1.4 ( $\pm 0.3$ )	0.51 ( $\pm 0.17$ )
WIN-2	2.3 ( $\pm 0.1$ )	0.15 ( $\pm 0.01$ )	0.03 ( $\pm 0.01$ )	0.82 ( $\pm 0.02$ )	13 ( $\pm 3$ )	13 ( $\pm 3$ )	1.0	1.3 ( $\pm 0.3$ )	1.6 ( $\pm 0.4$ )	0.84 ( $\pm 0.31$ )
WIN-0.7	3.8 ( $\pm 0.1$ )	0.12 ( $\pm 0.01$ )	0.03 ( $\pm 0.01$ )	0.85 ( $\pm 0.04$ )	22 ( $\pm 5$ )	22 ( $\pm 5$ )	1.3	2.8 ( $\pm 0.7$ )	1.4 ( $\pm 0.4$ )	0.43 ( $\pm 0.18$ )
WIN-0.4	6.1 ( $\pm 0.3$ )	0.07 ( $\pm 0.01$ )	0.04 ( $\pm 0.01$ )	0.89 ( $\pm 0.05$ )	36 ( $\pm 9$ )	36 ( $\pm 9$ )	1.8	6.4 ( $\pm 1.6$ )	1.9 ( $\pm 0.5$ )	0.51 ( $\pm 0.20$ )
WIN-0.3	6.6 ( $\pm 0.3$ )	0.05 ( $\pm 0.01$ )	0.06 ( $\pm 0.01$ )	0.89 ( $\pm 0.03$ )	39 ( $\pm 10$ )	39 ( $\pm 10$ )	2.4	9.3 ( $\pm 3.0$ )	1.8 ( $\pm 0.5$ )	0.78 ( $\pm 0.39$ )
WIN-0.3D	2.5 ( $\pm 0.1$ )	0.10 ( $\pm 0.01$ )	0.02 ( $\pm 0.01$ )	0.88 ( $\pm 0.02$ )	15 ( $\pm 4$ )	15 ( $\pm 4$ )	1.0	1.6 ( $\pm 0.5$ )	1.9 ( $\pm 0.6$ )	0.95 ( $\pm 0.39$ )
SUM-10	0.57 ( $\pm 0.02$ )	0.05 ( $\pm 0.01$ )	0.03 ( $\pm 0.02$ )	0.92 ( $\pm 0.04$ )	0.35 ( $\pm 0.09$ )	0.37 ( $\pm 0.10$ )	0.87	0.33 ( $\pm 0.08$ )	0.85 ( $\pm 0.21$ )	0.23 ( $\pm 0.07$ )
SUM-2	2.1 ( $\pm 0.1$ )	0.03 ( $\pm 0.01$ )	0.06 ( $\pm 0.01$ )	0.91 ( $\pm 0.03$ )	13 ( $\pm 3$ )	13 ( $\pm 4$ )	1.2	1.6 ( $\pm 0.4$ )	0.80 ( $\pm 0.22$ )	0.41 ( $\pm 0.15$ )
SUM-0.7	3.5 ( $\pm 0.1$ )	0.08 ( $\pm 0.01$ )	0.08 ( $\pm 0.01$ )	0.84 ( $\pm 0.02$ )	20 ( $\pm 5$ )	21 ( $\pm 6$ )	1.9	4.0 ( $\pm 1.1$ )	0.78 ( $\pm 0.22$ )	0.30 ( $\pm 0.12$ )
SUM-0.4	4.9 ( $\pm 0.1$ )	0.10 ( $\pm 0.01$ )	0.08 ( $\pm 0.01$ )	0.82 ( $\pm 0.03$ )	27 ( $\pm 7$ )	27 ( $\pm 8$ )	2.9	7.9 ( $\pm 2.2$ )	0.81 ( $\pm 0.23$ )	0.40 ( $\pm 0.16$ )
SUM-0.3	5.2 ( $\pm 0.2$ )	0.09 ( $\pm 0.01$ )	0.09 ( $\pm 0.03$ )	0.82 ( $\pm 0.03$ )	29 ( $\pm 7$ )	29 ( $\pm 8$ )	3.5	10 ( $\pm 3$ )	0.78 ( $\pm 0.22$ )	0.44 ( $\pm 0.19$ )
PME-NR	4.4 ( $\pm 0.1$ )	0.06 ( $\pm 0.01$ )	0.03 ( $\pm 0.01$ )	0.91 ( $\pm 0.03$ )	27 ( $\pm 7$ )	28 ( $\pm 16$ )	2.1	5.8 ( $\pm 3.2$ )	2.6 ( $\pm 1.5$ )	0.52 ( $\pm 0.40$ )
PME-R	4.8 ( $\pm 0.1$ )	0.06 ( $\pm 0.01$ )	0.03 ( $\pm 0.01$ )	0.91 ( $\pm 0.02$ )	29 ( $\pm 7$ )	41 ( $\pm 10$ )	2.0	8.4 ( $\pm 2.1$ )	3.6 ( $\pm 0.1$ )	0.60 ( $\pm 0.20$ )
Field blanks										
FB1 <sup>k</sup>	2.75 ( $\pm 0.04$ )	0.01 ( $\pm 0.01$ )	0.00 ( $\pm 0.01$ )	0.99 ( $\pm 0.14$ )	18.1 ( $\pm 5.0$ )	20.1 ( $\pm 7.0$ )				
FB2	0.016 ( $\pm 0.005$ )	0.22 ( $\pm 0.03$ )	0.07 ( $\pm 0.01$ )	0.71 ( $\pm 0.32$ )	0.078 ( $\pm 0.040$ )	0.084 ( $\pm 0.043$ )				
FB3	0.030 ( $\pm 0.012$ )	0.31 ( $\pm 0.04$ )	0.05 ( $\pm 0.01$ )	0.64 ( $\pm 0.38$ )	0.13 ( $\pm 0.08$ )	0.13 ( $\pm 0.08$ )				

- <sup>a</sup> Davis winter-solstice-normalized value of the measured pseudo-first-order rate constant for loss of PTA after correction for PTA direct photodegradation. PTA direct photodegradation accounted for (0.9-12) % of PTA total decay in PME samples, with an average of 3%. It accounted for (2-79) % of PTA total decay in field blanks.
- <sup>b</sup> Contribution of hydroxyl radical to the loss of PTA, calculated as  $f_{\text{PTA,OH}} = (k_{\text{PTA+OH}} \times [\bullet\text{OH}])/k'_{\text{PTA}}$ . Hydroxyl radical concentrations are in Table S4.5.
- <sup>c</sup> Contribution of singlet oxygen to the loss of PTA, calculated as  $f_{\text{PTA,1O}_2^*} = (k_{\text{PTA+1O}_2^*} \times [^1\text{O}_2^*])/k'_{\text{PTA}}$ . Singlet oxygen concentration is in the Table S4.8.
- <sup>d</sup> Fraction of PTA loss due to triplets, calculated as  $f_{\text{PTA,3C}^*} = (1 - f_{\text{PTA,OH}} - f_{\text{PTA,1O}_2^*})$ .
- <sup>e</sup> Uncorrected triplet steady-state concentration calculated from PTA loss as  $k'_{\text{PTA,3C}^*}/k_{\text{PTA+3DMB}^*}$ .
- <sup>f</sup> Triplet concentration after correction for inhibition of PTA loss, calculated as  $[^3\text{C}^*]_{\text{PTA,uncorr}}/IF_{\text{PTA,corr}}$ .
- <sup>g</sup> Apparent pseudo-first-order rate constant for quenching of  $^3\text{C}^*$  determined by PTA due to natural organic sinks and dissolved oxygen. This was calculated as  $k'_{^3\text{C}^*,\text{PTA}} = k_{\text{rxn+Q},^3\text{C}^*}[\text{DOC}] + k_{^3\text{C}^*+\text{O}_2}$ , where  $k_{\text{rxn+Q},^3\text{C}^*}$  is estimated from the fitting between  $[^3\text{C}^*]_{\text{PTA}}$  and DOC using equation (4.10) in the main text (values are in Table S4.9), and  $k_{^3\text{C}^*+\text{O}_2} = 2.8 (\pm 0.4) \times 10^9 \text{ M}^{-1} \text{ s}^{-1}$  from Kaur et al. (2019).
- <sup>h</sup> Production rate of triplet determined by PTA, calculated as  $P_{^3\text{C}^*,\text{PTA}} = [^3\text{C}^*]_{\text{PTA}} \times k'_{^3\text{C}^*,\text{PTA}}$ .
- <sup>i</sup> Apparent quantum yield of  $^3\text{C}^*$  determined by PTA during simulated sunlight illumination, calculated as  $\Phi_{^3\text{C}^*,\text{PTA}} = P_{^3\text{C}^*,\text{PTA}}/R_{\text{abs}}$ .
- <sup>j</sup> Ratio of triplet concentration determined by PTA to that determined by SYR.
- <sup>k</sup> This field blank sample was contaminated by a pH electrode, leading to fast decay of PTA.

#### Section S4.1. Inhibition factor determination and $^3\text{C}^*$ concentration correction

The dissolved organic matter in PME may inhibit the decay of SYR or PTA by triplets, leading to an underestimation of triplet concentration. Based on our previous research, SYR is more strongly inhibited than PTA (Ma et al., 2022). To investigate and quantify the inhibition effect of PME on these two triplet probes, we measured inhibition factors (*IF*s) of FFA, SYR, and PTA for the -10, -0.7 and -0.3 extracts of the WIN and SUM composites, and used the *IF* values to correct measured  $^3\text{C}^*$  concentrations in PME. Details of inhibition factors are described in Canonica et al. (2008), Wenk et al. (2011), and Ma et al. (2022). To measure *IF*, we monitored the loss of 10  $\mu\text{M}$  probe in three illuminated solutions: (1) PME; (2) Milli-Q water at pH 4.2 with 80  $\mu\text{M}$  of the triplet precursor 3,4-dimethoxybenzaldehyde (DMB); (3) PME with 80  $\mu\text{M}$  DMB. During each illumination we determined the first-order rate constant of probe decay. The inhibition factor for the probe was calculated using

$$IF_P = \frac{k'_{\text{DMB,PME}} - k'_{\text{PME}}}{k'_{\text{DMB}}} \quad (\text{S4.1})$$

where  $k'_{DMB,PME}$  is the first-order decay rate constant of probe in solution containing both DMB and PME, while  $k'_{PME}$  and  $k'_{DMB}$  are the probe loss rate constants in PME alone and in Milli-Q water with DMB, respectively. All  $k'$  values were corrected for internal light screening with screening factors ( $S_i$ ). An  $IF$  value of 1 indicates there is no DOM inhibition on probe decay, while  $IF = 0$  indicates complete inhibition of probe decay. Since  $IF_P$  can also be affected by the suppression of  $^3DMB^*$  concentration by DOM, we use  $IF_{FFA}$  to quantify this triplet suppression. To exclude the effect of triplet suppression on  $IF_{SYR}$  and  $IF_{PTA}$  (i.e., to quantify only inhibition due to probe regeneration), we use  $IF_{SYR,corr}$  and  $IF_{PTA,corr}$ :

$$IF_{P,corr} = \frac{IF_P}{IF_{FFA}} \quad (S4.2)$$

Theoretically,  $IF$  should not exceed 1, but we sometimes see this result. For cases when  $IF_{FFA}$  or  $IF_P$  is greater than 1, this suggests there is no suppression of the  $^3DMB^*$  concentration by DOM. Therefore, there is no need to correct  $IF_P$  in this case and we assume  $IF_{P,corr} = IF_P$ . Also,  $IF_P > 1$  indicates no inhibition effect, so we do not correct the  $^3C^*$  concentration in this case.  $IF_{PTA}$  and  $IF_{SYR}$  values are expected to be lower than  $IF_{FFA}$  because the probes are affected by both triplet suppression and probe inhibition, while  $IF_{FFA}$  is only impacted by triplet suppression. However, in some samples  $IF_{PTA}$  was greater than  $IF_{FFA}$ ; we suspect this might be due to the sometimes large errors in  $IF_{FFA}$  measurement, i.e., when the difference between  $k'_{DMB,PME}$  and  $k'_{PME}$  is small. In this case, we assume  $IF_{FFA} = IF_{PTA}$  and use this value to calculate  $IF_{P,corr}$ . The determined  $IF$  and  $IF_{P,corr}$  values are shown in Table S4.4. Due to limited PME volumes, we did not measure  $IF$  values for the -2 and -0.4 extracts. Instead, their  $IF_{SYR,corr}$  and  $IF_{PTA,corr}$  values were estimated from the linear regression of  $1/IF_{P,corr}$  from the -10, -0.7, and -0.3 extracts versus DOC (Ma et al., 2022; Wenk et al., 2011).

The uncorrected  $^3C^*$  concentration is calculated with:

$$[^3C^*]_{P,uncorr} = \frac{k'_{P,3C^*}}{k_{P+3DMB^*}} \quad (S4.3)$$

where  $k'_{P,{}^3C^*}$  is measured first-order rate constant of probe loss due to triplets and  $k_{P+{}^3DMB^*}$  is the second-order rate constant of probe reacting with  ${}^3DMB^*$ . To correct for the probe inhibition effect,  $[{}^3C^*]$  is calculated using

$$[{}^3C^*]_P = \frac{[{}^3C^*]_{P,uncorr}}{IF_{P,corr}} \quad (S4.4)$$

The  ${}^3C^*$  concentrations shown in the main text are the values after  $IF$  correction.



**Table S4.7.** Inhibition factors for FFA, SYR, and PTA

Sample ID	$IF_{\text{FFA}}$	$IF_{\text{SYR}}$	$IF_{\text{PTA}}$	$IF_{\text{SYR,corr}}$	$IF_{\text{PTA,corr}}$
WIN-10	0.91 ( $\pm 0.06$ )	0.40 ( $\pm 0.02$ )	1.00 ( $\pm 0.04$ )	0.41 ( $\pm 0.03$ )	1.00 ( $\pm 0.06$ )
WIN-2 <sup>a</sup>				0.28 ( $\pm 0.04$ )	1.00 ( $\pm 0.09$ )
WIN-0.7	0.62 ( $\pm 0.10$ )	0.18 ( $\pm 0.03$ )	0.90 ( $\pm 0.07$ )	0.20 ( $\pm 0.04$ )	1.00 ( $\pm 0.11$ )
WIN-0.4 <sup>a</sup>				0.17 ( $\pm 0.04$ )	1.00 ( $\pm 0.16$ )
WIN-0.3	0.28 ( $\pm 0.08$ )	0.09 ( $\pm 0.01$ )	0.67 ( $\pm 0.10$ )	0.13 ( $\pm 0.03$ )	1.00 ( $\pm 0.21$ )
WIN-0.3D <sup>b</sup>	0.89 ( $\pm 0.13$ )	0.25 ( $\pm 0.02$ )	0.85 ( $\pm 0.06$ )	0.28 ( $\pm 0.05$ )	0.97 ( $\pm 0.17$ )
SUM-10	1.08 ( $\pm 0.09$ )	0.56 ( $\pm 0.02$ )	0.95 ( $\pm 0.08$ )	0.56 ( $\pm 0.02$ )	0.94 ( $\pm 0.07$ )
SUM-2 <sup>a</sup>				0.53 ( $\pm 0.07$ )	0.95 ( $\pm 0.12$ )
SUM-0.7	0.48 ( $\pm 0.06$ )	0.22 ( $\pm 0.03$ )	0.46 ( $\pm 0.04$ )	0.45 ( $\pm 0.09$ )	0.96 ( $\pm 0.14$ )
SUM-0.4 <sup>a</sup>				0.35 ( $\pm 0.06$ )	0.98 ( $\pm 0.14$ )
SUM-0.3	0.19 ( $\pm 0.12$ )	0.10 ( $\pm 0.02$ )	0.32 ( $\pm 0.03$ )	0.30 ( $\pm 0.06$ )	1.00 ( $\pm 0.14$ )
PME-NR <sup>c</sup>	0.68 ( $\pm 0.32$ )	0.52 ( $\pm 0.05$ )	0.65 ( $\pm 0.04$ )	0.77 ( $\pm 0.37$ )	0.95 ( $\pm 0.48$ )
PME-R <sup>c</sup>	1.29 ( $\pm 0.22$ )	0.63 ( $\pm 0.07$ )	0.71 ( $\pm 0.05$ )	0.63 ( $\pm 0.07$ )	0.71 ( $\pm 0.05$ )
Field blanks					
FB1	0.95 ( $\pm 0.12$ )	0.52 ( $\pm 0.05$ )	0.86 ( $\pm 0.13$ )	0.54 ( $\pm 0.08$ )	0.90 ( $\pm 0.19$ )
FB2	1.10 ( $\pm 0.05$ )	0.95 ( $\pm 0.19$ )	0.93 ( $\pm 0.06$ )	0.95 ( $\pm 0.19$ )	0.93 ( $\pm 0.06$ )
FB3	1.21 ( $\pm 0.06$ )	1.20 ( $\pm 0.08$ )	1.15 ( $\pm 0.09$ )	1.20 ( $\pm 0.08$ )	1.15 ( $\pm 0.09$ )

<sup>a</sup>  $IF$  values in these samples were not measured.  $IF_{\text{SYR,corr}}$  and  $IF_{\text{PTA,corr}}$  for these samples were estimated from the linear regression of  $1/IF_{\text{P,corr}}$  vs. DOC in each dilution series.

<sup>b</sup> The  $IF$  values were measured for WIN-0.3D, which had an equivalent dilution to the WIN-2 sample.

<sup>c</sup>  $IF_{\text{FFA}}$  values for PME-NR and PME-R have large uncertainties because there were very small differences between  $k'_{\text{PME,DMB}}$  and  $k'_{\text{PME}}$  for a given extract. In this case a small difference in  $k'_{\text{PME,DMB}}$  can lead to significant change of  $IF_{\text{FFA}}$ , likely explaining the very different values of  $IF_{\text{FFA}}$  in PME-R and PME-NR.

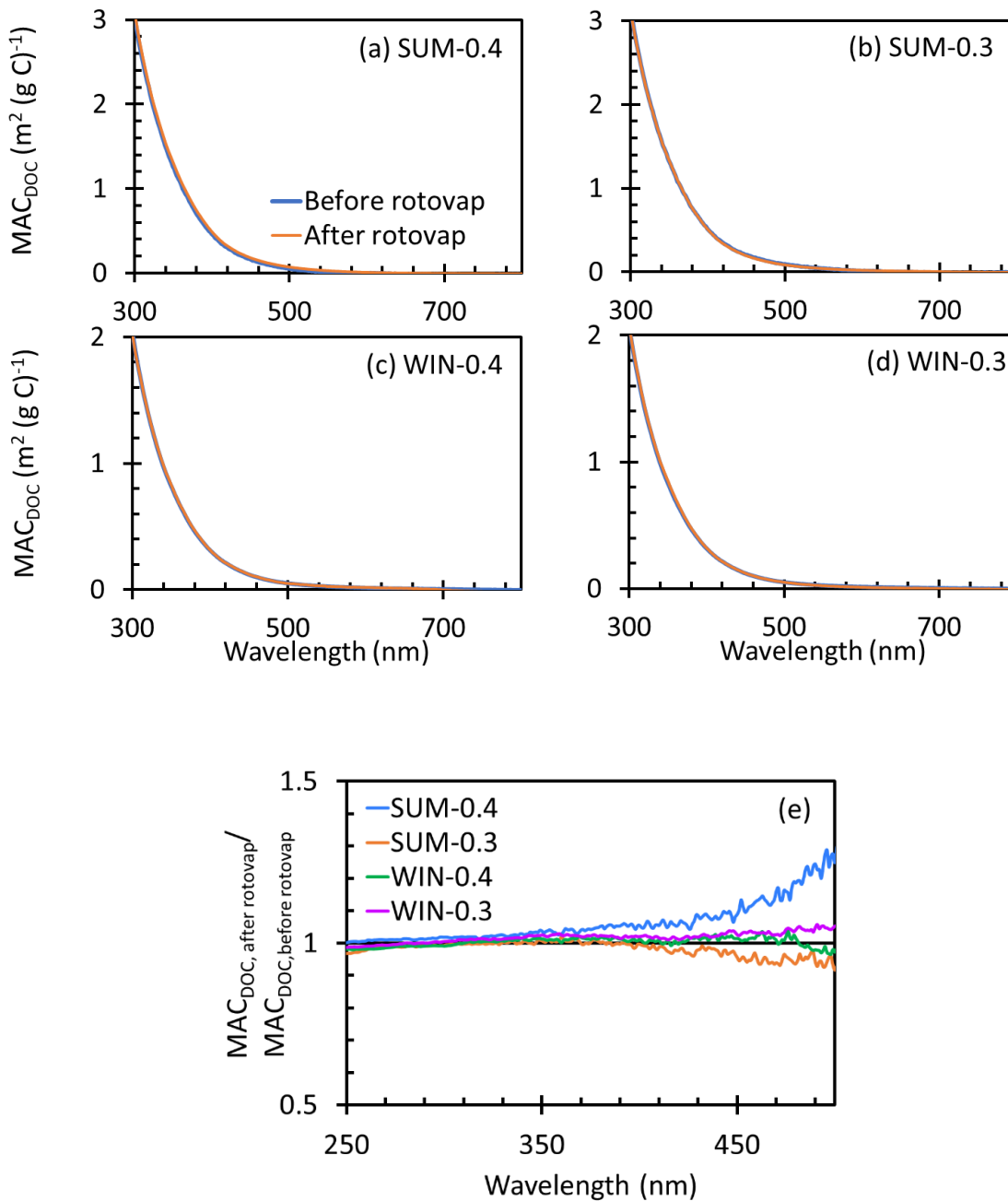


**Figure S4.1.** Mass absorption coefficients in particle extracts normalized by dissolved organic carbon before (blue) and after (orange) rotary evaporation for (a) SUM-0.4, (b) SUM-0.3, (c) WIN-0.4, and (d) WIN-0.3. (e) The ratio of  $MAC_{DOC,300nm}$  after and before rotary evaporation for the four extracts.

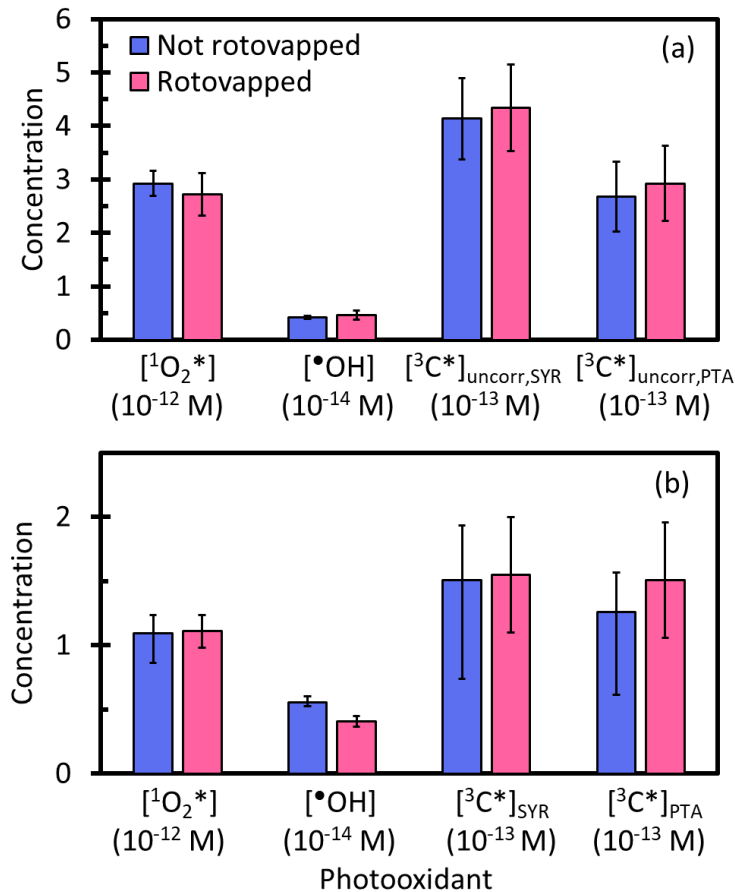


**Figure S4.2.** Influence of roto-vapping on steady-state concentrations of  $^1\text{O}_2^*$ ,  $^{\bullet}\text{OH}$ , and  $^3\text{C}^*$  in not rotovapped (blue) and rotovapped (red) particle extracts of (a) PME-NR vs. PME-R and (b) WIN-2 vs. WIN-0.3D. In each case, the rotovapped sample was concentrated to the concentration factor (i.e., PM mass/water mass ratio) of the not rotovapped sample. Error bars represents  $\pm 1$  standard error propagated from uncertainties in the kinetic regression and rate constants. In (a) we show  $^3\text{C}^*$  concentrations that are not *IF*-corrected because  $IF_{\text{FFA}}$  values for PME-NR and PME-R differ by a factor of nearly two but have large uncertainties (Table S4.7).

**Table S4.8.** Singlet oxygen measurements

Sample ID	$[^1\text{O}_2^*]^a$ ( $10^{-12}$ M)	$P_{1\text{O}_2^*}^b$ ( $10^{-7}$ M s $^{-1}$ )	$f_{\text{FFA},1\text{O}_2^*}^c$	$f_{\text{FFA},\text{OH}}^d$	$10^2 \times \Phi_{1\text{O}_2^*}^e$	$\Phi_{3\text{C}^*,\text{SYR}}/(\Phi_{1\text{O}_2^*}/f_{\Delta})^f$	$\Phi_{3\text{C}^*,\text{PTA}}/(\Phi_{1\text{O}_2^*}/f_{\Delta})^g$	$[^3\text{C}^*]_{\text{SYR}}/[^1\text{O}_2^*]^h$	$[^3\text{C}^*]_{\text{PTA}}/[^1\text{O}_2^*]^i$
WIN-10	0.21 ( $\pm 0.04$ )	0.45 ( $\pm 0.08$ )	0.53 ( $\pm 0.10$ )	0.87 ( $\pm 0.14$ )	3.1 ( $\pm 0.5$ )	0.47 ( $\pm 0.13$ )	0.24 ( $\pm 0.07$ )	0.23 ( $\pm 0.07$ )	0.12 ( $\pm 0.04$ )
WIN-2	1.1 ( $\pm 0.1$ )	2.4 ( $\pm 0.3$ )	0.62 ( $\pm 0.09$ )	0.45 ( $\pm 0.03$ )	3.1 ( $\pm 0.4$ )	0.36 ( $\pm 0.11$ )	0.28 ( $\pm 0.08$ )	0.14 ( $\pm 0.04$ )	0.12 ( $\pm 0.03$ )
WIN-0.7	2.3 ( $\pm 0.4$ )	5.0 ( $\pm 0.9$ )	0.65 ( $\pm 0.12$ )	0.61 ( $\pm 0.02$ )	2.6 ( $\pm 0.4$ )	0.76 ( $\pm 0.27$ )	0.29 ( $\pm 0.09$ )	0.22 ( $\pm 0.08$ )	0.10 ( $\pm 0.03$ )
WIN-0.4	4.3 ( $\pm 0.8$ )	9.4 ( $\pm 1.9$ )	0.69 ( $\pm 0.14$ )	0.31 ( $\pm 0.03$ )	2.8 ( $\pm 0.5$ )	0.84 ( $\pm 0.30$ )	0.36 ( $\pm 0.11$ )	0.17 ( $\pm 0.06$ )	0.09 ( $\pm 0.03$ )
WIN-0.3	8.2 ( $\pm 0.8$ )	18 ( $\pm 2$ )	0.83 ( $\pm 0.09$ )	0.14 ( $\pm 0.01$ )	3.2 ( $\pm 0.3$ )	0.43 ( $\pm 0.17$ )	0.27 ( $\pm 0.09$ )	0.06 ( $\pm 0.02$ )	0.05 ( $\pm 0.02$ )
WIN-0.3D	0.98 ( $\pm 0.13$ )	2.2 ( $\pm 0.3$ )	0.62 ( $\pm 0.08$ )	0.64 ( $\pm 0.07$ )	2.7 ( $\pm 0.3$ )	0.43 ( $\pm 0.14$ )	0.38 ( $\pm 0.12$ )	0.16 ( $\pm 0.05$ )	0.15 ( $\pm 0.05$ )
SUM-10	0.33 ( $\pm 0.19$ )	0.72 ( $\pm 0.04$ )	0.54 ( $\pm 0.32$ )	0.20 ( $\pm 0.02$ )	1.9 ( $\pm 1.1$ )	1.10 ( $\pm 0.67$ )	0.24 ( $\pm 0.15$ )	0.48 ( $\pm 0.30$ )	0.11 ( $\pm 0.07$ )
SUM-2	2.2 ( $\pm 0.2$ )	4.9 ( $\pm 0.4$ )	0.94 ( $\pm 0.10$ )	0.12 ( $\pm 0.01$ )	2.5 ( $\pm 0.2$ )	0.52 ( $\pm 0.13$ )	0.17 ( $\pm 0.05$ )	0.15 ( $\pm 0.04$ )	0.06 ( $\pm 0.02$ )
SUM-0.7	5.3 ( $\pm 0.4$ )	12 ( $\pm 1$ )	1.03 ( $\pm 0.10$ )	0.24 ( $\pm 0.03$ )	2.3 ( $\pm 0.2$ )	0.86 ( $\pm 0.24$ )	0.18 ( $\pm 0.05$ )	0.13 ( $\pm 0.04$ )	0.04 ( $\pm 0.01$ )
SUM-0.4	7.7 ( $\pm 0.6$ )	17 ( $\pm 1$ )	0.91 ( $\pm 0.09$ )	0.24 ( $\pm 0.01$ )	1.8 ( $\pm 0.1$ )	0.96 ( $\pm 0.27$ )	0.25 ( $\pm 0.07$ )	0.09 ( $\pm 0.02$ )	0.04 ( $\pm 0.01$ )
SUM-0.3	8.5 ( $\pm 2.7$ )	19 ( $\pm 6$ )	0.79 ( $\pm 0.25$ )	0.20 ( $\pm 0.02$ )	1.5 ( $\pm 0.5$ )	1.02 ( $\pm 0.45$ )	0.28 ( $\pm 0.12$ )	0.08 ( $\pm 0.03$ )	0.03 ( $\pm 0.01$ )
PME-NR	2.9 ( $\pm 0.2$ )	6.4 ( $\pm 0.5$ )	0.62 ( $\pm 0.06$ )	0.25 ( $\pm 0.02$ )	2.9 ( $\pm 0.2$ )	0.90 ( $\pm 0.47$ )	0.48 ( $\pm 0.27$ )	0.18 ( $\pm 0.10$ )	0.10 ( $\pm 0.05$ )
PME-R	2.7 ( $\pm 0.4$ )	6.0 ( $\pm 0.9$ )	0.59 ( $\pm 0.09$ )	0.28 ( $\pm 0.05$ )	2.6 ( $\pm 0.4$ )	1.22 ( $\pm 0.32$ )	0.75 ( $\pm 0.22$ )	0.25 ( $\pm 0.07$ )	0.15 ( $\pm 0.04$ )
Averages									
WIN					2.9 ( $\pm 0.3$ )	0.55 ( $\pm 0.20$ )	0.22 ( $\pm 0.05$ )	0.16 ( $\pm 0.06$ )	0.10 ( $\pm 0.04$ )
SUM					2.0 ( $\pm 0.4$ )	0.89 ( $\pm 0.23$ )	0.30 ( $\pm 0.06$ )	0.18 ( $\pm 0.17$ )	0.06 ( $\pm 0.03$ )
Field blanks									
FB1 <sup>j</sup>	0.016 ( $\pm 0.001$ )		0.81 ( $\pm 0.15$ )	8.3 ( $\pm 4.8$ )					
FB2	0.021 ( $\pm 0.001$ )		0.66 ( $\pm 0.33$ )	0.54 ( $\pm 0.07$ )					
FB3	0.028 ( $\pm 0.001$ )		0.97 ( $\pm 0.17$ )	0.73 ( $\pm 0.09$ )					

<sup>a</sup> Davis winter solstice sunlight-normalized steady-state concentration of  $^1\text{O}_2^*$ .

<sup>b</sup> Production rate of  $^1\text{O}_2^*$ , calculated as  $P_{1\text{O}_2^*} = [^1\text{O}_2^*] \times k'_{\text{H}_2\text{O}}$ , where  $k'_{\text{H}_2\text{O}}$  is the first-order rate constant for loss of  $^1\text{O}_2^*$  in  $\text{H}_2\text{O}$  ( $2.2 \times 10^5 \text{ s}^{-1}$ ) (Bilski et al., 1997).

<sup>c</sup> Fraction of probe FFA lost due to  $^1\text{O}_2^*$  in PME diluted with  $\text{H}_2\text{O}$ , calculated as  $f_{\text{FFA},1\text{O}_2^*} = ([^1\text{O}_2^*]/2 \times k_{\text{FFA}+1\text{O}_2^*})/k'_{\text{FFA},\text{H}_2\text{O}}$ , where  $k_{\text{FFA}+1\text{O}_2^*}$  is the second-order rate constant of FFA reacting with  $^1\text{O}_2^*$  and  $k'_{\text{FFA},\text{H}_2\text{O}}$  is the normalized first-order decay rate of FFA in the PME diluted with  $\text{H}_2\text{O}$ .

<sup>d</sup> Fraction of probe FFA lost due to  $\bullet\text{OH}$  in PME diluted with  $\text{H}_2\text{O}$ , calculated as  $f_{\text{FFA},\text{OH}} = ([\bullet\text{OH}] \times k_{\text{FFA}+\text{OH}})/k'_{\text{FFA},\text{H}_2\text{O}}$ , where  $k_{\text{FFA}+\text{OH}}$  is the second-order rate constant of FFA reacting with  $\bullet\text{OH}$  ( $1.5 \times 10^{10} \text{ M}^{-1} \text{ s}^{-1}$ ) (Ross and Ross, 1977), assuming the  $\bullet\text{OH}$  concentration is the same in the diluted and undiluted portions of PME.

<sup>e</sup> Apparent quantum yield of  $^1\text{O}_2^*$ , calculated as  $\Phi_{1\text{O}_2^*} = P_{1\text{O}_2^*}/R_{\text{abs}}$ .

<sup>f</sup> Fraction of oxidizing triplets (determined by SYR) in the total triplet pool (Kaur and Anastasio, 2018).  $f_{\Delta}$  is the yield of singlet oxygen from the quenching of triplet states by dissolved oxygen, which we assume is 0.53 (McNeill and Canonica, 2016).

<sup>g</sup> Fraction of oxidizing triplets determined by PTA to the total triplet pool.

<sup>h</sup> Ratio of triplet concentration determined by SYR to the singlet oxygen concentration.

<sup>i</sup> Ratio of triplet concentration determined by PTA to the singlet oxygen concentration.

<sup>j</sup> This field blank sample was contaminated by a pH electrode and other unknown sources.

**Table S4.9.** Parameters in hyperbolic fitting between photooxidant concentration and DOC using Eqn. 4.11

	WIN		SUM	
	<i>a</i>	<i>b</i> (M <sup>-1</sup> )	<i>a</i>	<i>b</i> (M <sup>-1</sup> )
<sup>1</sup> O <sub>2</sub> *	2.8 (± 0.1) × 10 <sup>-10a</sup>	6 <sup>a</sup>	4.4 (± 0.3) × 10 <sup>-10</sup>	27 (± 4)
<sup>3</sup> C* <sub>SYR</sub>	0.85 (± 0.46) × 10 <sup>-10</sup>	97 (± 86)	1.2 (± 0.4) × 10 <sup>-10</sup>	149 (± 65)
<sup>3</sup> C* <sub>PTA</sub>	0.44 (± 0.05) × 10 <sup>-10</sup>	73 (± 15)	0.31 (± 0.03) × 10 <sup>-10</sup>	84 (± 13)

<sup>a</sup> Since winter samples show no curvature for [<sup>1</sup>O<sub>2</sub>\*] with DOC, to fit data with equation 4.11, *a* was obtained as the slope of linear regression between [<sup>1</sup>O<sub>2</sub>\*] and DOC, while *b* was obtained by having the fitted line passed through the first 4 data points.

**Table S4.10.** Second-order rate constants of triplet quenching and reaction with dissolved organic carbon<sup>a</sup>

	<i>k</i> <sub>rxn+Q,3C*</sub> (L (mol C) <sup>-1</sup> s <sup>-1</sup> )		<sup>3</sup> C* probe used
	WIN	SUM	
This work	0.47 × 10 <sup>7b</sup>	2.1 (± 0.3) × 10 <sup>7</sup>	FFA
	7.6 (± 6.8) × 10 <sup>7</sup>	12 (± 5) × 10 <sup>7</sup>	SYR
	5.7 (± 1.2) × 10 <sup>7</sup>	6.6 (± 1.0) × 10 <sup>7</sup>	PTA
Kaur et al. (2019) <sup>c</sup>	9.3 (± 1.3) × 10 <sup>7</sup>		SYR
Wenk et al. (2013)	(1.3 – 3.9) × 10 <sup>7</sup>		-

<sup>a</sup> Rate constants are for DOM quenching and reaction with the pool of triplets that are seen by a given probe. FFA, by reacting with <sup>1</sup>O<sub>2</sub>\*, is likely seeing the DOM reactivity of the entire triplet pool (i.e., both oxidizing and non-oxidizing triplets), SYR is probing the reactivity of both strongly and weakly oxidizing triplets, while PTA is probing only the strongly oxidizing triplets.

<sup>b</sup> This value was calculated using the *b* value (Table S4.8) that was estimated by having the fitted line with equation 4.11 between [<sup>1</sup>O<sub>2</sub>\*] and DOC passed through the first 4 data points.

<sup>c</sup> Value is uncertain because triplet concentrations were not corrected for inhibition of SYR loss caused by DOM.

## Section S4.2. Kinetic model for singlet oxygen

We modified the equation for the steady-state  $^1\text{O}_2^*$  concentration from McNeill et al. (2016) by adding DOC as an additional sink for  $^1\text{O}_2^*$ :

$$[^1\text{O}_2^*] = \frac{k_{\text{O}_2+3\text{C}^*} [^3\text{C}^*] [\text{O}_2] f_{\Delta}}{k'_{\text{H}_2\text{O}} + k_{\text{rxn}+\text{Q},1\text{O}_2^*} [\text{DOC}]} \quad (\text{S4.5})$$

where  $k_{\text{O}_2+3\text{C}^*}$  is the bimolecular rate constant of  $\text{O}_2$  quenching  $^3\text{C}^*$ ,  $[^3\text{C}^*]$  is the concentration of triplets that can transfer energy to  $\text{O}_2$  (i.e., essentially all triplets),  $[\text{O}_2]$  is the dissolved oxygen concentration,  $f_{\Delta}$  is the fraction of oxygen quenching triplets that produces  $^1\text{O}_2^*$ ,  $k'_{\text{H}_2\text{O}}$  is the first-order rate constant for loss of  $^1\text{O}_2^*$  by  $\text{H}_2\text{O}$ , and  $k_{\text{rxn}+\text{Q},1\text{O}_2^*}$  is the bimolecular rate constant of DOC reacting and quenching  $^1\text{O}_2^*$ .

While DOC will be an important sink for  $^1\text{O}_2^*$  under ALW conditions (Kaur et al., 2019), in our PM extracts it appears the curvature of  $[^1\text{O}_2^*]$  with increasing DOC observed in SUM (Fig. 4.2) is only due to  $^3\text{C}^*$  since triplets are more sensitive to the presence of organics than is  $^1\text{O}_2^*$ . Therefore,  $\text{H}_2\text{O}$  is the dominant sink, and the quenching of  $^1\text{O}_2^*$  by DOC is negligible (i.e.  $k_{\text{rxn}+\text{Q},1\text{O}_2^*} [\text{DOC}] \ll k'_{\text{H}_2\text{O}}$ ). From Kaur et al. (2019),  $^3\text{C}^*$  in PME can be expressed as

$$[^3\text{C}^*] = \frac{\left( \frac{j_{\text{abs}} \Phi_{\text{ISC}} f}{k_{\text{O}_2+3\text{C}^*} [\text{O}_2]} \right) [\text{DOC}]}{1 + \left( \frac{k_{\text{rxn}+\text{Q},3\text{C}^*}}{k_{\text{O}_2+3\text{C}^*} [\text{O}_2]} \right) [\text{DOC}]} \quad (\text{S4.6})$$

where  $j_{\text{abs}}$  is the rate constant for light absorption,  $\Phi_{\text{ISC}}$  is the quantum yield of intersystem crossing,  $f$  is the fraction of DOC that are chromophores (mol-C in chromophores mol-C<sup>-1</sup>), and  $k_{\text{rxn}+\text{Q},3\text{C}^*}$  is the bimolecular rate constant of DOC reacting with and quenching  $^3\text{C}^*$ .

Substituting this equation for  $[^3\text{C}^*]$  into the simplified version of equation S4.5 yields

$$[{}^1O_2^*] = \frac{\frac{(\frac{j_{abs}\Phi_{ISC}f}{k_{O_2+3C^*}[O_2]})[DOC]}{1 + (\frac{k_{rxn+Q,3C}}{k_{O_2+3C^*}[O_2]})[DOC]} \times k_{O_2+3C^*}[O_2]f_{\Delta}}{k'_{H_2O}} = \frac{\frac{j_{abs}\Phi_{ISC}f \times f_{\Delta}}{k'_{H_2O}}[DOC]}{1 + (\frac{k_{rxn+Q,3C}}{k_{O_2+3C^*}[O_2]})[DOC]} \quad (S4.7)$$

This equation is of the form

$$[{}^1O_2^*] = \frac{a[DOC]}{1 + b[DOC]} \quad (S4.8)$$

where

$$a = \frac{j_{abs}\Phi_{ISC}f \times f_{\Delta}}{k'_{H_2O}} \quad (S4.9)$$

$$b = \frac{k_{rxn+Q,3C^*}}{k_{O_2+3C^*}[O_2]} \quad (S4.10)$$

Since  $[{}^1O_2^*] = P_{1O_2^*} / k'_{H_2O}$ , the production rate of singlet oxygen can be calculated by

$$P_{1O_2^*} = \frac{a[DOC]}{1 + b[DOC]} \times k'_{H_2O} \quad (S4.11)$$

Thus, in our relatively dilute extracts we calculate  $P_{1O_2^*}$  as  $[{}^1O_2^*] \times k'_{H_2O}$ , while for extrapolating to ALW conditions we use Eq. S4.11.



**Table S4.11.** Parameters used for photooxidant concentration extrapolation

Parameters		WIN	SUM
Average DOC/(PM/H <sub>2</sub> O) <sup>a</sup> (mol C L <sup>-1</sup> )/(μg PM/μg H <sub>2</sub> O)		16.5	30.7
•OH	$\Delta P_{OH,aq}/\Delta DOC$ (M s <sup>-1</sup> /(mol C L <sup>-1</sup> ) <sup>b</sup>	$1.6 \times 10^{-6}$	-
	$\Delta k'_{OH}/\Delta DOC$ (M s <sup>-1</sup> /(mol C L <sup>-1</sup> ) <sup>b</sup>	$3.0 \times 10^8$	$2.5 \times 10^8$
<sup>1</sup> O <sub>2</sub> *	$a$ <sup>c</sup>	$2.8 \times 10^{-10}$	$4.4 \times 10^{-10}$
	$b$ (M <sup>-1</sup> ) <sup>c</sup>	6	27
	$k_{DOC+^{1}O_2^*}$ (L (mol C) <sup>-1</sup> s <sup>-1</sup> ) <sup>d</sup>	$1.0 \times 10^5$	
<sup>3</sup> C* <sub>SYR</sub>	$\Delta P_{3C^*}/\Delta DOC$ (M s <sup>-1</sup> /(mol C L <sup>-1</sup> ) <sup>b</sup>	$6.2 \times 10^{-5}$	$9.2 \times 10^{-5}$
	$k_{rxn+Q,3C^*}$ (L (mol C) <sup>-1</sup> s <sup>-1</sup> )	$7.6 \times 10^7$	$12 \times 10^8$
<sup>3</sup> C* <sub>PTA</sub>	$\Delta P_{3C^*}/\Delta DOC$ (M s <sup>-1</sup> /(mol C L <sup>-1</sup> ) <sup>b</sup>	$3.4 \times 10^{-5}$	$2.4 \times 10^{-5}$
	$k_{rxn+Q,3C^*}$ (L (mol C) <sup>-1</sup> s <sup>-1</sup> )	$5.7 \times 10^7$ <sup>a</sup>	$6.6 \times 10^7$

<sup>a</sup> Average ratio of DOC to particle mass/water mass ratio.

<sup>b</sup> Slope of linear regression between production rates or sinks for photooxidant and DOC.

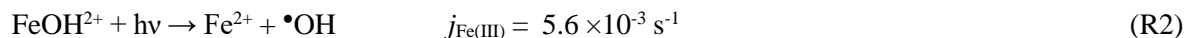
<sup>c</sup> Parameters in regression fit between [<sup>1</sup>O<sub>2</sub>\*] and DOC using Eqn. 4.11 in the main text. Production rates of <sup>1</sup>O<sub>2</sub>\* were calculated with Eqn. S4.11.

<sup>d</sup> Second order rate constant for loss of <sup>1</sup>O<sub>2</sub>\* by DOC. The value was estimated by Kaur et al. (2019).

### Section S4.3. Modeling the •OH production rate in SUM by photo-Fenton reactions

To simulate the •OH production rate as a function of particle mass/water mass ratio in SUM, we assume that photo-Fenton reactions are the dominant sources for •OH. We modeled this using two reactions (R1 and R2) and tuned the reactant concentrations to have the calculated •OH production rates match measured values.

We simplified the suite of photo-Fenton reactions that produce •OH from hydrogen peroxide (H<sub>2</sub>O<sub>2</sub>) using two reactions (Benkelberg and Warneck, 1995; Christensen et al., 1993; Mao et al., 2013):



We assume that Fe<sup>2+</sup> and FeOH<sup>2+</sup> are the dominant Fe(II) and Fe(III) hydroxide species, respectively, which is reasonable at pH 4.2 or lower (Faust and Hoigné, 1990; Morgan and Lahav, 2007). Fe(III)–carboxylate complexes can also undergo photolysis to produce •OH (Southworth and Voelker, 2003; Weller et al., 2014), but we neglect them here. The •OH production rate from these two reactions is

$$P_{\text{OH}} = k_1[\text{Fe}^{2+}][\text{H}_2\text{O}_2] + j_{\text{Fe(III)}}[\text{FeOH}^{2+}] \quad (\text{S12})$$

Next, we estimate the total dissolved iron and H<sub>2</sub>O<sub>2</sub> concentrations so that our calculated  $P_{\text{OH}}$  approximately match the measured values in SUM. To do this, we assume that: (1) The ratio of [Fe(II)]/([Fe(II)]+Fe(III)) is a constant 0.85 during daytime (i.e. during our illumination) (Deguillaume et al., 2005; Weller et al., 2014); (2) H<sub>2</sub>O<sub>2</sub> reaches a steady-state concentration during the illumination; (3) The concentrations of dissolved iron and H<sub>2</sub>O<sub>2</sub> increase proportionally with concentration factor (PM mass/water mass ratio) in our extracts. By setting dissolved iron and H<sub>2</sub>O<sub>2</sub> concentrations to 0.4 μM and 3 μM in SUM-10, respectively, the simulated  $P_{\text{OH}}$  and [•OH] fit well with the measured values across all dilutions (Figure S4.4). Meanwhile, the estimated concentrations in SUM-10 are in a reasonable range for

dilute cloud/fog water (Anastasio et al., 1994; Deguillaume et al., 2005; Faust et al., 1993). We next extrapolate this simple model to ambient PM conditions with one modification: since the aqueous  $\text{H}_2\text{O}_2$  concentration cannot increase with the particle mass/water mass ratio without limitation (because  $\text{H}_2\text{O}_{2(\text{aq})}$  can partition into the gas phase), we set an upper limit for  $\text{H}_2\text{O}_{2(\text{aq})}$  of 100  $\mu\text{M}$ , which corresponds to a typical gas-phase  $\text{H}_2\text{O}_2$  mixing ratio of 1 ppb (Tilgner et al., 2021; Vione et al., 2003) assuming Henry's law equilibrium ( $K_{\text{H}} = 10^5 \text{ M atm}^{-1}$ ) (Seinfeld and Pandis, 2008). We assume that the  $\text{H}_2\text{O}_{2(\text{aq})}$  concentration increases proportionally with PM mass/water mass ratio until it reaches 100  $\mu\text{M}$  and then is constant under more concentrated conditions. Our estimated soluble iron concentration of 0.4  $\mu\text{M}$  in SUM-10 predicts a dissolved Fe concentration under ALW conditions (1  $\mu\text{g PM}/\mu\text{g H}_2\text{O}$ ) of 9.6 mM; we assume this is all dissolved, with no precipitation. This soluble iron concentration is similar to expected iron concentrations in aqueous aerosols (Gen et al., 2020; Tilgner et al., 2021).

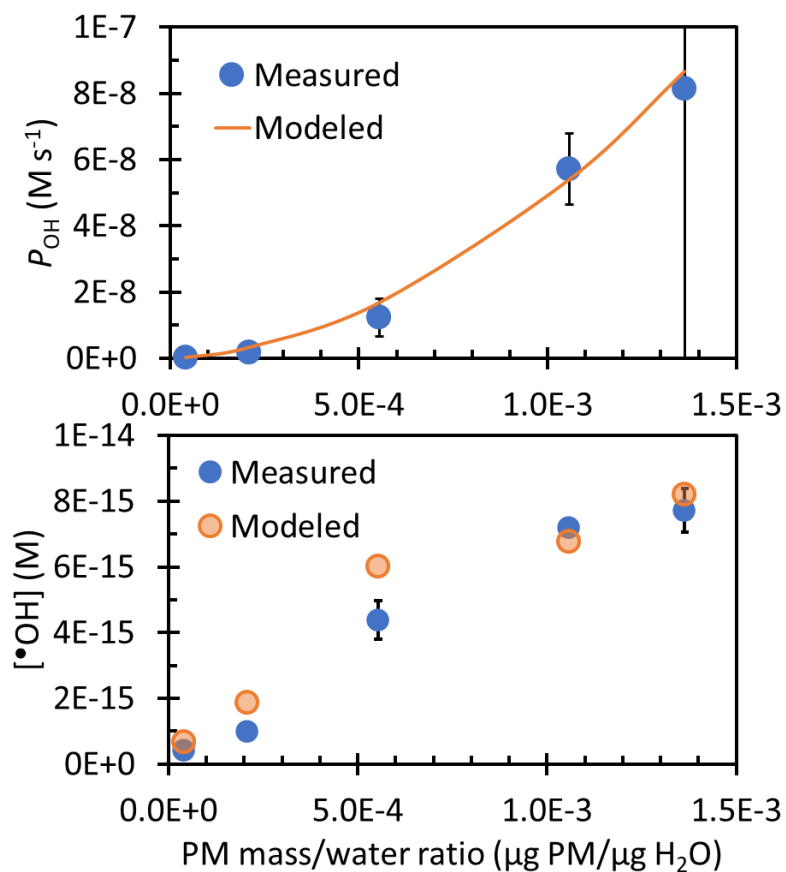


**Figure S4.3.** Comparison of measured (blue) and modeled (orange)  $•OH$  production rates (top panel) and concentrations (bottom panel) in SUM as a function of particle mass/water mass ratio. The modeled  $•OH$  concentration is calculated using the modeled production rate divided by the measured  $•OH$  sink ( $k'_{OH}$ ) at each dilution.

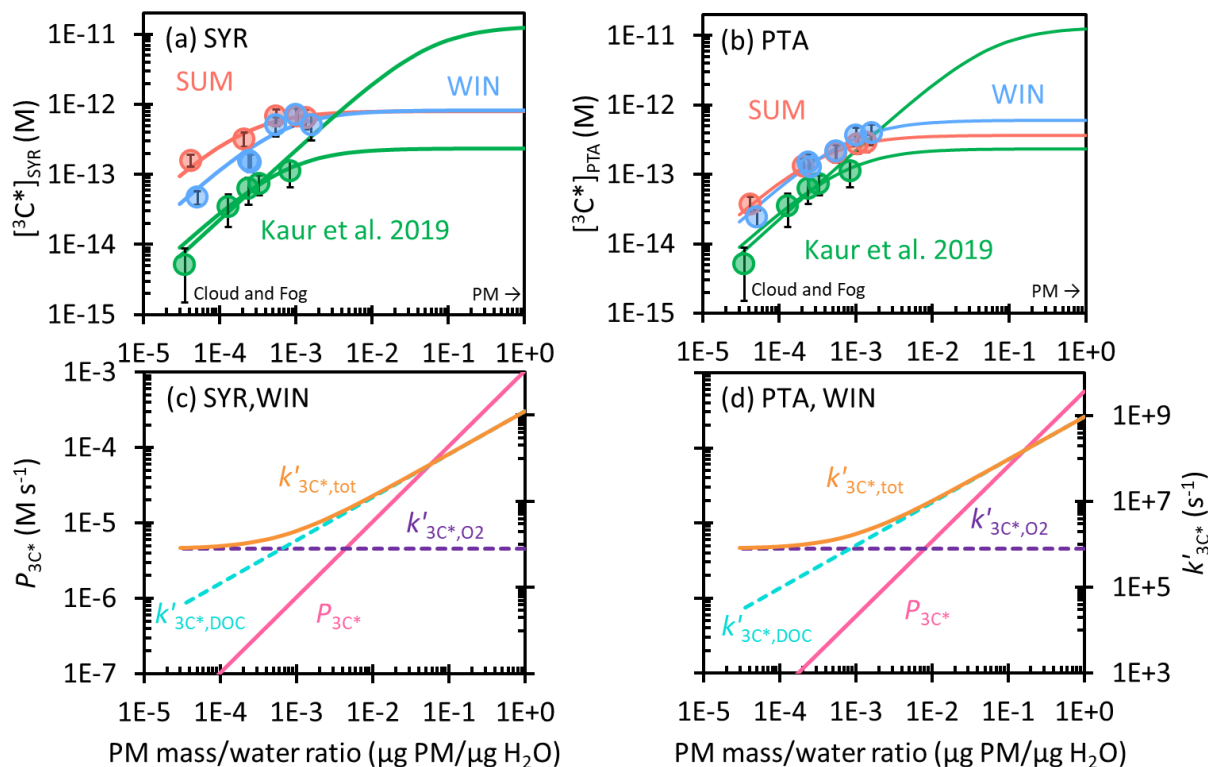


**Figure S4.4.** Top row: Triplet excited state concentrations determined by (a) SYR and (b) PTA as a function of particle mass/water mass ratio in WIN extracts (blue) and SUM (red). Solid circles are measured values in dilution experiments, while lines are extrapolations to ALW conditions. Previous measurements and extrapolations (best fit and high estimate) for Davis winter particle extracts are in green (Kaur et al., 2019). Bottom row: Dependence of triplet production rate (red line), and rate constants for  $^3\text{C}^*$  loss, including quenching by oxygen ( $k'_{3\text{C}^*,\text{O}_2}$ , purple dashed line), dissolved organic carbon ( $k'_{3\text{C}^*,\text{DOC}}$ , blue dashed line), and total sinks ( $k'_{3\text{C}^*,\text{tot}} = k'_{3\text{C}^*,\text{O}_2} + k'_{3\text{C}^*,\text{DOC}}$ , orange solid line), on particle mass/water mass ratio for the WIN sample. Panels (c) and (d) show data determined using SYR and PTA, respectively.

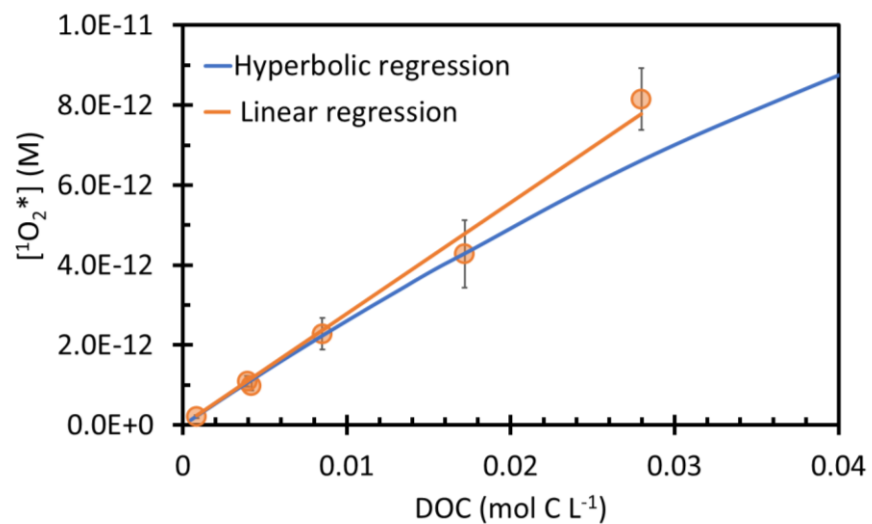


**Figure S4.5.**  $^1\text{O}_2^*$  concentration as a function of DOC in winter samples (circles). The orange line represents linear regression, while the blue line represents hyperbolic regression with equation 4.11 in the main text, with the fitted line passed through the first 4 data points.

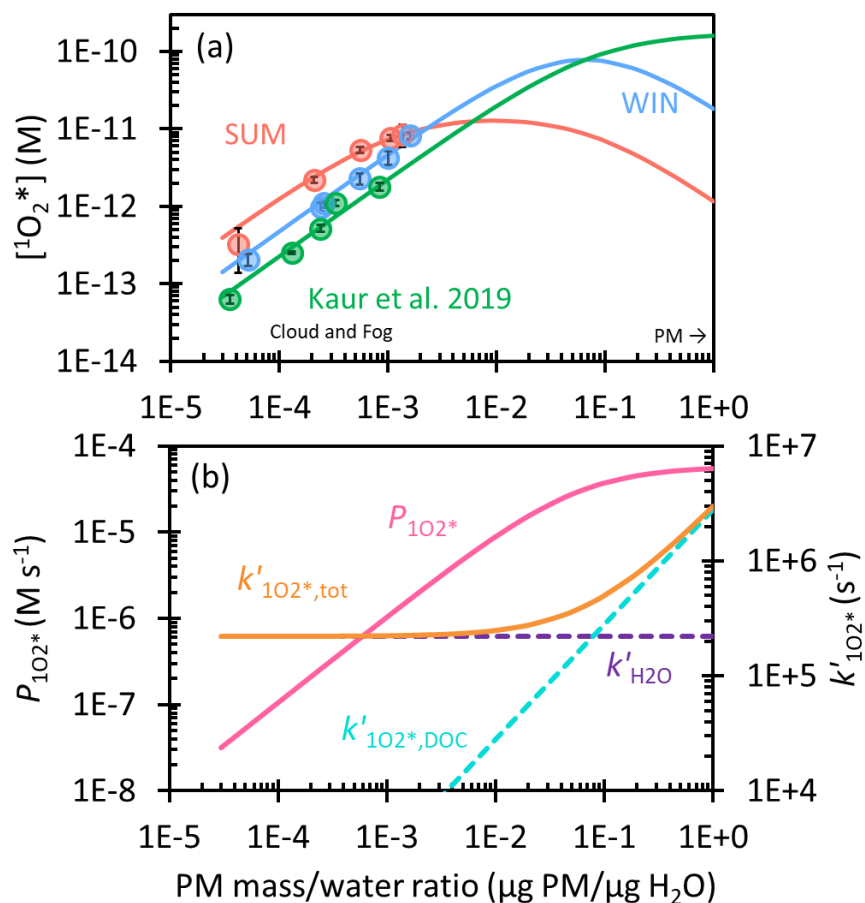


**Figure S4.6.** (a) Dependence of singlet molecular oxygen concentration on particle mass/water mass ratio in winter extracts (blue) and summer (red) samples. Solid circles are measured values in dilution experiments, while lines are extrapolations to ALW conditions. Previous measurements and extrapolation with Davis winter particle extracts are in green (Kaur et al., 2019). (b) Dependence of singlet oxygen production rate, ( $P_{102^*}$ , red line) and rate constants for  $^1\text{O}_2^*$  loss, including deactivation by water ( $k'_{\text{H}_2\text{O}}$ , purple), quenching by dissolved organic carbon ( $k'_{102^*,\text{DOC}}$ , blue), and total sinks ( $k'_{102^*,\text{tot}} = k'_{\text{H}_2\text{O}} + k'_{102^*,\text{DOC}}$ , orange), on particle mass/water mass ratio for winter samples.

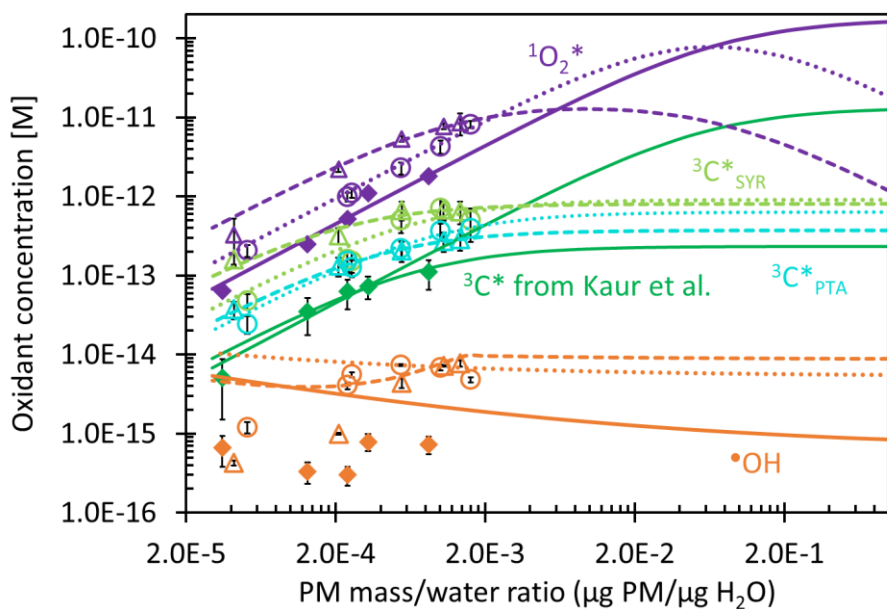


**Figure S4.7.** Dependence of photooxidant concentrations on particle mass/water mass ratio in WIN, SUM, and previous Davis winter particle extracts from Kaur et al. (2019). Symbols represent measured values under lab dilution conditions for WIN (open circles), SUM (open triangles), and Kaur et al. (filled diamonds), respectively. Lines represent extrapolations of experimental data to aerosol liquid water conditions for WIN (dotted lines), SUM (dashed lines), and Kaur et al. (solid lines) samples. The lines for  $\bullet\text{OH}$  are generally higher than the experimental measurements because the extrapolations include mass transfer of gas-phase hydroxyl radical to the drop/particle. The gas phase does not appear to be a significant source or sink of particle-phase  $^3\text{C}^*$  or  $^1\text{O}_2^*$ .



## 4.7. References

- Anastasio, C., Faust, B. C. and Allen, J. M.: Aqueous phase photochemical formation of hydrogen peroxide in authentic cloud waters, *J. Geophys. Res.*, 99(D4), 8231, doi:10.1029/94JD00085, 1994.
- Anastasio, C. and McGregor, K. G.: Chemistry of fog waters in California's Central Valley: 1. In situ photoformation of hydroxyl radical and singlet molecular oxygen, *Atmos. Environ.*, 35(6), 1079–1089, doi:10.1016/S1352-2310(00)00281-8, 2001.
- Anastasio, C. and Newberg, J. T.: Sources and sinks of hydroxyl radical in sea-salt particles, *J. Geophys. Res.*, 112(D10), doi:10.1029/2006JD008061, 2007.
- Andreae, M. O.: Soot carbon and excess fine potassium: long-range transport of combustion-derived aerosols., *Science*, 220(4602), 1148–1151, doi:10.1126/science.220.4602.1148, 1983.
- Appiani, E., Ossola, R., Latch, D. E., Erickson, P. R. and McNeill, K.: Aqueous singlet oxygen reaction kinetics of furfuryl alcohol: effect of temperature, pH, and salt content, *Environ. Sci.: Processes Impacts*, 19(4), 507–516, doi:10.1039/C6EM00646A, 2017.
- Arakaki, T., Anastasio, C., Kuroki, Y., Nakajima, H., Okada, K., Kotani, Y., Handa, D., Azechi, S., Kimura, T., Tsuhako, A. and Miyagi, Y.: A general scavenging rate constant for reaction of hydroxyl radical with organic carbon in atmospheric waters., *Environ. Sci. Technol.*, 47(15), 8196–8203, doi:10.1021/es401927b, 2013.
- Arakaki, T. and Faust, B. C.: Sources, sinks, and mechanisms of hydroxyl radical ( $\cdot\text{OH}$ ) photoproduction and consumption in authentic acidic continental cloud waters from Whiteface Mountain, New York: The role of the Fe(r) (r = II, III) photochemical cycle, *J. Geophys. Res.*, 103(D3), 3487–3504, doi:10.1029/97JD02795, 1998.
- Ashton, L., Buxton, G. V. and Stuart, C. R.: Temperature dependence of the rate of reaction of OH with some aromatic compounds in aqueous solution. Evidence for the formation of a  $\pi$ -complex intermediate?, *J. Chem. Soc., Faraday Trans.*, 91(11), 1631–1633, doi:10.1039/FT9959101631, 1995.
- Badali, K. M., Zhou, S., Aljawhary, D., Antiñolo, M., Chen, W. J., Lok, A., Mungall, E., Wong, J. P. S., Zhao, R. and Abbatt, J. P. D.: Formation of hydroxyl radicals from photolysis of secondary organic aerosol material, *Atmos. Chem. Phys.*, 15(14), 7831–7840, doi:10.5194/acp-15-7831-2015, 2015.
- Benkelberg, H.-J. and Warneck, P.: Photodecomposition of Iron(III) Hydroxo and Sulfato Complexes in Aqueous Solution: Wavelength Dependence of OH and SO<sub>4</sub><sup>-</sup> Quantum Yields, *J. Phys. Chem.*, 99(14), 5214–5221, doi:10.1021/j100014a049, 1995.
- Bilski, P., Holt, R. N. and Chignell, C. F.: Properties of singlet molecular oxygen in binary solvent mixtures of different polarity and proticity, *J. Photochem. Photobiol. A*, 109(3), 243–249, doi:10.1016/S1010-6030(97)00147-0, 1997.
- Canonica, S. and Freiburghaus, M.: Electron-rich phenols for probing the photochemical reactivity of freshwaters., *Environ. Sci. Technol.*, 35(4), 690–695, doi:10.1021/es0011360, 2001.
- Canonica, S., Hellrung, B. and Wirz, J.: Oxidation of phenols by triplet aromatic ketones in aqueous solution, *The Journal of Physical Chemistry A*, 104(6), 1226–1232, 2000.

- Canonica, S. and Laubscher, H.-U.: Inhibitory effect of dissolved organic matter on triplet-induced oxidation of aquatic contaminants, *Photochem. Photobiol. Sci.*, 7(5), 547, doi:10.1039/b719982a, 2008.
- Christensen, H., Sehested, K. and Løgager, T.: The reaction of hydrogen peroxide with Fe(II) ions at elevated temperatures, *Radiation Physics and Chemistry*, 41(3), 575–578, doi:10.1016/0969-806X(93)90022-M, 1993.
- Deguillaume, L., Leriche, M., Desboeufs, K., Mailhot, G., George, C. and Chaumerliac, N.: Transition metals in atmospheric liquid phases: sources, reactivity, and sensitive parameters., *Chem. Rev.*, 105(9), 3388–3431, doi:10.1021/cr040649c, 2005.
- Ervens, B.: Progress and problems in modeling chemical processing in cloud droplets and wet aerosol particles, in *Multiphase environmental chemistry in the atmosphere*, vol. 1299, edited by S. W. Hunt, A. Laskin, and S. A. Nizkorodov, pp. 327–345, American Chemical Society, Washington, DC., 2018.
- Ervens, B., Sorooshian, A., Lim, Y. B. and Turpin, B. J.: Key parameters controlling OH-initiated formation of secondary organic aerosol in the aqueous phase (aqSOA), *J. Geophys. Res. Atmos.*, 119(7), 3997–4016, doi:10.1002/2013JD021021, 2014.
- Ervens, B., Turpin, B. J. and Weber, R. J.: Secondary organic aerosol formation in cloud droplets and aqueous particles (aqSOA): a review of laboratory, field and model studies, *Atmos. Chem. Phys.*, 11(21), 11069–11102, doi:10.5194/acp-11-11069-2011, 2011.
- Ervens, B. and Volkamer, R.: Glyoxal processing by aerosol multiphase chemistry: towards a kinetic modeling framework of secondary organic aerosol formation in aqueous particles, *Atmos. Chem. Phys.*, 10(17), 8219–8244, 2010.
- Faust, B. C. and Allen, J. M.: Aqueous-phase photochemical sources of peroxy radicals and singlet molecular oxygen in clouds and fog, *J. Geophys. Res.*, 97(D12), 12913, doi:10.1029/92JD00843, 1992.
- Faust, B. C. and Allen, J. M.: Aqueous-phase photochemical formation of hydroxyl radical in authentic cloudwaters and fogwaters, *Environ. Sci. Technol.*, 27(6), 1221–1224, doi:10.1021/es00043a024, 1993.
- Faust, B. C., Anastasio, C., Allen, J. M. and Arakaki, T.: Aqueous-phase photochemical formation of peroxides in authentic cloud and fog waters., *Science*, 260(5104), 73–75, doi:10.1126/science.8465202, 1993.
- Faust, B. C. and Hoigné, J.: Photolysis of Fe (III)-hydroxy complexes as sources of OH radicals in clouds, fog and rain, *Atmospheric Environment. Part A. General Topics*, 24(1), 79–89, doi:10.1016/0960-1686(90)90443-Q, 1990.
- Faust, J. A., Wong, J. P. S., Lee, A. K. Y. and Abbatt, J. P. D.: Role of Aerosol Liquid Water in Secondary Organic Aerosol Formation from Volatile Organic Compounds., *Environ. Sci. Technol.*, 51(3), 1405–1413, doi:10.1021/acs.est.6b04700, 2017.
- Fleming, L. T., Lin, P., Roberts, J. M., Selimovic, V., Yokelson, R., Laskin, J., Laskin, A. and Nizkorodov, S. A.: Molecular composition and photochemical lifetimes of brown carbon chromophores in biomass burning organic aerosol, *Atmos. Chem. Phys.*, 20(2), 1105–1129, doi:10.5194/acp-20-1105-2020, 2020.
- Forrister, H., Liu, J., Scheuer, E., Dibb, J., Ziemba, L., Thornhill, K. L., Anderson, B., Diskin, G., Perring, A. E., Schwarz, J. P., Campuzano-Jost, P., Day, D. A., Palm, B. B., Jimenez, J. L., Nenes, A. and Weber,

- R. J.: Evolution of brown carbon in wildfire plumes, *Geophys. Res. Lett.*, 42(11), 4623–4630, doi:10.1002/2015GL063897, 2015.
- Galbavy, E. S., Ram, K. and Anastasio, C.: 2-Nitrobenzaldehyde as a chemical actinometer for solution and ice photochemistry, *J. Photochem. Photobiol. A*, 209(2-3), 186–192, doi:10.1016/j.jphotochem.2009.11.013, 2010.
- Gemayel, R., Emmelin, C., Perrier, S., Tomaz, S., Baboornian, V. J., Fishman, D. A., Nizkorodov, S. A., Dumas, S. and George, C.: Quenching of ketone triplet excited states by atmospheric halides, *Environ. Sci.: Atmos.*, 1(1), 31–44, doi:10.1039/D0EA00011F, 2021.
- Gen, M., Zhang, R., Li, Y. and Chan, C. K.: Multiphase Photochemistry of Iron-Chloride Containing Particles as a Source of Aqueous Chlorine Radicals and Its Effect on Sulfate Production., *Environ. Sci. Technol.*, 54(16), 9862–9871, doi:10.1021/acs.est.0c01540, 2020.
- Gilardoni, S., Massoli, P., Paglione, M., Giulianelli, L., Carbone, C., Rinaldi, M., Decesari, S., Sandrini, S., Costabile, F., Gobbi, G. P., Pietrogrande, M. C., Visentin, M., Scotto, F., Fuzzi, S. and Facchini, M. C.: Direct observation of aqueous secondary organic aerosol from biomass-burning emissions., *Proc. Natl. Acad. Sci. USA*, 113(36), 10013–10018, doi:10.1073/pnas.1602212113, 2016.
- González Palacios, L., Corral Arroyo, P., Aregahegn, K. Z., Steimer, S. S., Bartels-Rausch, T., Nozière, B., George, C., Ammann, M. and Volkamer, R.: Heterogeneous photochemistry of imidazole-2-carboxaldehyde: HO<sub>2</sub> radical formation and aerosol growth, *Atmos. Chem. Phys.*, 16(18), 11823–11836, doi:10.5194/acp-16-11823-2016, 2016.
- Haag, W. R., Hoigne, J., Gassman, E. and Braun, A.: Singlet oxygen in surface waters — Part I: Furfuryl alcohol as a trapping agent, *Chemosphere*, 13(5-6), 631–640, doi:10.1016/0045-6535(84)90199-1, 1984.
- De Haan, D. O., Jansen, K., Rynaski, A. D., Sueme, W. R. P., Torkelson, A. K., Czer, E. T., Kim, A. K., Rafla, M. A., De Haan, A. C. and Tolbert, M. A.: Brown Carbon Production by Aqueous-Phase Interactions of Glyoxal and SO<sub>2</sub>., *Environ. Sci. Technol.*, 54(8), 4781–4789, doi:10.1021/acs.est.9b07852, 2020.
- Hecobian, A., Zhang, X., Zheng, M., Frank, N., Edgerton, E. S. and Weber, R. J.: Water-Soluble Organic Aerosol material and the light-absorption characteristics of aqueous extracts measured over the Southeastern United States, *Atmos. Chem. Phys.*, 10(13), 5965–5977, doi:10.5194/acp-10-5965-2010, 2010.
- Herrmann, H., Hoffmann, D., Schaefer, T., Brüner, P. and Tilgner, A.: Tropospheric aqueous-phase free-radical chemistry: radical sources, spectra, reaction kinetics and prediction tools., *ChemPhysChem*, 11(18), 3796–3822, doi:10.1002/cphc.201000533, 2010.
- Herrmann, H., Schaefer, T., Tilgner, A., Styler, S. A., Weller, C., Teich, M. and Otto, T.: Tropospheric aqueous-phase chemistry: kinetics, mechanisms, and its coupling to a changing gas phase., *Chem. Rev.*, 115(10), 4259–4334, doi:10.1021/cr500447k, 2015.
- Hoffer, A., Gelencsér, A., Guyon, P., Kiss, G., Schmid, O., Frank, G. P., Artaxo, P. and Andreae, M. O.: Optical properties of humic-like substances (HULIS) in biomass-burning aerosols, *Atmos. Chem. Phys.*, 6(11), 3563–3570, doi:10.5194/acp-6-3563-2006, 2006.

- Kaur, R. and Anastasio, C.: Light absorption and the photoformation of hydroxyl radical and singlet oxygen in fog waters, *Atmos. Environ.*, 164, 387–397, doi:10.1016/j.atmosenv.2017.06.006, 2017.
- Kaur, R. and Anastasio, C.: First measurements of organic triplet excited states in atmospheric waters., *Environ. Sci. Technol.*, 52(9), 5218–5226, doi:10.1021/acs.est.7b06699, 2018.
- Kaur, R., Labins, J. R., Helbock, S. S., Jiang, W., Bein, K. J., Zhang, Q. and Anastasio, C.: Photooxidants from brown carbon and other chromophores in illuminated particle extracts, *Atmos. Chem. Phys.*, 19(9), 6579–6594, doi:10.5194/acp-19-6579-2019, 2019.
- Li, M., Bao, F., Zhang, Y., Sheng, H., Chen, C. and Zhao, J.: Photochemical aging of soot in the aqueous phase: release of dissolved black carbon and the formation of IO<sub>2</sub>., *Environ. Sci. Technol.*, 53(21), 12311–12319, doi:10.1021/acs.est.9b02773, 2019.
- Lim, Y. B., Tan, Y., Perri, M. J., Seitzinger, S. P. and Turpin, B. J.: Aqueous chemistry and its role in secondary organic aerosol (SOA) formation, *Atmospheric Chemistry & Physics Discussions*, 10(6), 2010.
- Lin, G., Sillman, S., Penner, J. E. and Ito, A.: Global modeling of SOA: the use of different mechanisms for aqueous-phase formation, *Atmos. Chem. Phys.*, 14(11), 5451–5475, doi:10.5194/acp-14-5451-2014, 2014.
- Ma, L., Guzman, C., Niedek, C., Tran, T., Zhang, Q. and Anastasio, C.: Kinetics and Mass Yields of Aqueous Secondary Organic Aerosol from Highly Substituted Phenols Reacting with a Triplet Excited State., *Environ. Sci. Technol.*, 55(9), 5772–5781, doi:10.1021/acs.est.1c00575, 2021.
- Ma, L., Worland, R., Tran, T., Jiang, W., Niedek, C., Zhang, Q. and Anastasio, C.: An evaluation of probes to measure oxidizing triplet excited states in aerosol liquid water, In preparation, 2022.
- Maizel, A. C. and Remucal, C. K.: The effect of probe choice and solution conditions on the apparent photoreactivity of dissolved organic matter., *Environ. Sci. Process. Impacts*, 19(8), 1040–1050, doi:10.1039/c7em00235a, 2017.
- Manfrin, A., Nizkorodov, S. A., Malecha, K. T., Getzinger, G. J., McNeill, K. and Borduas-Dedekind, N.: Reactive Oxygen Species Production from Secondary Organic Aerosols: The Importance of Singlet Oxygen., *Environ. Sci. Technol.*, 53(15), 8553–8562, doi:10.1021/acs.est.9b01609, 2019.
- Mao, J., Fan, S., Jacob, D. J. and Travis, K. R.: Radical loss in the atmosphere from Cu-Fe redox coupling in aerosols, *Atmos. Chem. Phys.*, 13(2), 509–519, doi:10.5194/acp-13-509-2013, 2013.
- McCabe, A. J. and Arnold, W. A.: Reactivity of Triplet Excited States of Dissolved Natural Organic Matter in Stormflow from Mixed-Use Watersheds., *Environ. Sci. Technol.*, 51(17), 9718–9728, doi:10.1021/acs.est.7b01914, 2017.
- McNeill, K. and Canonica, S.: Triplet state dissolved organic matter in aquatic photochemistry: reaction mechanisms, substrate scope, and photophysical properties., *Environ. Sci. Process. Impacts*, 18(11), 1381–1399, doi:10.1039/c6em00408c, 2016.
- McNeill, V. F.: Aqueous organic chemistry in the atmosphere: sources and chemical processing of organic aerosols., *Environ. Sci. Technol.*, 49(3), 1237–1244, doi:10.1021/es5043707, 2015.

- Mekic, M., Brigante, M., Vione, D. and Gligorovski, S.: Exploring the ionic strength effects on the photochemical degradation of pyruvic acid in atmospheric deliquescent aerosol particles, *Atmos. Environ.*, 185, 237–242, doi:10.1016/j.atmosenv.2018.05.016, 2018.
- Monge, M. E., Rosenørn, T., Favez, O., Müller, M., Adler, G., Abo Riziq, A., Rudich, Y., Herrmann, H., George, C. and D’Anna, B.: Alternative pathway for atmospheric particles growth., *Proc. Natl. Acad. Sci. USA*, 109(18), 6840–6844, doi:10.1073/pnas.1120593109, 2012.
- Morgan, B. and Lahav, O.: The effect of pH on the kinetics of spontaneous Fe(II) oxidation by O<sub>2</sub> in aqueous solution--basic principles and a simple heuristic description., *Chemosphere*, 68(11), 2080–2084, doi:10.1016/j.chemosphere.2007.02.015, 2007.
- Ossola, R., Clerc, B. and McNeill, K.: Mechanistic Insights into Dissolved Organic Sulfur Photomineralization through the Study of Cysteine Sulfinic Acid., *Environ. Sci. Technol.*, 54(20), 13066–13076, doi:10.1021/acs.est.0c04340, 2020.
- Parworth, C. L., Young, D. E., Kim, H., Zhang, X., Cappa, C. D., Collier, S. and Zhang, Q.: Wintertime water-soluble aerosol composition and particle water content in Fresno, California, *J. Geophys. Res. Atmos.*, 122(5), 3155–3170, doi:10.1002/2016JD026173, 2017.
- Paulson, S. E., Gallimore, P. J., Kuang, X. M., Chen, J. R., Kalberer, M. and Gonzalez, D. H.: A light-driven burst of hydroxyl radicals dominates oxidation chemistry in newly activated cloud droplets., *Sci. Adv.*, 5(5), eaav7689, doi:10.1126/sciadv.aav7689, 2019.
- Reid, J. S., Koppmann, R., Eck, T. F. and Eleuterio, D. P.: A review of biomass burning emissions part II: intensive physical properties of biomass burning particles, *Atmos. Chem. Phys.*, 5(3), 799–825, doi:10.5194/acp-5-799-2005, 2005.
- Renard, P., Reed Harris, A. E., Rapf, R. J., Ravier, S., Demelas, C., Coulomb, B., Quivet, E., Vaida, V. and Monod, A.: Aqueous phase oligomerization of methyl vinyl ketone by atmospheric radical reactions, *J. Phys. Chem. C*, 118(50), 29421–29430, doi:10.1021/jp5065598, 2014.
- Ross, F. and Ross, A. B.: Selected specific rates of reactions of transients from water in aqueous solution. III. Hydroxyl radical and perhydroxyl radical and their radical ions, *Historical Energy Database (United States)*, 1977.
- Rossignol, S., Aregahegn, K. Z., Tinel, L., Fine, L., Nozière, B. and George, C.: Glyoxal induced atmospheric photosensitized chemistry leading to organic aerosol growth., *Environ. Sci. Technol.*, 48(6), 3218–3227, doi:10.1021/es405581g, 2014.
- Schauer, J. J., Kleeman, M. J., Cass, G. R. and Simoneit, B. R.: Measurement of emissions from air pollution sources. 3. C<sub>1</sub>-C<sub>29</sub> organic compounds from fireplace combustion of wood., *Environ. Sci. Technol.*, 35(9), 1716–1728, doi:10.1021/es001331e, 2001.
- Seinfeld, J. and Pandis, S.: *Atmospheric chemistry and physics*. 1997., New York, 2008.
- Smith, J. D., Kinney, H. and Anastasio, C.: Aqueous benzene-diols react with an organic triplet excited state and hydroxyl radical to form secondary organic aerosol., *Phys. Chem. Chem. Phys.*, 17(15), 10227–10237, doi:10.1039/c4cp06095d, 2015.

- Smith, J. D., Kinney, H. and Anastasio, C.: Phenolic carbonyls undergo rapid aqueous photodegradation to form low-volatility, light-absorbing products, *Atmos. Environ.*, 126, 36–44, doi:10.1016/j.atmosenv.2015.11.035, 2016.
- Smith, J. D., Sio, V., Yu, L., Zhang, Q. and Anastasio, C.: Secondary organic aerosol production from aqueous reactions of atmospheric phenols with an organic triplet excited state., *Environ. Sci. Technol.*, 48(2), 1049–1057, doi:10.1021/es4045715, 2014.
- Southworth, B. A. and Voelker, B. M.: Hydroxyl radical production via the photo-Fenton reaction in the presence of fulvic acid., *Environ. Sci. Technol.*, 37(6), 1130–1136, doi:10.1021/es0207571, 2003.
- Tan, Y., Lim, Y. B., Altieri, K. E., Seitzinger, S. P. and Turpin, B. J.: Mechanisms leading to oligomers and SOA through aqueous photooxidation: insights from OH radical oxidation of acetic acid and methylglyoxal, *Atmos. Chem. Phys.*, 12(2), 801–813, doi:10.5194/acp-12-801-2012, 2012.
- Tilgner, A., Bräuer, P., Wolke, R. and Herrmann, H.: Modelling multiphase chemistry in deliquescent aerosols and clouds using CAPRAM3.0i, *J Atmos Chem*, 70(3), 221–256, doi:10.1007/s10874-013-9267-4, 2013.
- Tilgner, A. and Herrmann, H.: Tropospheric Aqueous-Phase OH Oxidation Chemistry: Current Understanding, Uptake of Highly Oxidized Organics and Its Effects, in *Multiphase environmental chemistry in the atmosphere*, vol. 1299, edited by S. W. Hunt, A. Laskin, and S. A. Nizkorodov, pp. 49–85, American Chemical Society, Washington, DC., 2018.
- Tilgner, A., Schaefer, T., Alexander, B., Barth, M., Collett Jr., J. L., Fahey, K. M., Nenes, A., Pye, H. O. T., Herrmann, H. and McNeill, V. F.: Acidity and the multiphase chemistry of atmospheric aqueous particles and clouds, *Atmos. Chem. Phys.*, 21(17), 13483–13536, doi:10.5194/acp-21-13483-2021, 2021.
- Tratnyek, P. G. and Hoigne, J.: Oxidation of substituted phenols in the environment: a QSAR analysis of rate constants for reaction with singlet oxygen, *Environ. Sci. Technol.*, 25(9), 1596–1604, 1991.
- Urban, R. C., Lima-Souza, M., Caetano-Silva, L., Queiroz, M. E. C., Nogueira, R. F. P., Allen, A. G., Cardoso, A. A., Held, G. and Campos, M. L. A. M.: Use of levoglucosan, potassium, and water-soluble organic carbon to characterize the origins of biomass-burning aerosols, *Atmos. Environ.*, 61, 562–569, doi:10.1016/j.atmosenv.2012.07.082, 2012.
- Vione, D., Maurino, V., Minero, C. and Pelizzetti, E.: The atmospheric chemistry of hydrogen peroxide: a review., *Ann. Chim.*, 93(4), 477–488, 2003.
- Volkamer, R., San Martini, F., Molina, L. T., Salcedo, D., Jimenez, J. L. and Molina, M. J.: A missing sink for gas-phase glyoxal in Mexico City: Formation of secondary organic aerosol, *Geophys. Res. Lett.*, 34(19), doi:10.1029/2007GL030752, 2007.
- Wander, R., Neta, P. and Dorfman, L. M.: Pulse radiolysis studies. XII. Kinetics and spectra of the cyclohexadienyl radicals in aqueous benzoic acid solution, *J. Phys. Chem.*, 72(8), 2946–2949, doi:10.1021/j100854a044, 1968.
- Wang, X., Gemayel, R., Hayeck, N., Perrier, S., Charbonnel, N., Xu, C., Chen, H., Zhu, C., Zhang, L., Wang, L., Nizkorodov, S. A., Wang, X., Wang, Z., Wang, T., Mellouki, A., Riva, M., Chen, J. and George, C.: Atmospheric photosensitization: A new pathway for sulfate formation., *Environ. Sci. Technol.*, 54(6), 3114–3120, doi:10.1021/acs.est.9b06347, 2020.

- Washenfelder, R. A., Young, C. J., Brown, S. S., Angevine, W. M., Atlas, E. L., Blake, D. R., Bon, D. M., Cubison, M. J., de Gouw, J. A., Dusanter, S., Flynn, J., Gilman, J. B., Graus, M., Griffith, S., Grossberg, N., Hayes, P. L., Jimenez, J. L., Kuster, W. C., Lefer, B. L., Pollack, I. B., Ryerson, T. B., Stark, H., Stevens, P. S. and Trainer, M. K.: The glyoxal budget and its contribution to organic aerosol for Los Angeles, California, during CalNex 2010, *J. Geophys. Res.*, 116(D21), doi:10.1029/2011JD016314, 2011.
- Weller, C., Tilgner, A., Bräuer, P. and Herrmann, H.: Modeling the impact of iron-carboxylate photochemistry on radical budget and carboxylate degradation in cloud droplets and particles., *Environ. Sci. Technol.*, 48(10), 5652–5659, doi:10.1021/es4056643, 2014.
- Wenk, J., Aeschbacher, M., Sander, M., von Gunten, U. and Canonica, S.: Photosensitizing and Inhibitory Effects of Ozonated Dissolved Organic Matter on Triplet-Induced Contaminant Transformation., *Environ. Sci. Technol.*, 49(14), 8541–8549, doi:10.1021/acs.est.5b02221, 2015.
- Wenk, J. and Canonica, S.: Phenolic Antioxidants Inhibit the Triplet-Induced Transformation of Anilines and Sulfonamide Antibiotics in Aqueous Solution, *Environ. Sci. Technol.*, 46(10), 5455–5462, doi:10.1021/es300485u, 2012.
- Wenk, J., Eustis, S. N., McNeill, K. and Canonica, S.: Quenching of excited triplet states by dissolved natural organic matter., *Environ. Sci. Technol.*, 47(22), 12802–12810, doi:10.1021/es402668h, 2013.
- Wenk, J., von Gunten, U. and Canonica, S.: Effect of dissolved organic matter on the transformation of contaminants induced by excited triplet states and the hydroxyl radical., *Environ. Sci. Technol.*, 45(4), 1334–1340, doi:10.1021/es102212t, 2011.
- Wong, J. P. S., Tsagkaraki, M., Tsiotra, I., Mihalopoulos, N., Violaki, K., Kanakidou, M., Sciare, J., Nenes, A. and Weber, R. J.: Atmospheric evolution of molecular-weight-separated brown carbon from biomass burning, *Atmos. Chem. Phys.*, 19(11), 7319–7334, doi:10.5194/acp-19-7319-2019, 2019.
- Wu, Z., Wang, Y., Tan, T., Zhu, Y., Li, M., Shang, D., Wang, H., Lu, K., Guo, S., Zeng, L. and Zhang, Y.: Aerosol Liquid Water Driven by Anthropogenic Inorganic Salts: Implying Its Key Role in Haze Formation over the North China Plain, *Environ. Sci. Technol. Lett.*, 5(3), 160–166, doi:10.1021/acs.estlett.8b00021, 2018.
- Xia, S.-S., Eugene, A. J. and Guzman, M. I.: Cross photoreaction of glyoxylic and pyruvic acids in model aqueous aerosol., *J. Phys. Chem. A*, 122(31), 6457–6466, doi:10.1021/acs.jpca.8b05724, 2018.
- Zepp, R. G., Faust, B. C. and Hoigne, J.: Hydroxyl radical formation in aqueous reactions (pH 3–8) of iron(II) with hydrogen peroxide: the photo-Fenton reaction, *Environ. Sci. Technol.*, 26(2), 313–319, doi:10.1021/es00026a011, 1992.
- Zhang, H., Surratt, J. D., Lin, Y. H., Bapat, J. and Kamens, R. M.: Effect of relative humidity on SOA formation from isoprene/NO photooxidation: enhancement of 2-methylglyceric acid and its corresponding oligoesters under dry conditions, *Atmos. Chem. Phys.*, 11(13), 6411–6424, doi:10.5194/acp-11-6411-2011, 2011.
- Zhou, W., Mekić, M., Liu, J., Loisel, G., Jin, B., Vione, D. and Gligorovski, S.: Ionic strength effects on the photochemical degradation of acetosyringone in atmospheric deliquescent aerosol particles, *Atmos. Environ.*, 198, 83–88, doi:10.1016/j.atmosenv.2018.10.047, 2019.

Zhou, X., Davis, A. J., Kieber, D. J., Keene, W. C., Maben, J. R., Maring, H., Dahl, E. E., Izaguirre, M. A., Sander, R. and Smoydzyń, L.: Photochemical production of hydroxyl radical and hydroperoxides in water extracts of nascent marine aerosols produced by bursting bubbles from Sargasso seawater, *Geophys. Res. Lett.*, 35(20), doi:10.1029/2008GL035418, 2008.



## Chapter 5: Seasonal variation of photooxidant formation in aqueous extracts of ambient particles

### ABSTRACT

Atmospheric waters – including fog/cloud drops and aerosol liquid water – are important sites for the transformations of atmospheric species, largely through reactions with photoformed oxidants such as hydroxyl radical ( $\bullet\text{OH}$ ), singlet molecular oxygen ( $^1\text{O}_2^*$ ), and oxidizing triplet excited states of organic matter ( $^3\text{C}^*$ ). Despite this, there are few measurements of these photooxidants (especially in extracts of ambient particles) and very little information is available about how oxidant levels vary with season or particle type. To address this gap, we collected ambient  $\text{PM}_{2.5}$  from Davis, California, over the course of a year, and measured photooxidant concentrations in dilute aqueous extracts of the particles. We categorized samples into four groups: Winter & Spring (Win-Spr), Summer & Fall (Sum-Fall) without wildfire influence, fresh biomass burning (FBB), and aged biomass burning (ABB). FBB contains significant amounts of brown carbon (BrC) from wildfires, and the highest mass absorption coefficients (MAC) normalized by dissolved organic carbon, with an average value of  $3.3 (\pm 0.4) \text{ m}^2 (\text{g C})^{-1}$  at 300 nm. Win-Spr and ABB have similar MAC averages,  $1.9 (\pm 0.4)$  and  $1.5 (\pm 0.3) \text{ m}^2 (\text{g C})^{-1}$ , respectively, while Sum-Fall has the lowest MAC ( $0.65 (\pm 0.19) \text{ m}^2 (\text{g C})^{-1}$ ).  $\bullet\text{OH}$  concentrations in extracts range from  $(0.2\text{-}4.7) \times 10^{-15} \text{ M}$  and generally increase with concentration of dissolved organic carbon (DOC), although this might be because DOC is a proxy for extract concentration. Win-Spr and ABB have higher average quantum yields for  $\bullet\text{OH}$  formation, though there is no statistical difference among sample types.  $^1\text{O}_2^*$  concentrations in extracts have a range of  $(0.7\text{-}45) \times 10^{-13} \text{ M}$ , exhibiting a good linearity with DOC that is independent of sample type. Fresh BB samples have the highest  $[^1\text{O}_2^*]$  but the lowest average  $\Phi_{1\text{O}_2^*}$ , while Sum-Fall samples are the opposite.  $\Phi_{1\text{O}_2^*}$  is negatively correlated with  $\text{MAC}_{\text{DOC}}$ , indicating that less light-absorbing samples form  $^1\text{O}_2^*$  more efficiently. We quantified  $^3\text{C}^*$  concentrations with two triplet probes: syringol (SYR), which captures both strongly and weakly oxidizing triplets, and (phenylthio)acetic acid (PTA), which is only sensitive to strongly oxidizing triplets. Concentrations of  $^3\text{C}^*$  are in the range of  $(0.03 - 7.9)$

$\times 10^{-13}$  M and linearly increase with DOC; this relationship for  $[^3\text{C}^*]_{\text{SYR}}$  is independent of sample type. The average ratio of  $[^3\text{C}^*]_{\text{PTA}}/[^3\text{C}^*]_{\text{SYR}}$  is 0.58 ( $\pm 0.38$ ), indicating that near 60% of oxidizing triplets are strongly oxidizing. Win-Spr samples have the highest fraction of strongly oxidizing  $^3\text{C}^*$ , with an average of 86 ( $\pm 43$ )%.  $\Phi_{^3\text{C}^*,\text{SYR}}$  is in the range of (0.6-8.8) %, with an average value, 3.3 ( $\pm 1.9$ )%, two times higher than  $\Phi_{^3\text{C}^*,\text{PTA}}$ . FBB has the lowest average  $\Phi_{^3\text{C}^*}$ , while the aging process tends to enhance  $\Phi_{^3\text{C}^*}$ , as well as  $\Phi_{^1\text{O}_2^*}$ .

To estimate photooxidant concentrations in particle water, we extrapolate the photooxidant kinetics in our dilute particle extracts to aerosol liquid water conditions and predict their concentrations at 1  $\mu\text{g PM}/\mu\text{g H}_2\text{O}$  for each sample type. The estimated ALW  $\bullet\text{OH}$  concentration is  $7 \times 10^{-15}$  M when including mass transport of gas-phase  $\bullet\text{OH}$  to the particles.  $^1\text{O}_2^*$  and  $^3\text{C}^*$  concentrations have ranges of  $(0.6 - 7) \times 10^{-12}$  M and  $(0.08 - 1) \times 10^{-12}$  M, respectively. In the Win-Spr and Sum-Fall samples, photooxidant concentrations in ALW increase significantly comparing to that in particle extracts, while the changes for the FBB and ABB samples are minor. The small increases for the biomass burning particles are likely due to the high amounts of organic compounds, which lead to strong quenching of  $^1\text{O}_2^*$  and  $^3\text{C}^*$  even in our dilute extracts. Based on our concentration estimates, the lifetime of organic compounds in an aerosol can be significantly shorter than in a cloud or fog, due to enhanced photooxidant concentrations in the particles. Our results indicate that  $^3\text{C}^*$  and  $^1\text{O}_2^*$  in ALW dominate the processing of organic compounds that react quickly with these oxidants (such as phenols and furans, respectively), while  $\bullet\text{OH}$  is more important for less reactive organics.

## 5.1. Introduction

Atmospheric waters, including fog/cloud drops and liquid water on aerosol particles, are important media for photochemical transformations of chemical species (Herrmann et al., 2010, 2015). These include formation of aqueous secondary organic aerosol (aqSOA), formation and photobleaching of brown carbon (BrC), oxidation of reduced sulfur, and aerosol aging (Ervens, 2018; Ervens et al., 2011; Gilardoni et al., 2016; Laskin et al., 2015; McNeill, 2015; Seinfeld and Pandis, 2016; Wang et al., 2016; Zhao et al., 2015).

Many of these processes are driven by photochemically generated oxidants, including hydroxyl radical ( $\bullet\text{OH}$ ), triplet excited states of organic matter ( $^3\text{C}^*$ ), and singlet molecular oxygen ( $^1\text{O}_2^*$ ) (Ervens et al., 2014; Finlayson-Pitts and Jr, 1999; He et al., 2013; Herrmann, 2003; Kaur et al., 2019; Lim et al., 2010).

Hydroxyl radical ( $\bullet\text{OH}$ ), the best studied aqueous oxidant in the atmosphere, is highly reactive with most reduced species but has a relatively low abundance compared to  $^3\text{C}^*$  and  $^1\text{O}_2^*$ . Concentrations of  $\bullet\text{OH}$  in fog and cloud waters, as well as aqueous extracts of ambient particles and lab-generated secondary organic aerosol are typically  $10^{-17}$  to  $10^{-15}$  M (Anastasio and McGregor, 2001; Arakaki et al., 2013; Dorfman and Adams, 1973; Kaur and Anastasio, 2017; Kaur et al., 2019; Manfrin et al., 2019; Tilgner and Herrmann, 2018). Sources of  $\bullet\text{OH}$  in the aqueous phase include mass transfer from the gas phase, Fenton or Fenton-like reactions of reduced metals with hydrogen peroxide, and photolysis of nitrate, nitrite, iron complexes, hydrogen peroxide, and organic hydroperoxides (Badali et al., 2015; Herrmann et al., 2010; Tilgner and Herrmann, 2018; Tong et al., 2016). Additionally, organic compounds in atmospheric waters can affect  $\bullet\text{OH}$  production. For example, the interaction of humic-like substances (HULIS) or SOA with Fe(II) can enhance or suppress  $\bullet\text{OH}$  formation (Baba et al., 2015; Gonzalez et al., 2017; Hems and Abbatt, 2018; Tong et al., 2016; Zuo and Hoigne, 1992). This suggests that seasonal variations in particle composition (e.g., SOA and Fe) can affect  $\bullet\text{OH}$  kinetics, as reported recently for  $\bullet\text{OH}$  photoproduction in extracts of particulate matter (PM) from Colorado: winter  $\bullet\text{OH}$  originated from nitrate photolysis while summer  $\bullet\text{OH}$  was more linked to soluble iron (Leresche et al., 2021). But very little is known about how  $\bullet\text{OH}$  concentrations in particles vary with season or among particle types.

Triplet excited states ( $^3\text{C}^*$ ) are formed when organic chromophores (i.e., brown carbon (BrC)) absorb sunlight and are promoted to a higher energy state (McNeill and Canonica, 2016). Oxidizing triplets, i.e., the subset of triplets that have high reduction potentials, are effective oxidants, reacting with phenols and biogenic volatile compounds to form SOA and BrC, and oxidizing bisulfite to sulfate (González Palacios et al., 2016; Monge et al., 2012; Rossignol et al., 2014; Smith et al., 2014; Wang et al., 2020b; Yu et al., 2014). For compounds (like phenols) that react rapidly with triplets,  $^3\text{C}^*$  can be as important an oxidant as

•OH in cloud and fog drops, where triplet concentrations are  $10^{-15}$ - $10^{-13}$  M (Kaur and Anastasio, 2018; Kaur et al., 2019; Ma et al., 2021; Smith et al., 2015). Moreover, triplet concentrations are estimated to be enhanced by one or two orders of magnitude in aerosol liquid water (Kaur et al., 2019; Ma et al., 2022a). The ability of dissolved organic matter (DOM) to form  $^3\text{C}^*$  depends on its composition. In surface waters, quantum yields of  $^3\text{C}^*$  are higher for organic compounds with lower average molecular weights and lower aromaticity (Berg et al., 2019; Maizel and Remucal, 2017; McCabe and Arnold, 2017, 2018; McKay et al., 2017). However, little is known about how  $^3\text{C}^*$  formation in atmospheric waters depends on BrC characteristics or season.

The final oxidant we consider, singlet molecular oxygen ( $^1\text{O}_2^*$ ), is formed when triplet excited states transfer energy to dissolved molecular oxygen.  $^1\text{O}_2^*$  reacts rapidly with electron-rich compounds such as furans, polycyclic aromatic hydrocarbons, some amino acids, and substituted alkenes (Gollnick and Griesbeck, 1985; McGregor and Anastasio, 2001; Richards-Henderson et al., 2015; Wilkinson et al., 1995; Zeinali et al., 2019).  $^1\text{O}_2^*$  concentrations in fog and cloud waters and aqueous particle extracts are the highest of the three oxidants, in the range of  $10^{-14}$ - $10^{-12}$  M (Kaur and Anastasio, 2017; Kaur et al., 2019; Leresche et al., 2021; Manfrin et al., 2019). Dissolved black carbon also can produce  $^1\text{O}_2^*$ , resulting in concentrations on the order of  $10^{-12}$  M (Li et al., 2019). Though  $^1\text{O}_2^*$  is not as reactive as  $^3\text{C}^*$  and •OH, its concentration increases by orders of magnitude when moving from dilute cloud/fog conditions towards the more concentrated conditions of aerosol liquid water (Kaur et al., 2019; Ma et al., 2022a). Since  $^1\text{O}_2^*$  is born from  $^3\text{C}^*$ , these two oxidants are tightly linked. For example, in surface waters the quantum yield of  $^1\text{O}_2^*$  ( $\Phi_{1\text{O}_2^*}$ ) is also higher in samples with lower average molecular weight DOM, as seen for  $^3\text{C}^*$  (Berg et al., 2019; Maizel and Remucal, 2017; Ossola et al., 2021; Wang et al., 2020a). Some studies on the seasonal trend of  $\Phi_{1\text{O}_2^*}$  in surface waters hypothesized that DOM photodegradation appears to be the main cause (McCabe and Arnold, 2016; Ossola et al., 2021; Sharpless et al., 2014). However, there are differences in singlet oxygen generation and concentrations between surface and atmospheric waters. For example, while ozonation and photodegradation of DOM enhances  $\Phi_{1\text{O}_2^*}$  in surface waters,

photodegradation of particle water extracts has no significant effect on  $\Phi_{1O_2^*}$  (Leresche et al., 2019, 2021; Sharpless et al., 2014). In addition, we know very little about the seasonality of  $^1O_2^*$  concentrations in particles or how this oxidant varies between sample types.

Although  $\bullet OH$ ,  $^3C^*$ , and  $^1O_2^*$  are important in the transformation of atmospheric species, there are few measurements of these photooxidants in atmospheric condensed phases, especially in extracts of ambient particles. In addition, very little is known about seasonal variations in oxidant concentrations and kinetics. To address this gap, we collected  $PM_{2.5}$  from November 2019 to October 2020 in Davis CA, extracted them in water, and measured light absorption and photooxidant formation. This period included four main types of samples: winter samples influenced by residential wood combustion and high humidity, summer samples impacted by fresh wildfires, summer samples impacted by aged wildfires, and spring/summer samples with little to no biomass burning (BB). We measured photooxidant concentrations ( $\bullet OH$ ,  $^1O_2^*$ ,  $^3C^*$ ) in water extracts of the particles, and investigated how photooxidant formation depends on particle type, optical properties, and biomass burning influence. Finally, we extrapolated our dilute extract results to predict photooxidant concentrations, and assess the importance of photooxidants in processing organic compounds, in aerosol liquid water (ALW).

## 5.2. Experimental Methods

### 5.2.1. Chemicals

Furfuryl alcohol (FFA, 98%), benzoic acid (BA,  $\geq 99.5\%$ ), *p*-hydroxybenzoic acid (*p*HBA, 99%), (phenylthio)acetic acid (PTA, 96%), syringol (SYR, 99%), 3,4-dimethoxybenzaldehyde (DMB, 99%), deuterium oxide ( $D_2O$ , 99.9% D-atom) were received from Millipore Sigma. All chemical solutions and particulate matter extracts were prepared using air-saturated ultrapure water (Milli-Q water) from a Milli-Q Advantage A10 system (Millipore;  $\geq 18.2 M\Omega cm$ ) that was pretreated with a Barnstead activated carbon cartridge.

### 5.2.2. Particle Collection and Extraction

More detailed descriptions of sampling and extraction procedures are provided in Ma et al. (2022) and are only briefly discussed here. Fine particle ( $PM_{2.5}$ ) sampling was conducted from November 2019 to October 2020 on the roof of Ghausi Hall on the University of California, Davis campus. Winter in Davis is humid and sometimes foggy, and the air quality is often impacted by residential wood combustion, while Davis in summer is hot and dry. During the summer of 2020, several severe wildfires occurred in Northern California and Oregon, including the largest wildfires in the recorded history of California: the August complex (size: 4179 km<sup>2</sup>), LNU Lightning complex (1605 km<sup>2</sup>), and SCU lightning complex (1470 km<sup>2</sup>) (<https://www.fire.ca.gov/incidents/2020>; last access: 15 July 2022). These fires caused extremely heavy air pollution in Davis with daily  $PM_{2.5}$  concentrations sometimes exceeding 80  $\mu\text{g m}^{-3}$  (<https://www.arb.ca.gov/aqmis2/aqmis2.php>, last access: 20 June 2022). Particles were collected with a high-volume sampler containing a  $PM_{10}$  inlet (Graseby Andersen) and two offset, slotted impactor plates (Tisch Environmental, Inc., 230 series) to remove particles larger than 2.5  $\mu\text{m}$ .  $PM_{2.5}$  was collected onto pre-cleaned Teflon-coated borosilicate glass microfiber filters (Pall Corporation, EmFab™ filters, 8 in.  $\times$  10 in.) and stored at  $-20\text{ }^{\circ}\text{C}$  immediately after collection. The sampling duration was either 24 hr or up to a week (Table S5.1). The sampling campaign was paused from March to June 2020 because of COVID-related restrictions on campus activities.

To prepare particulate matter extracts (PMEs), filters were cut into 2 cm  $\times$  2 cm squares, and then extracted with 1.0 mL Milli-Q water by shaking for 4 h in the dark. The extracts from the same filter were combined, filtered (0.22  $\mu\text{m}$  PTFE; Pall corporation), and adjusted to pH 4.2 by sulfuric acid to mimic the acidity of winter particle water in the Central Valley of California (Parworth et al., 2017). The acidity of extracts was measured by a pH microelectrode (MI-414 series, protected tip; Microelectrodes, Inc.). PMEs were flash-frozen in liquid nitrogen immediately after preparation and were later thawed on the day of the experiment. Particle mass extracted was determined by weighing filter squares before and after extraction with a microbalance (M2P, Sartorius). UV-Vis spectra of PMEs were measured with a Shimadzu UV-

2501PC spectrophotometer. Dissolved organic carbon (DOC) and major ions were measured by a total organic carbon analyzer (TOC-VCPH, Shimadzu) and ion chromatographs (881 Compact IC Pro, Metrohm) equipped with conductivity detectors, respectively. PME sample information is provided in Table S5.1, while DOC and ion concentrations are in Table S5.2.

### 5.2.3. Sample Illumination and Chemical Analysis

Illumination experiments were conducted using light from a 1000 W xenon arc lamp that was passed through optical filters to simulate tropospheric sunlight (Kaur and Anastasio, 2017). 1.0 mL extract at pH 4.2 was spiked with a photooxidant probe and illuminated in a silicone-plugged GE 021 quartz tube (5 mm inner diameter, 1.0 mL volume) at 20 °C. Dark control samples were wrapped in aluminum foil and kept in the same photoreactor chamber. During illumination, aliquots were removed from the illuminated and dark tubes periodically to measure probe concentrations with high-performance liquid chromatography (HPLC, Shimadzu LC-20AB pump, Thermo Scientific Accucore XL C18 column (50 × 3 mm, 4 μm bead), and Shimadzu-M20A UV-Vis detector). The photon flux in an identical quartz tube was determined on each experiment day by measuring the photolysis rate constant of a 10 μM 2-nitrobenzaldehyde (2NB) solution (Galbavy et al., 2010).

### 5.2.4. Photooxidant Measurements

Photooxidant concentration measurements are detailed in past papers (Anastasio and McGregor, 2001; Kaur and Anastasio, 2017; Ma et al., 2022a) and are only briefly described here.

#### 5.2.4.1. Hydroxyl radical ( $\bullet\text{OH}$ )

$\bullet\text{OH}$  concentration was quantified using benzoic acid (BA) as a probe and then monitoring the rate of probe decay and rate of formation of *p*-hydroxybenzoic acid (*p*-HBA). In our experiment, 10 μM benzoic acid was spiked into 1.0 mL PME. For dilute samples (DOC < 15 mg C L<sup>-1</sup>), 2 μM BA was used in order not to perturb the natural  $\bullet\text{OH}$  sink in PME. Aliquots were taken during illumination to measure BA and *p*-

HBA concentrations. From the BA probe loss, a linear regression of  $\ln([\text{probe}]_t/[\text{probe}]_0)$  versus illumination time ( $t$ ) was fitted, where  $[\text{probe}]_0$  is the concentrations at time zero. The negative value of the regression slope is the BA pseudo-first order decay rate constant ( $k'_{BA}$ ).  $\bullet\text{OH}$  concentration was then determined using:

$$[\bullet\text{OH}]_{exp} = \left[ \frac{k'_{BA}}{k_{BA+\bullet\text{OH}}} \right] \quad (5.1)$$

where  $k_{BA+\bullet\text{OH}}$  is the second-order rate constant of BA reacting with  $\bullet\text{OH}$  at pH 4.2 ( $5.1 \times 10^9 \text{ M}^{-1} \text{ s}^{-1}$ ) (Ashton et al., 1995; Wander et al., 1968). Next,  $[\bullet\text{OH}]_{exp}$  was normalized to sunlight conditions at midday on the winter solstice at Davis (solar zenith =  $62^\circ$ ;  $j_{2NB,win} = 0.0070 \text{ s}^{-1}$ ) (Galbavy et al., 2010) and corrected for internal light screening due to absorption by chromophores in PME:

$$[\bullet\text{OH}]_{win} = \left[ \frac{[\bullet\text{OH}]_{exp}}{S_\lambda \times j_{2NB,exp}} \right] \times j_{2NB,win} \quad (5.2)$$

where  $S_\lambda$  is the internal light screening factor in an individual sample (Table S5.1), and  $j_{2NB,exp}$  is the photolysis rate constant of 2NB measured on the experiment day.

We also determined the  $\bullet\text{OH}$  concentration in each sample from *p*-HBA formation. The initial formation rate of *p*-HBA was determined from the regression between *p*-HBA concentration and illumination time, either using a linear regression or a three-parameter exponential fit:

$$[p\text{-HBA}]_t = [p\text{-HBA}]_0 + a(1 - e^{-bt}) \quad (5.3)$$

where  $[p\text{-HBA}]_t$  and  $[p\text{-HBA}]_0$  are the measured concentrations at illumination times  $t$  and zero, respectively, and  $a$  and  $b$  are regression fit parameters. With this fitting, the initial formation rate of *p*-HBA,  $R_p$ , is calculated with:

$$R_p = a \times b \quad (5.4)$$



And then the  $\bullet\text{OH}$  concentration was calculated using:

$$[\bullet\text{OH}]_{exp} = \frac{R_p}{[BA] \times k_{BA+\bullet\text{OH}} \times Y_{p\text{-HBA}}} \quad (5.5)$$

where [BA] is the initial BA concentration (either 10 or 2  $\mu\text{M}$ ) and  $Y_{p\text{-HBA}}$  is the yield of *p*-HBA from the reaction of BA with  $\bullet\text{OH}$ , which is 0.18 (Anastasio and McGregor, 2001).  $\bullet\text{OH}$  concentrations were normalized by  $j_{2\text{NB}}$  and screening factor using Eq. 5.2. In some samples BA decay and *p*-HBA formation were faster at the beginning of illumination and then slowed (e.g., Fig. S5.1), indicating an initially higher  $\bullet\text{OH}$  concentration compared to later times, as seen previously (Paulson et al., 2019). For each sample we generally used the average value of [ $\bullet\text{OH}$ ] obtained from BA and *p*-HBA as the final concentration (Table S5.3). In the few samples where the BA decay was noisy, we used the  $\bullet\text{OH}$  concentration determined from *p*-HBA.

#### 5.2.4.2. Singlet molecular oxygen ( $^1\text{O}_2^*$ )

To determine  $^1\text{O}_2^*$  concentrations, FFA was used as a probe and deuterium oxide ( $\text{D}_2\text{O}$ ) was used as a diagnostic tool (Anastasio and McGregor, 2001) because  $^1\text{O}_2^*$  decays more rapidly in  $\text{H}_2\text{O}$  than  $\text{D}_2\text{O}$ . Therefore, the difference of FFA decay rates in  $\text{H}_2\text{O}$  and  $\text{D}_2\text{O}$  is attributed to  $^1\text{O}_2^*$  (instead of other oxidants). For each sample, 1.0 mL of PME was divided into two 0.5 mL aliquots, with one diluted with 0.5 mL  $\text{H}_2\text{O}$  and the other 0.5 mL  $\text{D}_2\text{O}$ . 10  $\mu\text{M}$  FFA was spiked into both solutions and pseudo-first order rate constants of FFA loss during illumination were determined ( $k_{\text{EXP,H}_2\text{O}}$  and  $k_{\text{EXP,D}_2\text{O}}$ ). The difference between the FFA first-order rate constants was used to calculate the steady-state  $^1\text{O}_2^*$  concentration (Anastasio and McGregor, 2001). This experimental  $^1\text{O}_2^*$  concentration was normalized by photon flux and light screening factors of PME using Eq. 5.2 to determine winter-solstice values of  $^1\text{O}_2^*$  (Table S5.4).

### 5.2.4.3. Oxidizing triplet excited state of organic matter ( $^3C^*$ )

Triplets were measured with two probes, syringol (SYR) and (phenylthiol)acetic acid (PTA). SYR reacts rapidly with all oxidizing triplets, but its decay by  $^3C^*$  can be inhibited by high concentrations of dissolved organic matter (DOM)(Ma et al., 2022a, 2022b; Maizel and Remucal, 2017; McCabe and Arnold, 2017). In contrast, PTA is more resistant to this inhibition, but it can only capture strongly oxidizing triplets (Ma et al., 2022b). To determine  $^3C^*$  concentrations, two 1.0 ml aliquots PME were either spiked with 10  $\mu$ M of SYR or PTA, and then illuminated to determine the pseudo-first order rate constant for loss of each probe ( $k'_{P,exp}$ ). We then removed the contributions of direct photodegradation,  $^{\bullet}OH$  and  $^1O_2^*$  to triplet probe decay (Ma et al., 2022a). Since  $^3C^*$  is a mixture of reactive species with a wide range of reactivities, there is no exact value for the second-order rate constant of  $^3C^*$  in PME reacting with probes. Therefore, we assume that  $^3C^*$  in PME has the same average reactivity as  $^3DMB^*$  (Fleming et al., 2020; Kaur et al., 2019). We quantified the inhibition effect of DOM on the decay of SYR and PTA by measuring inhibition factors of each probe ( $IF_P$ ) in each sample, and used them to correct  $^3C^*$  concentrations (Canonica and Laubscher, 2008; Ma et al., 2022b; McCabe and Arnold, 2017; Wenk et al., 2011). Details about determining inhibition factors and correcting  $^3C^*$  concentrations are provided in Supplemental Information Section S5.1.  $^3C^*$  concentrations in PME during each experiment were calculated with:

$$[^3C^*]_{P,exp} = \frac{k'_{P,3C^*}}{k_{P+3DMB^*} \times IF_P} \quad (5.6)$$

where  $k_{P+3DMB^*}$  is the second-order rate constant of probe with  $^3DMB^*$  (Table S5.5). These values were converted to  $^3C^*$  concentrations expected on midday of the winter solstice in Davis (after correction for internal light screening) using an equation analogous to Eq. 5.2; these are the concentrations reported in the main text.  $^3C^*$  measurements by SYR and PTA are in Tables S5.7 and S5.8, respectively.

## 5.3. Results and Discussion

### 5.3.1. General Extract Characteristics

To investigate the seasonal variation of photooxidant formation, we studied 18 samples across the year of sampling. Samples were from all seasons, but there was only one Spring sample because of COVID-related restrictions on campus activities from March through June of 2020 (Fig. 5.1 and Table S5.1). Most particle samples were collected for 24 h, while four of the winter samples were collected for seven days to obtain more particle mass. Winters were marked by residential wood burning and high relative humidities, while the summer samples represented both periods influenced by fresh and aged biomass burning (from wildfires) and clean conditions. From August to October 2020, Davis periodically experienced severe air pollution caused by wildfires in California and Oregon, with daily  $\text{PM}_{2.5}$  in Davis up to  $130 \mu\text{g m}^{-3}$ . Section S5.2 provides satellite images with fire points detected by the NASA Visible Infrared Imaging Radiometer Suite (VIIRS) and 24-h back trajectories ending at the sampling site estimated by the Hybrid Single Particle Lagrangian Integrated Trajectory (HYSPLIT) on the day of sampling for wildfire periods (Rolph et al., 2017; Stein et al., 2015). Based on the satellite images and back trajectories, smoke plumes were transported from their sources to Davis in as short as 1~2 h or as long as 12~24 h or more.

Figure 5.1 shows the average  $\text{PM}_{2.5}$  concentration during each extract sampling period. We categorized the 18 samples into four groups based on sampling date and positive matrix factorization (PMF) results obtained using UV/Vis absorption spectra and aerosol mass spectrometer chemical characterization (Jiang et al., 2022). The first group is termed Winter & Spring samples (Win-Spr), which were collected from November 2019 to March 2020 and have an average  $\text{PM}_{2.5}$  concentration of  $9.9 (\pm 1.5) \mu\text{g m}^{-3}$  (Table S5.1). Three samples collected in July, August, and October without wildfire influence are classified as Summer & Fall samples (Sum-Fall), with an average  $\text{PM}_{2.5}$  of  $7.4 (\pm 0.4) \mu\text{g m}^{-3}$ . The seven wildfire-influenced samples collected from August to October are classified as fresh biomass burning (FBB) and aged biomass burning (ABB) samples, with average  $\text{PM}_{2.5}$  values of  $55 (\pm 10)$  and  $24 (\pm 8) \mu\text{g m}^{-3}$ ,



Dissolved organic carbon concentrations in the extracts range from 5 to 192 mg C L<sup>-1</sup> (Table S5.1). The ratio of organic carbon (OC) mass to total extracted PM mass is high in the wildfire samples, with average values of 31 (± 6) % and 26 (± 6) % for FBB and ABB, respectively. These fractions are lower than values for BB particles in other studies (43-59%) (Schauer et al., 2001; Vicente et al., 2013), probably because we used water as the extraction solvent, thereby missing water insoluble organics. The OC/PM fractions for Win-Spr and Sum-Fall samples are comparable, with values of 16 (± 5) % and 11 (± 3) %, respectively. Win-Spr PMEs have high concentrations of nitrate (NO<sub>3</sub><sup>-</sup>), 84-3300 μM (Table S5.2), which contributed up to 33 % of PM mass. PMEs in the other three groups have nitrate concentrations from 25 to 300 μM, with contributions to the PM mass of less than 10 %. Win-Spr samples also have the highest ammonium concentrations, 168-4900 μM, followed by wildfire-influenced samples (46-803 μM), and Sum-Fall samples (< 100 μM). Potassium, a marker of biomass burning (Silva et al., 1999), has its highest concentrations in winter and wildfire samples with a range of 62-220 μM. The Sum-Fall samples have the highest fraction of sodium, an average of 11%, suggesting the influence of sea salt (Parworth et al., 2017). We employed three field blanks in this study at the beginning, middle, and end of the sampling campaign. Ions and DOC concentrations in field blanks are less than 10% of their concentrations in most PME samples, though FB1 was contaminated by the filling solution of a pH electrode, resulting in extremely high chloride concentrations (Table S5.1).

### 5.3.2. Light Absorption in Particle Extracts

DOC-normalized mass absorption coefficients at 300 nm (MAC<sub>DOC,300nm</sub>) are shown in Figure 5.1. For wildfire samples, MAC is correlated with the PM<sub>2.5</sub> concentration, which probably reflects the dominant influence of BB emissions on both PM levels and light absorbance since FBB has the highest MAC among sample types, with an average of 3.3 (± 0.4) (g C)<sup>-1</sup>. This is expected because fresh biomass burning organic aerosols (BBOA) contain abundant highly light-absorbing products from lignin-pyrolysis including substituted aromatics with high unsaturation and nitroaromatics (Budisulistiorini et al., 2017; Claeys et al., 2012; Fleming et al., 2020; Hettiyadura et al., 2021; Lin et al., 2016, 2017). Additionally, the average MAC

for FBB at 365 nm is  $1.2 (\pm 0.4) (\text{g C})^{-1}$ , similar to past values determined in water extracts of biomass burning particles ( $0.9 - 1.4 (\text{g C})^{-1}$ ) (Du et al., 2014; Fan et al., 2018; Park and Yu, 2016). The average MAC at 300 nm of ABB is  $1.5 (\pm 0.3) \text{ m}^2 (\text{g C})^{-1}$ , half the value of FBB, likely because of photobleaching of brown carbon during aging (Hems and Abbatt, 2018; Hems et al., 2021; Laskin et al., 2015; Wong et al., 2017; Zhao et al., 2015). Win-Spr has an average  $\text{MAC}_{\text{DOC}}$  ( $1.9 (\pm 0.4) \text{ m}^2 (\text{g C})^{-1}$ ) that is three times higher than that of Sum-Fall ( $0.65 (\pm 0.19) \text{ m}^2 (\text{g C})^{-1}$ ), though they have similar  $\text{PM}_{2.5}$  concentrations. This indicates that winter wood combustion can significantly enhance light absorption by particles. Our winter MAC value is similar to the values ( $2.2 (\pm 0.7) \text{ m}^2 (\text{g C})^{-1}$ ) determined in previous water extracts of Davis winter particles (Kaur et al., 2019).

We also calculated the average  $\text{MAC}_{\text{DOC}}$  for each sample type in the wavelength range of 300-600 nm, as shown in Figure 5.2. Fresh wildfire samples have the highest MAC values across the wavelength range and also has the lowest absorption Ångström exponent (AAE), which is  $7.3 (\pm 0.2)$ . ABB shows slightly lower MAC values than Win-Spr. This might be explained by the higher actinic flux and temperature in summer, which likely accelerate the aging and photobleaching of particles, leading to a larger fraction of less light absorbing SOA. AAE values of ABB and Win-Spr are similar,  $7.7 (\pm 0.3)$  and  $7.9 (\pm 0.3)$ , respectively, and are comparable to previously reported values of water-soluble organic carbon from biomass burning (Du et al., 2014; Hecobian et al., 2010; Lin et al., 2017). Sum-Fall has the lowest MAC but the highest AAE ( $9.1 (\pm 0.5)$ ).

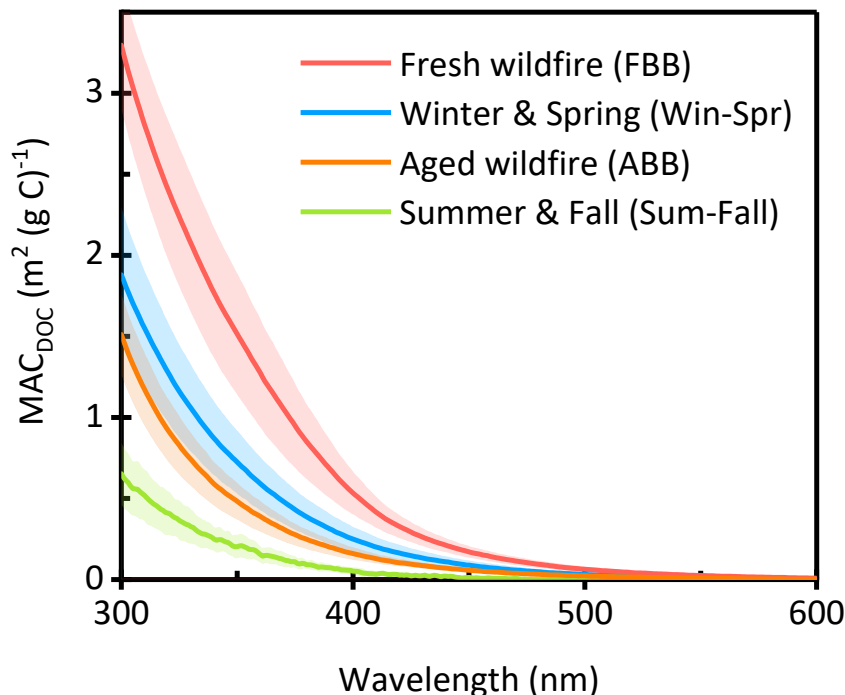


**Figure 5.2.** Average DOC-normalized mass absorption coefficients for Fresh wildfire samples (red), Winter & Spring samples (blue), aged wildfire samples (orange), and Summer & Fall samples (green). Each shaded area represents  $\pm 1$  standard deviation.

An optical property frequently used to characterize surface waters is  $E_2/E_3$ , which is the ratio of absorbance at 250 nm to that at 365 nm. In surface waters, this ratio is an indicator of the molecular weight of dissolved organic matter, with low  $E_2/E_3$  representing high molecular-weight DOM and a high ratio representative of lower DOM weights (Ossola et al., 2021).  $E_2/E_3$  in our PMEs ranges from 4.2 to 17 and is related to MAC values: as shown in Fig. 5.3, MAC decreases with increasing  $E_2/E_3$ , i.e., absorbance decreases as DOM molecular weight decreases. FBB has the lowest average  $E_2/E_3$  ( $5.8 (\pm 1.5)$ ) of our sample types, including ABB ( $12.5 (\pm 2.3)$ ), which suggests that organic molecules in fresh BB are fragmented during aging. This is consistent with the observation that high-molecular weight compounds are less abundant in aged BBOA (Farley et al., 2022). Therefore,  $E_2/E_3$  may be an easy and effective indicator to differentiate fresh and aged samples.  $E_2/E_3$  ratios for the Win-Spr samples are intermediate between the summer fresh and aged BB samples, again suggesting these biomass-burning influenced winter samples are less aged than ABB.

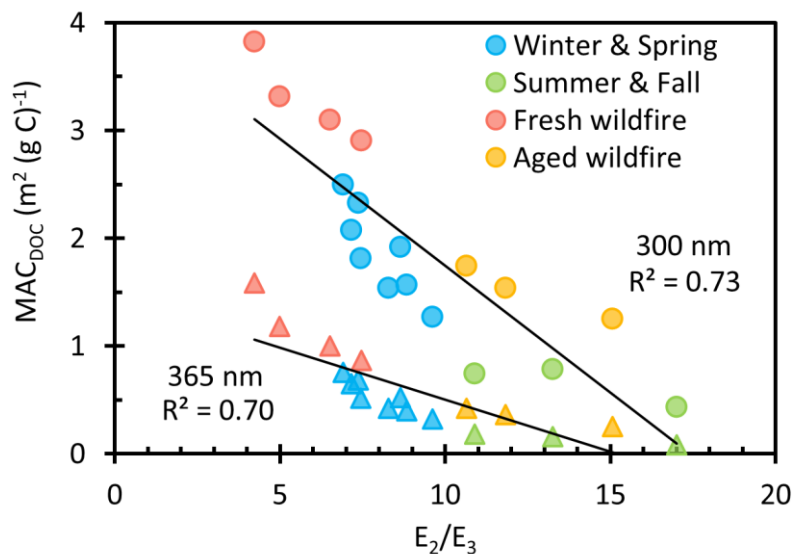


**Figure 5.3.** Mass absorption coefficients of dissolved organic carbon at 300 nm (circles) and 365 nm (triangles) as a function of E<sub>2</sub>/E<sub>3</sub> for each sample type. Solid lines represent linear regressions.

Since the light absorption of methanol extracts of particles are usually greater than those of water extracts (Liu et al., 2013; Zhang et al., 2013), we also examined light absorption from squares of the same FBB filter extracted with different solvents (water, methanol, and hexane). As shown in Fig. S5.10, the absorbance of the methanol extract is more than twice as high as the water extract, and 5 times higher than the hexane extract, indicating this FBB contains a high fraction of water-insoluble brown carbon. We also did a sequential extraction with this FBB sample and with a Win-Spr sample, with 1<sup>st</sup>, 2<sup>nd</sup>, and 3<sup>rd</sup> extraction solvents of water, methanol, and hexane, respectively. The UV-Vis spectra and PM mass extracted for each solvent extraction are shown in Fig. S5.11. For the Win-Spr and FBB samples, the PM mass recovered by the second extraction (in methanol) are only 20% and 56% of the mass extracted by the first extraction (in water), respectively, but the MeOH extract absorbance at 365 nm is similar or even greater than the water extracts. This is consistent with a previous study of sequential extraction with US western wildfire samples (Zeng et al., 2022) that water-insoluble brown carbon (e.g., polycyclic aromatic hydrocarbons) is highly light-absorbing, despite accounting for little of the PM mass. The third extraction with hexane for both samples has negligible absorbance. The high light absorption in methanol extracts suggests that the water-



insoluble chromophores have high potential to produce photooxidants. However, since our oxidant probes have been developed for the aqueous phase instead of an organic phase, we did not study the photooxidants in methanol or hexane extracts in this work.

### **5.3.3. Photooxidant Concentrations**

#### **5.3.3.1. Normalization by sample duration**

While most of our PM samples were collected for 1 day, we also collected four samples for 7 days, which resulted in extracts that were more concentrated and that had higher oxidant concentrations. To properly compare these longer samples with the rest, we normalized photooxidant concentrations in the 7-day samples to what would be expected for a 24-h sample. For  $^1\text{O}_2^*$  and  $^3\text{C}^*$ , the production rate is proportional to the brown carbon mass (Faust and Allen, 1992; Kaur et al., 2019) and so we normalized their concentrations by dividing by the duration of sampling (i.e., number of sampling days). The case for hydroxyl radical is more complicated, since past work has found that  $\bullet\text{OH}$  concentration is independent of extract concentration (Arakaki et al., 2013; Kaur et al., 2019), but unnormalized  $\bullet\text{OH}$  concentrations in our 7-day samples are clearly higher than in the adjacent 24-h samples (Fig S12). If we normalize  $\bullet\text{OH}$  using the same method as for  $^1\text{O}_2^*$  and  $^3\text{C}^*$  (i.e. normalized by the duration of sampling), the resulting  $\bullet\text{OH}$  concentrations are lower than the adjacent 24 h samples (Fig. S5.12). To obtain more reasonable estimates for  $[\bullet\text{OH}]$  in the 7-day samples, we fitted the plot of  $\bullet\text{OH}$  concentration versus particle mass/water mass ratio for Win-Spr samples with a linear regression (Fig. S5.13), and then used the regression to estimate  $\bullet\text{OH}$  concentrations in the 7-day samples using the time-normalized particle mass/water mass ratio values (i.e. measured particle mass/water ratio divided by 7).

#### **5.3.3.2. Hydroxyl radical ( $\bullet\text{OH}$ )**

As shown in Fig. 5.4a, normalized  $\bullet\text{OH}$  concentrations have a range of  $(0.2\text{-}3.2) \times 10^{-15}$  M. The values are similar to those in illuminated particle extracts from Davis and Colorado (Kaur et al., 2019; Leresche et al., 2021), but much higher than those in illuminated extracts of lab SOA and  $\text{PM}_{10}$  from

Switzerland  $(2.2-4.9) \times 10^{-17}$  M) that had low DOC ( $5 \text{ mg C L}^{-1}$ ) (Manfrin et al., 2019). Among our four sample types, fresh biomass burning samples have the highest average [ $\bullet\text{OH}$ ],  $2.5 (\pm 0.3) \times 10^{-15}$  M, while aged BB particles have a similar average concentration that is statistically indistinguishable,  $1.7 (\pm 1.4) \times 10^{-15}$  M. This is parallel to a previous finding that BBOA, compared to other types of organic aerosols, has the highest oxidative potential as measured by the DTT assay and this potential decreases with simulated atmospheric aging (Verma et al., 2015; Wong et al., 2019). Win-Spr has a similar average [ $\bullet\text{OH}$ ],  $1.5 (\pm 0.3) \times 10^{-15}$  M, while Sum-Fall is lowest at  $0.4 (\pm 0.3) \times 10^{-15}$  M. Our winter values are roughly three to four times higher than average values in previous Davis winter particle extracts and fog waters ( $0.51 (\pm 0.24) \times 10^{-15}$  M and  $0.42 (\pm 0.07) \times 10^{-15}$  M, respectively) (Kaur and Anastasio, 2017; Kaur et al., 2019). While nitrate and nitrite can be important sources of  $\bullet\text{OH}$  in atmospheric waters (Anastasio and McGregor, 2001; Kaur and Anastasio, 2017; Kaur et al., 2019; Leresche et al., 2021), these species account for less than 10% of  $\bullet\text{OH}$  in most of our current samples (Table S5.3). In our kinetic experiments, in 6 of our 18 samples (5 winter samples and one wildfire sample) BA decayed faster at the beginning of irradiation and then slowed down, with a rate difference up to a factor of 3.4 (Fig. S5.1). This indicates [ $\bullet\text{OH}$ ] in some samples is higher during the initial stage of irradiation, possibly because of rapid decomposition of labile compounds that produce  $\bullet\text{OH}$ . A similar effect was seen in biomass burning aerosols from Fresno CA, where a burst of  $\bullet\text{OH}$  was observed within the first few minutes of irradiation and was hypothesized to be due to the decomposition of peroxides through photo-Fenton reactions (Paulson et al., 2019).

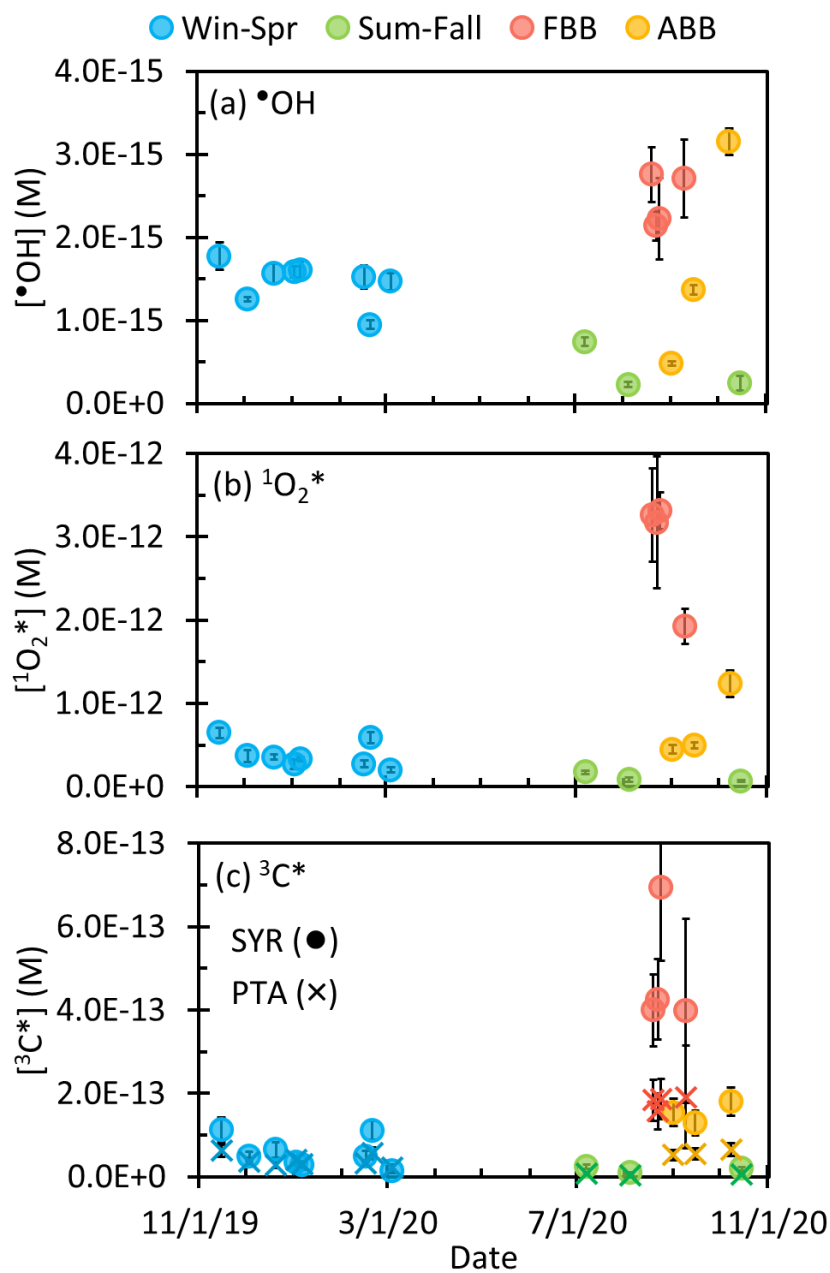


**Figure 5.4.** Steady-state concentrations of (a) hydroxyl radical, (b) singlet molecular oxygen, and (c) oxidizing triplet excited states of light-absorbing organics determined by syringol (circles) and (phenylthio)acetic acid (crosses) in particle extracts. Concentrations are all normalized by sampling duration and to midday winter solstice sunlight in Davis to highlight seasonal differences in particle reactivity; the equivalent plots with concentrations calculated for the midday sunlight of each sample collection period is shown in Figure S5.14. Error bars represent standard error propagated from linear regression and error in rate constants,

Fig. 5.5a shows  $\bullet\text{OH}$  concentration as a function of dissolved organic carbon for the four sample types. For comparison, we also include data from Kaur et al. (2019), who measured photooxidant concentrations in Davis winter particle extracts. Though samples in Kaur et al. (2019) have similar values of DOC as our 24-h Win-Spr samples, their  $[\bullet\text{OH}]$  is 5 times lower and independent of DOC. While  $\bullet\text{OH}$  appears to increase with DOC (Fig. 5.5a), the data is noisy and the linear correlation is weak ( $R^2 = 0.40$ ). A previous study on Minnesota surface waters observed a logarithmic relationship between  $[\bullet\text{OH}]$  and absorbance coefficient at 440 nm (Chen et al., 2020), which in turn was correlated to DOC. They speculated this is because the dominant  $\bullet\text{OH}$  sink changes from bicarbonate/carbonate at low DOC to DOC at high DOC levels, but bicarbonate/carbonate are negligible sinks in our extracts since they are acidic (pH 4.2).  $[\bullet\text{OH}]$  in FBB is independent of DOC, but the three ABB samples show  $\bullet\text{OH}$  increasing with DOC. We recently found that  $[\bullet\text{OH}]$  increases with DOC in a dilution series of summer wildfire PM and hypothesized that  $\bullet\text{OH}$  production is a bimolecular reaction that increases as the square of sample concentration (Ma et al., 2022a). This might explain the ABB results.

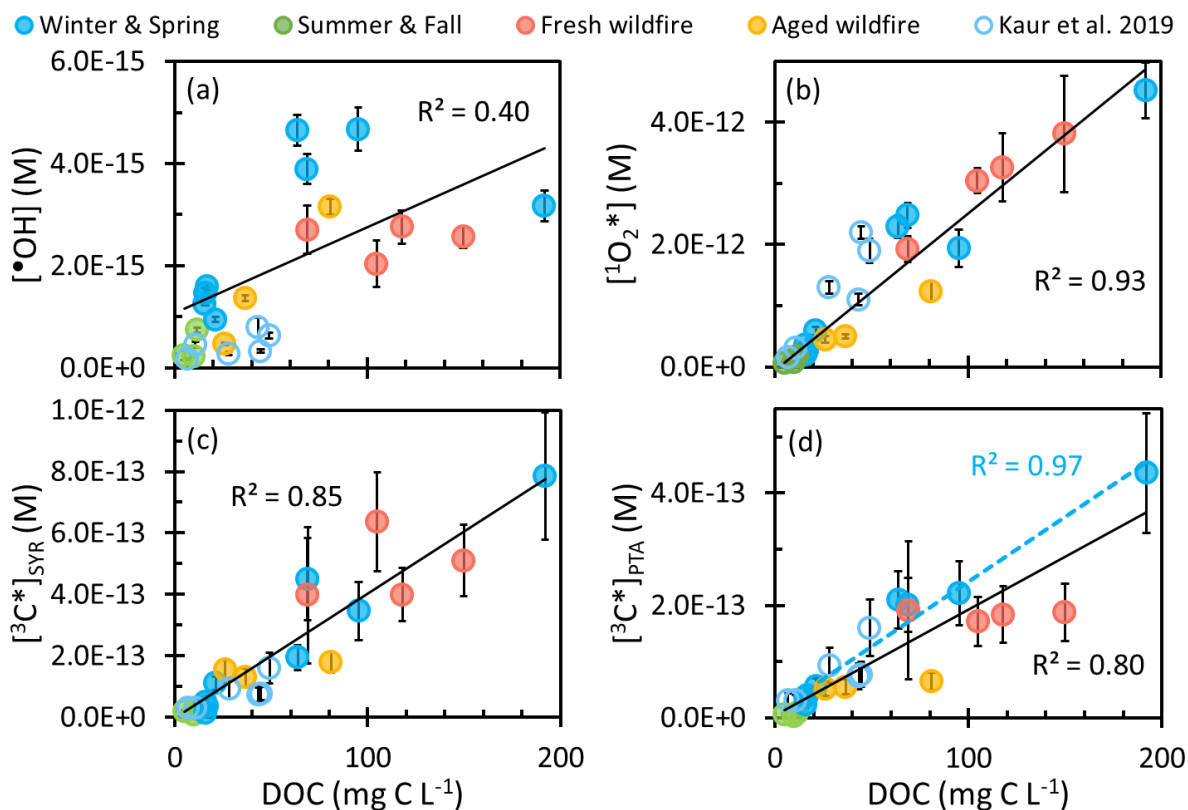


**Figure 5.5.** Steady-state concentrations of (a) hydroxyl radical, (b) singlet molecular oxygen, and oxidizing triplet excited states of organic matter determined by (c) syringol and (d) (phenylthio)acetic acid as a function of dissolved organic matter for each sample type (solid circles). Previous measurements made in Davis winter particle extracts are in open circles (Kaur et al., 2019). Solid black lines are linear regressions between oxidant concentrations in this work and DOC. The blue dashed line in panel (d) is the linear regression of the Win-Spr samples ( $R^2 = 0.97$ ). Error bars represent standard error propagated from linear regression and error in rate constants.

### 5.3.3.3. Singlet molecular oxygen ( $^1\text{O}_2^*$ )

Winter-solstice-sunlight normalized  $^1\text{O}_2^*$  has a concentration range of  $(0.7\text{-}32) \times 10^{-13}$  M (Fig. 5.4b) and correlates well with ambient  $\text{PM}_{2.5}$  concentration. (Fig. S5.15). These concentrations are similar to previously reported values in particle extracts  $(0.6\text{-}22) \times 10^{-13}$  M (Kaur et al., 2019; Leresche et al., 2021), but are roughly 100 times higher than concentrations in illuminated extracts of biogenic and anthropogenic SOA,  $(0.8\text{-}45) \times 10^{-15}$  M (Manfrin et al., 2019). Our higher  $^1\text{O}_2^*$  concentrations are only partially explained by our 1 – 40 times higher DOC concentrations, but the remaining difference is likely due to more light

absorption in our samples. Our values are also similar to [ $^1\text{O}_2^*$ ] in illuminated solutions of dissolved soot with simulated sunlight,  $(0.6 - 65) \times 10^{-13}$  M (Li et al., 2019), even though their samples absorbed very little light. Among our samples, Fresh BB has the highest average [ $^1\text{O}_2^*$ ], followed by ABB, with values of  $29 (\pm 7) \times 10^{-13}$  M and  $7.3 (\pm 0.4) \times 10^{-13}$  M, respectively. Leresche et al. (2021) found that [ $^1\text{O}_2^*$ ] decreased by a factor of two in particle extracts after sunlight irradiation, which is consistent with our observation that aged particle extracts have lower [ $^1\text{O}_2^*$ ]. Win-Spr and Sum-Fall samples have average [ $^1\text{O}_2^*$ ] values of  $3.8 (\pm 1.6) \times 10^{-13}$  M and  $1.1 (\pm 0.6) \times 10^{-13}$  M, respectively. The higher Win-Spr concentrations are probably because of the influence of biomass burning.

As shown in Fig. 5.5(b),  $^1\text{O}_2^*$  concentrations linearly increase with DOC ( $R^2 = 0.93$ ), consistent with our understanding that organic matter is the primary source of  $^1\text{O}_2^*$ . Moreover, all four types of samples share the same slope, suggesting the relationship between [ $^1\text{O}_2^*$ ] and DOC is independent of particle type or chemical composition, which is somewhat surprising given the large differences in light absorption for the different types (Fig. 5.2). This might be because this relationship is mostly driven by the high DOC samples, so the contributions from Sum-Fall and ABB samples to the slope are minor. When plotting [ $^1\text{O}_2^*$ ] as a function of absorbance at 300 nm and at 365 nm (Figs. S5.16b and S5.17b, respectively), we do observe differences among sample types. Win-Spr samples present a steeper slope (as do samples from Kaur et al. (2019)) compared to wildfire samples, consistent with our previous work (Ma et al., 2022a). The  $^1\text{O}_2^*$  concentrations in previous Davis winter particle extracts (Kaur et al., 2019) also follow the linear regression of this work. While this suggests DOC is a robust descriptor for  $^1\text{O}_2^*$  concentrations, most of our particle samples were influenced by biomass burning. Other particle types - such as biogenic SOA and fossil fuel combustion - might have different relationships between  $^1\text{O}_2^*$  and DOC, as suggested by the Manfrin et al. (2019) results.

#### 5.3.3.4. Oxidizing triplet excited states of brown carbon ( $^3\text{C}^*$ )

We used two probes – syringol (SYR) and (phenylthio)acetic acid (PTA) – to quantify oxidizing triplet excited states. SYR reacts rapidly with both strongly and weakly oxidizing triplets, while PTA is only reactive with strongly oxidizing triplets (Ma et al., 2022b). However, syringol has a disadvantage that its decay by  $^3\text{C}^*$  can be inhibited by dissolved organic matter, while PTA is largely resistant to inhibition (Ma et al., 2022b; Maizel and Remucal, 2017; McCabe and Arnold, 2017; Wenk et al., 2011). As shown in Fig. 5.4c, winter-solstice-normalized (and inhibition-corrected)  $^3\text{C}^*$  concentrations have a range of  $(0.13 - 6.9) \times 10^{-13}$  M as determined by SYR and  $(0.03 - 1.9) \times 10^{-13}$  M by PTA. The  $^3\text{C}^*$  concentration follows  $\text{PM}_{2.5}$  concentration well, with low values during non-wildfire periods and very high values during wildfire-influenced periods (Fig. S5.15). For nearly all samples,  $[\text{}^3\text{C}^*]_{\text{SYR}}$  is higher than  $[\text{}^3\text{C}^*]_{\text{PTA}}$ . As seen for  $^1\text{O}_2^*$ , FBB has the highest average  $[\text{}^3\text{C}^*]$ ,  $4.8 (\pm 1.4) \times 10^{-13}$  M from SYR and  $1.8 (\pm 1.6) \times 10^{-13}$  M from PTA, due to the high organic amounts in these samples. Normalized to the FBB average, the FBB, ABB, Win-Spr, and Sum-Fall samples have triplet concentration ratios of  $1 : 0.32 : 0.12 : 0.04$  as determined by SYR and  $1 : 0.32 : 0.21 : 0.03$  as determined by PTA. Since dissolved oxygen is the major triplet sink in all of these relatively dilute extracts, the variations in triplet concentrations reflect differences in  $^3\text{C}^*$  formation rates, which is driven by DOC concentrations.

Figure 5.5c shows the correlation between  $[\text{}^3\text{C}^*]_{\text{SYR}}$  and DOC for each sample type, along with data from Kaur et al. (2019).  $[\text{}^3\text{C}^*]_{\text{SYR}}$  linearly increases with DOC ( $R^2 = 0.83$ ) independent of sample type, likely because SYR reacts rapidly with a wide range of triplets (Kaur and Anastasio, 2018). However, Figs. S5.16c and S17c show some differences between sample types in the relationship between  $[\text{}^3\text{C}^*]_{\text{SYR}}$  and absorbance at 300 or 365 nm, with Win-Spr samples having a greater slope. However, it is hard to tell the trend of FBB samples, in part because there are only four samples. As shown in Fig. 5.5d,  $[\text{}^3\text{C}^*]_{\text{PTA}}$  also linearly increases with DOC, though the correlation is not as good as  $[\text{}^1\text{O}_2^*]$  or  $[\text{}^3\text{C}^*]_{\text{SYR}}$ . Win-Spr samples present a slightly higher slope than wildfire samples (FBB and ABB); oddly,  $[\text{}^3\text{C}^*]_{\text{PTA}}$  is nearly independent of DOC within either biomass burning group. The greater slope of  $[\text{}^3\text{C}^*]_{\text{PTA}}$  with DOC for the Win-Spr samples suggests

these samples contain a higher fraction of highly oxidizing  ${}^3\text{C}^*$  than the wildfire samples. The difference in slopes is more obvious in Figs. S5.16d and S5.17d, where  $[\text{}^3\text{C}^*]_{\text{PTA}}$  is a function of absorbance at 300 or 365 nm.

Since PTA only captures  ${}^3\text{C}^*$  that have high reduction potentials, while SYR reacts rapidly with both strongly and weakly oxidizing triplets, the ratio  $[\text{}^3\text{C}^*]_{\text{PTA}}/[\text{}^3\text{C}^*]_{\text{SYR}}$  provides an estimate of the fraction of oxidizing  ${}^3\text{C}^*$  that are strong oxidants. As shown in Fig. 5.6, the ratio  $[\text{}^3\text{C}^*]_{\text{PTA}}/[\text{}^3\text{C}^*]_{\text{SYR}}$  ranges from 0.27 to 1.7 with an average value of  $0.58 (\pm 0.38)$ , indicating roughly 60% of oxidizing triplets are strong oxidants. The Win-Spr samples have an average ratio of  $0.86 (\pm 0.43)$ , significantly higher than the rest of the samples ( $0.37 \pm 0.07$ ), indicating that they produce a higher fraction of strongly oxidizing  ${}^3\text{C}^*$ . Precursors for more oxidizing triplets include quinones, aromatic ketones and aromatic aldehydes, while weakly oxidizing triplet precursors include polycyclic aromatic compounds (McNeill and Canonica, 2016).

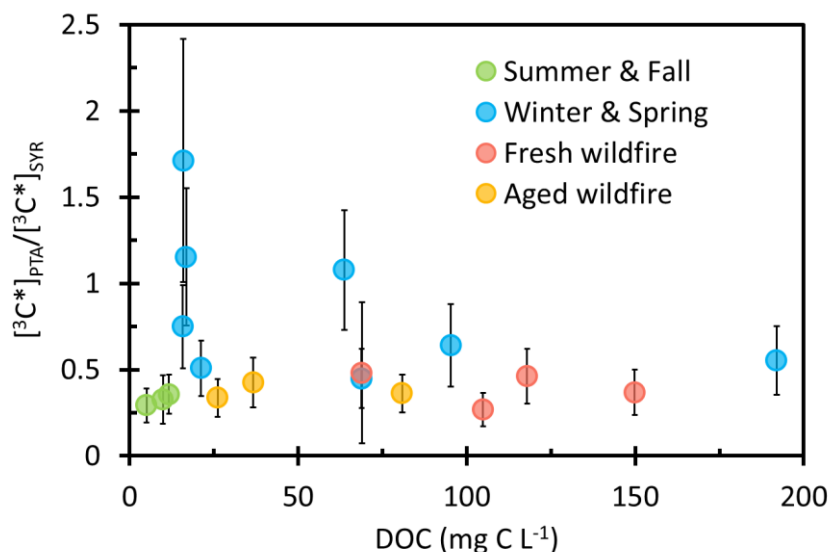


**Figure 5.6.** The ratio of oxidizing triplet excited state concentrations determined by PTA to those determined by SYR as a function of DOC for each sample type.

We can also gain some insight into extract compositions from the inhibition factors (*IF*) (Section S5.1) for SYR and PTA in each sample. An *IF* of 1 represents no inhibition of probe decay by the sample,



while an  $IF$  of 0 indicates that the triplet-mediated decay of probe is completely reversed by DOM in the sample. Among our samples,  $IF$  for SYR ( $IF_{\text{SYR,corr}}$ ) ranges from 1.2 to 0.21, with an average value of 0.64 ( $\pm 0.29$ ) (Table S5.6 and Fig. S5.18). This indicates that SYR decay by  $^3\text{C}^*$  in PME can be heavily inhibited, suggesting that our PMEs contain abundant antioxidants such as phenolic or aniline moieties (Wenk and Canonica, 2012; Wenk et al., 2011). As shown in Fig. S5.18b,  $IF_{\text{SYR,corr}}$  generally decreases with increasing DOC, consistent with previous surface water studies (Cannonica and Laubscher, 2008; McCabe and Arnold, 2017). We fit  $IF_{\text{SYR,corr}}^{-1}$  versus DOC using a linear regression with all samples (Ma et al., 2022b; Wenk et al., 2011) as shown in Fig S18b. The fitted slope  $0.015 \text{ L mg C}^{-1}$ ; the inverse of the slope,  $67 (\pm 13) \text{ mg C L}^{-1}$ , represents the DOC concentration that causes  $IF_{\text{SYR,corr}}$  to equal 0.5. All of the sample groups essentially fit on the same line. The  $IF$  for PTA ( $IF_{\text{PTA,corr}}$ ) ranges from 1.5 to 0.6, with an average value of  $1.1 (\pm 0.2)$ , demonstrating its better resistance to inhibition (Fig. S5.18c). We also measured the inhibition factor of furfuryl alcohol ( $IF_{\text{FFA}}$ ) as the indicator of the ability of DOM in PME to quench  $^3\text{C}^*$  (Fig. S5.18a).  $IF_{\text{FFA}}$  decreases with increasing DOC, ranging from 0.5 (i.e., DOM is reducing the triplet concentration to 50 % of its non-quenched value) to 1.4 (i.e., no quenching of triplets by PME DOM). From the linear fit between  $IF_{\text{FFA}}^{-1}$  and DOC, we can obtain the second-order rate constant of DOM quenching  $^3\text{DMB}^*$  (Ma et al., 2022b; Wenk et al., 2011, 2013), which is  $2.7 (\pm 0.7) \times 10^7 \text{ L (mol-C)}^{-1} \text{ s}^{-1}$ . This value is at the same order of magnitude as rate constants of DOM quenching oxidizing  $^3\text{C}^*$  in Davis particle extracts ( $(5.7 - 12) \times 10^7 \text{ L (mol C)}^{-1} \text{ s}^{-1}$ ) (Ma et al., 2022a) and the value of surface water DOM quenching  $^3\text{C}^*$  determined by laser flash photolysis ( $(1.3-7.9) \times 10^7 \text{ L (mol C)}^{-1} \text{ s}^{-1}$ ) (Wenk et al., 2013).

### 5.3.3.5. Normalization by photon flux

Photooxidant concentrations in Figures 5.4 and 5.5 are all normalized to the same actinic flux condition (i.e., solar noon on the winter solstice in Davis CA,  $j_{2\text{-NB}} = 0.007 \text{ s}^{-1}$ ) to highlight seasonal differences in particle reactivity. However, photon fluxes vary throughout the year, which will affect the rate of photooxidant formation and accompanying concentration. To account for this effect, we calculated midday  $j_{2\text{NB}}$  values as a function of date during our sampling campaign, as shown in Fig. S5.19 and

described in Section S5.3. The estimated  $j_{2NB}$  value on midday of the summer solstice is  $0.013 \text{ s}^{-1}$ , which is near 2 times higher than the winter value (Table S5.9). Next, we estimated midday  $j_{2NB}$  values for each sampling day and normalized photooxidant concentrations to that sunlight condition. Figure S5.14 shows the equivalent plot of Figure 5.3 after photon flux normalization, which increased oxidant concentrations by factors of 1.0 to 1.9. The average factors for FBB and Sum-Fall samples are 1.7, while ABB and Win-Spr have average factors of 1.5 and 1.2, respectively. At this point we do not have enough information to understand how seasonal variations in temperature affect oxidant concentrations, so we have not attempted to include this factor.

### 5.3.4. Quantum Yields for Photooxidants

#### 5.3.4.1. Hydroxyl radical

To investigate how sample type affects the efficiency of photooxidant formation, we determined apparent quantum yields of photooxidant formation ( $\Phi_{Ox}$ ), i.e., the fraction of absorbed photons that result in formation of a particular photooxidant:

$$\Phi_{Ox} = \frac{P_{Ox}}{R_{abs}} \quad (5.7)$$

where  $P_{Ox}$  is the oxidant production rate and  $R_{abs}$  is the rate of sunlight absorption by the sample between 300 and 450 nm (Kaur et al., 2019). We calculate the production rate of  $\bullet\text{OH}$ ,  $P_{OH}$ , by assuming it is equal to the  $\bullet\text{OH}$  consumption rate since hydroxyl radical (and the other photooxidants) are at steady state. Thus,  $P_{OH}$  is equal to the product of  $[\bullet\text{OH}]$  and the first-order rate constant of  $\bullet\text{OH}$  loss by natural sinks ( $k'_{OH}$ ). To estimate  $k'_{OH}$ , we assume that organic matter is the dominant sink for  $\bullet\text{OH}$  (Kaur et al., 2019) and that  $k'_{OH}$  is the product of DOC concentration and the second-order rate constant of DOC with  $\bullet\text{OH}$  ( $k_{DOC+OH}$ ). We used the average value of  $k_{DOC+OH}$  measured in Davis winter and summer wildfire particle extracts (Ma et al., 2022a), which is  $2.7 (\pm 0.4) \times 10^8 \text{ L (mol-C)}^{-1} \text{ s}^{-1}$ . This value is slightly lower than that determined by Arakaki et al. (2013) for a broad range of atmospheric waters ( $3.8 (\pm 1.9) \times 10^8 \text{ L (mol-C)}^{-1} \text{ s}^{-1}$ ) and the one

from Leresche et al. (2021) for Colorado PM extracts ( $4.9 (\pm 2.3) \times 10^8 \text{ L (mol-C)}^{-1} \text{ s}^{-1}$ ), but none of these are statistically different. In our samples, the calculated  $k'_{\text{OH}}$  is in the range  $(0.11 - 4.3) \times 10^6 \text{ s}^{-1}$  (Table S5.3), yielding  $P_{\text{OH}}$  in the range of  $(0.04-14) \times 10^{-9} \text{ M s}^{-1}$ , similar to past values for fog/cloud waters and particle extracts (Arakaki et al., 2013; Leresche et al., 2021; Tilgner and Herrmann, 2018).

Our calculated apparent quantum yields of  $\bullet\text{OH}$  are shown in Fig. 5.7a, along with past Davis winter PME samples from Kaur et al. (2019).  $\Phi_{\text{OH}}$  ranges from 0.01 % to 0.10 % in our samples, which are generally higher than values from Kaur et al. (2019) and from  $\text{PM}_{10}$  and lab SOA water extracts (Manfrin et al., 2019). As expected,  $\Phi_{\text{OH}}$  appears independent of DOC. Average  $\bullet\text{OH}$  quantum yields for Win-Spr, Sum-Fall, FBB, and ABB are  $0.044 (\pm 0.022) \%$ ,  $0.028 (\pm 0.010) \%$ ,  $0.021 (\pm 0.005) \%$ , and  $0.049 (\pm 0.050) \%$ , respectively. While there are some differences in these averages, none are statistically different ( $p > 0.05$ ).

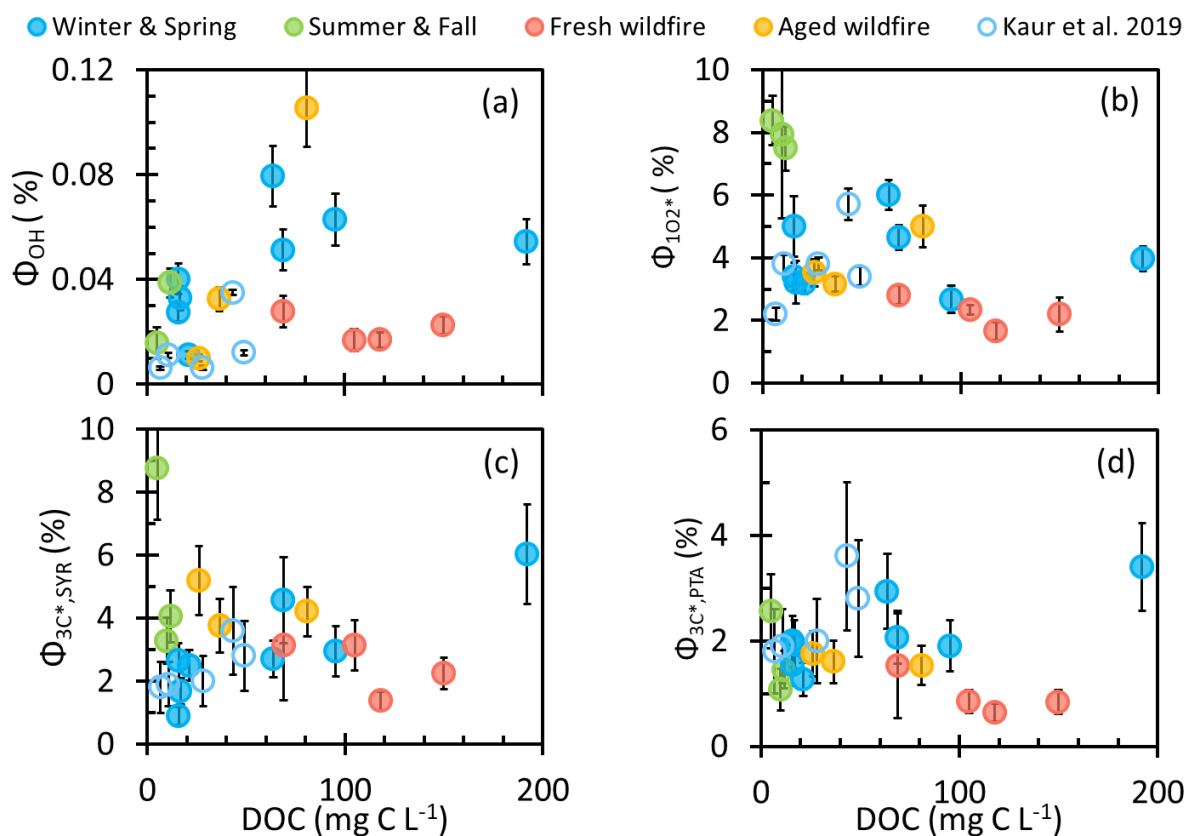


**Figure 5.7.** Apparent quantum yields of (a) hydroxyl radical, (b) singlet molecular oxygen, and oxidizing triplets determined by (c) syringol and (d) (phenylthio)acetic acid as a function of dissolved organic matter for each sample type (solid circles). Previous measurements made in Davis winter particle extracts are in open circles (Kaur et al., 2019).

### 5.3.4.2. Singlet molecular oxygen

To calculate the apparent quantum yields of  $^1\text{O}_2^*$  ( $\Phi_{1\text{O}_2^*}$ ), we assume that  $\text{H}_2\text{O}$  is the dominant sink for  $^1\text{O}_2^*$  in our PM extracts. This is a reasonable assumption since the first-order rate constants for  $^1\text{O}_2^*$  loss via DOC are  $(0.04 - 2) \times 10^3 \text{ s}^{-1}$  in our samples (based on an estimated  $^1\text{O}_2^* + \text{DOC}$  rate constant of  $1 \times 10^5 \text{ L (mol-C)}^{-1} \text{ s}^{-1}$ ; (Kaur et al., 2019)), while the rate constant for  $^1\text{O}_2^*$  loss by water is  $2.2 \times 10^5 \text{ s}^{-1}$  (Bilski et al., 1997). Therefore, we calculated the production rate of  $^1\text{O}_2^*$  ( $P_{1\text{O}_2^*}$ ) by multiplying the rate constant of  $\text{H}_2\text{O}$  quenching of  $^1\text{O}_2^*$  ( $k'_{\text{H}_2\text{O}}$ ) by  $[^1\text{O}_2^*]$ . As shown in Fig. 5.7b,  $\Phi_{1\text{O}_2^*}$  ranges from 1.7% to 8.4%, comparable to values from Kaur et al., which are shown as open circles in the figure, as well as from SOA and ambient particle extracts in other studies (0.3 – 4.5 %) (Kaur et al., 2019; Leresche et al., 2021; Manfrin et al., 2019). But our  $\Phi_{1\text{O}_2^*}$  values are significantly lower than those in dissolved soot extracts (33%) (Li et al., 2019) under 377 nm irradiation. Sum-Fall has the highest average  $\Phi_{1\text{O}_2^*}$ ,  $7.9 (\pm 0.4) \%$ , which is significantly different from the others, while Win-Spr and ABB have similar average values,  $4.0 (\pm 1.1)$  and  $3.9 (\pm 1.0)$ , respectively, while FBB shows the lowest average  $\Phi_{1\text{O}_2^*}$  of  $2.2 (\pm 0.5) \%$ . The higher quantum yield for aged biomass burning PM compared to fresh BB PM is broadly consistent with the enhancement in  $\Phi_{1\text{O}_2^*}$  resulting from ozonation of surface water DOM (Leresche et al., 2019). The difference among sample types is more pronounced when  $\Phi_{1\text{O}_2^*}$  is plotted as a function of MAC. As shown in Figs. S5.20b and S5.21b,  $\Phi_{1\text{O}_2^*}$  decreases with absorbance at 300 or 365 nm, indicating that less light-absorbing brown carbon (e.g., Sum-Fall) more efficiently produces  $^1\text{O}_2^*$  compared to high-MAC samples (e.g., FBB). In surface waters,  $\Phi_{1\text{O}_2^*}$  is positively correlated with  $E_2/E_3$ , i.e., the  $^1\text{O}_2^*$  quantum yield increases for DOM with lower average molecular weight molecules (Berg et al., 2019; Ossola et al., 2021). We find a similar linear relationship in our samples, with an  $R^2$  of 0.54 (Fig. S5.22). The fresh BB extract has low  $E_2/E_3$  (and low  $\Phi_{1\text{O}_2^*}$ ), suggesting that it contains more high-molecular-weight compounds that

absorb significant amounts of light but inefficiently produce  $^1\text{O}_2^*$ . It has been suggested that DOM with a high lignin content can have a high degree of charge transfer interactions, which results in low  $\Phi_{1\text{O}_2^*}$  (Ossola et al., 2021). Despite the relatively inefficient production of singlet oxygen by the fresh BB extracts, these samples have some of the highest  $^1\text{O}_2^*$  concentrations (Fig. 5.4), a result of their very strong light absorption (Fig. 5.2).

### 5.3.4.3. Oxidizing triplet excited states

To calculate the production rate of  $^3\text{C}^*$ , we first need to estimate the  $^3\text{C}^*$  sink, which is dominated by dissolved oxygen at low DOC but organic matter as DOC increases. We estimated average second-order rate constants for DOC reacting with and quenching  $^3\text{C}^*$  ( $k_{\text{rxn}+\text{Q},3\text{C}^*}$ ) in our samples by fitting  $[^3\text{C}^*]$  as a function of DOC with a hyperbolic regression (Fig. S5.23). Values of  $k_{\text{rxn}+\text{Q},3\text{C}^*}$  can be calculated from one of the regression fitting parameters (Kaur et al., 2019); the resulting rate constants are  $7.2 (\pm 2.2) \times 10^7 \text{ L (mol-C)}^{-1} \text{ s}^{-1}$  for  $^3\text{C}^*$  determined by SYR and  $7.4 (\pm 2.5) \times 10^7 \text{ L (mol-C)}^{-1} \text{ s}^{-1}$  for  $^3\text{C}^*$  by PTA. We then calculate the production rate of  $^3\text{C}^*$  with:

$$P_{3\text{C}^*} = (k_{\text{rxn}+\text{Q},3\text{C}^*}[\text{DOC}] + k_{3\text{C}^*+\text{O}_2}[\text{O}_2]) \times [^3\text{C}^*] \quad (5.8)$$

where  $k_{3\text{C}^*+\text{O}_2}$  is the second-order rate constant of dissolved oxygen reacting with  $^3\text{C}^*$  ( $2.8 \times 10^9 \text{ M}^{-1} \text{ s}^{-1}$ ) (Kaur et al., 2019) and  $[\text{O}_2]$  is the dissolved oxygen concentration, 280  $\mu\text{M}$  at 20 °C for an air-saturated solution (U.S. Geological Survey, 2020). The apparent quantum yield of  $^3\text{C}^*$  is then calculated using  $P_{3\text{C}^*}$  divided by the rate of light absorption (Eq. 5.7).

Figures 5.7c and 5.7d show quantum yields of  $^3\text{C}^*$  determined by SYR ( $\Phi_{3\text{C}^*,\text{SYR}}$ ) and PTA ( $\Phi_{3\text{C}^*,\text{PTA}}$ ).  $\Phi_{3\text{C}^*,\text{SYR}}$  has a range of (0.9-8.8) % and an average value of  $3.5 (\pm 1.8)$  %. Our values are similar to  $\Phi_{3\text{C}^*}$  in past Davis winter PM extracts (as shown by the open circles in the figures), as well as fog waters and surface waters, which are in the range (0.3-14) % (Kaur and Anastasio, 2018; McCabe and Arnold, 2018). We do not observe significant differences in  $\Phi_{3\text{C}^*,\text{SYR}}$  among sample types (Fig. S5.24), consistent with the

similarities among sample types in the relationship of  $[^3\text{C}^*]_{\text{SYR}}$  versus DOC (Fig. 5.4).  $\Phi_{3\text{C}^*,\text{PTA}}$  has a range of (0.6-3.4) %, with an average value of  $1.7 (\pm 0.7)$  %, half of the average  $\Phi_{3\text{C}^*,\text{SYR}}$ . Win-Spr has the highest average  $\Phi_{3\text{C}^*,\text{PTA}}$ ,  $2.1 (\pm 0.7)$  %, while FBB has the lowest,  $0.96 (\pm 0.39)$  %, but they are not statistically different. Through  $^3\text{C}^*$  is the precursor of  $^1\text{O}_2^*$ ,  $\Phi_{3\text{C}^*}$  does not correlate well with MAC, unlike  $\Phi_{1\text{O}_2^*}$  (Fig. S5.20). In surface waters,  $\Phi_{3\text{C}^*}$  often increases with  $E_2/E_3$ , similar to  $\Phi_{1\text{O}_2^*}$  (Berg et al., 2019; Maizel and Remucal, 2017; McCabe and Arnold, 2017), but we do not see this behavior in our samples (Fig. S5.25).

We next use our quantum yields to estimate the fraction of the total triplet pool that can oxidize SYR or PTA. Since almost all triplets can transfer energy to dissolved oxygen to make  $^1\text{O}_2^*$ , we estimate the quantum yield of total  $^3\text{C}^*$  as  $\Phi_{1\text{O}_2^*}/f_{\Delta}$ , where  $f_{\Delta}$  is the fraction of  $^3\text{C}^*$  interaction with dissolved oxygen that forms  $^1\text{O}_2^*$ , assuming 0.53 (Kaur and Anastasio, 2018; McNeill and Canonica, 2016). Therefore, the fraction of oxidizing triplets can be calculated as  $\Phi_{3\text{C}^*}/(\Phi_{1\text{O}_2^*}/f_{\Delta})$ , with values shown in Fig. S5.26. For  $^3\text{C}^*$  determined by SYR, the fraction ranges from 0.14 to 0.81, with an average of  $0.47 (\pm 0.20)$  and no statistical difference between the four sample types. This average value is similar to those determined in fog waters ( $0.55 \pm 0.44$ ) as well as in previous Davis winter particle extracts ( $0.31 \pm 0.11$ ) (Kaur and Anastasio, 2018; Kaur et al., 2019), indicating that roughly half of the triplets in Davis PM and fog samples are oxidizing. For  $^3\text{C}^*$  determined by PTA, the strongly oxidizing triplet fraction ranges from 0.07 to 0.45, with an average of  $0.24 (\pm 0.09)$ ; this is half the SYR value, suggesting that approximately half of oxidizing  $^3\text{C}^*$  possesses a high reduction potential, consistent with the results of Fig. 5.6. For  $^3\text{C}^*$  determined by PTA, Sum-Fall has a statistically lower average value,  $0.11 (\pm 0.05)$ , compared to Win-Spr ( $0.29 \pm 0.09$ ), FBB ( $0.22 \pm 0.04$ ), and ABB ( $0.23 \pm 0.06$ ). This is reasonable because Sum-Fall samples were not significantly influenced by biomass burning, leading to a lower aromatic content and more weakly oxidizing triplets (McNeill and Canonica, 2016).

### 5.3.5. Extrapolation of Photooxidant Concentrations to ALW Conditions

Particle mass/water mass ratios in our PM extracts range from  $10^{-5}$  to  $10^{-3}$   $\mu\text{g PM}/\mu\text{g H}_2\text{O}$  (Table S5.1), which are typical for dilute hydrometeors like cloud and fog drops (Hess et al., 1998; Nguyen et al., 2016; Parworth et al., 2017). While the results in dilute extracts are interesting and applicable to cloud and fog chemistry, our ultimate goal is to understand photooxidant concentrations in aerosol liquid water, which is orders of magnitude more concentrated (typically near  $1 \mu\text{g PM}/\mu\text{g H}_2\text{O}$ ). Due to the very limited water content of particles, we cannot study this condition directly using our current probe techniques. Instead, our approach has been to quantify photooxidant kinetics (i.e., formation rates and loss rate constants) in a single PM sample as a function of particle dilution and then extrapolate to ALW conditions (Kaur et al., 2019; Ma et al., 2022a). To do this with our current samples, we use parameters obtained from our recent dilution study of a winter (WIN) and a summer (SUM)  $\text{PM}_{2.5}$  sample and apply them to the seasonality samples in this paper. Details about the prediction calculation and the parameters used in the extrapolation are provided in Section S5.4 and Table 5.9.

We calculate  $[\bullet\text{OH}]$  in ALW using the average  $P_{\text{OH}}$  and  $k'_{\text{OH}}$  values that were determined from the Davis winter and summer wildfire particle extracts in our previous study (Ma et al., 2022a). Since we do not observe significant differences in relationships of  $[\bullet\text{OH}]$  and DOC (Figure 5.4a) among our four sample types (Figure 5.5), we do not consider the effect of sample type on  $[\bullet\text{OH}]$  in our extrapolations. As shown in Fig. S5.27, the predicted  $\bullet\text{OH}$  concentration is relatively constant across drop to particle conditions, with a range of  $(6 - 9) \times 10^{-15}$  M. The predicted  $[\bullet\text{OH}]$  in dilute condition is higher than our measured values because we included  $\bullet\text{OH}$  from the gas phase in our calculation (Kaur et al., 2019). As shown in Figure 5.8,  $[\bullet\text{OH}]$  at  $1 \mu\text{g PM}/\mu\text{g H}_2\text{O}$  is  $7 \times 10^{-15}$  M. This value is near 10 times higher than the predicted value by Kaur et al. (2019).

We next consider singlet oxygen. As shown in Fig. S5.29,  $[^1\text{O}_2^*]$  for each sample type increases with particle mass/water mass ratio under dilute conditions, peaks near  $0.01 - 0.1 \mu\text{g PM}/\mu\text{g H}_2\text{O}$ , and then

decreases under more concentrated conditions. As shown in Fig. 5.8, at  $1 \mu\text{g PM}/\mu\text{g H}_2\text{O}$ , Win-Spr has the highest  $[^1\text{O}_2^*]$  ( $7 \times 10^{-12} \text{ M}$ ), followed by Sum-Fall ( $2 \times 10^{-12} \text{ M}$ ), FBB ( $0.9 \times 10^{-12} \text{ M}$ ), and ABB ( $0.6 \times 10^{-12} \text{ M}$ ). Win-Spr is characterized by its high  $^1\text{O}_2^*$  quantum yield but low rate of DOC quenching for both  $^3\text{C}^*$  and  $^1\text{O}_2^*$ . In contrast, FBB and ABB have more brown carbon (and therefore greater sources of  $^1\text{O}_2^*$ ) but high DOC, which leads to greater sinks for triplets and singlet oxygen. Moreover, DOC in FBB and ABB quenches  $^3\text{C}^*$  more efficiently than that in Win-Spr (i.e., the BB samples have higher values of  $k_{3\text{C}^*+\text{DOC}}$ ). Therefore, their  $[^1\text{O}_2^*]$  in ALW is similar to or even lower than  $[^1\text{O}_2^*]$  measured in FBB and ABB extracts, while the ALW singlet oxygen concentrations for Win-Spr and Sum-Fall are nearly 20 times higher than their corresponding averages in extracts. Our estimated  $[^1\text{O}_2^*]$  is 20 – 200 times lower than the value derived by Kaur et al. (2019),  $1.6 \times 10^{-10} \text{ M}$ , for Davis winter particle water. This is because we account for the suppressing effect of the reaction between DOC with  $^3\text{C}^*$  on  $^1\text{O}_2^*$  production.

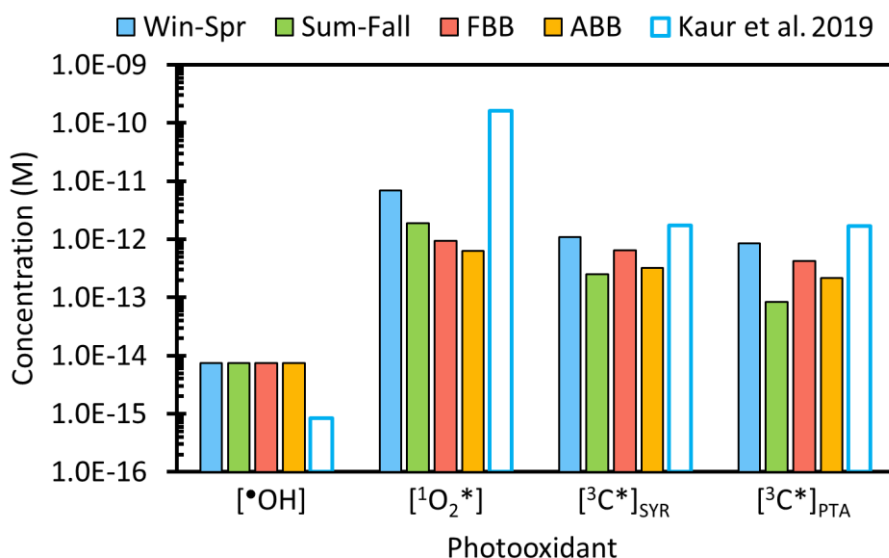


**Figure 5.8.** Predicted photooxidant concentrations for each sample type under aerosol liquid water conditions ( $1 \mu\text{g PM}/\mu\text{g H}_2\text{O}$ ). Previous extrapolation made in Davis winter particle extracts are in blank bars (Kaur et al., 2019), where  $^3\text{C}^*$  is the geometric mean of their best fit and high estimate (Kaur et al., 2019).

Our final ALW predictions are for oxidizing triplets.  $[^3\text{C}^*]$  for all sample types increases with particle mass concentration under dilute conditions, but then reaches a plateau as solutions become more



concentrated (Fig. S5.30). As shown in Fig. 5.8,  $[^3\text{C}^*]_{\text{SYR}}$  and  $[^3\text{C}^*]_{\text{PTA}}$  at  $1 \mu\text{g PM}/\mu\text{g H}_2\text{O}$  have a range of  $(0.3 - 1) \times 10^{-12} \text{ M}$  and  $(0.08 - 0.9) \times 10^{-12} \text{ M}$ , respectively, with Win-Spr and Sum-Fall having the maximum and minimum values, respectively. Sum-Fall samples might contain fewer carbonyl or ketone compounds compared to other sample types, leading to lower production of oxidizing  $^3\text{C}^*$  (McNeill and Canonica, 2016). Compared to our average measured  $^3\text{C}^*$  concentration in the PM extracts,  $[^3\text{C}^*]$  in ALW for Win-Spr and Sum-Fall samples increases by a factor of approximately 20, while ALW concentrations for FBB and ABB are only around 2 times higher than their extract values.

From our predictions, the concentration ratio of  $^1\text{O}_2^* : ^3\text{C}^* : \bullet\text{OH}$  in ambient particle water is  $(900 - 90) : (150 - 10) : 1$ , while the ratio in cloud/fog drops is  $(40 - 5) : (1 - 10) : 1$ . Comparing to the ratio of photooxidant concentration in ALW predicted by Kaur et al. (2019) ( $[^1\text{O}_2^*] : [^3\text{C}^*] : [\bullet\text{OH}] = 10^5 : 10^2 - 10^4 : 1$ ), our results show higher  $\bullet\text{OH}$  but lower  $^1\text{O}_2^*$  concentration. Since organic compounds appear to be the major sink for all three photooxidants in ALW, and the oxidant consumption rate equals their production rate under steady-state condition, the rates of oxidant formation correspond to the rate of DOM processing by each oxidant. Kaur predicted the ratio of formation rates in ALW for  $^1\text{O}_2^*$ ,  $^3\text{C}^*$ ,  $\bullet\text{OH}$  (including mass transfer from the gas phase) is 290: 170: 1, while in our prediction the ratio is 0.23: 25:1, taking Win-Spr as an example. The lower production rate for  $^1\text{O}_2^*$  is because organic compounds suppress the  $^3\text{C}^*$  concentration, and thereby  $^1\text{O}_2^*$  production (Ma et al., 2022a). Since the triplet formation rate is much higher than those of  $\bullet\text{OH}$  or  $^1\text{O}_2^*$ , our results indicate that  $^3\text{C}^*$  might be more important for the overall oxidation of organic compounds compared to the other two oxidants. However, the picture for any particular organic compound depends on its rate constants with each oxidant. For example,  $\bullet\text{OH}$  will be relatively more important for organics that are less reactive with  $^3\text{C}^*$  and  $^1\text{O}_2^*$ .

Finally, to understand how photooxidants affect the fate of organic compounds in ALW, we revisited two of our past estimates for the lifetimes of model organic compounds in particle water. First, we re-examined the five organics studied by Kaur et al. (2019) - syringol, methyl jasmonate, tyrosine, 1,2,4-butanetriol, and 3-hydroxy-2,5-bis(hydroxymethyl)furan - employing rate constants in Kaur et al. (2019)

and our predicted ALW photooxidant concentrations in Win-Spr ( $[\bullet\text{OH}] = 7 \times 10^{-15} \text{ M}$ ,  $[\text{}^1\text{O}_2^*] = 7 \times 10^{-12} \text{ M}$ ,  $[\text{}^3\text{C}^*]_{\text{SYR}} = 1 \times 10^{-12} \text{ M}$ ). The aqueous lifetime of these compounds ranges from 0.06 – 7 h (Fig. S5.31), which can be more than 10 times shorter than that in fog water (Kaur et al., 2019) because of the enhanced photooxidant concentration in ALW.  $\text{}^3\text{C}^*$  is the dominant oxidant for the phenol (SYR), alkene (methyl jasmonate), and amino acid (tyrosine), while  $\bullet\text{OH}$  and  $\text{}^1\text{O}_2^*$  control the fates of the triol and furan, respectively. This suggests that triplet excited states are important for the processing of organic compounds in aerosol liquid water, while  $\bullet\text{OH}$  is more important for organics that are less reactive towards  $\text{}^3\text{C}^*$ , such as 1,2,4-butanetriol.  $\text{}^1\text{O}_2^*$  importance can be enhanced in aerosol liquid water and it is more important to furan compounds.

#### 5.4. Conclusions, Implications, and Uncertainties

In this work, we measured concentrations of three photooxidants – hydroxyl radical, singlet molecular oxygen, and oxidizing triplet excited states of brown carbon – in particle extracts. Our extracts have particle mass/liquid water mass ratios in the range of  $(0.7\text{-}9.1) \times 10^{-4} \mu\text{g PM}/\mu\text{g H}_2\text{O}$ , which are close to fog/cloud water conditions but much more dilute than aerosol liquid water. We categorized samples into four types based on sampling dates and chemical characterization: Winter & Spring (Win-Spr), Summer & Fall (Sum-Fall) without wildfire influence, fresh biomass burning (FBB), and aged biomass burning (ABB). FBB contains the highest amounts of BrC, leading to the highest mass absorption coefficient of dissolved organic carbon with an average value of  $3.3 (\pm 0.4) \text{ m}^2 (\text{g C})^{-1}$ . Win-Spr and ABB have similar MAC of  $(1.9 (\pm 0.4) \text{ m}^2 (\text{g C})^{-1})$  and  $1.5 (\pm 0.3) \text{ m}^2 (\text{g C})^{-1}$ , respectively, while Sum-Fall has lowest MAC  $(0.65 (\pm 0.19) \text{ m}^2 (\text{g C})^{-1})$ .

$\bullet\text{OH}$  concentrations in the particle extracts are in the range  $(0.2\text{-}4.7) \times 10^{-15} \text{ M}$  and generally increase with concentrations of dissolved organic carbon (DOC), with a range of  $(5 - 192) \text{ mg C L}^{-1}$ , although this might be because DOC is a proxy for extract concentration.  $\text{}^1\text{O}_2^*$  concentrations in extracts have a range of  $(0.07\text{-}4.5) \times 10^{-12} \text{ M}$  and exhibit good linearity with DOC that is independent of sample type. Fresh BB

samples have the highest [ $^1\text{O}_2^*$ ] but the lowest average  $\Phi_{1\text{O}_2^*}$ , while Sum-Fall samples are the opposite.  $\Phi_{1\text{O}_2^*}$  is negatively correlated with  $\text{MAC}_{\text{DOC}}$ , indicating that less light-absorbing samples form  $^1\text{O}_2^*$  more efficiently.  $^3\text{C}^*$  concentrations were quantified by SYR and PTA, with a range of  $(0.03 - 7.9) \times 10^{-13}$  M. Triplet concentrations determined by both probes linearly increase with DOC, and this relationship for  $[^3\text{C}^*]_{\text{SYR}}$  is independent of sample type. The average ratio of  $[^3\text{C}^*]_{\text{PTA}}/[^3\text{C}^*]_{\text{SYR}}$  is  $0.58 (\pm 0.38)$ , indicating that roughly 60% of oxidizing triplets are strongly oxidizing. FBB has the lowest average  $\Phi_{3\text{C}^*}$ , while atmospheric aging appears to enhance  $\Phi_{3\text{C}^*}$ , as well as  $\Phi_{1\text{O}_2^*}$ , based on the higher quantum yields for ABB samples.

Based on our results in dilute PM extracts (as well as past work), it is clear that light absorption by brown carbon produces significant amounts of photooxidants in particles. To estimate the corresponding photooxidant concentrations, we extrapolate measured photooxidant kinetics in our particle extracts to an aerosol liquid water condition ( $1 \mu\text{g PM}/\mu\text{g H}_2\text{O}$ ) for each sample type. Estimated concentrations of  $\bullet\text{OH}$ ,  $^1\text{O}_2^*$ , and  $^3\text{C}^*$  are on the order of  $10^{-15}$ ,  $10^{-12}$ , and  $10^{-13}$  M. For Win-Spr and Sum-Fall samples, photooxidant concentrations increase significantly from particle extracts to ALW, while the changes in FBB and ABB are minor, likely due to the high DOC in the extracts which cause strong quenching of  $^1\text{O}_2^*$  and  $^3\text{C}^*$ . Based on our estimated ALW concentrations, lifetime of organic compounds in ALW can be significantly shortened comparing to foggy condition, due to enhanced photooxidant concentrations. Also,  $^3\text{C}^*$  is important for the processing of organic compounds in aerosol liquid water, while  $\bullet\text{OH}$  is more important for organics that has low reactivity with  $^3\text{C}^*$ .  $^1\text{O}_2^*$  importance can be enhanced in aerosol liquid water and it is more important to compounds that have high reactivity with it, such as furans.

There are a number of important uncertainties in our work. Foremost, predicting photooxidant concentrations from our dilute extracts to ALW conditions is highly uncertain as it requires extrapolating over a concentration difference of approximately a factor of 1000. However, our current extracts have more DOC than those in our past work (Kaur et al., 2019), which allows us to get closer to ALW chemistry; for example, we see evidence of DOC suppressing  $^1\text{O}_2^*$  concentrations (via reactions of DOC with  $^3\text{C}^*$ ), which

was not present in our past work. Despite this improvement, additional approaches – such as chamber and flow tube studies – are needed to measure photooxidants and their chemical impacts under conditions more similar to ambient aerosols. Another uncertainty with our current (and past) results is that we are missing the water-insoluble chromophores. Consistent with past results from other groups, we find that there are significant amounts of highly light-absorbing water-insoluble brown carbon in particles, indicating that we are probably underestimating the concentrations and significance of particle photooxidants in our aqueous extracts. This issue should be addressed in future photochemistry studies.

### **5.5. Acknowledgement**

We gratefully acknowledge the following agencies for their publicly available data: the California Air Resources Board for PM<sub>2.5</sub> data, NASA's Land, Atmosphere Near real-time Capability for EOS (LANCE) system (<https://earthdata.nasa.gov/lance>), part of the Earth Observing System Data and Information System (EOSDIS) for wildfire and smoke images, and the NOAA Air Resources Laboratory (ARL) for the HYSPLIT model and READY website (<https://www.ready.noaa.gov>).

### **5.6. Financial Support**

This research has been supported by the National Science Foundation (AGS-1649212 and AGS-2220307); the California Agricultural Experiment Station (Projects CA-D-LAW-6403-RR and CA-D-ETX-2102-H); and the University of California, Davis (Donald G. Crosby Graduate Fellowships in Environmental Chemistry and Jastro Shields Research Awards).

## 5.7. Supporting Information

**Table S5.1.** Particle collection and PME sample information

Sample Type	Sample ID	Collection dates <sup>a</sup>	Sampling duration (days)	Average PM <sub>2.5</sub> conc <sup>b</sup> (μg/m <sup>3</sup> )	Particle mass/water ratio <sup>c</sup> (10 <sup>-4</sup> μg PM/μg H <sub>2</sub> O)	α <sub>300</sub> <sup>d</sup> (cm <sup>-1</sup> )	α <sub>365</sub> <sup>e</sup> (cm <sup>-1</sup> )	R <sub>abs</sub> (300-450 nm) (10 <sup>-6</sup> mol-photons L <sup>-1</sup> s <sup>-1</sup> ) <sup>f</sup>	AAE <sup>g</sup>	E <sub>2</sub> /E <sub>3</sub> <sup>h</sup>	MAC <sub>DOC</sub> (300 nm) (m <sup>2</sup> (g C) <sup>-1</sup> ) <sup>i</sup>	MAC <sub>DOC</sub> (365 nm) (m <sup>2</sup> (g C) <sup>-1</sup> ) <sup>i</sup>	DOC (mg C L <sup>-1</sup> )	Light screening factor <sup>j</sup>
Winter & Spring	111519	11/12/19-11/19/19	7.00	13.2	9.1 (0.3)	1.534	0.431	25	7.59	7.45	1.82	0.52	192	0.67
	120319	12/3/19	1.00	10.6	1.2 (0.2)	0.112	0.027	1.6	8.17	8.84	1.57	0.40	16	0.97
	122019	12/17/19-12/24/19	7.01	9.0	5.4 (0.4)	0.718	0.206	12	7.64	7.37	2.33	0.69	69	0.82
	010220	1/2/20	1.01	10.2	1.1 (0.1)	0.116	0.031	1.8	7.78	8.28	1.54	0.43	17	0.97
	010620	1/3/20-1/10/20	7.01	10.0	6.2 (0.5)	0.552	0.144	8.4	7.57	8.65	1.92	0.52	64	0.86
	021620 <sup>k</sup>	2/5/20-2/28/20	7.07	9.1	4.6 (0.5)	0.868	0.269	16	7.21	7.16	2.08	0.65	95	0.60
	022020	2/20/20	1.00	9.0	0.89 (0.10)	0.231	0.070	4.1	7.26	6.91	2.50	0.76	21	0.94
	030420	3/4/20	1.01	8.4	1.2 (0.2)	0.090	0.022	1.3	8.05	9.61	1.27	0.32	16	0.98
Summer & Fall	070720	7/7/20	0.99	7.0	1.0 (0.2)	0.039	0.009	0.50	8.77	10.9	0.74	0.18	12	0.99
	080420	8/4/20	1.01	7.2	0.79 (0.14)	0.019	0.004	0.22	8.97	17.0	0.43	0.09	9.9	1.00
	101520	10/15/20	1.00	7.9	0.66 (0.25)	0.017	0.004	0.18	9.63	13.3	0.78	0.16	5.0	1.00
Fresh wildfire	081920	8/19/20	0.99	67.9	3.7 (0.3)	1.960	0.812	43	7.26	4.22	3.82	1.59	118	0.55
	082220 <sup>k</sup>	8/21/20-8/24/20	1.20	49.3	4.1 (0.1)	2.017	0.653	38	7.15	6.50	3.10	1.00	150	0.78
	082420	8/24/20	0.92	57.2	3.1 (0.2)	1.511	0.540	29	7.57	5.00	3.32	1.19	105	0.64
	090920	9/9/20	1.00	44.6	3.0 (0.2)	0.871	0.259	15	7.42	7.46	2.90	0.86	69	0.78
Aged wildfire	090120	9/1/20	0.99	19.2	1.4 (0.1)	0.199	0.048	2.8	8.19	10.6	1.75	0.42	26	0.95
	091520	9/15/20	1.00	19.5	1.3 (0.1)	0.245	0.058	3.5	7.85	11.8	1.54	0.36	37	0.94
	100820	10/8/20	0.99	33.9	2.7 (0.2)	0.441	0.090	5.4	7.58	15.1	1.25	0.26	81	0.90
Averages														
Winter & Spring (Win-Spr)				9.9 (1.5)					7.7 (0.3)	8.0 (1.0)	1.88 (0.42)	0.53 (0.15)		
Summer & Fall (Sum-Fall)				7.4 (0.4)					9.1 (0.5)	13.7 (3.1)	0.65 (0.19)	0.14 (0.05)		
Fresh wildfire (FBB)				55 (10)					7.3 (0.2)	5.8 (1.5)	3.29 (0.40)	1.16 (0.31)		

Aged wildfire (ABB)			24 (8)					7.9 (0.3)	12.5 (2.3)	1.51 (0.25)	0.35 (0.08)		
Field blanks <sup>l</sup>													
FB1	8/4/20	3 min	6.9	0.16 (0.06)	0.0022	0.0004	0.017				0	2.12	1
FB2	1/2/20	3 min	15.6	0.13 (0.06)	0.0015	0	0.0013				0.16	2.04	1
FB3	10/5/20	3 min	39.6	0.47 (0.38)	0.0065	0.0014	0.086				0	2.98	1

Listed uncertainties (in parentheses) are  $\pm 1$  standard deviation.

<sup>a</sup> For 24-h samples, sampling started in the morning of the first date shown and ended on the second date.

<sup>b</sup> Average PM<sub>2.5</sub> concentration for each sampling period measured at the UC Davis sampling site by the California Air Resources as reported on the iADAM online database (California Air Resources Board, 2019-2020).

<sup>c</sup> Particle mass/water mass ratio ( $\pm 1\sigma$ ) is calculated as the extracted particle mass per square (determined as the difference of filter weights before and after extraction) divided by the volume of water used to extract the square.

<sup>d</sup> Base-10 absorption coefficient of the extract (in cm<sup>-1</sup>) at 300 nm.

<sup>e</sup> Base-10 absorption coefficient of the extract (in cm<sup>-1</sup>) at 365 nm.

<sup>f</sup> Rate of sunlight absorption by PME between 300 and 450 nm, calculated by equation 2 in Kaur et al. (2019), using midday actinic flux on the winter solstice in Davis (photons cm<sup>-2</sup> s<sup>-1</sup> nm<sup>-1</sup>) from the Tropospheric Ultraviolet and Visible (TUV) Radiation Model version 4.1.

<sup>g</sup> AAE is calculated as the negative slope of a linear regression between ln(absorbance) vs. ln(wavelength) in the 300 – 450 nm wavelength range.

<sup>h</sup> The ratio of absorbance at 250 nm divided by absorbance at 365 nm.

<sup>i</sup> Mass absorption coefficient normalized by dissolved organic carbon at 300 or 365 nm, calculated as  $MAC_{DOC,\lambda} = \frac{\alpha_{\lambda} \times \ln(10) \times 10^6}{[DOC]}$  (Kaur et al., 2019). The nitrate and nitrite contributions to absorbance at each wavelength were subtracted but were very small, < 5 % of total absorbance at either wavelength.

<sup>j</sup> Light-absorption-weighted internal screening factor, calculated with equation 2 in Smith et al. (2016), using the midday winter solstice actinic flux in Davis. The wavelength range used is 280-364 nm. A value of 1 indicates no light screening while a low value represents a strong screening effect.

<sup>k</sup> These two samples are the interpolations of the winter and summer samples, respectively, from our previous work on the dependence of photooxidant concentration on dilution (Ma et al., 2022a). Their particle mass/water mass ratios, absorbances, and DOC values were estimated for an equivalent extraction volume of 1.0 mL water/square by interpolating from the winter or summer linear trend for each variable with concentration factor.

<sup>l</sup> Field blank filters were obtained using the same way as the samples, by loading clean filters into the sampler and turning on the pump for 3 min. Field blank samples were extracted with 1.0 mL water/square.

**Table S5.2.** Ion concentrations in PMEs

Sample Type	Sample ID	Sampling duration (days)	[NO <sub>3</sub> <sup>-</sup> ] (μM)	[NO <sub>2</sub> <sup>-</sup> ] (μM)	[SO <sub>4</sub> <sup>2-</sup> ] (μM) <sup>a</sup>	[Cl <sup>-</sup> ] (μM)	[HCOO <sup>-</sup> ] (μM)	[NH <sub>4</sub> <sup>+</sup> ] (μM)	[Na <sup>+</sup> ] (μM)	[K <sup>+</sup> ] (μM)	[Ca <sup>2+</sup> ] (μM)
Winter & Spring	111519	7.00	2660	8.98	838	811 <sup>b</sup>	76.4	4857	718	1187 <sup>b</sup>	373
	120319	1.00	541	0.87	39.6	17.4	3.5	653	151	79.1	28.0
	122019	7.01	3309	2.65	296	167 <sup>b</sup>	61.0	2198	246	84.7 <sup>b</sup>	70.1
	010220	1.01	424	0.69	25.2	10.7	3.4	516	147	64.7	28.0
	010620	7.01	3075	3.14	400	750 <sup>b</sup>	56.0	1620	183	272 <sup>b</sup>	141
	021620 <sup>e</sup>	7.07	1480	6.08	617	37.3	51.5	1300	1159	214	402
	022020	1.00	84.0	0.81	58.0	0.3	3.8	168	165	61.8	28.1
030420	1.01	356	0.75	65.2	66.7	18.2	99.4	138	26.3	28.0	
Summer & Fall	070720	0.99	117	0.63	69.5	238	5.8	65.5	548	36.9	187
	080420	1.01	90.0	0.50	87.1	1654 <sup>b</sup>	10.3	78.7	457	1559 <sup>b</sup>	143
	101520	1.00	25.5	0.44	-9.1	17.1	0.5	58.5	240	22.7	28.0
Fresh wildfire	081920	0.99	288	1.88	76.3	72.3	81.6	46.2	127	122	200
	082220 <sup>e</sup>	1.20	299	2.50	173	51.8	64.2	460	529	219	233
	082420	0.92	179	1.72	157	516 <sup>b</sup>	32.9	502	292	676 <sup>b</sup>	184
	090920	1.00	219	1.42	82.9	23.7	69.3	66.3	109	64.3	210
Aged wildfire	090120	0.99	180	0.75	99.1	64.1	14.6	65.8	538	53.8	193
	091520	1.00	66.1	0.63	29.8	0.5	< LOD <sup>d</sup>	112	195	55.3	111
	100820	0.99	204	1.26	83.0	1164 <sup>b</sup>	20.8	803	300	1310 <sup>b</sup>	137
Field blanks											
	FB1 <sup>c</sup>	3 min	3.12	<LOD <sup>d</sup>	< 0	2458	3.03	0.12	96.0	ND <sup>f</sup>	7.01
	FB2	3 min	4.58	<LOD <sup>d</sup>	< 0	1.07	2.94	1.42	93.8	5.92	7.02
	FB3	3 min	1.99	<LOD <sup>d</sup>	12.4	0.65	5.54	1.11	124.6	8.88	7.08

<sup>a</sup> The amount of added sulfuric acid for pH adjustment (typically 90 μM) has been subtracted.

<sup>b</sup> These samples were contaminated by pH electrode filling solution (potassium chloride) during pH adjustment. These samples are not included in the discussion of K<sup>+</sup> concentrations in the main text.

<sup>c</sup> This field blank sample was contaminated by the pH electrode filling solution, resulting in an extremely high Cl<sup>-</sup> concentration.

<sup>d</sup> Below limit of detection.

<sup>e</sup> These two samples are the interpolations of winter and summer samples, respectively, in our previous work on the dependence of photooxidant concentration on dilution effect (Ma et al., 2022a). Their ion concentration values were estimated by interpolation from the winter or summer linear trend for each variable with concentration factor to an equivalent extraction volume of 1.0 mL water/square.

<sup>f</sup> Not determined due to the poor ion chromatogram result.

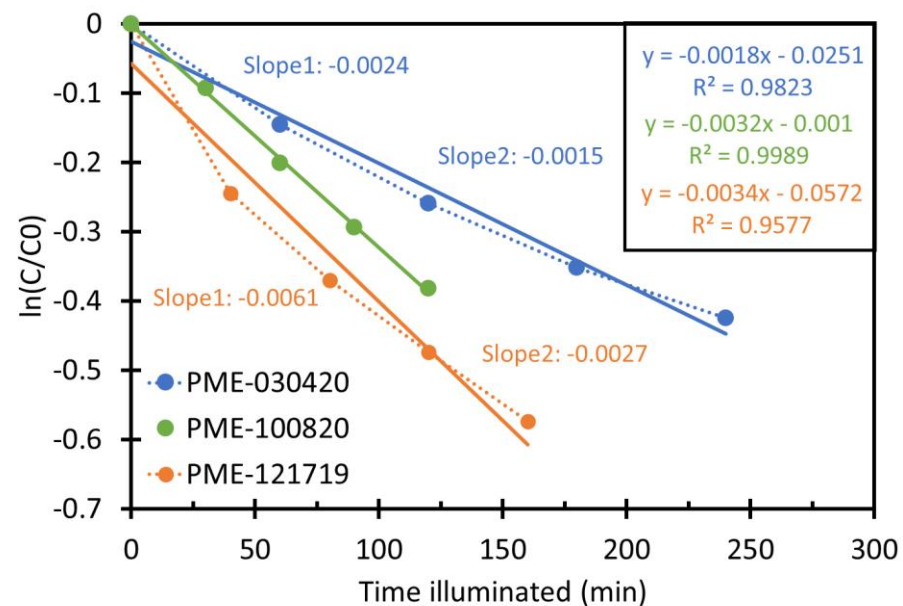


**Figure S5.1.** Representative plots of benzoic acid decay kinetics in aqueous particle extracts showing samples where the initial rate of BA loss is over twice as fast as the later rate (orange), the initial rate is over 50% higher than the later rate (blue) and there is no difference in BA decay over the course of illumination (green). Solid lines are linear regressions to all points for a given sample, while their regression equations are shown in the right top box. For the orange and blue data, Slope 1 and Slope 2 represent slopes from linear regressions of the first two and last four data points, respectively.



**Table S5.3.** Hydroxyl radical measurements

Sample Type	Sample ID	$P_{OH}$ ( $10^{-9} M^{-1}s^{-1}$ ) <sup>a</sup>	$k'_{OH}$ ( $10^6 s^{-1}$ ) <sup>b</sup>	[•OH] <sup>c</sup> ( $10^{-15} M$ ) from BA	[•OH] <sup>d</sup> ( $10^{-15} M$ ) from <i>p</i> -HBA	Average [•OH] ( $10^{-15} M$ ) <sup>e</sup>	$10^{-4} \times \Phi_{OH}^f$	% $P_{OH,NO_3}$ <sup>g</sup>	% $P_{OH,NO_2}$ <sup>h</sup>
Winter & Spring	111519	14 (2)	4.3 (0.6)	2.4 (0.3)	3.9 (0.5)	3.2 (0.3)	5.4 (0.9)	2.7 (0.4)	1.7 (0.3)
	120319	0.44 (0.06)	0.36 (0.05)	1.4 (0.1)	1.1 (0.1)	1.2 (0.1)	2.7 (0.4)	17 (2)	5.1 (0.7)
	122019	6.0 (0.9)	1.6 (0.2)	3.0 (0.4)	4.8 (0.5)	3.9 (0.3)	5.1 (0.8)	7.7 (1.2)	1.1 (0.2)
	010220	0.60 (0.08)	0.38 (0.05)	1.6 (0.1)	1.5 (0.1)	1.6 (0.1)	3.3 (0.4)	9.9 (1.3)	3.0 (0.4)
	010620	6.7 (1.0)	1.4 (0.2)	3.5 (0.3)	5.8 (0.5)	4.7 (0.3)	7.9 (1.1)	6.5 (0.9)	1.2 (0.2)
	021620 <sup>i</sup>	10 (2)	2.1 (0.3)			4.7 (0.4)	6.3 (0.1)	2.1 (0.4)	1.6 (0.2)
	022020	0.45 (0.06)	0.48 (0.06)	1.1 (0.1)	0.83 (0.1)	0.94 (0.05)	1.1 (0.2)	2.6 (0.4)	4.7 (0.7)
	030420	0.52 (0.08)	0.36 (0.05)	1.4 (0.1)	1.5 (0.2)	1.5 (0.1)	4.0 (0.6)	9.5 (1.4)	3.7 (0.6)
Summer & Fall	070720	0.20 (0.03)	0.26 (0.03)	0.90 (0.03)	0.59 (0.1)	0.74 (0.05)	3.9 (0.6)	8.4 (1.2)	8.4 (1.2)
	080420	0.050 (0.026)	0.22 (0.03)		0.36 (0.19)	0.23 (0.11)	2.3 (0.4)	25 (13)	26 (13)
	101520	0.038 (0.015)	0.11 (0.01)	0.28 (0.19)	0.30 (0.15)	0.34 (0.12)	1.6 (0.6)	9.2 (3.5)	30 (11)
Fresh wildfire	081920	7.3 (1.3)	2.7 (0.3)	2.6 (0.5)	2.9 (0.4)	2.8 (0.3)	1.7 (0.3)	0.55 (0.10)	0.67 (0.12)
	082220 <sup>i</sup>	8.7 (1.3)	3.4 (0.4)			2.6 (0.2)	2.3 (0.3)	0.48 (0.07)	0.75 (0.11)
	082420	4.8 (1.2)	2.4 (0.3)	2.1 (0.2)	1.9 (0.9)	2.0 (0.4)	1.7 (0.3)	0.52 (0.13)	0.93 (0.24)
	090920	4.2 (0.9)	1.6 (0.2)	2.0 (0.1)	3.4 (0.9)	2.7 (0.5)	2.8 (0.3)	0.73 (0.16)	0.88 (0.19)
Aged wildfire	090120	0.28 (0.04)	0.59 (0.08)	0.43 (0.01)	0.53 (0.1)	0.48 (0.03)	1.0 (0.1)	9.0 (1.3)	7.0 (1.0)
	091520	1.1 (0.1)	0.82 (0.11)	1.6 (0.01)	1.2 (0.1)	1.4 (0.1)	3.2 (0.4)	0.82 (0.11)	1.4 (0.2)
	100820	5.7 (0.8)	1.8 (0.2)	3.0 (0.2)	3.3 (0.2)	3.2 (0.2)	10 (1.5)	0.50 (0.07)	0.57 (0.08)
Averages <sup>j</sup>									
Winter & Spring						1.5 (0.3)	4.5 (2.2)	7.2 (5.0)	2.8 (1.6)
Summer & Fall						0.41 (0.03)	2.8 (1.0)	7.1 (6.5)	17 (22)
Fresh wildfire						2.5 (0.3)	2.1 (0.5)	0.57 (0.11)	0.81 (0.12)
Aged wildfire						1.7 (1.4)	4.9 (5.0)	3.4 (4.8)	3.0 (3.5)
Field Blanks									
FB1						0.57 (0.03)			
FB2 <sup>k</sup>		0.0011 (0.0001)	0.20 (0.02)			0.06 (0.01)		5.7 (0.5)	36 (3)
FB3 <sup>k</sup>		0.0008 (0.0001)	0.05 (0.02)			0.15 (0.01)		3.6 (0.4)	26 (3)

Listed uncertainties (in parentheses) are  $\pm 1$  standard error from the errors in regressions, except for the averages, which are  $\pm 1\sigma$ .

<sup>a</sup> Davis winter solstice-normalized rate of •OH photoproduction, calculated as  $P_{OH} = k'_{OH} \times [•OH]$ .

- <sup>b</sup> Apparent pseudo-first-order rate constant for destruction of  $\bullet\text{OH}$  due to natural sinks, estimated as  $k'_{\text{OH}} = k_{\text{OH+DOC}} \times [\text{DOC}]$ , where  $k_{\text{OH+DOC}}$  is the second-order rate constant of DOC reacting with  $\bullet\text{OH}$  ( $2.7 (\pm 0.4) \times 10^7 \text{ L (mol C)}^{-1} \text{ s}^{-1}$ ), which is the average of samples in Ma et al. (2022).
- <sup>c</sup> Winter solstice-normalized steady-state concentration of  $\bullet\text{OH}$  determined from BA decay.
- <sup>d</sup> Winter solstice-normalized steady-state concentration of  $\bullet\text{OH}$  determined from *p*-HBA formation.
- <sup>e</sup> Average of concentrations of  $\bullet\text{OH}$  determined by BA and *p*-HBA. For samples with a poor BA decay, only the value from *p*-HBA is used.
- <sup>f</sup> Apparent quantum yield of  $\bullet\text{OH}$  during simulated sunlight illumination, calculated as  $\Phi_{\text{OH}} = P_{\text{OH}}/R_{\text{abs}}$ .
- <sup>g</sup> Percentage of  $\bullet\text{OH}$  photoproduction due to nitrate photolysis. This was calculated as  $(j_{\text{NO}_3 \rightarrow \text{OH}} \times [\text{NO}_3^-])/P_{\text{OH}}$ , using an aqueous nitrate photolysis rate constant,  $j_{\text{NO}_3 \rightarrow \text{OH}} = 1.4 \times 10^{-7} \text{ s}^{-1}$  (Anastasio and McGregor, 2001) and the measured molar concentration of  $\text{NO}_3^-$ .
- <sup>h</sup> Percentage of  $\bullet\text{OH}$  photoproduction due to of nitrite photolysis. This was calculated as  $(j_{\text{NO}_2 \rightarrow \text{OH}} \times [\text{NO}_2^-])/P_{\text{OH}}$ , using an aqueous nitrite photolysis rate constant,  $j_{\text{NO}_2 \rightarrow \text{OH}} = 2.6 \times 10^{-5} \text{ s}^{-1}$  (Anastasio and McGregor, 2001) and the measured molar concentration of  $\text{NO}_2^-$ .
- <sup>i</sup> These two samples are the interpolated winter and summer samples, respectively, from our previous work on the dependence of photooxidant concentration on dilution (Ma et al., 2022a). The  $\bullet\text{OH}$  concentration in PME-021620 was the average concentration of the winter dilution series because their concentration is independent of concentration factor. The  $\bullet\text{OH}$  concentration in PME-081920 was estimated by interpolating the linear trends between  $[\bullet\text{OH}]$  and concentration factor in the summer dilution series, to an equivalent extraction volume of 1 mL water/square.
- <sup>j</sup> The average value of each sample type. For the average  $[\bullet\text{OH}]$  calculation, the  $\bullet\text{OH}$  concentration normalized by sampling duration is used.
- <sup>k</sup> The  $\bullet\text{OH}$  production rate in field blanks was determined by adding 1.2 mM benzoic acid to 1.0 mL FB sample and monitoring the formation of *p*-hydroxy benzoic acid, assuming that all  $\bullet\text{OH}$  produced reacts with benzoic acid.

**Table S5.4.** Singlet molecular oxygen measurements

Sample Type	Sample ID	[ <sup>1</sup> O <sub>2</sub> *] <sup>a</sup> (10 <sup>-12</sup> M)	<i>P</i> <sub>1O2*</sub> <sup>b</sup> (10 <sup>-7</sup> M s <sup>-1</sup> )	<i>f</i> <sub>FFA,1O2*</sub> <sup>c</sup>	<i>f</i> <sub>FFA,OH</sub> <sup>d</sup>	10 <sup>2</sup> × Φ <sub>1O2*</sub> <sup>e</sup>	Φ <sub>3C*,SYR</sub> / (Φ <sub>1O2*/f<sub>Δ</sub></sub> ) <sup>f</sup>	Φ <sub>3C*,PTA</sub> / (Φ <sub>1O2*/f<sub>Δ</sub></sub> ) <sup>g</sup>	[ <sup>3</sup> C*] <sub>SYR</sub> / [ <sup>1</sup> O <sub>2</sub> *] <sup>h</sup>	[ <sup>3</sup> C*] <sub>PTA</sub> / [ <sup>1</sup> O <sub>2</sub> *] <sup>i</sup>
Winter & Spring	111519	4.5 (0.4)	9.9 (1.0)	0.85 (0.09)	0.17 (0.02)	4.0 (0.4)	0.81 (0.23)	0.45 (0.12)	0.17 (0.05)	0.10 (0.03)
	120319	0.37 (0.07)	0.81 (0.16)	0.73 (0.15)	0.35 (0.01)	5.0 (1.0)	0.28 (0.08)	0.21 (0.07)	0.13 (0.04)	0.10 (0.03)
	122019	2.5 (0.2)	5.5 (0.4)	0.76 (0.07)	0.37 (0.03)	4.6 (0.4)	0.52 (0.16)	0.24 (0.06)	0.18 (0.06)	0.08 (0.02)
	010220	0.27 (0.06)	0.59 (0.12)	0.51 (0.11)	0.83 (0.04)	3.2 (0.7)	0.28 (0.09)	0.32 (0.10)	0.13 (0.04)	0.15 (0.05)
	010620	2.3 (0.2)	5.1 (0.4)	0.81 (0.07)	0.47 (0.03)	6.0 (0.5)	0.24 (0.05)	0.26 (0.07)	0.08 (0.02)	0.09 (0.02)
	021620 <sup>j</sup>	1.9 (0.3)	4.2 (0.7)			2.7 (0.4)	0.58 (0.18)	0.38 (0.11)	0.18 (0.06)	0.11 (0.03)
	022020	0.59 (0.06)	1.3 (0.1)	0.92 (0.11)	0.42 (0.02)	3.2 (0.3)	0.42 (0.09)	0.21 (0.06)	0.19 (0.04)	0.10 (0.03)
	030420	0.20 (0.03)	0.44 (0.06)	0.52 (0.07)	1.03 (0.07)	3.4 (0.5)	0.14 (0.05)	0.24 (0.07)	0.07 (0.02)	0.11 (0.03)
Summer & Fall	070720	0.17 (0.02)	0.38 (0.04)	1.01 (0.11)	1.23 (0.08)	7.5 (0.7)	0.29 (0.06)	0.10 (0.03)	0.14 (0.03)	0.05 (0.01)
	080420	0.081 (0.027)	0.18 (0.06)	0.97 (0.33)	0.78 (0.39)	7.9 (2.7)	0.22 (0.09)	0.07 (0.04)	0.11 (0.04)	0.04 (0.02)
	101520	0.068 (0.006)	0.15 (0.01)	1.46 (0.31)	0.82 (0.30)	8.4 (0.8)	0.54 (0.11)	0.15 (0.05)	0.28 (0.06)	0.08 (0.02)
Fresh wildfire	081920	3.3 (0.6)	7.2 (1.2)	1.13 (0.22)	0.26 (0.03)	1.7 (0.3)	0.44 (0.12)	0.20 (0.07)	0.12 (0.03)	0.06 (0.02)
	082220 <sup>j</sup>	3.8 (1.0)	8.4 (2.1)			2.2 (0.6)	0.54 (0.18)	0.20 (0.07)	0.13 (0.05)	0.05 (0.02)
	082420	3.0 (0.2)	6.7 (0.5)	0.80 (0.06)	0.02 (0.01)	2.3 (0.2)	0.71 (0.19)	0.19 (0.05)	0.21 (0.06)	0.06 (0.01)
	090920	1.9 (0.2)	4.2 (0.5)	0.73 (0.09)	0.15 (0.03)	2.8 (0.3)	0.59 (0.34)	0.29 (0.19)	0.21 (0.12)	0.10 (0.06)
Aged wildfire	090120	0.45 (0.06)	0.99 (0.12)	0.65 (0.09)	0.20 (0.01)	3.5 (0.4)	0.78 (0.19)	0.26 (0.07)	0.34 (0.08)	0.12 (0.03)
	091520	0.50 (0.04)	1.1 (0.1)	0.56 (0.05)	0.44 (0.02)	3.2 (0.2)	0.63 (0.15)	0.27 (0.07)	0.26 (0.06)	0.11 (0.03)
	100820	1.2 (0.2)	2.7 (0.4)	0.98 (0.13)	0.71 (0.04)	5.0 (0.7)	0.45 (0.10)	0.16 (0.04)	0.15 (0.03)	0.05 (0.01)
Averages <sup>k</sup>										
Winter & Spring		0.38 (0.16)				4.0 (1.1)	0.41 (0.22)	0.29 (0.09)	0.14 (0.05)	0.11 (0.02)
Summer & Fall		0.11 (0.06)				7.9 (0.4)	0.35 (0.17)	0.11 (0.04)	0.17 (0.09)	0.05 (0.02)
Fresh wildfire		2.9 (0.7)				2.2 (0.5)	0.57 (0.11)	0.22 (0.04)	0.17 (0.05)	0.07 (0.02)
Aged wildfire		0.73 (0.44)				3.9 (1.0)	0.62 (0.17)	0.23 (0.06)	0.25 (0.10)	0.09 (0.04)
Field blanks										
FB1		0.016 (±0.001)		0.81 (±0.15)	8.3 (±4.8)					
FB2		0.021 (±0.001)		0.66 (±0.33)	0.54 (±0.07)					
FB3		0.028 (±0.001)		0.97 (±0.17)	0.73 (±0.09)					

Listed uncertainties (in parentheses) are ± 1 standard error propagated from the errors in regressions and rate constants, except for the averages, where uncertainties are ± 1σ.

<sup>a</sup> Davis winter solstice-normalized steady-state concentration of <sup>1</sup>O<sub>2</sub>\*.

- <sup>b</sup> Production rate of  $^1\text{O}_2^*$ , calculated as  $P_{^1\text{O}_2^*} = [^1\text{O}_2^*] \times k'_{\text{H}_2\text{O}}$ , where  $k'_{\text{H}_2\text{O}}$  is the first-order rate constant for loss of  $^1\text{O}_2^*$  in  $\text{H}_2\text{O}$  ( $2.2 \times 10^5 \text{ s}^{-1}$ ) (Bilski et al., 1997).
- <sup>c</sup> Fraction of FFA lost due to  $^1\text{O}_2^*$  in PME diluted with  $\text{H}_2\text{O}$  (i.e. 0.5 mL PME + 0.5 mL  $\text{H}_2\text{O}$ ), calculated as  $f_{\text{FFA},^1\text{O}_2^*} = [^1\text{O}_2^*]/2 \times k_{\text{FFA},^1\text{O}_2^*}/k'_{\text{FFA},\text{H}_2\text{O}}$ , where  $k_{\text{FFA},^1\text{O}_2^*}$  is the second-order rate constant of FFA reacting with  $^1\text{O}_2^*$ , and  $k'_{\text{FFA},\text{H}_2\text{O}}$  is the normalized first-order decay rate of FFA in the PME diluted with  $\text{H}_2\text{O}$ .
- <sup>d</sup> Fraction of FFA lost due to  $\bullet\text{OH}$  in PME diluted with  $\text{H}_2\text{O}$ , estimated as  $f_{\text{FFA},\bullet\text{OH}} = [\bullet\text{OH}] \times k_{\text{FFA},\bullet\text{OH}}/k'_{\text{FFA},\text{H}_2\text{O}}$ , where  $k_{\text{FFA},\bullet\text{OH}}$  is the second-order rate constant of FFA reacting with  $\bullet\text{OH}$  ( $1.5 \times 10^{10} \text{ M}^{-1} \text{ s}^{-1}$ ) (Ross and Ross, 1977), assuming  $\bullet\text{OH}$  concentration is the same in the diluted and undiluted PME.
- <sup>e</sup> Apparent quantum yield of  $^1\text{O}_2^*$ , calculated as  $\Phi_{^1\text{O}_2^*} = P_{^1\text{O}_2^*}/R_{\text{abs}}$ .
- <sup>f</sup> Fraction of oxidizing triplets determined by SYR to the total triplet pool (Kaur and Anastasio, 2018).  $f_{\Delta}$  is the yield of  $^1\text{O}_2^*$  from oxygen quenching of triplet states, assumed to be 0.53 (McNeill and Canonica, 2016).  $\Phi_{^3\text{C}^*,\text{SYR}}$  is the apparent quantum yield of  $^3\text{C}^*$  determined by SYR (See Table S5.7).
- <sup>g</sup> Fraction of oxidizing triplets determined by PTA to the total triplet pool.
- <sup>h</sup> Ratio of triplet concentration determined by SYR to the singlet oxygen concentration.
- <sup>i</sup> Ratio of triplet concentration determined by PTA to the singlet oxygen concentration.
- <sup>j</sup> These two samples are the interpolated winter and summer samples, respectively, from Ma et al. (2022a).  $^1\text{O}_2^*$  concentrations were estimated by interpolating the linear trends between  $[^1\text{O}_2^*]$  and concentration factor in PME-10, PME-2, and PME-0.7 samples, to an equivalent extraction volume of 1 mL water/square.
- <sup>k</sup> Average value of each sample type. The  $^1\text{O}_2^*$  concentration normalized by sampling duration was used for calculating average  $^1\text{O}_2^*$  concentrations.

**Table S5.5.** Rate constants of SYR and PTA reacting with triplet excited states, singlet oxygen, and hydroxyl radical at pH 4.2

Oxidants	$k_{\text{SYR+O}_x} (\text{M}^{-1} \text{s}^{-1})$	Reference	$k_{\text{PTA+O}_x} (\text{M}^{-1} \text{s}^{-1})$	Reference
$\bullet\text{OH}$	$20 (\pm 4) \times 10^9$	(Smith et al., 2015)	$10.3 (\pm 0.6) \times 10^9$	(Ma et al., 2022b)
$^1\text{O}_2^*$	$3.6 (\pm 0.7) \times 10^7$	(Tratnyek and Hoigne, 1991)	$8.8 (\pm 0.6) \times 10^6$	
$^3\text{DMB}^*$	$3.9 (\pm 0.7) \times 10^9$	(Smith et al., 2015)	$2.5 (\pm 0.6) \times 10^9$	
Direct photodegradation	$j_{\text{SYR}} (\text{s}^{-1})$		$j_{\text{PTA}} (\text{s}^{-1})$	
	$< 4.3 \times 10^{-6}$	(Kaur and Anastasio, 2018)	$6.2 (\pm 0.2) \times 10^{-4}$	(Ma et al., 2022b)

### Section S5.1. Determining inhibition factors and correcting $^3\text{C}^*$ concentrations

Dissolved organic matter in PME may inhibit the decay of SYR or PTA by triplets, leading to an underestimation of triplet concentration. Based on our previous research, SYR is more strongly inhibited than PTA (Ma et al., 2022b). To investigate and quantify the inhibition effect of PME on these two triplet probes, we measured inhibition factors ( $IF$ s) of FFA, SYR, and PTA for each sample, and used the  $IF$  values to correct measured  $^3\text{C}^*$  concentrations in PME. Details of inhibition factors are described in Canonica et al. (2008), Wenk et al. (2011), and Ma et al. (2022). To measure  $IF$ , we monitored the loss of 10  $\mu\text{M}$  probe in three illuminated solutions for each sample: (1) in the PME; (2) in pH 4.2 Milli-Q water containing 80  $\mu\text{M}$  of triplet precursor 3,4-dimethoxybenzaldehyde (DMB); and (3) in the PME with added 80  $\mu\text{M}$  DMB. During each illumination we determined the first-order rate constant of probe decay. The inhibition factor for the probe was calculated using

$$IF_P = \frac{k'_{DMB,PME} - k'_{PME}}{k'_{DMB}} \quad (S5.1)$$

where  $k'_{DMB,PME}$  is the first-order decay rate constant of probe in solution containing both DMB and PME, while  $k'_{PME}$  and  $k'_{DMB}$  are the probe loss rate constants in PME alone and in Milli-Q water with DMB, respectively. All  $k'$  values were corrected for internal light screening with screening factors ( $S_\lambda$ ). An  $IF$  value of 1 indicates there is no DOM inhibition on probe decay, while  $IF = 0$  indicates complete inhibition of probe decay. Since  $IF_P$  can also be affected by DOM suppressing the  $^3\text{DMB}^*$  concentration, we use  $IF_{FFA}$  to quantify this triplet suppression. To exclude the effect of triplet suppression on  $IF_{SYR}$  and  $IF_{PTA}$  (i.e., to quantify only inhibition due to probe regeneration), we use  $IF_{SYR,corr}$  and  $IF_{PTA,corr}$

$$IF_{P,corr} = \frac{IF_P}{IF_{FFA}} \quad (S5.2)$$

Theoretically,  $IF$  should not exceed 1, but we sometimes see this result. When  $IF$  is greater than 1, it suggests there is interaction between DOM in PME with DMB to form reactive species, and thus indicates no inhibition or suppression. Therefore, when  $IF_{FFA}$  or  $IF_P$  is greater than 1, we assume that  $IF_{P,corr} = IF_P$  and we do not correct  $^3C^*$  concentration if  $IF_{P,corr} > 1$ . In addition,  $IF_{PTA}$  and  $IF_{SYR}$  values are expected to be lower than  $IF_{FFA}$  because  $IF_{PTA}$  and  $IF_{SYR}$  are affected by both the triplet suppression and probe inhibition effects, while  $IF_{FFA}$  is only impacted by triplet suppression. However, in some samples  $IF_{PTA}$  value was greater than  $IF_{FFA}$ , which might be attributed to the large error in  $IF_{FFA}$  measurement in cases where the difference between  $k'_{DMB,PME}$  and  $k'_{PME}$  is small for FFA. In this case, we assume the  $IF_{FFA}$  value equals  $IF_{PTA}$  (since PTA is very resistant to suppression) and use this value to calculate  $IF_{P,corr}$ . The determined  $IF$  and  $IF_{P,corr}$  values are shown in Table S5.6.

The uncorrected  $^3C^*$  concentration is calculated with:

$$[{}^3C^*]_{P,uncorr} = \frac{k'_{P,3C^*}}{k_{P+3DMB^*}} \quad (S5.3)$$

where  $k'_{P,3C^*}$  is measured first-order rate constant of probe loss due to triplets and  $k_{P+3DMB^*}$  is the second-order rate constant of probe reacting with  $^3DMB^*$ . To correct for the probe inhibition effect,  $[{}^3C^*]$  is calculated using

$$[{}^3C^*]_P = \frac{[{}^3C^*]_{P,uncorr}}{IF_{P,corr}} \quad (S5.4)$$

The  $^3C^*$  concentrations shown in the main text are the values after  $IF$  correction.

**Table S5.6.** Inhibition factors for FFA, SYR, and PTA

Sample Type	Sample ID	$IF_{FFA}$	$IF_{SYR}$	$IF_{PTA}$	$IF_{SYR,corr}$	$IF_{PTA,corr}$
Winter & Spring	111519	0.60 (0.45)	0.27 (0.04)	1.06 (0.13)	0.27 (0.04)	1.06 (0.13)
	120319	1.15 (0.12)	0.78 (0.04)	1.16 (0.07)	0.78 (0.04)	1.16 (0.07)
	122019	1.30 (0.12)	0.21 (0.04)	1.26 (0.03)	0.21 (0.04)	1.26 (0.03)
	010220	1.06 (0.10)	0.53 (0.04)	1.24 (0.04)	0.53 (0.04)	1.24 (0.04)
	010620	0.97 (0.20)	0.48 (0.03)	1.24 (0.06)	0.48 (0.03)	1.24 (0.06)
	021620 <sup>a</sup>	0.62 (0.07)	0.20 (0.02)	0.87 (0.19)	0.24 (0.03)	1.00 (0.08)
	022020	1.36 (0.08)	0.81 (0.05)	1.40 (0.08)	0.81 (0.05)	1.40 (0.08)
	030420	1.16 (0.03)	0.58 (0.05)	1.28 (0.08)	0.58 (0.06)	1.28 (0.08)
Summer & Fall	070720	1.28 (0.05)	0.76 (0.06)	1.47 (0.07)	0.76 (0.03)	1.47 (0.07)
	080420	1.14 (0.07)	0.76 (0.03)	0.75 (0.02)	0.76 (0.05)	0.75 (0.02)
	101520	1.03 (0.04)	1.02 (0.05)	1.15 (0.05)	1.02 (0.05)	1.15 (0.05)
Fresh wildfire	081920	0.27 (0.05)	0.23 (0.01)	0.51 (0.04)	0.46 (0.05)	1.00 (0.12)
	082220 <sup>a</sup>	0.52 (0.05)	0.25 (0.02)	0.57 (0.07)	0.47 (0.05)	0.96 (0.11)
	082420	1.01 (0.12)	0.31 (0.02)	0.60 (0.04)	0.31 (0.02)	0.60 (0.04)
	090920	0.90 (0.47)	0.88 (0.03)	0.79 (0.03)	0.98 (0.51)	0.88 (0.52)
Aged wildfire	090120	1.18 (0.12)	0.85 (0.09)	0.98 (0.04)	0.85 (0.09)	0.98 (0.04)
	091520	0.95 (0.04)	0.82 (0.11)	0.87 (0.04)	0.87 (0.12)	0.92 (0.06)
	100820	1.18 (0.09)	1.19 (0.15)	1.32 (0.10)	1.19 (0.15)	1.32 (0.10)
Averages						
Winter & Spring					0.49 (0.23)	1.20 (0.13)
Summer & Fall					0.85 (0.15)	1.12 (0.36)
Fresh wildfire					0.55 (0.29)	0.86 (0.18)
Aged wildfire					0.97 (0.19)	1.07 (0.22)
Field blanks						
FB1		0.95 ( $\pm 0.12$ )	0.52 ( $\pm 0.05$ ) <sup>b</sup>	0.86 ( $\pm 0.13$ )	0.54 ( $\pm 0.08$ ) <sup>b</sup>	0.90 ( $\pm 0.19$ )
FB2		1.10 ( $\pm 0.05$ )	0.95 ( $\pm 0.19$ )	0.93 ( $\pm 0.06$ )	0.95 ( $\pm 0.19$ )	0.93 ( $\pm 0.06$ )
FB3		1.21 ( $\pm 0.06$ )	1.20 ( $\pm 0.08$ )	1.15 ( $\pm 0.09$ )	1.20 ( $\pm 0.08$ )	1.15 ( $\pm 0.09$ )

Listed uncertainties (in parentheses) are  $\pm 1$  standard error propagated from the errors in data regression, except for the averages ( $\pm 1\sigma$ )

<sup>a</sup> These two samples are interpolated from the winter and summer samples, respectively, in Ma et al. (2022a).  $IF$  values were estimated by interpolating the linear regression between  $1/IF$  for each probe vs. concentration factor, to an equivalent extraction volume of 1 mL water/square.

<sup>b</sup> The low  $IF_{SYR}$  might be attributed to the contamination of this field blank by pH electrode filling solution.



**Table S5.7.** Oxidizing triplet excited state measurements by syringol (SYR)

Sample Type	Sample ID	$k'_{\text{SYR}}^{\text{a}}$ ( $10^{-4} \text{ s}^{-1}$ )	$f_{\text{SYR,OH}}^{\text{b}}$	$f_{\text{SYR,IO}_2}^{\text{c}}$	$f_{\text{SYR,3C}}^{\text{d}}$	$[\text{C}^*]_{\text{SYR,uncorr}}^{\text{e}}$ ( $10^{-14} \text{ M}$ )	$[\text{C}^*]_{\text{SYR}}^{\text{f}}$ ( $10^{-14} \text{ M}$ )	$k'_{\text{3C}^*,\text{SYR}}^{\text{g}}$ ( $10^6 \text{ s}^{-1}$ )	$P_{\text{3C}^*,\text{SYR}}^{\text{h}}$ ( $10^{-7} \text{ M s}^{-1}$ )	$10^2 \times \Phi_{\text{3C}^*,\text{SYR}}^{\text{i}}$
Winter & Spring	111519	11 (0.7)	0.06 (0.01)	0.15 (0.04)	0.79 (0.09)	22 (4)	79 (21)	1.9	15 (4)	6.0 (1.6)
	120319	1.9 (0.1)	0.14 (0.03)	0.07 (0.02)	0.79 (0.10)	3.8 (0.8)	4.9 (1.0)	0.88	0.43 (0.09)	2.6 (0.6)
	122019	5.3 (0.5)	0.15 (0.03)	0.17 (0.04)	0.69 (0.12)	9.4 (2.2)	45 (13)	1.2	5.4 (1.6)	4.6 (1.4)
	010220	1.1 (0.1)	0.29 (0.06)	0.09 (0.03)	0.63 (0.11)	1.8 (0.4)	3.4 (0.9)	0.88	0.31 (0.08)	1.7 (0.4)
	010620	5.4 (0.2)	0.17 (0.04)	0.15 (0.03)	0.67 (0.06)	9.3 (1.9)	19 (4)	1.2	2.3 (0.5)	2.7 (0.6)
	021620 <sup>j</sup>						35 (9)	1.4	4.7 (1.3)	2.9 (0.8)
	022020	3.9 (0.2)	0.05 (0.01)	0.05 (0.01)	0.90 (0.05)	9.0 (1.7)	11 (2)	0.91	1.0 (0.2)	2.5 (0.5)
	030420	0.66 (0.04)	0.44 (0.10)	0.11 (0.03)	0.45 (0.12)	0.77 (0.24)	1.3 (0.4)	0.88	0.12 (0.04)	0.9 (0.3)
Summer & Fall	070720	0.91 (0.2)	0.16 (0.03)	0.07 (0.01)	0.77 (0.05)	1.8 (0.3)	2.4 (0.5)	0.85	0.20 (0.04)	4.0 (0.8)
	080420	0.33 (0.03)	0.14 (0.08)	0.09 (0.04)	0.77 (0.13)	0.66 (0.15)	0.87 (0.21)	0.84	0.073 (0.017)	3.3 (0.8)
	101520	0.81 (0.02)	0.08 (0.03)	0.03 (0.01)	0.89 (0.05)	1.9 (0.3)	1.9 (0.3)	0.81	0.15 (0.03)	8.5 (1.6)
Fresh wildfire	081920	8.8 (0.1)	0.06 (0.01)	0.13 (0.03)	0.80 (0.04)	18.3 (3.5)	40 (9)	1.5	5.9 (1.3)	1.4 (0.3)
	082220 <sup>j</sup>						51 (12)	1.7	8.6 (2.0)	2.2 (0.5)
	082420	9.2 (1.2)	0.04 (0.01)	0.12 (0.03)	0.84 (0.18)	20 (5)	64 (16)	1.4	9.0 (2.3)	3.1 (0.8)
	090920	16 (4)	0.03 (0.01)	0.04 (0.01)	0.92 (0.04)	39 (7)	40 (22)	1.2	4.8 (2.6)	3.1 (1.7)
Aged wildfire	090120	5.3 (0.1)	0.02 (0.01)	0.03 (0.01)	0.95 (0.04)	13 (8)	15 (3)	0.94	1.5 (0.3)	5.2 (1.1)
	091520	4.8 (0.1)	0.06 (0.01)	0.04 (0.01)	0.91 (0.03)	11 (2)	13 (3)	1.0	1.3 (0.3)	3.8 (0.9)
	100820	8.0 (0.3)	0.08 (0.02)	0.06 (0.01)	0.87 (0.05)	18 (3)	18 (3)	1.3	2.3 (0.4)	4.2 (0.8)
Averages <sup>k</sup>										
Winter & Spring							5.8 (3.7)			3.3 (1.6)
Summer & Fall							1.2 (0.78)			5.3 (2.8)
Fresh wildfire							48 (14)			2.5 (0.8)
Aged wildfire							16 (2.5)			4.4 (0.7)
Field blanks										
	FB1	0.052 ( $\pm 0.004$ )	2.20 ( $\pm 1.34$ )	0.11 ( $\pm 0.02$ )	-1.31 ( $\pm 1.34$ )	-0.018 ( $\pm 0.018$ )	-0.32 ( $\pm 0.33$ )			
	FB2	0.13 ( $\pm 0.01$ )	0.09 ( $\pm 0.02$ )	0.05 ( $\pm 0.01$ )	0.86 ( $\pm 0.03$ )	0.30 ( $\pm 0.05$ )	0.32 ( $\pm 0.08$ )			
	FB3	0.20 ( $\pm 0.01$ )	0.15 ( $\pm 0.04$ )	0.05 ( $\pm 0.01$ )	0.80 ( $\pm 0.06$ )	0.42 ( $\pm 0.08$ )	0.42 ( $\pm 0.08$ )			

Listed uncertainties (in parentheses) are  $\pm 1$  standard error propagated from the errors in the regression and rate constants, except for the averages, which are  $\pm 1\sigma$ .

- <sup>a</sup> Davis winter-solstice-normalized pseudo-first-order rate constant for loss of syringol (SYR)
- <sup>b</sup> Fraction of SYR loss due to hydroxyl radical, calculated as  $f_{\text{SYR,OH}} = (k_{\text{SYR+OH}} \times [\bullet\text{OH}]) / k'_{\text{SYR}}$
- <sup>c</sup> Fraction of SYR loss due to singlet oxygen, calculated as  $f_{\text{SYR,1O2}^*} = (k_{\text{SYR+1O2}^*} \times [^1\text{O}_2^*]) / k'_{\text{SYR}}$ .
- <sup>d</sup> Fraction of SYR loss due to triplets, calculated as  $f_{\text{SYR,3C}^*} = (1 - f_{\text{SYR,OH}} - f_{\text{SYR,1O2}^*})$ .
- <sup>e</sup> Uncorrected triplet steady-state concentration calculated from syringol loss as  $k'_{\text{SYR,3C}^*} / k_{\text{SYR+3DMB}^*}$ .
- <sup>f</sup> Triplet concentration after correction for SYR inhibition, calculated as  $[^3\text{C}^*]_{\text{SYR,uncorr}} / IF_{\text{SYR,corr}}$ .
- <sup>g</sup> First-order rate constant for loss of oxidizing  $^3\text{C}^*$  due to DOC and dissolved oxygen, as determined by SYR. This is calculated as  $k'_{^3\text{C}^*,\text{SYR}} = k_{\text{rxn+Q,3C}^*}[\text{DOC}] + k_{^3\text{C}^*+\text{O}_2}[\text{O}_2]$ , where  $k_{\text{rxn+Q,3C}^*}$  is estimated from the fitting between  $[^3\text{C}^*]_{\text{SYR}}$  and DOC using samples from this work and Ma et al. (2022) using the equation  $[^3\text{C}^*]_{\text{SYR}} = \frac{a[\text{DOC}]}{1+b[\text{DOC}]}$  (Kaur et al., 2019). The resulting  $k_{\text{rxn+Q,3C}^*}$  value is  $7.2 (\pm 2.2) \times 10^7 \text{ M}^{-1} \text{ s}^{-1}$ , while  $k_{^3\text{C}^*+\text{O}_2}$  is  $2.8 (\pm 0.4) \times 10^9 \text{ M}^{-1} \text{ s}^{-1}$  from Kaur et al. (2019).
- <sup>h</sup> Production rate of oxidizing triplets determined by SYR, calculated as  $P_{^3\text{C}^*,\text{SYR}} = [^3\text{C}^*]_{\text{SYR}} \times k'_{^3\text{C}^*,\text{SYR}}$ .
- <sup>i</sup> Apparent quantum yield of  $^3\text{C}^*$  determined by SYR during simulated sunlight illumination, calculated as  $\Phi_{^3\text{C}^*,\text{SYR}} = P_{^3\text{C}^*,\text{SYR}} / R_{\text{abs}}$ .
- <sup>j</sup> These two samples are the interpolated winter and summer samples, respectively, from our previous work (Ma et al., 2022a).  $^3\text{C}^*$  concentrations were estimated at an extraction volume of 1 mL water/square by interpolating the hyperbolic regression between  $[^3\text{C}^*]$  and concentration factor.
- <sup>k</sup> Average value of each sample type. The  $^3\text{C}^*$  concentration normalized by sampling duration was used for the average  $[^3\text{C}^*]_{\text{SYR}}$  calculation.

**Table S5.8.** Oxidizing triplet excited state measurements by (phenylthio)acetic acid (PTA)

Sample Type	Sample ID	$k'_{\text{PTA}}^{\text{a}}$ ( $10^{-4} \text{ s}^{-1}$ )	$f_{\text{PTA,OH}}^{\text{b}}$	$f_{\text{PTA,IO}_2^{\text{c}}}$	$f_{\text{PTA,3C}^{\text{d}}}$	$[\text{C}^*]_{\text{PTA,un}}^{\text{e}}$ ( $10^{-14} \text{ M}$ )	$[\text{C}^*]_{\text{PTA}}^{\text{f}}$ ( $10^{-14} \text{ M}$ )	$k'_{3\text{C}^*,\text{PTA}}^{\text{g}}$ ( $10^6 \text{ s}^{-1}$ )	$P_{3\text{C}^*,\text{PTA}}^{\text{h}}$ ( $10^{-7} \text{ M s}^{-1}$ )	$10^2 \times \Phi_{3\text{C}^*,\text{PTA}}^{\text{i}}$	$[\text{C}^*]_{\text{PTA}} / [\text{C}^*]_{\text{SYR}}^{\text{j}}$
Winter & Spring	111519	12 (1)	0.03 (0.01)	0.03 (0.01)	0.94 (0.06)	44 (11)	44 (11)	2.0	8.5 (2.1)	3.4 (0.8)	0.55 (0.20)
	120319	1.1 (0.1)	0.12 (0.01)	0.03 (0.01)	0.85 (0.02)	3.6 (0.9)	3.6 (0.9)	0.88	0.32 (0.08)	2.0 (0.5)	0.75 (0.24)
	122019	5.7 (0.1)	0.07 (0.01)	0.04 (0.01)	0.89 (0.01)	20 (5)	20 (5)	1.2	2.4 (0.6)	2.1 (0.5)	0.45 (0.17)
	010220	1.2 (0.1)	0.14 (0.01)	0.02 (0.01)	0.84 (0.02)	4.0 (1.0)	4.0 (1.0)	0.89	0.35 (0.08)	1.9 (0.5)	1.2 (0.4)
	010620	5.9 (0.1)	0.08 (0.01)	0.03 (0.01)	0.89 (0.03)	21 (5)	21 (5)	1.2	2.5 (0.6)	2.9 (0.7)	1.1 (0.4)
	021620 <sup>k</sup>						22 (6)	1.4	3.0 (0.8)	1.9 (0.5)	0.64 (0.24)
	022020	1.6 (0.1)	0.06 (0.02)	0.03 (0.01)	0.90 (0.08)	5.7 (1.4)	5.7 (1.4)	0.91	0.52 (0.13)	1.3 (0.3)	0.51 (0.16)
	030420	0.74 (0.06)	0.20 (0.02)	0.02 (0.01)	0.77 (0.07)	2.3 (0.6)	2.3 (0.6)	0.88	0.20 (0.05)	1.5 (0.4)	1.7 (0.7)
Summer & Fall	070720	0.31 (0.01)	0.25 (0.02)	0.05 (0.01)	0.70 (0.04)	0.85 (0.21)	0.85 (0.21)	0.86	0.073 (0.018)	1.4 (0.4)	0.36 (0.11)
	080420	0.084 (0.014)	0.28 (0.15)	0.08 (0.03)	0.64 (0.25)	0.21 (0.09)	0.28 (0.12)	0.84	0.024 (0.010)	1.1 (0.5)	0.33 (0.16)
	101520	0.17 (0.02)	0.21 (0.08)	0.03 (0.01)	0.76 (0.14)	0.52 (0.15)	0.52 (0.15)	0.81	0.042 (0.012)	2.4 (0.7)	0.28 (0.10)
Fresh wildfire	081920	5.2 (0.1)	0.05 (0.01)	0.06 (0.01)	0.89 (0.03)	18 (4)	18 (4)	1.5	2.8 (0.8)	0.64 (0.17)	0.46 (0.16)
	082220 <sup>k</sup>						19 (5)	1.7	3.2 (0.9)	0.84 (0.23)	0.37 (0.13)
	082420	3.0 (0.2)	0.07 (0.02)	0.09 (0.01)	0.84 (0.07)	10 (3)	17 (4)	1.4	2.4 (0.6)	0.85 (0.22)	0.27 (0.10)
	090920	4.6 (0.1)	0.06 (0.01)	0.04 (0.01)	0.90 (0.04)	17 (4)	19 (12)	1.2	2.3 (1.5)	1.5 (1.0)	0.48 (0.41)
Aged wildfire	090120	1.4 (0.1)	0.04 (0.01)	0.03 (0.01)	0.94 (0.03)	5.1 (1.2)	5.2 (1.3)	0.94	0.49 (0.12)	1.8 (0.4)	0.34 (0.11)
	091520	1.5 (0.1)	0.10 (0.01)	0.03 (0.01)	0.87 (0.04)	5.1 (1.2)	5.5 (1.4)	1.0	0.56 (0.14)	1.6 (0.4)	0.42 (0.14)
	100820	2.1 (0.1)	0.16 (0.01)	0.05 (0.01)	0.79 (0.03)	6.5 (1.6)	6.5 (1.6)	1.3	0.83 (0.20)	1.5 (0.4)	0.36 (0.11)
Averages <sup>m</sup>											
Winter & Spring							3.9 (1.4)			2.1 (0.7)	0.86 (0.43)
Summer & Fall							0.57 (0.29)			1.6 (0.7)	0.32 (0.04)
Fresh wildfire							18 (0.16)			0.96 (0.39)	0.39 (0.10)
Aged wildfire							5.7 (0.7)			1.6 (0.1)	0.37 (0.05)
Field blanks											
FBI <sup>1</sup>		4.6 ( $\pm 0.6$ )	0.01 ( $\pm 0.01$ )	0.00 ( $\pm 0.01$ )	0.99 ( $\pm 0.14$ )	18.1 ( $\pm 5.0$ )	20.1 ( $\pm 7.0$ )				
FB2		0.028 ( $\pm 0.009$ )	0.22 ( $\pm 0.03$ )	0.07 ( $\pm 0.01$ )	0.71 ( $\pm 0.32$ )	0.078 ( $\pm 0.040$ )	0.084 ( $\pm 0.043$ )				

FB3	0.051 (±0.019)	0.31 (±0.04)	0.05 (±0.01)	0.64 (±0.38)	0.13 (±0.08)	0.13 (±0.08)				
-----	-------------------	-----------------	-----------------	-----------------	-----------------	-----------------	--	--	--	--

Listed uncertainties (in parentheses) are  $\pm 1$  standard error propagated from the errors in the regression and rate constants, except for the averages, which are  $\pm 1\sigma$ .

<sup>a</sup> Davis winter-solstice-normalized value of the measured pseudo-first-order rate constant for loss of PTA. Contribution from PTA direct photodegradation was subtracted. The PTA direct photodegradation accounted for (0.9-55) % of PTA total decay in PME samples, with an average of 11 ( $\pm 15$ ) %. It accounted for (2-79) % of PTA total decay in field blanks.

<sup>b</sup> Fraction of hydroxyl radical contribution to the loss of PTA, calculated as  $f_{PTA,OH} = (k_{PTA+OH} \times [^{\bullet}OH])/k'_{PTA}$

<sup>c</sup> Fraction of singlet oxygen contribution to the loss of PTA, calculated as  $f_{PTA,1O2^*} = (k_{PTA+1O2^*} \times [^1O_2^*])/k'_{PTA}$ .

<sup>d</sup> Fraction of PTA loss due to triplets, calculated as  $f_{PTA,3C^*} = (1 - f_{PTA,OH} - f_{PTA,1O2^*})$ .

<sup>e</sup> Uncorrected triplet steady-state concentration calculated from PTA loss as  $k'_{PTA,3C^*}/k_{PTA+3DMB^*}$ .

<sup>f</sup> Triplet concentration with inhibition factor correction, calculated as  $[^3C^*]_{PTA,uncorr}/IF_{PTA,corr}$ .

<sup>g</sup> Apparent pseudo-first-order rate constant for quenching  $^3C^*$  determined by PTA due to natural sinks and dissolved oxygen, calculated as  $k'_{3C^*,PTA} = k_{rxn+Q,3C^*}[DOC] + k_{3C^*+O_2}[O_2]$ , where  $k_{rxn+Q,3C^*}$  is estimated from the fitting between  $[^3C^*]_{PTA}$  and DOC using samples from this work and Ma et al. (2022) using an equation of  $[^3C^*]_{PTA} = \frac{a[DOC]}{1+b[DOC]}$  (Kaur et al., 2019). The corresponding  $k_{rxn+Q,3C^*} = 7.4 (\pm 2.5) \times 10^7 M^{-1} s^{-1}$  and  $k_{3C^*+O_2} = 2.8 (\pm 0.4) \times 10^9 M^{-1} s^{-1}$  from Kaur et al. (Kaur et al., 2019).

<sup>h</sup> Production rate of triplet determined by PTA, calculated as  $P_{3C^*,PTA} = [^3C^*]_{PTA} \times k'_{3C^*,PTA}$ .

<sup>i</sup> Apparent quantum yield of  $^3C^*$  determined by PTA during simulated sunlight illumination, calculated as  $\Phi_{3C^*,PTA} = P_{3C^*,PTA}/R_{abs}$ .

<sup>j</sup> Ratio of triplet concentration determined by PTA to that determined by SYR.

<sup>k</sup> These two samples are the interpolation of winter and summer samples, respectively, in our previous work (Ma et al., 2022a).  $^3C^*$  concentrations were estimated by interpolating the hyperbolic regression between  $[^3C^*]_{PTA}$  and concentration factor, to an equivalent extraction volume of 1 mL water/square.

<sup>l</sup> This field blank sample was contaminated by a pH electrode and possibly other unknown sources, leading to fast decay of PTA.

<sup>m</sup> Average value of each sample type. The  $^3C^*$  concentration normalized by sampling duration was used in the calculation of average  $[^3C^*]_{PTA}$ .



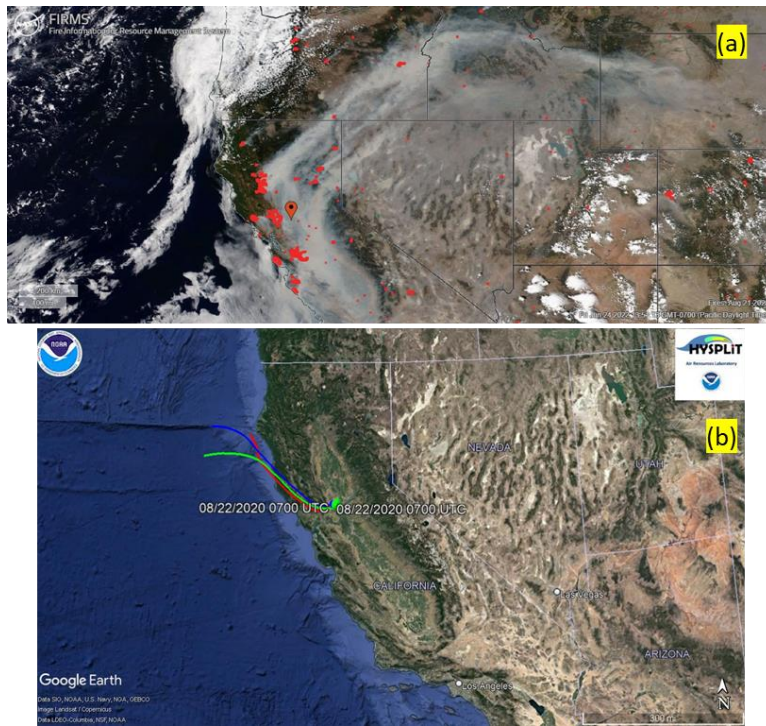


**Figure S5.3.** (a) Satellite image on 22 August 2020, with fires detected by VIIRS labeled by red dots. The location symbol represents Davis CA. (b) 24 hr back trajectories ending at the sampling site at heights of 20 m (red), 600 m (blue), and 1200 m (green) above the ground. It took approximately 1-2 h for the smoke plume from the Lake Berryessa area west of Davis to be transported to the sampling site.

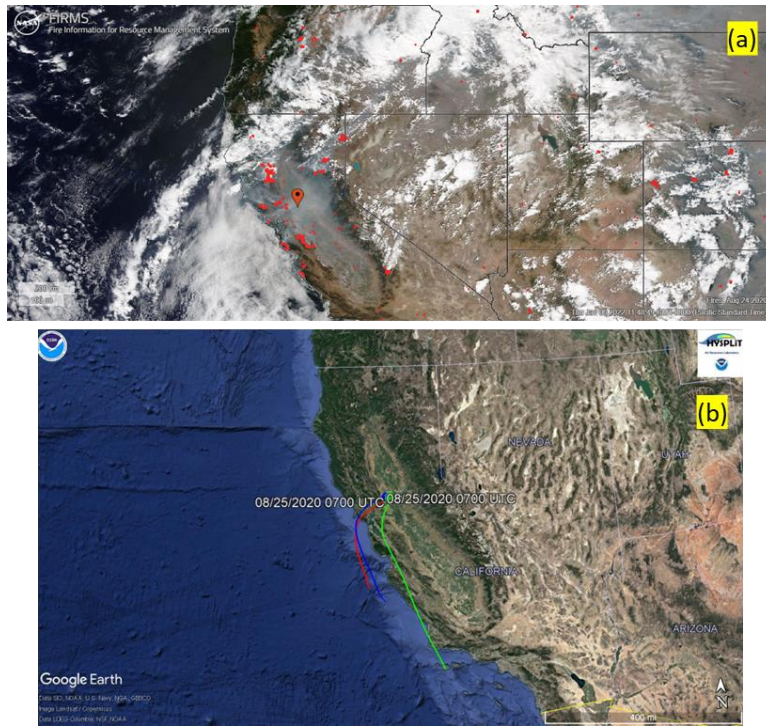


**Figure S5.4.** (a) Satellite image on 24 August 2020, with fires detected by VIIRS labeled by red dots. The location symbol represents Davis CA. (b) 24 hr-back trajectories ending at the sampling site at heights of 20 m (red), 600 m (blue), and 1200 m (green) above the ground.

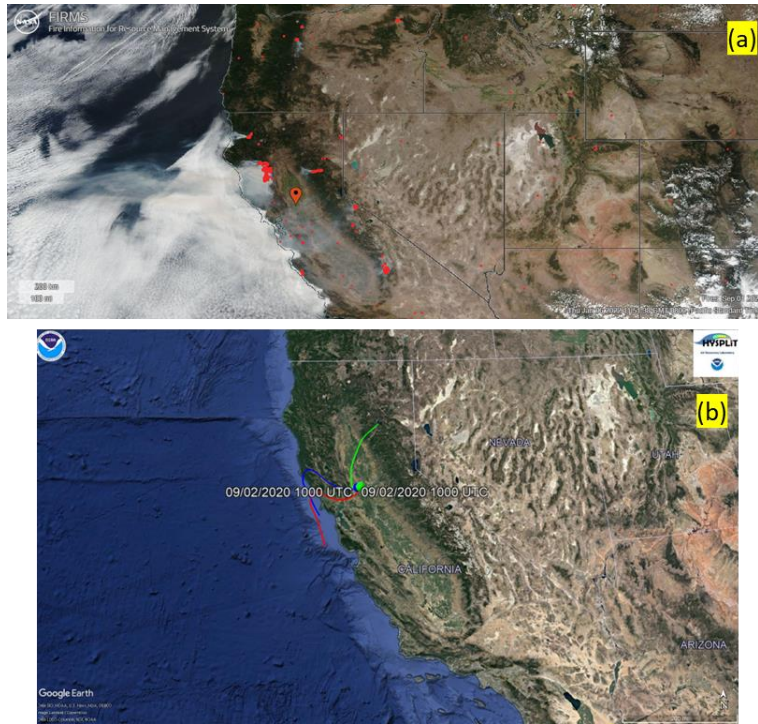


**Figure S5.5.** (a) Satellite image on 1 September 2020, with fires detected by VIIRS labeled by red dots. The location symbol represents Davis CA. (b) 24-hr back trajectories ending at the sampling site at heights of 20 m (red), 600 m (blue), and 1200 m (green) above the ground. Wildfire plumes from the Mendocino National Forest and Chico area took approximately 9 -12 h to transport to Davis.



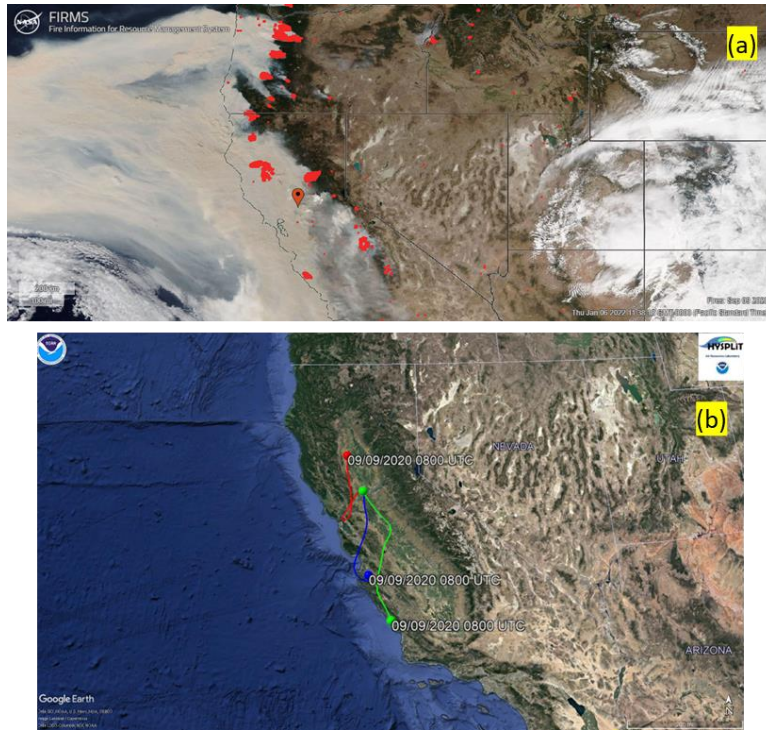


**Figure S5.6.** (a) Satellite image on 9 September 2020, with fires detected by VIIRS labeled by red dots. The location symbol represents Davis CA. (b) 24-hr back trajectories ending at the sampling site at heights of 20 m (red), 600 m (blue), and 1200 m (green) above the ground. Wildfire plumes from the Mendocino National Forest, the Chico area, and Oregon required approximately 7 to 24 h to transport to Davis during this time.

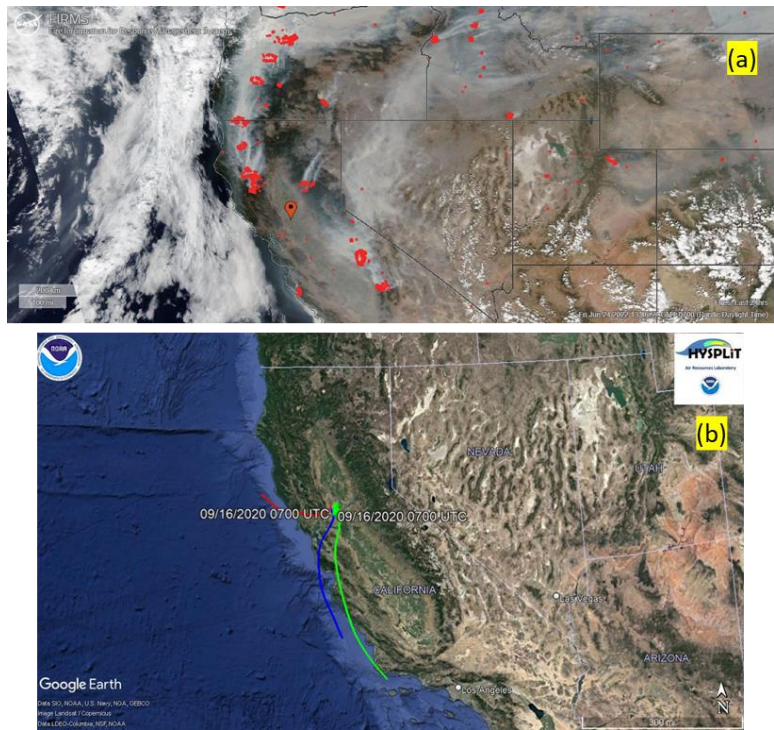


**Figure S5.7.** (a) Satellite image on 15 September 2020, with fires detected by VIIRS labeled by red dots. The location symbol represents Davis CA. (b) 24-hr back trajectories ending at the sampling site at heights of 20 m (red), 600 m (blue), and 1200 m (green) above the ground. Because the back trajectories do not pass through the burning regions it is difficult to estimate a plume aging time.

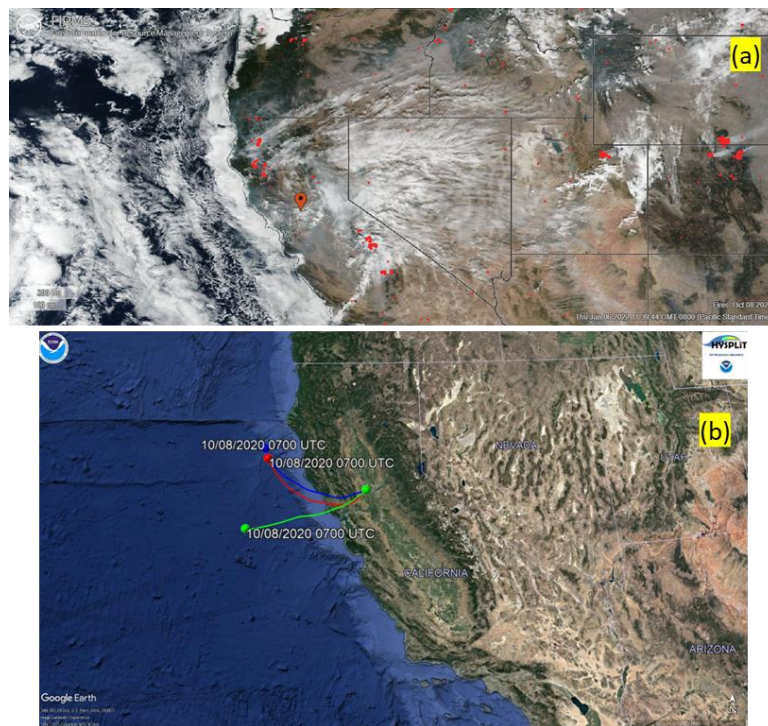


**Figure S5.8.** (a) Satellite image on 10 October 2020, with fire points detected by VIIRS labeled by red dots. The location symbol represents Davis CA. (b) 24-hr back trajectories ending at the sampling site at heights of 20 m (red), 600 m (blue), and 1200 m (green) above the ground. The back trajectories appeared not to pass through the burning areas directly, making it difficult to estimate the aging time.

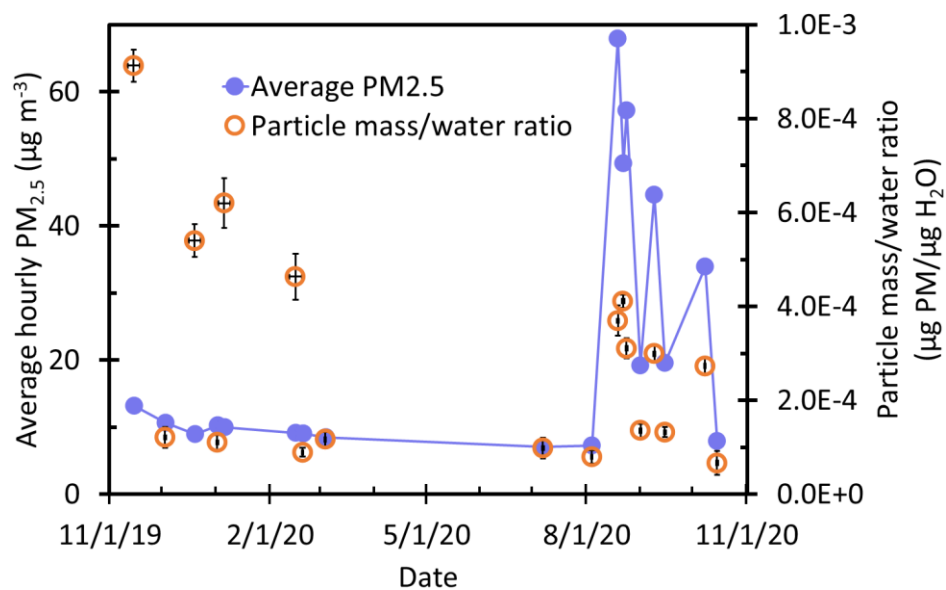


**Figure S5.9.** Average PM<sub>2.5</sub> concentration during sampling period (blue) from a regulatory monitor during each sampling period and measured particle mass/water mass ratios (orange) from filter extracts for each sample. Vertical error bars represent  $\pm 1$  standard deviation, while horizontal error bars represent the duration of sampling (either 1 or 7 days).

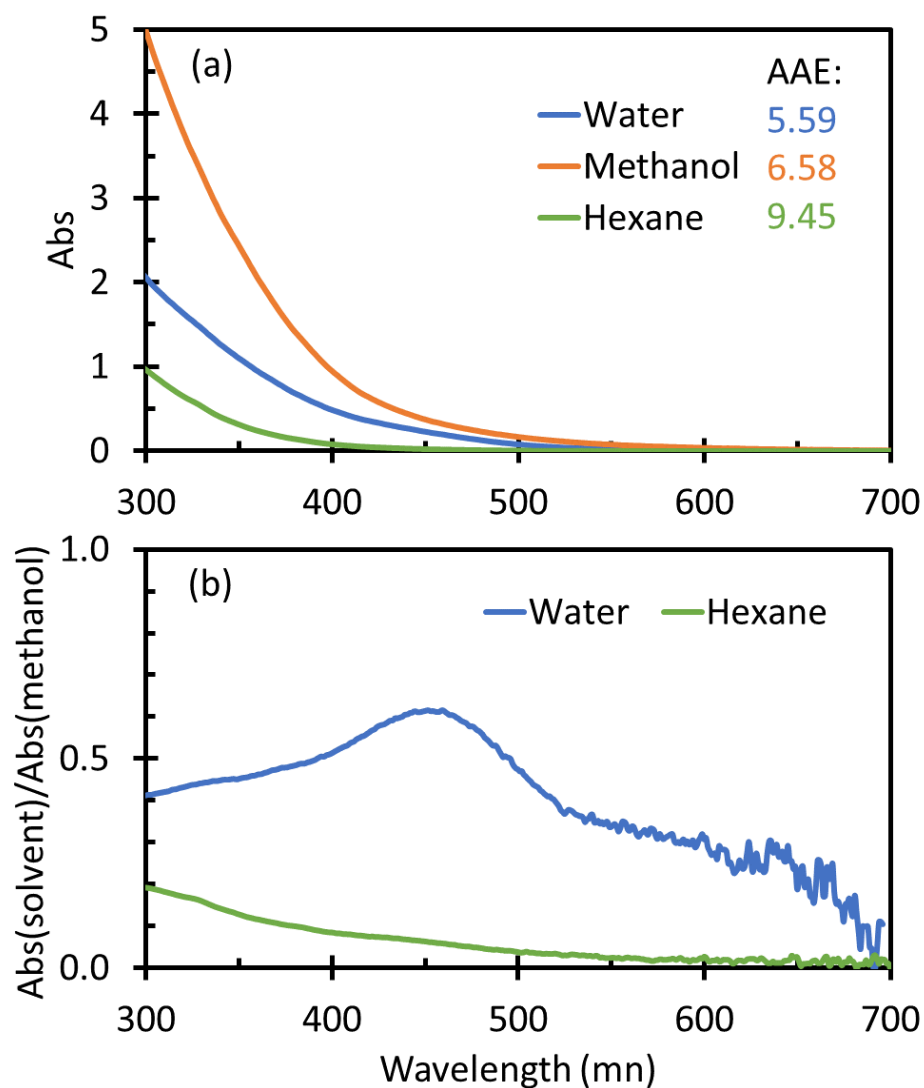


**Figure S5.10.** (a) UV-Vis spectra of different solvent extracts of the particle sample collected on 8/19/2020. Each line represents the absorbance spectrum for a square of filter that was extracted in the listed solvent then filtered. AAE values were determined for each spectrum based on absorbance over 300 to 450 nm. Spectra were measured in 1-cm cuvettes. (b) Ratio of the absorbance in the water (blue) and hexane (green) extracts to the absorbance of the methanol extract.

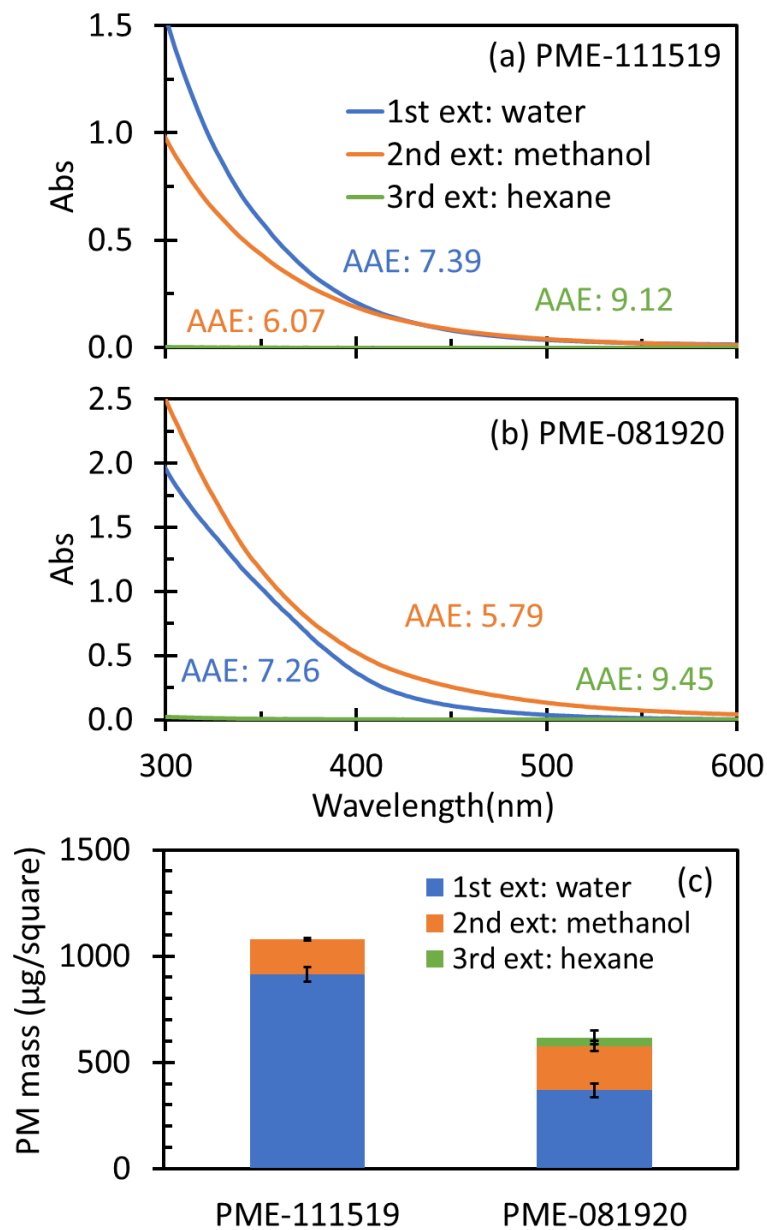


**Figure S5.11.** UV-Vis spectra for sequential extracts of a given filter square, each with 1.0 mL of the solvent listed, as measured in a 1-cm cuvette. The blue line or bar represents the first extraction, which was with water; the orange line or bar represents the second extraction, which was in methanol, and the green line or bar represents the third extraction, which was done with hexane. Panel (a) shows results for sample PME-111519, while panel (b) is for PME-081920. Panel (c) shows the particle mass extracted per filter square in the sequential extraction sequence with water, methanol, and hexane. The particle mass extracted by hexane in PME-111519 was not measured.

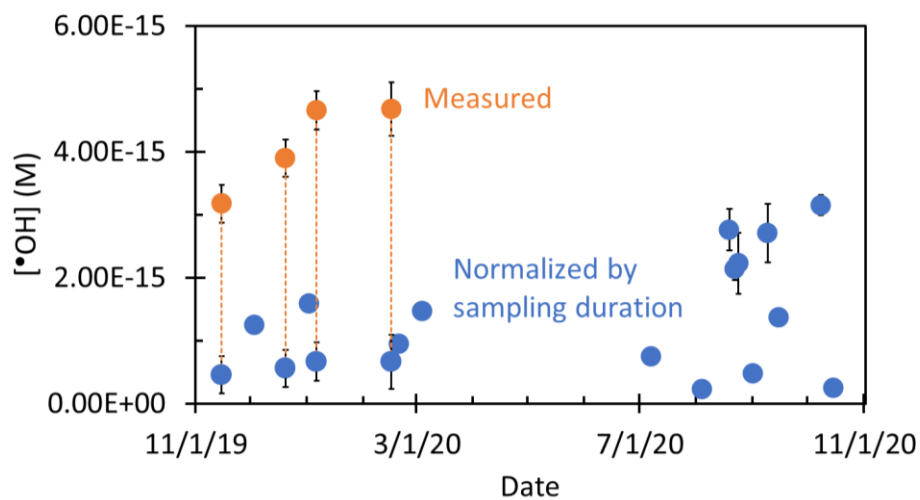


**Figure S5.12.** Comparison between measured  $\bullet\text{OH}$  concentrations (orange) and values normalized by sampling duration in four 7-day samples (blue). Figure 5.4 shows the  $\bullet\text{OH}$  data normalized by PM mass/water mass ratio, which was what we used as the standard normalization for these 7-day samples.

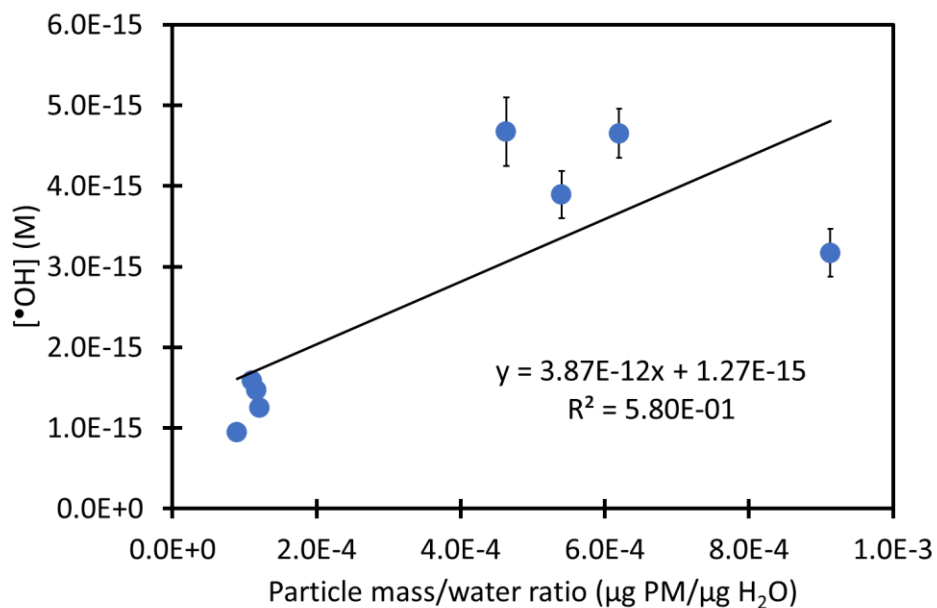


**Figure S5.13.** Dependence of hydroxyl radical concentration on particle mass/water mass ratio for Winter & Spring samples. The line represents the linear regression.

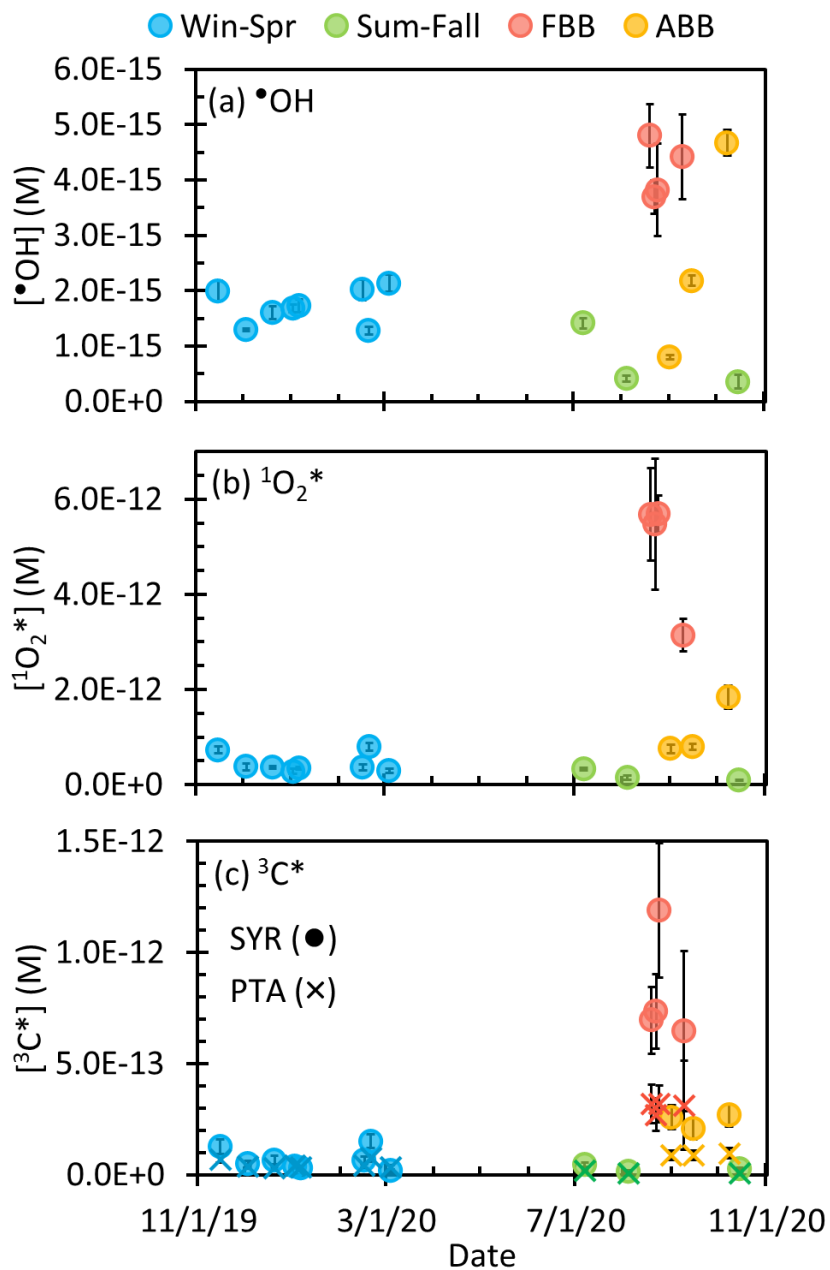


**Figure S5.14.** Steady-state concentrations of (a) hydroxyl radical, (b) singlet molecular oxygen, and (c) oxidizing triplet excited states of light-absorbing organics determined by syringol (SYR) and (phenylthio)acetic acid (PTA, cross symbols) in particle extracts. Concentrations are normalized to the midday sunlight of each sampling period to account for the seasonal differences in actinic flux and the seven-day samples were normalized to the expected one-day result as described in section 5.3.3.1 and Table S5.9.



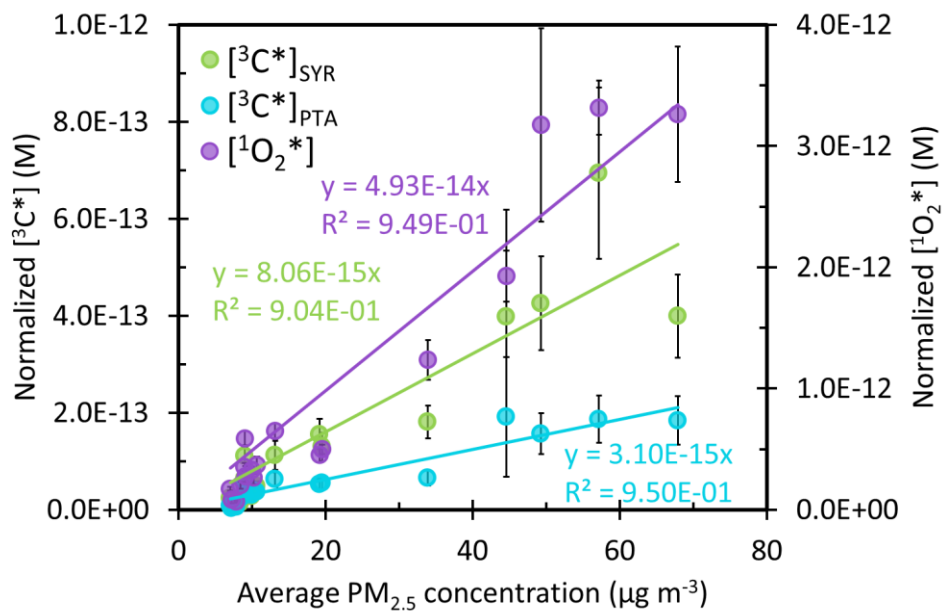


**Figure S5.15.** Normalized singlet oxygen (purple, right y-axis) and triplet excited state of organic matter determined by syringol (green) and (phenylthio)acetic acid (blue) as a function of average PM<sub>2.5</sub> concentration. Solid lines are linear regressions.

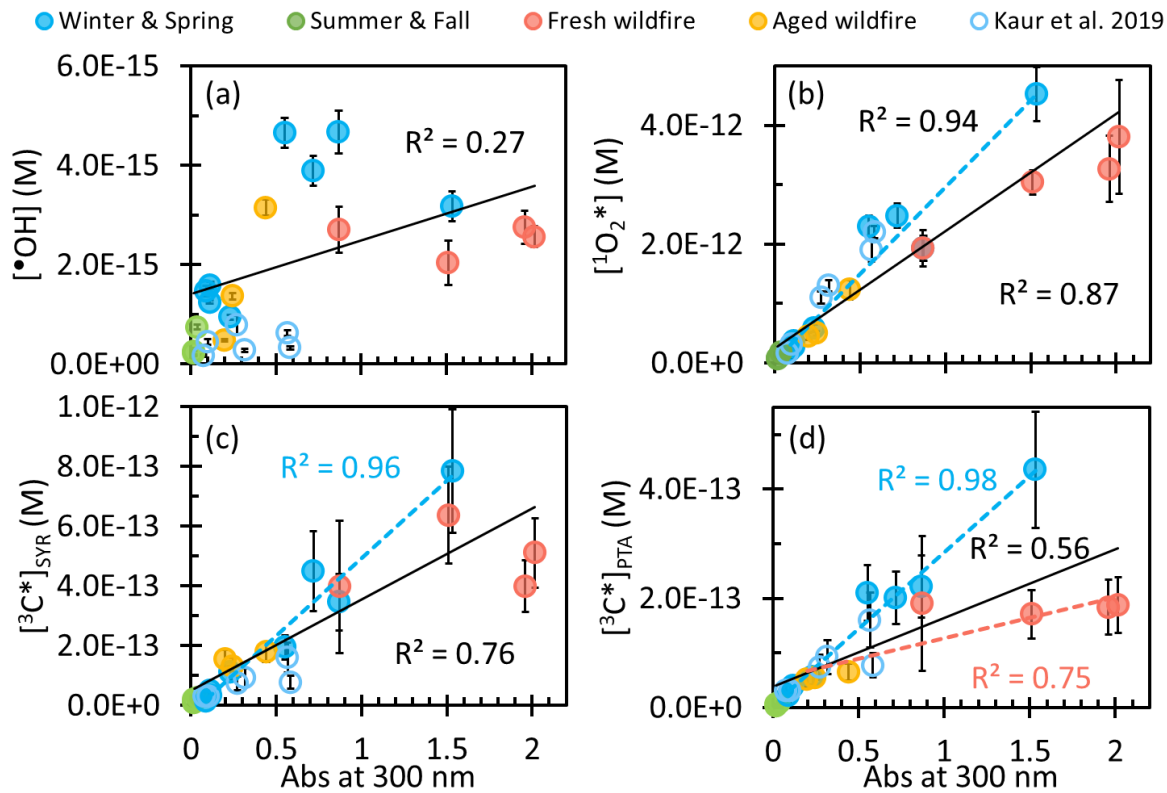


**Figure S5.16.** Steady-state concentrations of (a) hydroxyl radical, (b) singlet molecular, and oxidizing triplet excited states of organic matter determined by (c) syringol and (d) (phenylthio)acetic acid as a function of absorbance at 300 nm for each sample type (solid circles). Previous measurements made on Davis winter particle extracts are shown by open blue circles (Kaur et al., 2019). Solid lines are linear regressions between oxidant concentrations of all samples in this work and extract absorbance in a 1-cm cell. Blue dashed lines are the linear regressions of our Win-Spr samples, while the red dashed line is a regression of the FBB and ABB samples.

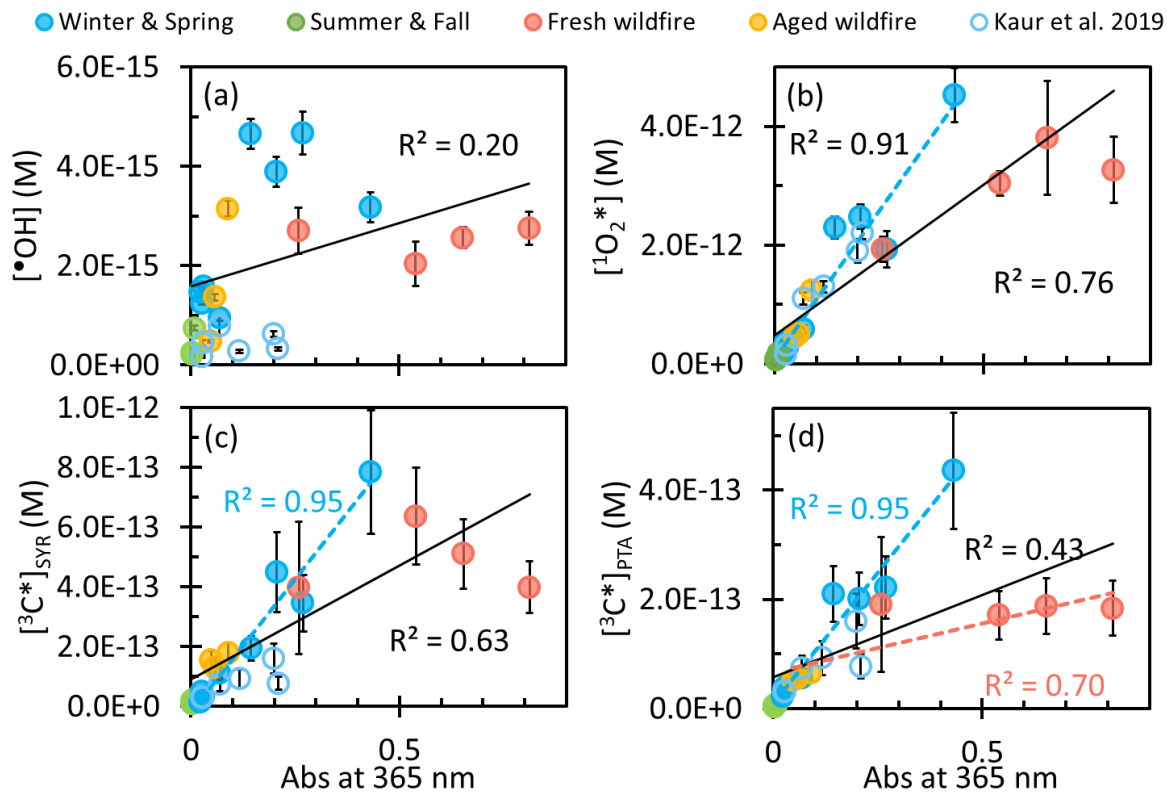


**Figure S5.17.** Steady-state concentrations of (a) hydroxyl radical, (b) singlet molecular, and oxidizing triplet excited state of organic matter determined by (c) syringol and (d) (phenylthio)acetic acid as a function of absorbance (in a 1 cm cell) at 365 nm for each sample type (solid circles). Previous measurements made in Davis winter particle extracts are included (open circles) (Kaur et al., 2019). Solid lines are linear regressions between oxidant concentration and absorbance. Blue dashed lines are the linear regressions of Win-Spr samples, while the red dashed line is the regression of the combined FBB and ABB samples.

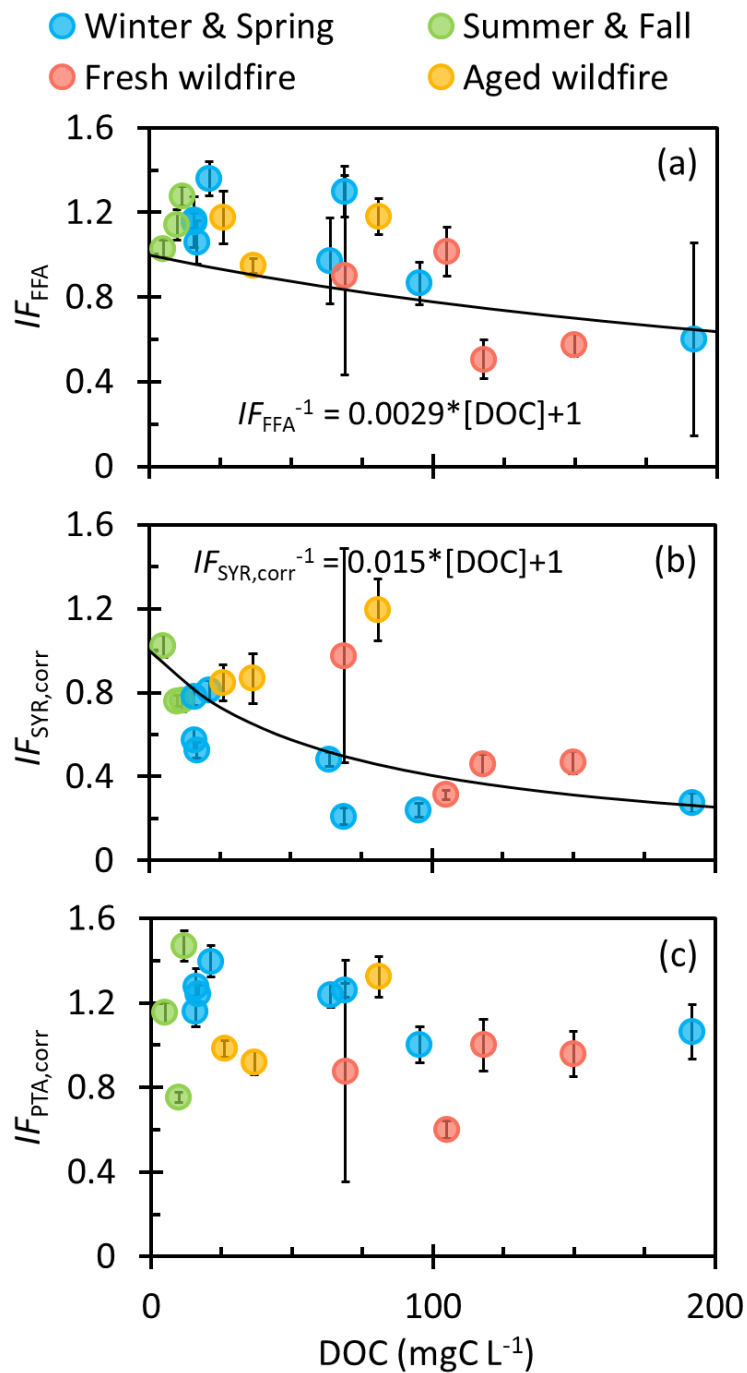


**Figure S5.18.** Inhibition factor of (a) furfuryl alcohol, and corrected inhibition factors of (b) syringol and (c) (phenylthio)acetic acid as a function of dissolved organic carbon. Solid lines represent linear regressions of  $IF_p^{-1} = a[DOC] + b$  (Ma et al., 2022b; Wenk et al., 2011).

### Section S5.3. Seasonal variation of $j_{2NB}$

We obtained the actinic flux (photons  $s^{-1} nm^{-1} cm^{-2}$ ) on the midday of the 15<sup>th</sup> of each month in Davis CA (38.545 ° N, 121.741 ° W) from November 2019 to October 2020 from the Tropospheric Ultraviolet and Visible (TUV) Radiation Model version 5.3 ([https://www.acom.ucar.edu/Models/TUV/Interactive\\_TUV/](https://www.acom.ucar.edu/Models/TUV/Interactive_TUV/), last access: 7 August 2022). For the TUV model runs, other input parameters like ozone column and aerosols were set as default.  $j_{2NB}$  values for each date were calculated using (Galbavy et al., 2010):

$$j_{2NB} = 2.303 \times (10^3 cm^3 L^{-1} \div N_A) \times \sum (I'_\lambda \times \Delta\lambda \times \varepsilon_{2NB,\lambda} \times \Phi_{2NB,\lambda}) \quad (S5.4)$$

where  $N_A$  is Avogadro's number,  $I'_\lambda$  is the actinic flux (photons  $s^{-1} nm^{-1} cm^{-2}$ ),  $\Delta\lambda$  is the wavelength interval between actinic flux data points (1 nm here),  $\varepsilon_{2NB}$  is the base-10 molar absorptivity of 2-nitrobenzaldehyde ( $M^{-1} cm^{-1}$ ) (Galbavy et al., 2010), and  $\Phi_{2NB}$  is the 2NB quantum yield (0.41 molecule photon<sup>-1</sup>, independent of wavelength (Galbavy et al., 2010)). From our calculations,  $j_{2NB}$  on the midday of the winter solstice is 0.0053  $s^{-1}$ , which is lower than the value (0.0070  $s^{-1}$ ) measured in Davis on this day (Anastasio and McGregor, 2001). To approximately compensate for the difference between the measured and modeled values, we added 0.0017  $s^{-1}$  to each calculated  $j_{2NB}$  value and plotted them as a function of date (Figure S5.19). We then fitted the data with a 4<sup>th</sup>-order polynomial with Excel dates as  $x$  values, and use this regression to calculate the  $j_{2NB}$  value on each day of sampling. The calculated  $j_{2NB}$  values are in Table S5.9.

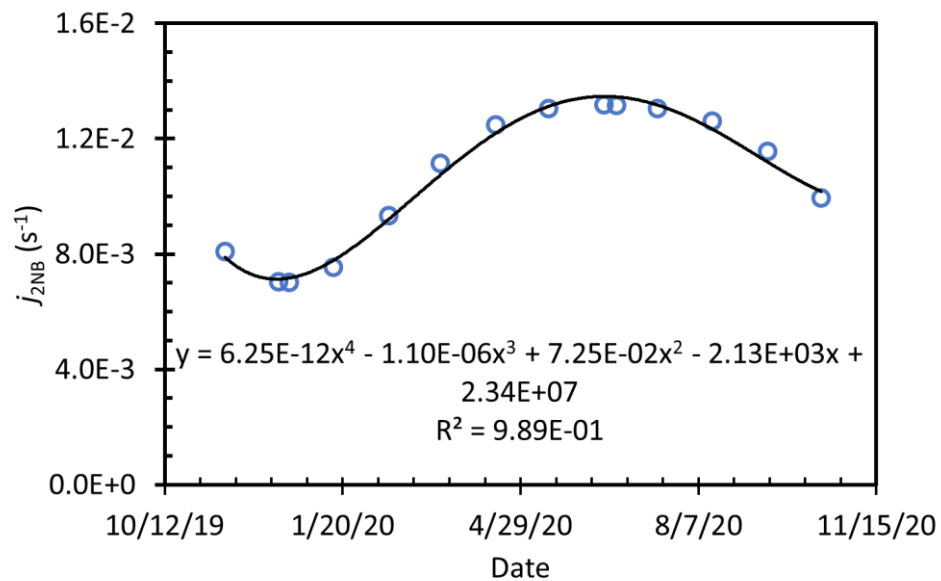


**Figure S5.19.** Estimated midday  $j_{2NB}$  values as a function of date based on TUV actinic fluxes (points) and the corresponding 4<sup>th</sup>-order polynomial fit (solid line). Details about the estimation of  $j_{2NB}$  values are provided in Section S5.3.

**Table S5.9.** Calculated  $j_{2NB}$  values for each sample

Sample Type	Sample ID	$j_{2NB}$ ( $s^{-1}$ ) <sup>a</sup>
Winter & Spring	111519	0.0079
	120319	0.0072
	122019	0.0072
	010220	0.0074
	010620	0.0075
	021620	0.0093
	022020	0.0095
Summer & Fall	030420	0.010
	070720	0.013
	080420	0.013
Fresh wildfire	101520	0.010
	081920	0.012
	082220	0.012
	082420	0.012
Aged wildfire	090920	0.011
	090120	0.012
	091520	0.011
Aged wildfire	100820	0.010
	Averages <sup>b</sup>	
Winter & Spring		0.0083
Summer & Fall		0.012
Fresh wildfire		0.012
Aged wildfire		0.011

<sup>a</sup> Values are calculated for midday on the middle day of each sampling period in Davis.

<sup>b</sup> Average value of each sample type.

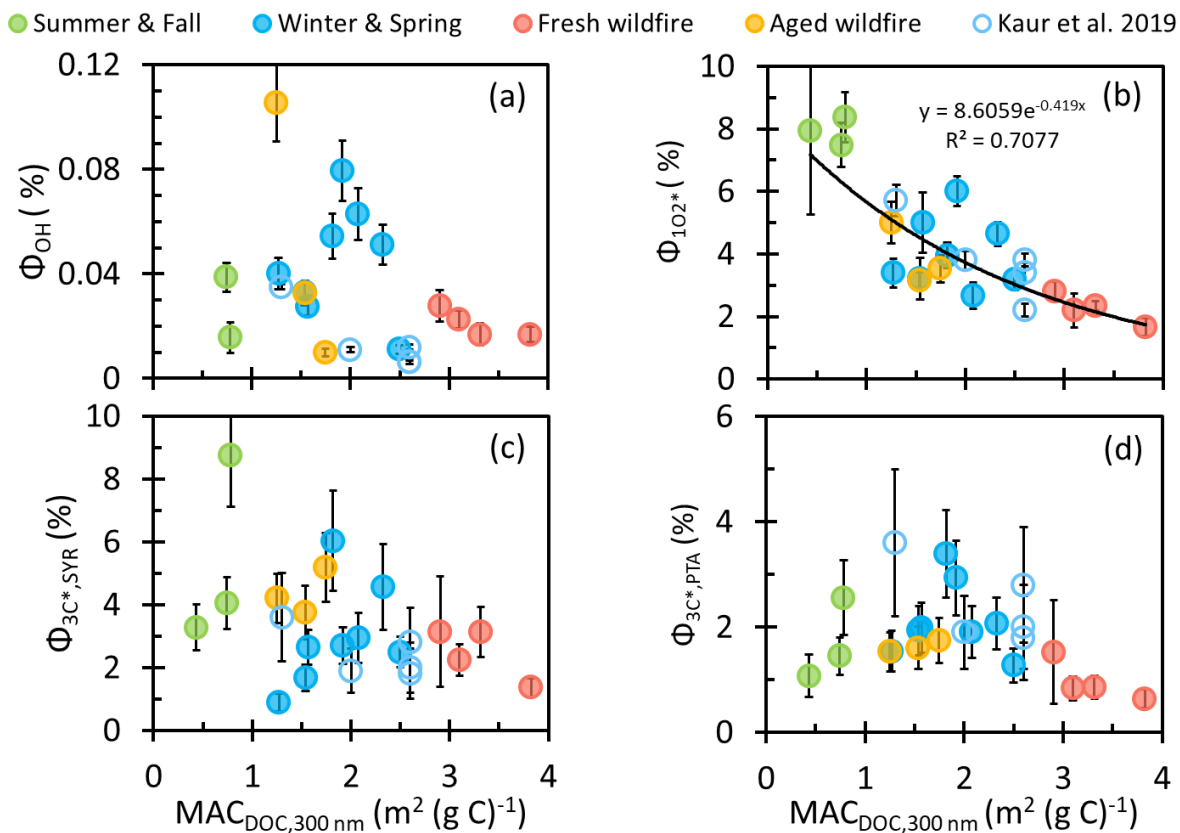


**Figure S5.20.** Apparent quantum yields of (a) hydroxyl radical, (b) singlet molecular oxygen, and oxidizing triplet excited states of organic matter determined by (c) syringol and (d) (phenylthio)acetic acid as a function of DOC-normalized mass absorption coefficient at 300 nm (solid circles). Previous measurements made in Davis winter particle extracts are shown in blue open circles (Kaur et al., 2019). Solid black lines represent exponential regressions.



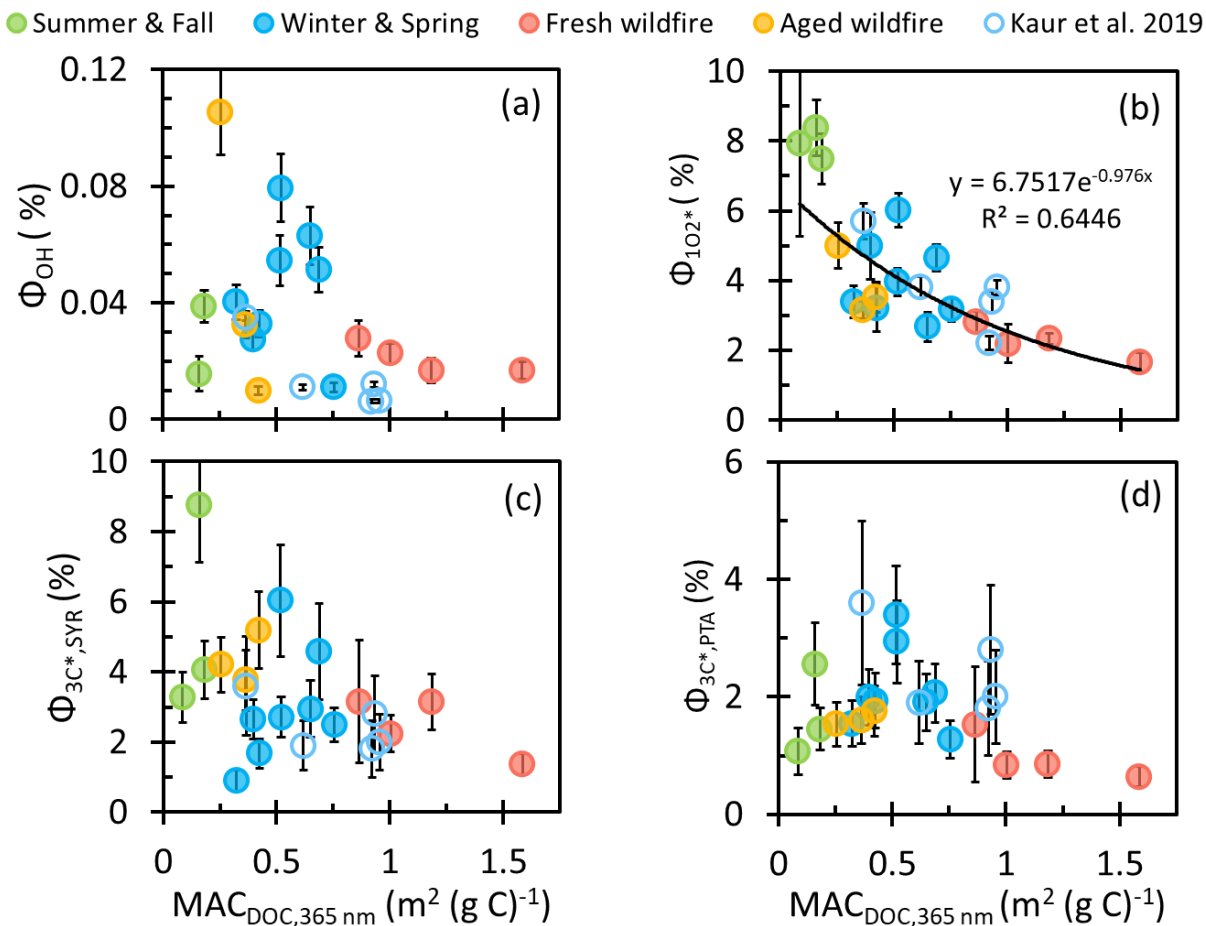


**Figure S5.21.** Apparent quantum yields of (a) hydroxyl radical, (b) singlet molecular oxygen, and oxidizing triplet excited states of organic matter determined by (c) syringol and (d) (phenylthio)acetic acid as a function of DOC-normalized mass absorption coefficient at 365 nm (solid circles). Previous measurements made in Davis winter particle extracts are shown in blue open circles (Kaur et al., 2019). Solid black lines represent exponential regressions.

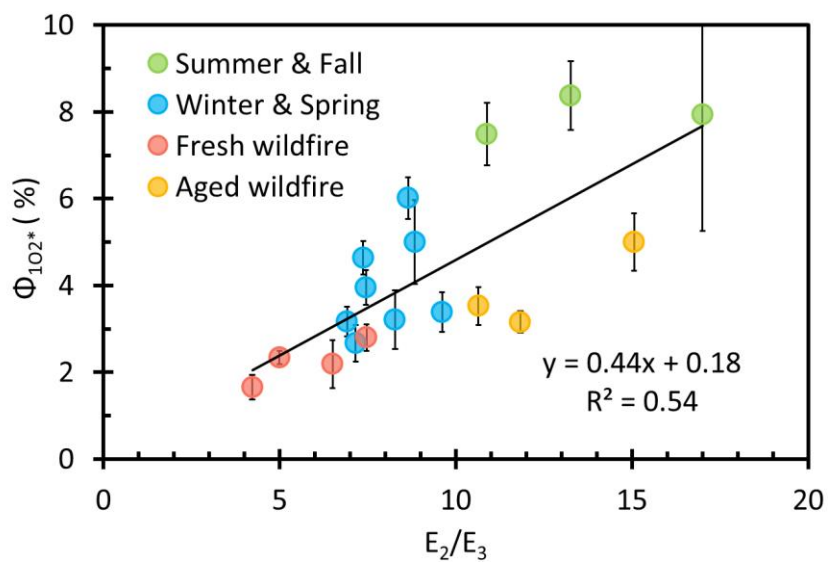


**Figure S5.22.** Apparent quantum yields of  $^1O_2^*$  as a function of  $E_2/E_3$ .

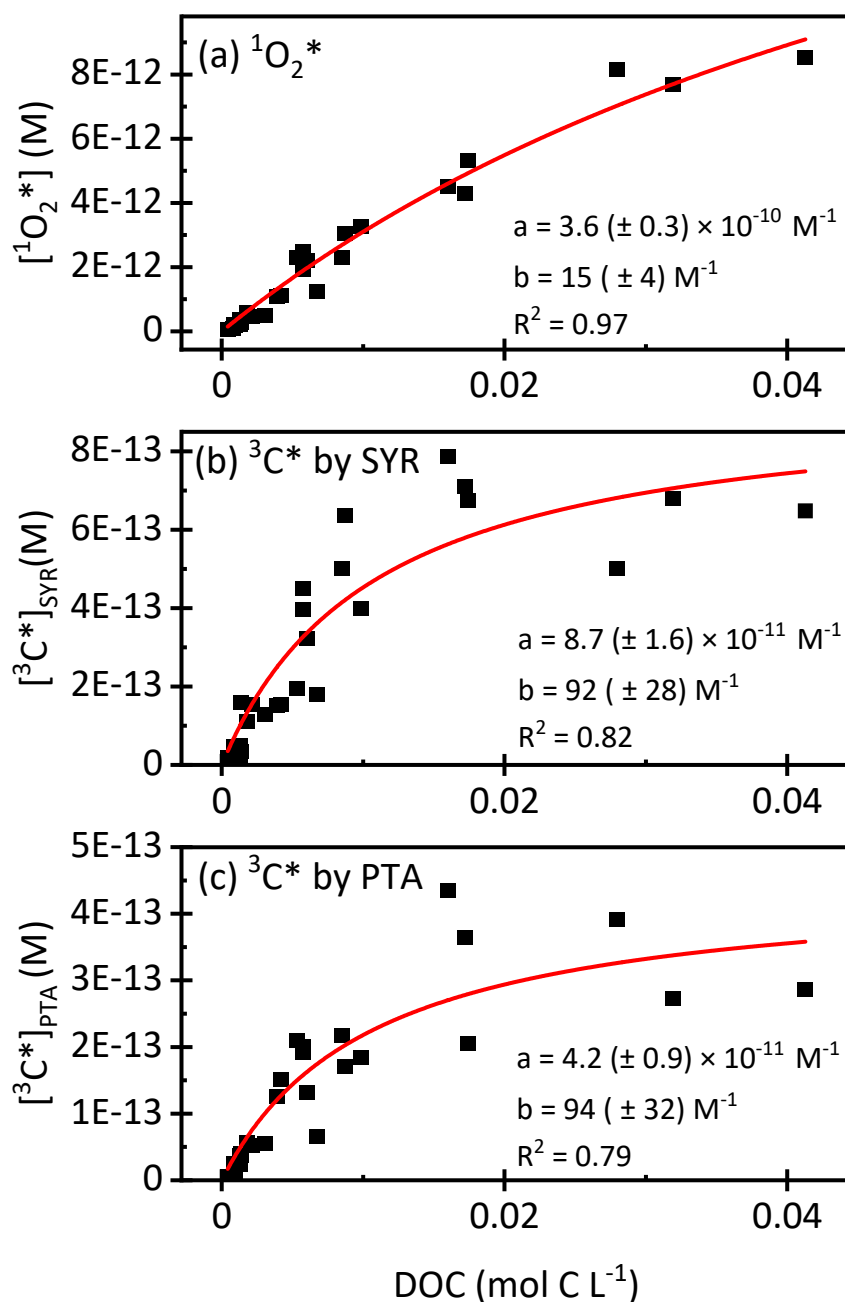


**Figure S5.23.** Dependence of (a)  $^1\text{O}_2^*$ , (b)  $^3\text{C}^*$  determined by SYR, and (c)  $^3\text{C}^*$  determined by PTA on dissolved organic carbon. Solid lines represent hyperbolic regressions with the equation  $[\text{Ox}] = \frac{a[\text{DOC}]}{1+b[\text{DOC}]}$ . The equation is derived in Kaur et al. (2019); as described in this past work, we obtain the rate constant for quenching and reaction of the oxidant by DOC using the fitted value of  $b$  parameter. The data points include the two previous measurements made in Davis winter particle and wildfire particle extracts from Ma et al. (2022a).

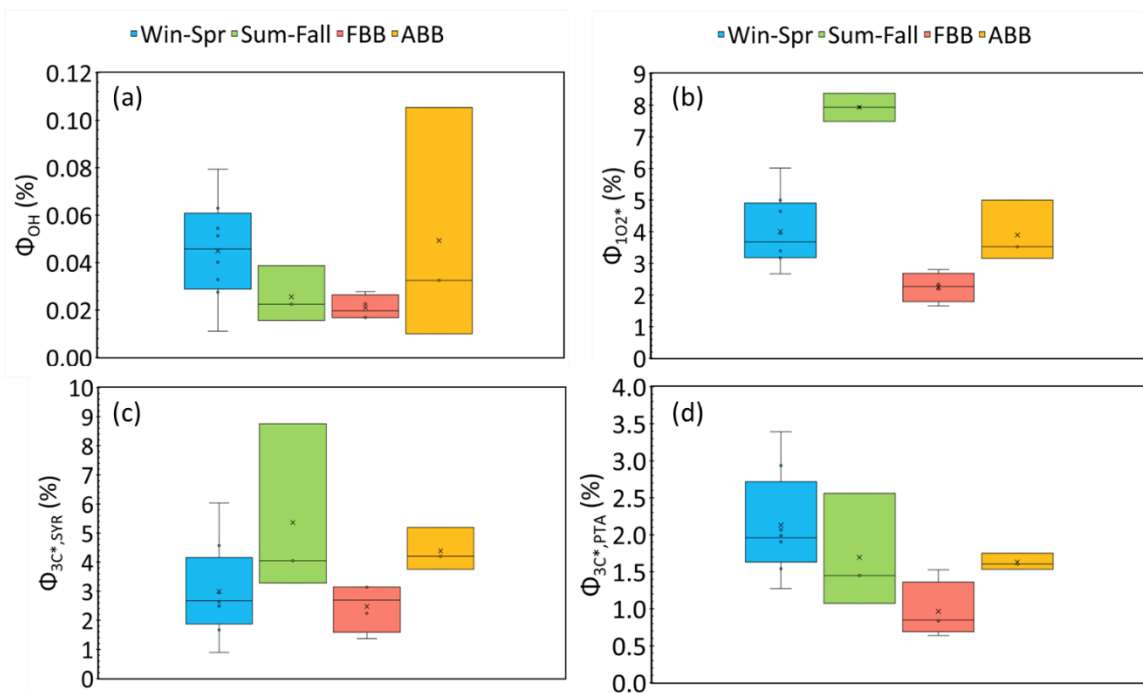


**Figure S5.24.** Box plots of apparent quantum yields of (a)  $\bullet OH$ , (b)  $^1O_2^*$ , (c)  $^3C^*$  determined by SYR, and (d)  $^3C^*$  determined by PTA for each sample type. For each box, the horizontal line within the box is the median value, while the top and bottom of the box represent the 75<sup>th</sup> and 25<sup>th</sup> percentiles, and the cross symbol and open circles are the mean value and data points, respectively. Whiskers represent the minimum and maximum data points.

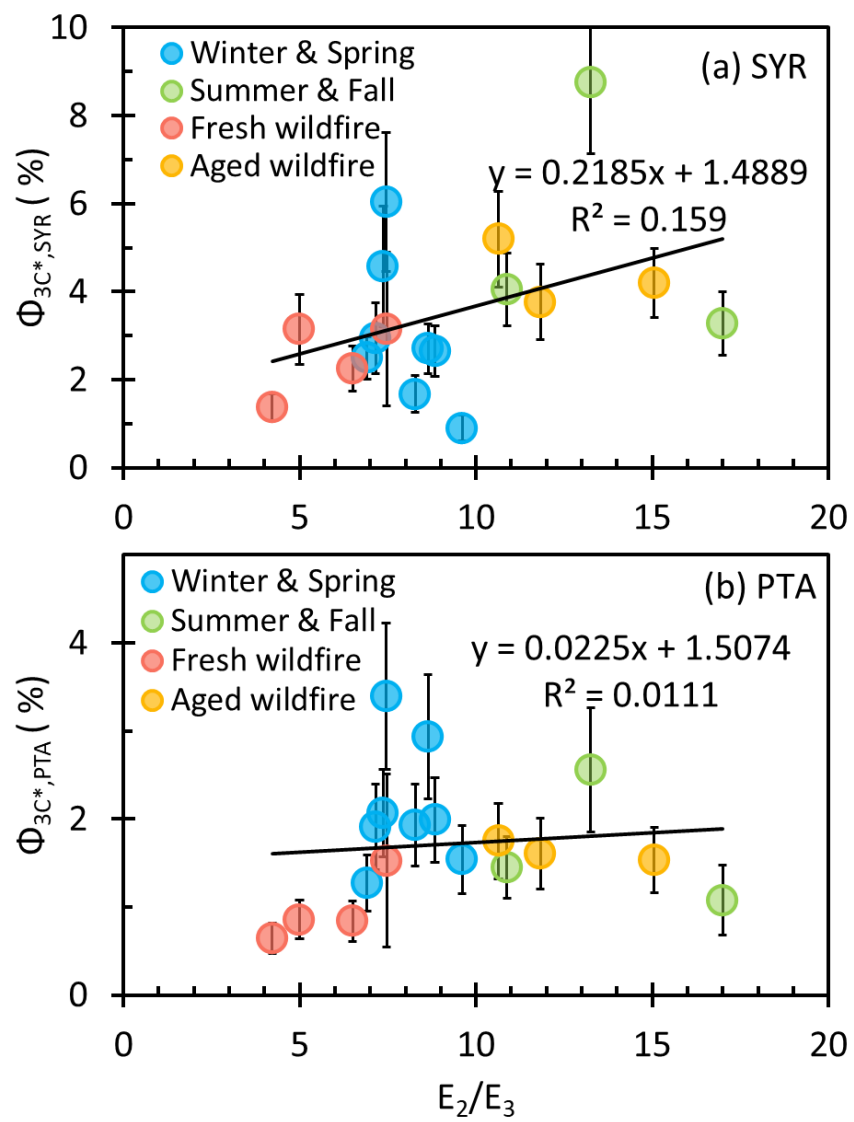


**Figure S5.25.** Apparent quantum yields of  $^3\text{C}^*$  determined by (a) SYR and (b) PTA as a function of  $E_2/E_3$ .

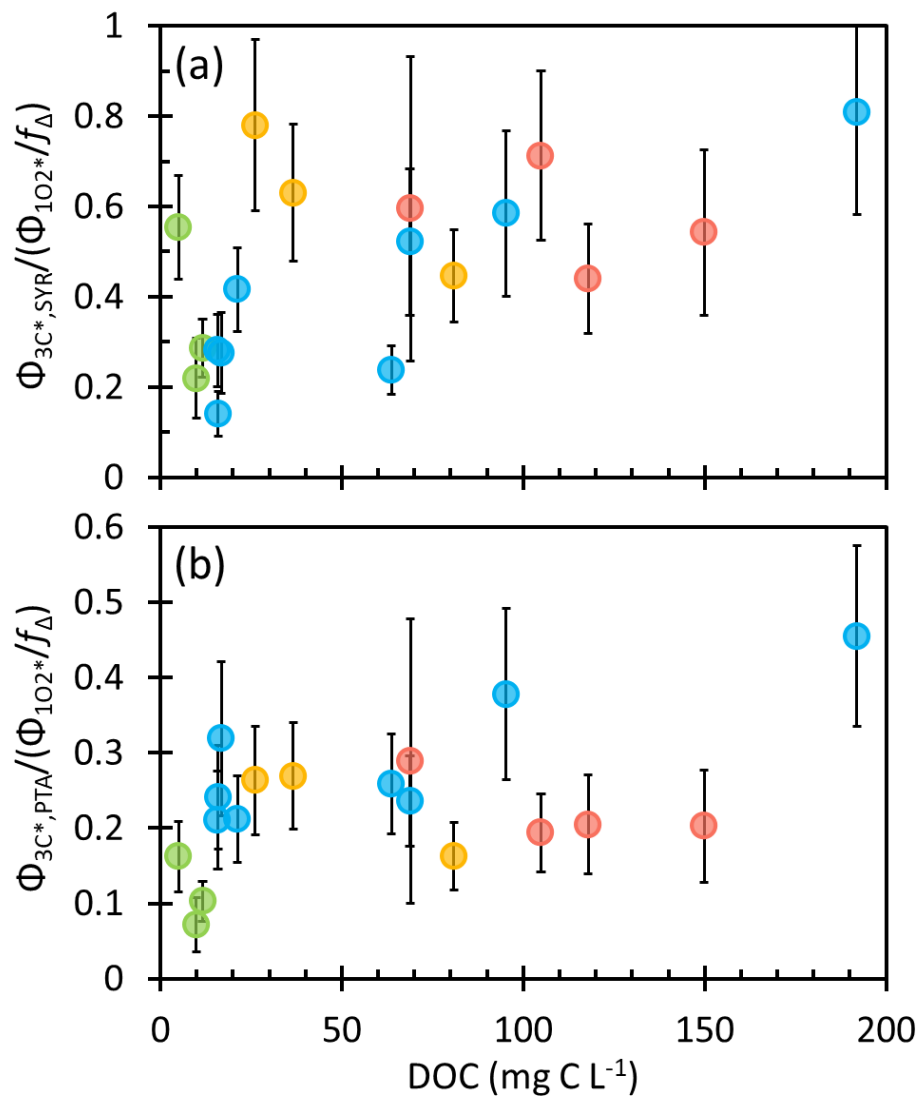


**Figure S5.26.** Approximate fraction of the total triplet pool (i.e., those that can generate singlet oxygen) that can oxidize (a) SYR and (b) PTA as function of DOC. Based on the averages ( $\pm 1 \sigma$ ) for these two plots ( $0.47 (\pm 0.20)$  and  $0.24 (\pm 0.09)$  for (a) and (b), respectively), approximately 24 % of the total triplets are strongly oxidizing (determined as the PTA average fraction) and roughly 23 % of the triplets are weakly oxidizing (determined as the SYR average fraction minus the PTA average).

#### **Section S5.4.** Extrapolating photooxidant concentrations in PME to aerosol liquid water (ALW) conditions

Photooxidant concentrations that we measured in PM extracts represent dilute conditions like cloud/fog water, while our goal is to estimate photooxidant concentrations in aerosol liquid water, which is orders of magnitude more concentrated. To predict photooxidant concentrations in ALW, we quantified photooxidant kinetics (i.e., formation rates and loss rates) for each sample type as a function of particle mass concentration and then extrapolate to ALW conditions (Kaur et al., 2019; Ma et al., 2022a).

We start by considering hydroxyl radical. Based on results from the three samples that have been studied (Kaur et al., 2019; Ma et al., 2022a), there are at least two ways that the kinetics for  $\bullet\text{OH}$  production vary as a function of extract concentration. In the two winter samples studied, the  $\bullet\text{OH}$  concentration is independent of DOC concentration (a proxy for extract concentration), which we interpret to mean that both the production rate ( $P_{\text{OH}}$ ) and  $\bullet\text{OH}$  sink ( $k'_{\text{OH}}$ ) linearly increase with DOC (Kaur et al., 2019; Ma et al., 2022a). However, in the third sample, which was collected in the summer and heavily influenced by relatively fresh biomass burning emissions, the  $\bullet\text{OH}$  concentration increases with DOC, which suggests that the major  $\bullet\text{OH}$  production pathway is a bimolecular reaction whose rate increases as the square of extract concentration (Ma et al., 2022a).

In our current work, we do not observe significant differences in the relationships of  $[\bullet\text{OH}]$  and DOC among the four sample types. Therefore, to predict  $[\bullet\text{OH}]$  in ALW for our current samples, we use the average  $P_{\text{OH}}$  and  $k'_{\text{OH}}$  values of the winter and summer samples at a given PM mass/water mass ratio in Ma et al. (2022) and do not consider the small differences among sample types. Figure S5.28 shows the average  $[\bullet\text{OH}]$  calculated with  $\bullet\text{OH}$  production only from aqueous reactions (Fig. S5.28a) and considering both aqueous reactions and gas-phase mass transport (Fig. S5.28b). Figure S5.28a shows that the average  $\bullet\text{OH}$  prediction fits well with the measured  $[\bullet\text{OH}]$  in more concentrated PME, but overestimates  $[\bullet\text{OH}]$  in PME with low particle mass/water mass ratio, i.e., in more dilute extracts. Including gas-phase mass transport of

$\bullet\text{OH}$  (Fig. S28b) increases the predicted  $[\bullet\text{OH}]$ , most notably at low particle mass/water ratios where  $\bullet\text{OH}$  transport from the gas phase is the dominant source of aqueous  $\bullet\text{OH}$ .

To extrapolate  ${}^3\text{C}^*$  concentrations determined by SYR, we first fitted measured  $P_{3\text{C}^*,\text{SYR}}$  versus DOC for each sample type to obtain the slope ( $\Delta P_{3\text{C}^*,\text{SYR}}/\Delta\text{DOC}$ ) (Fig. S29b), whose values are shown in Table S5.10. We then use these slopes to calculate  $P_{3\text{C}^*,\text{SYR}}$  in ambient PM conditions with the estimated DOC concentration in ALW, which is calculated as the product of the average ratio of DOC to PM mass/water mass ratio for each sample type (Table S5.10) and particle mass concentration. We estimate the pseudo-first order rate constant for the organic sink of  ${}^3\text{C}^*$  using the product of  $[\text{DOC}]$  and the second-order rate constant of DOC reacting with and quenching  ${}^3\text{C}^*$  determined by SYR ( $k_{\text{rxn}+\text{Q},3\text{C}^*,\text{SYR}}$ ). For the Win-Spr sample we use  $k_{\text{rxn}+\text{Q},3\text{C}^*,\text{SYR}}$  obtained from the Davis winter particle extracts (WIN) in our previous work, while for FBB and ABB samples, we use the rate constant from the summer wildfire sample (SUM) (Ma et al., 2022a). For the Sum-Fall samples, we use a rate constant obtained from fitting all samples (Fig. S23b). The rate constants used are also shown in Table S5.10.  ${}^3\text{C}^*$  concentrations are then calculated with:

$$[{}^3\text{C}^*] = \frac{P_{3\text{C}^*}}{k'_{3\text{C}^*}} = \frac{\Delta P_{3\text{C}^*}/\Delta\text{DOC} \times [\text{DOC}]}{k_{3\text{C}^*+\text{O}_2}[\text{O}_2] + k_{\text{rxn}+\text{Q},3\text{C}^*}[\text{DOC}]} \quad (\text{S5.5})$$

where  $k_{3\text{C}^*+\text{O}_2}$  is the second-order rate constant of  ${}^3\text{C}^*$  reacting with dissolved oxygen and  $[\text{O}_2]$  is the dissolved oxygen concentration. The DOC values in ambient PM condition are converted to particle mass/water mass ratio using the average ratio between DOC and PM mass to water mass ratio ( $\text{DOC}/(\text{PM}/\text{H}_2\text{O})$ ) for each sample type (Table S5.10). We predict  $[{}^3\text{C}^*]_{\text{PTA}}$  in ALW using the same method but different values for the triplet production rate ( $\Delta P_{3\text{C}^*,\text{PTA}}/\Delta\text{DOC}$ ) and triplet sink ( $k_{\text{rxn}+\text{Q},3\text{C}^*}$ ) (Table S5.10). Predictions for the SYR- and PTA-determined triplet concentrations as a function of PM mass/water mass ratio are in Figure S5.30.



The method we use to extrapolate  $^1\text{O}_2^*$  to ALW conditions is similar to what we do for  $^3\text{C}^*$ . First, we fit  $P_{1\text{O}_2^*}$  against DOC for each sample type to obtain the slopes ( $\Delta P_{1\text{O}_2^*}/\Delta\text{DOC}$ ) (Fig. S29a and Table S5.10). Next, we need to consider that since  $^3\text{C}^*$  is the precursor of  $^1\text{O}_2^*$ , the triplet concentration will affect production of  $^1\text{O}_2^*$ . Therefore, in addition to acting as a source of singlet oxygen, DOC also affects  $^1\text{O}_2^*$  in two other ways: (1) DOC is a direct sink for  $^1\text{O}_2^*$  and (2) DOC suppresses  $^1\text{O}_2^*$  production by quenching  $^3\text{C}^*$ . To quantify the first of these effects, we use an estimated average rate constant of DOC reacting with  $^1\text{O}_2^*$  ( $k_{1\text{O}_2^*+\text{DOC}}$ ) from previous work (Kaur et al., 2019; Ma et al., 2022a); the value of this second-order rate constant is  $1.0 \times 10^5 \text{ (L (mol C)}^{-1} \text{ s}^{-1})$ , assuming independent of the sample type. We then take the product of this rate constant with the DOC concentration under ALW conditions to calculate the pseudo-first order rate constant  $k'_{1\text{O}_2^*,\text{DOC}}$ . For the second effect, we apply  $k_{3\text{C}^*+\text{DOC}}$  determined from  $^1\text{O}_2^*$  data in our previous work. Note that  $k_{3\text{C}^*+\text{DOC}}$  values determined from  $^1\text{O}_2^*$  are different from  $k_{3\text{C}^*+\text{DOC}}$  determined by SYR or PTA. The latter represents the impact of DOC on the oxidizing triplet pool, while the former represents the total triplet pool, i.e., triplets that can react with  $^1\text{O}_2^*$ . We then calculate  $[^1\text{O}_2^*]$  with (Ma et al., 2022a):

$$[^1\text{O}_2^*] = \frac{\frac{\Delta P_{1\text{O}_2^*}}{\Delta\text{DOC}} \times [\text{DOC}]}{1 + \frac{k_{3\text{C}^*+\text{DOC}}[\text{DOC}]}{k_{3\text{C}^*+\text{O}_2}[\text{O}_2]}} / (k'_{\text{H}_2\text{O}} + k_{1\text{O}_2^*+\text{DOC}}[\text{DOC}]) \quad (\text{S5.6})$$

where  $k'_{\text{H}_2\text{O}}$  is the first-order rate constant for loss of  $^1\text{O}_2^*$  in  $\text{H}_2\text{O}$  ( $2.2 \times 10^5 \text{ s}^{-1}$ ; (Bilski et al., 1997)). The concentrations of singlet oxygen as a function of DOC are then transformed to a function of PM mass/water mass ratio using the relationships between these independent variables (Table S5.10). Predictions for the singlet oxygen concentration as a function of PM mass/water mass ratio are shown in Figure S5.31.

**Table S5.10.** Parameters used to extrapolate photooxidant concentrations to ALW conditions

Parameters		Win-Spr	Sum-Fall	FBB	ABB
Average DOC/(PM/H <sub>2</sub> O) (mol C L <sup>-1</sup> )/(μg PM/μg H <sub>2</sub> O)		13.6	8.9	26.1	21.3
•OH	$\Delta k'_{\text{DOC}}/\Delta(\text{PM}/\text{H}_2\text{O})$ (s <sup>-1</sup> )/(μg PM/μg H <sub>2</sub> O)	6.2 × 10 <sup>9a</sup>			
<sup>1</sup> O <sub>2</sub> *	$\Delta P_{1\text{O}_2^*}/\Delta\text{DOC}$ (M s <sup>-1</sup> /(mol C L <sup>-1</sup> ))	6.6 × 10 <sup>-5</sup>	3.2 × 10 <sup>-5</sup>	7.1 × 10 <sup>-5</sup>	4.0 × 10 <sup>-5</sup>
	$k_{\text{rxn}+\text{Q},3\text{C}^*}$ (L (mol C) <sup>-1</sup> s <sup>-1</sup> )	0.47 × 10 <sup>7</sup> (WIN) <sup>b</sup>	1.2 × 10 <sup>7</sup> (All) <sup>c</sup>	2.1 × 10 <sup>7</sup> (SUM) <sup>b</sup>	
	$k_{\text{DOC}+1\text{O}_2^*}$ (L (mol C) <sup>-1</sup> s <sup>-1</sup> )	1.0 × 10 <sup>5a</sup>			
<sup>3</sup> C* <sub>SYR</sub>	$\Delta P_{3\text{C}^*}/\Delta\text{DOC}$ (M s <sup>-1</sup> /(mol C L <sup>-1</sup> ))	8.4 × 10 <sup>-5</sup>	1.8 × 10 <sup>-5</sup>	7.5 × 10 <sup>-5</sup>	3.8 × 10 <sup>-5</sup>
	$k_{\text{rxn}+\text{Q},3\text{C}^*}$ (L (mol C) <sup>-1</sup> s <sup>-1</sup> )	7.6 × 10 <sup>7</sup> (WIN) <sup>b</sup>	7.2 × 10 <sup>7</sup> (All) <sup>c</sup>	12 × 10 <sup>7</sup> (SUM) <sup>b</sup>	
<sup>3</sup> C* <sub>PTA</sub>	$\Delta P_{3\text{C}^*}/\Delta\text{DOC}$ (M s <sup>-1</sup> /(mol C L <sup>-1</sup> ))	4.9 × 10 <sup>-5</sup>	0.61 × 10 <sup>-5</sup>	2.8 × 10 <sup>-5</sup>	1.4 × 10 <sup>-5</sup>
	$k_{\text{rxn}+\text{Q},3\text{C}^*}$ (L (mol C) <sup>-1</sup> s <sup>-1</sup> )	5.7 × 10 <sup>7</sup> (WIN) <sup>b</sup>	7.4 × 10 <sup>7</sup> (All) <sup>c</sup>	6.6 × 10 <sup>7</sup> (SUM) <sup>b</sup>	

<sup>a</sup> Value is calculated as the average of slopes of  $k'_{\text{DOC}}$  with PM mass/water mass ratio in winter and summer samples from our previous work (Ma et al., 2022a).

<sup>b</sup> Values from our previous work (Ma et al., 2022a), using either the winter sample data (WIN) or the summer sample data (SUM).

<sup>c</sup> Values are calculated from the hyperbolic regressions shown in Figure S5.23, which use all samples from this work as well as the WIN and SUM samples from our previous work (Ma et al., 2022a).

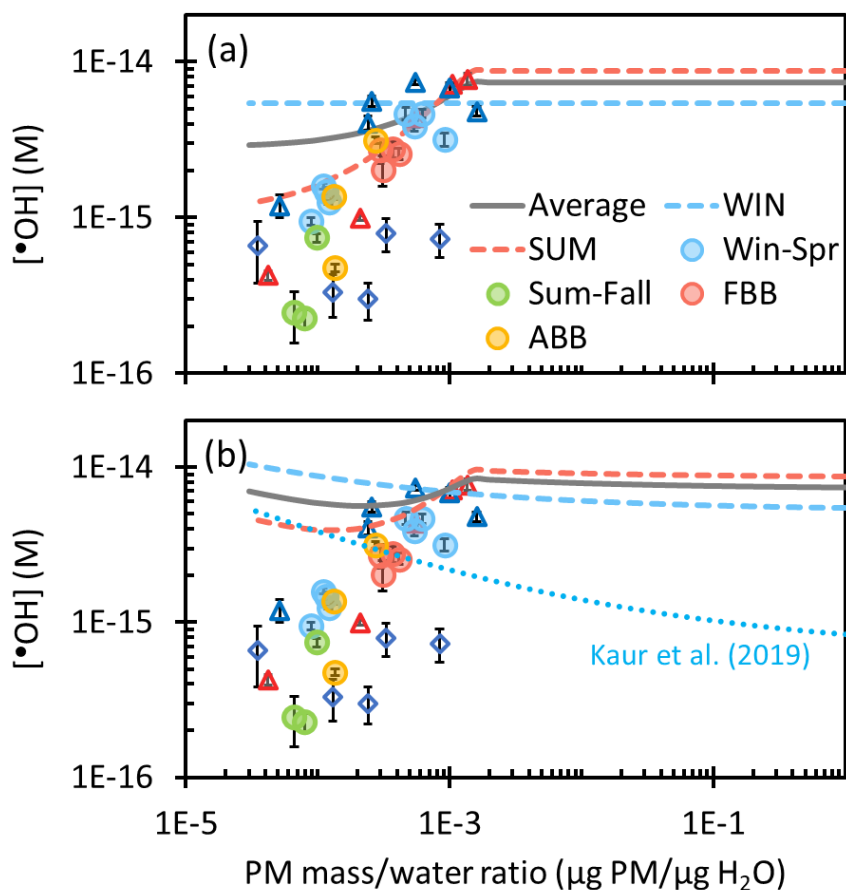


**Figure S5.27.** Dependence of  $\bullet\text{OH}$  concentration on particle mass/water mass ratio calculated with (a) only aqueous  $\bullet\text{OH}$  production and (b)  $\bullet\text{OH}$  from both aqueous reactions and mass transport from the gas phase (Kaur et al., 2019) using a gas-phase  $\bullet\text{OH}$  concentration of  $1 \times 10^6 \text{ mlc cm}^{-3}$ . Circles are measured values. Previous measurements and extrapolations by Ma et al. (2022) for Davis winter (WIN, blue) and summer wildfire (SUM, red) particle extracts are shown with triangles and dashed lines, while previous measurements and extrapolation by Kaur et al. (2019) for Davis winter particle extracts are shown with blue open diamonds and a dotted line. The grey line represents an extrapolation of the average WIN and SUM  $\bullet\text{OH}$  kinetics to ALW conditions; this is our recommended prediction for all of the seasonality samples studied in the current work.

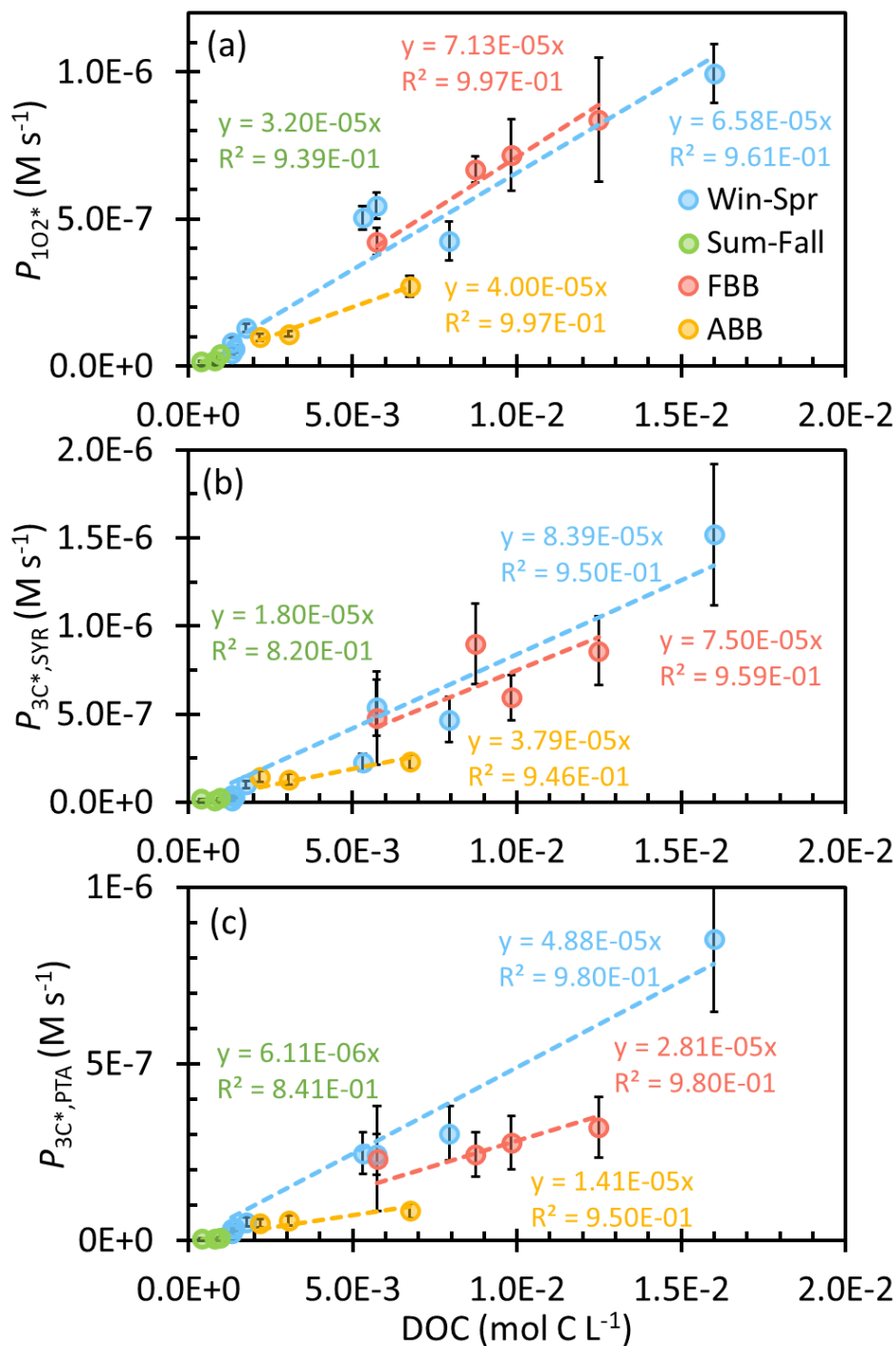


**Figure S5.28.** Production rates of (a) <sup>102</sup>O<sub>2</sub>\*, <sup>3</sup>C\* determined by (b) SYR and by (c) PTA as a function of DOC. Dashed lines represent linear regressions for each sample type.

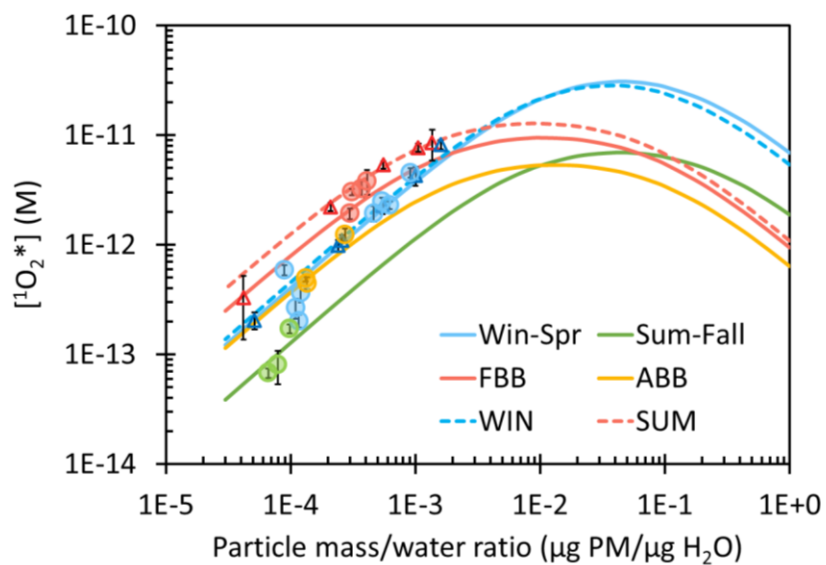


**Figure S5.29.** Dependence of  $^1\text{O}_2^*$  concentrations for each sample type on particle mass/water mass ratio. Circles are measured values, while lines are extrapolations to ALW conditions. Previous measurements and extrapolations by Ma et al. (2022) for Davis winter (WIN, blue) and summer wildfire (SUM, red) particle extracts are shown by triangles and dashed lines, while previous measurements and extrapolation by Kaur et al. (2019) for Davis winter particle extracts are shown with blue open diamonds and a dotted line.

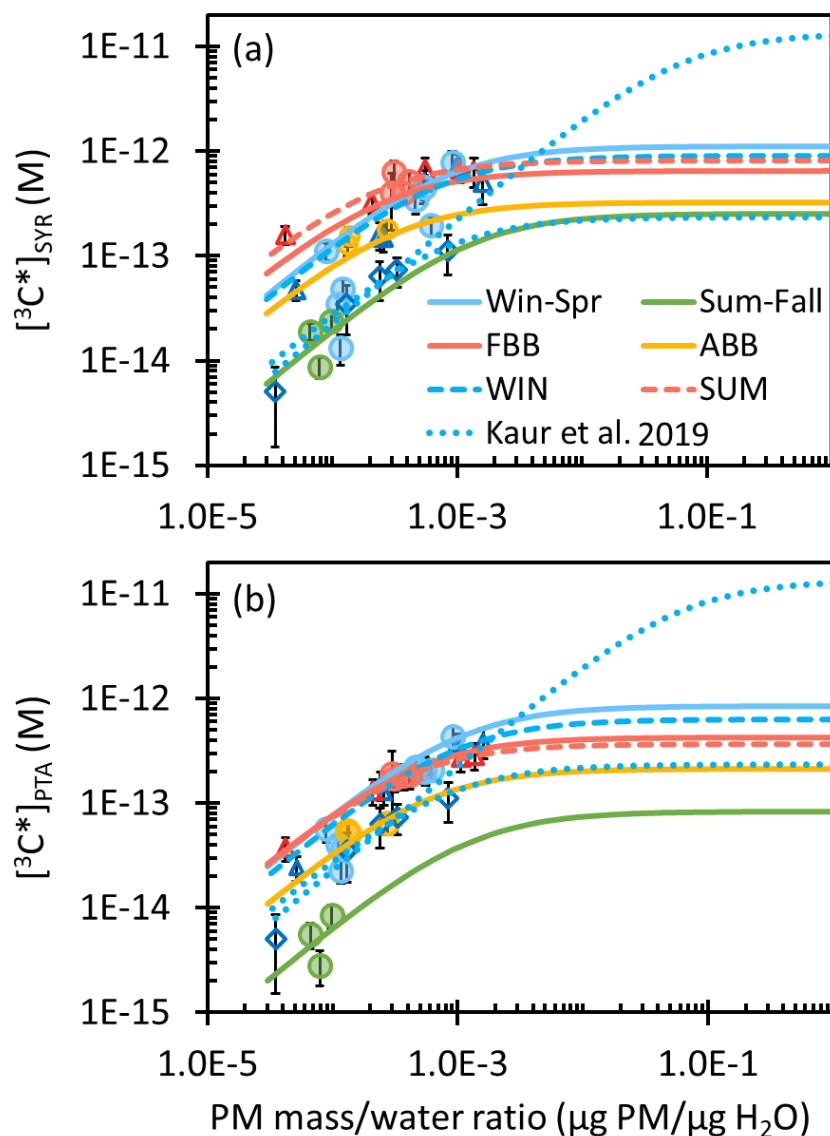


**Figure S5.30.** Dependence of  $^{3}\text{C}^*$  concentration for each sample type determined by (a) SYR and (b) PTA on particle mass/water mass ratio. Circles are measured values, while lines are extrapolations to ALW conditions based on equation S5.5. Previous measurements and extrapolations by Ma et al. (2022) for Davis winter (WIN, blue) and summer wildfire (SUM, red) particle extracts are shown by triangles and dashed lines, while previous measurements and extrapolation by Kaur et al. (2019) for Davis winter particle extracts are shown with blue open diamonds and dotted lines.

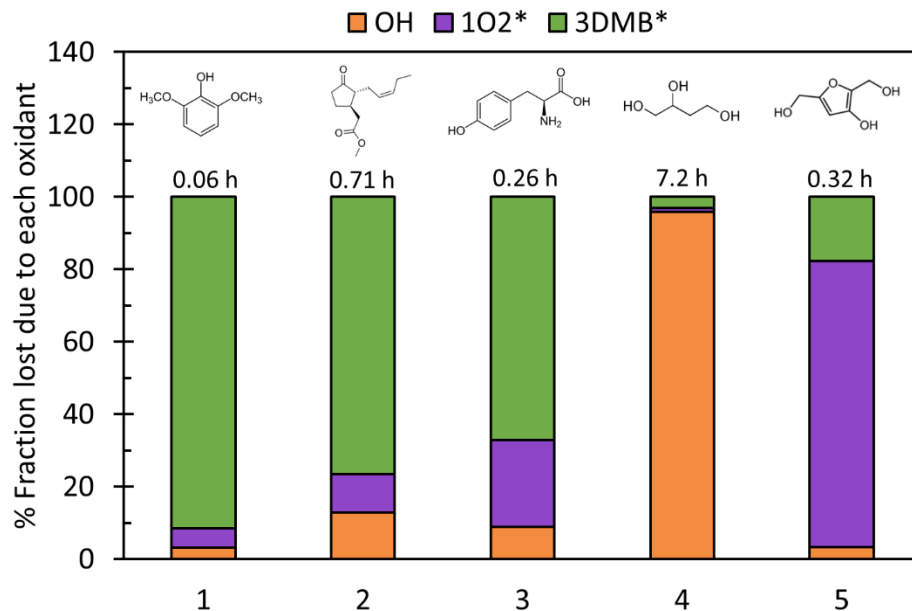


**Figure S5.31.** Calculated contributions of aqueous photooxidant to loss of five model organic compounds – (1) syringol, (2) methyl jasmonate, (3) tyrosine, (4) 1,2,4-butanetriol, and (5) 3-hydroxy-2,5-bis(hydroxymethyl)furan – in aerosol liquid water (1  $\mu\text{g PM}/\mu\text{g H}_2\text{O}$ ). The number on the top of each column is the overall lifetime in the aqueous phase. ALW photooxidant concentrations are predictions from the Win-Spr sample (Fig. 5.8), using the SYR-determined value for oxidizing triplets.

## 5.8. References

- Alfarra, M. R., Prevot, A. S. H., Szidat, S., Sandradewi, J., Weimer, S., Lanz, V. A., Schreiber, D., Mohr, M. and Baltensperger, U.: Identification of the Mass Spectral Signature of Organic Aerosols from Wood Burning Emissions, *Environ. Sci. Technol.*, 41(16), 5770–5777, doi:10.1021/es062289b, 2007.
- Anastasio, C. and McGregor, K. G.: Chemistry of fog waters in California's Central Valley: 1. In situ photoformation of hydroxyl radical and singlet molecular oxygen, *Atmos. Environ.*, 35(6), 1079–1089, doi:10.1016/S1352-2310(00)00281-8, 2001.
- Arakaki, T., Anastasio, C., Kuroki, Y., Nakajima, H., Okada, K., Kotani, Y., Handa, D., Azechi, S., Kimura, T., Tsuchi, A. and Miyagi, Y.: A general scavenging rate constant for reaction of hydroxyl radical with organic carbon in atmospheric waters., *Environ. Sci. Technol.*, 47(15), 8196–8203, doi:10.1021/es401927b, 2013.
- Ashton, L., Buxton, G. V. and Stuart, C. R.: Temperature dependence of the rate of reaction of OH with some aromatic compounds in aqueous solution. Evidence for the formation of a  $\pi$ -complex intermediate?, *J. Chem. Soc., Faraday Trans.*, 91(11), 1631–1633, doi:10.1039/FT9959101631, 1995.
- Baba, Y., Yatagai, T., Harada, T. and Kawase, Y.: Hydroxyl radical generation in the photo-Fenton process: Effects of carboxylic acids on iron redox cycling, *Chemical Engineering Journal*, 277, 229–241, doi:10.1016/j.cej.2015.04.103, 2015.
- Badali, K. M., Zhou, S., Aljawhary, D., Antiñolo, M., Chen, W. J., Lok, A., Mungall, E., Wong, J. P. S., Zhao, R. and Abbatt, J. P. D.: Formation of hydroxyl radicals from photolysis of secondary organic aerosol material, *Atmos. Chem. Phys.*, 15(14), 7831–7840, doi:10.5194/acp-15-7831-2015, 2015.
- Berg, S. M., Whiting, Q. T., Herrli, J. A., Winkels, R., Wammer, K. H. and Remucal, C. K.: The role of dissolved organic matter composition in determining photochemical reactivity at the molecular level., *Environ. Sci. Technol.*, 53(20), 11725–11734, doi:10.1021/acs.est.9b03007, 2019.
- Bilski, P., Holt, R. N. and Chignell, C. F.: Properties of singlet molecular oxygen in binary solvent mixtures of different polarity and proticity, *J. Photochem. Photobiol. A*, 109(3), 243–249, doi:10.1016/S1010-6030(97)00147-0, 1997.
- Budisulistiorini, S. H., Riva, M., Williams, M., Chen, J., Itoh, M., Surratt, J. D. and Kuwata, M.: Light-Absorbing Brown Carbon Aerosol Constituents from Combustion of Indonesian Peat and Biomass., *Environ. Sci. Technol.*, 51(8), 4415–4423, doi:10.1021/acs.est.7b00397, 2017.
- Canonica, S. and Laubscher, H.-U.: Inhibitory effect of dissolved organic matter on triplet-induced oxidation of aquatic contaminants, *Photochem. Photobiol. Sci.*, 7(5), 547, doi:10.1039/b719982a, 2008.
- Chen, Y., Hozalski, R. M., Olmanson, L. G., Page, B. P., Finlay, J. C., Brezonik, P. L. and Arnold, W. A.: Prediction of photochemically produced reactive intermediates in surface waters via satellite remote sensing., *Environ. Sci. Technol.*, 54(11), 6671–6681, doi:10.1021/acs.est.0c00344, 2020.
- Claeys, M., Vermeylen, R., Yasmeen, F., Gómez-González, Y., Chi, X., Maenhaut, W., Mészáros, T. and Salma, I.: Chemical characterisation of humic-like substances from urban, rural and tropical biomass



- burning environments using liquid chromatography with UV/vis photodiode array detection and electrospray ionisation mass spectrometry, *Environ. Chem.*, 9(3), 273, doi:10.1071/EN11163, 2012.
- Dorfman, L. M. and Adams, G. E.: Reactivity of the hydroxyl radical in aqueous solutions, 0 ed., National Bureau of Standards, Gaithersburg, MD., 1973.
- Du, Z., He, K., Cheng, Y., Duan, F., Ma, Y., Liu, J., Zhang, X., Zheng, M. and Weber, R.: A yearlong study of water-soluble organic carbon in Beijing II: Light absorption properties, *Atmos. Environ.*, 89, 235–241, doi:10.1016/j.atmosenv.2014.02.022, 2014.
- Ervens, B.: Progress and problems in modeling chemical processing in cloud droplets and wet aerosol particles, in *Multiphase environmental chemistry in the atmosphere*, vol. 1299, edited by S. W. Hunt, A. Laskin, and S. A. Nizkorodov, pp. 327–345, American Chemical Society, Washington, DC., 2018.
- Ervens, B., Sorooshian, A., Lim, Y. B. and Turpin, B. J.: Key parameters controlling OH-initiated formation of secondary organic aerosol in the aqueous phase (aqSOA), *J. Geophys. Res. Atmos.*, 119(7), 3997–4016, doi:10.1002/2013JD021021, 2014.
- Ervens, B., Turpin, B. J. and Weber, R. J.: Secondary organic aerosol formation in cloud droplets and aqueous particles (aqSOA): a review of laboratory, field and model studies, *Atmos. Chem. Phys.*, 11(21), 11069–11102, doi:10.5194/acp-11-11069-2011, 2011.
- Fan, X., Li, M., Cao, T., Cheng, C., Li, F., Xie, Y., Wei, S., Song, J. and Peng, P.: Optical properties and oxidative potential of water- and alkaline-soluble brown carbon in smoke particles emitted from laboratory simulated biomass burning, *Atmos. Environ.*, 194, 48–57, doi:10.1016/j.atmosenv.2018.09.025, 2018.
- Farley, R., Bernays, N., Jaffe, D. A., Ketcherside, D., Hu, L., Zhou, S., Collier, S. and Zhang, Q.: Persistent Influence of Wildfire Emissions in the Western United States and Characteristics of Aged Biomass Burning Organic Aerosols under Clean Air Conditions., *Environ. Sci. Technol.*, 56(6), 3645–3657, doi:10.1021/acs.est.1c07301, 2022.
- Faust, B. C. and Allen, J. M.: Aqueous-phase photochemical sources of peroxy radicals and singlet molecular oxygen in clouds and fog, *J. Geophys. Res.*, 97(D12), 12913, doi:10.1029/92JD00843, 1992.
- Finlayson-Pitts, B. J. and Jr, J. P.: *Chemistry of the upper and lower atmosphere: theory, experiments, and applications*, Elsevier., 1999.
- Fleming, L. T., Lin, P., Roberts, J. M., Selimovic, V., Yokelson, R., Laskin, J., Laskin, A. and Nizkorodov, S. A.: Molecular composition and photochemical lifetimes of brown carbon chromophores in biomass burning organic aerosol, *Atmos. Chem. Phys.*, 20(2), 1105–1129, doi:10.5194/acp-20-1105-2020, 2020.
- Galbavy, E. S., Ram, K. and Anastasio, C.: 2-Nitrobenzaldehyde as a chemical actinometer for solution and ice photochemistry, *J. Photochem. Photobiol. A*, 209(2-3), 186–192, doi:10.1016/j.jphotochem.2009.11.013, 2010.
- Gilardoni, S., Massoli, P., Paglione, M., Giulianelli, L., Carbone, C., Rinaldi, M., Decesari, S., Sandrini, S., Costabile, F., Gobbi, G. P., Pietrogrande, M. C., Visentin, M., Scotto, F., Fuzzi, S. and Facchini, M. C.:

- Direct observation of aqueous secondary organic aerosol from biomass-burning emissions., *Proc. Natl. Acad. Sci. USA*, 113(36), 10013–10018, doi:10.1073/pnas.1602212113, 2016.
- Gollnick, K. and Griesbeck, A.: ChemInform Abstract: Singlet Oxygen Photooxygenation of Furans. Isolation and Reactions of [4 + 2]-Cycloaddition Products (Unsaturated sec.-Ozonides), *Chemischer Informationsdienst*, 16(40), doi:10.1002/chin.198540196, 1985.
- Gonzalez, D. H., Cala, C. K., Peng, Q. and Paulson, S. E.: HULIS Enhancement of Hydroxyl Radical Formation from Fe(II): Kinetics of Fulvic Acid-Fe(II) Complexes in the Presence of Lung Antioxidants., *Environ. Sci. Technol.*, 51(13), 7676–7685, doi:10.1021/acs.est.7b01299, 2017.
- González Palacios, L., Corral Arroyo, P., Aregahegn, K. Z., Steimer, S. S., Bartels-Rausch, T., Nozière, B., George, C., Ammann, M. and Volkamer, R.: Heterogeneous photochemistry of imidazole-2-carboxaldehyde: HO<sub>2</sub> radical formation and aerosol growth, *Atmos. Chem. Phys.*, 16(18), 11823–11836, doi:10.5194/acp-16-11823-2016, 2016.
- He, C., Liu, J., Carlton, A. G., Fan, S., Horowitz, L. W., Levy II, H. and Tao, S.: Evaluation of factors controlling global secondary organic aerosol production from cloud processes, *Atmos. Chem. Phys.*, 13(4), 1913–1926, doi:10.5194/acp-13-1913-2013, 2013.
- Hecobian, A., Zhang, X., Zheng, M., Frank, N., Edgerton, E. S. and Weber, R. J.: Water-Soluble Organic Aerosol material and the light-absorption characteristics of aqueous extracts measured over the Southeastern United States, *Atmos. Chem. Phys.*, 10(13), 5965–5977, doi:10.5194/acp-10-5965-2010, 2010.
- Hems, R. F. and Abbatt, J. P. D.: Aqueous Phase Photo-oxidation of Brown Carbon Nitrophenols: Reaction Kinetics, Mechanism, and Evolution of Light Absorption, *ACS Earth Space Chem.*, 2(3), 225–234, doi:10.1021/acsearthspacechem.7b00123, 2018.
- Hems, R. F., Schnitzler, E. G., Liu-Kang, C., Cappa, C. D. and Abbatt, J. P. D.: Aging of atmospheric brown carbon aerosol, *ACS Earth Space Chem.*, doi:10.1021/acsearthspacechem.0c00346, 2021.
- Herrmann, H.: Kinetics of aqueous phase reactions relevant for atmospheric chemistry., *Chem. Rev.*, 103(12), 4691–4716, doi:10.1021/cr020658q, 2003.
- Herrmann, H., Hoffmann, D., Schaefer, T., Bräuer, P. and Tilgner, A.: Tropospheric aqueous-phase free-radical chemistry: radical sources, spectra, reaction kinetics and prediction tools., *ChemPhysChem*, 11(18), 3796–3822, doi:10.1002/cphc.201000533, 2010.
- Herrmann, H., Schaefer, T., Tilgner, A., Styler, S. A., Weller, C., Teich, M. and Otto, T.: Tropospheric aqueous-phase chemistry: kinetics, mechanisms, and its coupling to a changing gas phase., *Chem. Rev.*, 115(10), 4259–4334, doi:10.1021/cr500447k, 2015.
- Hess, M., Koepke, P. and Schult, I.: Optical properties of aerosols and clouds: the software package OPAC, *Bull. Amer. Meteor. Soc.*, 79(5), 831–844, doi:10.1175/1520-0477(1998)079<0831:OPOAAC>2.0.CO;2, 1998.
- Hettiyadura, A. P. S., Garcia, V., Li, C., West, C. P., Tomlin, J., He, Q., Rudich, Y. and Laskin, A.: Chemical Composition and Molecular-Specific Optical Properties of Atmospheric Brown Carbon

- Associated with Biomass Burning., *Environ. Sci. Technol.*, 55(4), 2511–2521, doi:10.1021/acs.est.0c05883, 2021.
- Jiang, W., Ma, L., Niedek, C., Anastasio, C. and Zhang, Q.: Chemical and light absorption properties of water-soluble organic aerosols in Northern California and insights into photooxidant production potentials of brown carbon components, In preparation, 2022.
- Kaur, R. and Anastasio, C.: Light absorption and the photoformation of hydroxyl radical and singlet oxygen in fog waters, *Atmos. Environ.*, 164, 387–397, doi:10.1016/j.atmosenv.2017.06.006, 2017.
- Kaur, R. and Anastasio, C.: First measurements of organic triplet excited states in atmospheric waters., *Environ. Sci. Technol.*, 52(9), 5218–5226, doi:10.1021/acs.est.7b06699, 2018.
- Kaur, R., Labins, J. R., Helbock, S. S., Jiang, W., Bein, K. J., Zhang, Q. and Anastasio, C.: Photooxidants from brown carbon and other chromophores in illuminated particle extracts, *Atmos. Chem. Phys.*, 19(9), 6579–6594, doi:10.5194/acp-19-6579-2019, 2019.
- Laskin, A., Laskin, J. and Nizkorodov, S. A.: Chemistry of atmospheric brown carbon., *Chem. Rev.*, 115(10), 4335–4382, doi:10.1021/cr5006167, 2015.
- Leresche, F., McKay, G., Kurtz, T., von Gunten, U., Canonica, S. and Rosario-Ortiz, F. L.: Effects of ozone on the photochemical and photophysical properties of dissolved organic matter., *Environ. Sci. Technol.*, 53(10), 5622–5632, doi:10.1021/acs.est.8b06410, 2019.
- Leresche, F., Salazar, J. R., Pfothenauer, D. J., Hannigan, M. P., Majestic, B. J. and Rosario-Ortiz, F. L.: Photochemical aging of atmospheric particulate matter in the aqueous phase., *Environ. Sci. Technol.*, 55(19), 13152–13163, doi:10.1021/acs.est.1c00978, 2021.
- Li, M., Bao, F., Zhang, Y., Sheng, H., Chen, C. and Zhao, J.: Photochemical aging of soot in the aqueous phase: release of dissolved black carbon and the formation of  $1O_2$ ., *Environ. Sci. Technol.*, 53(21), 12311–12319, doi:10.1021/acs.est.9b02773, 2019.
- Lim, Y. B., Tan, Y., Perri, M. J., Seitzinger, S. P. and Turpin, B. J.: Aqueous chemistry and its role in secondary organic aerosol (SOA) formation, *Atmospheric Chemistry & Physics Discussions*, 10(6), 2010.
- Lin, P., Aiona, P. K., Li, Y., Shiraiwa, M., Laskin, J., Nizkorodov, S. A. and Laskin, A.: Molecular characterization of brown carbon in biomass burning aerosol particles., *Environ. Sci. Technol.*, 50(21), 11815–11824, doi:10.1021/acs.est.6b03024, 2016.
- Lin, P., Bluvshstein, N., Rudich, Y., Nizkorodov, S. A., Laskin, J. and Laskin, A.: Molecular Chemistry of Atmospheric Brown Carbon Inferred from a Nationwide Biomass Burning Event., *Environ. Sci. Technol.*, 51(20), 11561–11570, doi:10.1021/acs.est.7b02276, 2017.
- Liu, J., Bergin, M., Guo, H., King, L., Kotra, N., Edgerton, E. and Weber, R. J.: Size-resolved measurements of brown carbon in water and methanol extracts and estimates of their contribution to ambient fine-particle light absorption, *Atmos. Chem. Phys.*, 13(24), 12389–12404, doi:10.5194/acp-13-12389-2013, 2013.

- Ma, L., Guzman, C., Niedek, C., Tran, T., Zhang, Q. and Anastasio, C.: Kinetics and Mass Yields of Aqueous Secondary Organic Aerosol from Highly Substituted Phenols Reacting with a Triplet Excited State., *Environ. Sci. Technol.*, 55(9), 5772–5781, doi:10.1021/acs.est.1c00575, 2021.
- Ma, L., Worland, R., Jiang, W., Niedek, C., Guzman, C., Bein, K. J., Zhang, Q. and Anastasio, C.: Predicting photooxidant concentrations in aerosol liquid water based on laboratory extracts of ambient particles , In preparation, 2022a.
- Ma, L., Worland, R., Tran, T., Jiang, W., Niedek, C., Zhang, Q. and Anastasio, C.: An evaluation of probes to measure oxidizing triplet excited states in aerosol liquid water, In preparation, 2022b.
- Maizel, A. C. and Remucal, C. K.: The effect of probe choice and solution conditions on the apparent photoreactivity of dissolved organic matter., *Environ. Sci. Process. Impacts*, 19(8), 1040–1050, doi:10.1039/c7em00235a, 2017.
- Manfrin, A., Nizkorodov, S. A., Malecha, K. T., Getzinger, G. J., McNeill, K. and Borduas-Dedekind, N.: Reactive Oxygen Species Production from Secondary Organic Aerosols: The Importance of Singlet Oxygen., *Environ. Sci. Technol.*, 53(15), 8553–8562, doi:10.1021/acs.est.9b01609, 2019.
- McCabe, A. J. and Arnold, W. A.: Seasonal and spatial variabilities in the water chemistry of prairie pothole wetlands influence the photoproduction of reactive intermediates., *Chemosphere*, 155, 640–647, doi:10.1016/j.chemosphere.2016.04.078, 2016.
- McCabe, A. J. and Arnold, W. A.: Reactivity of Triplet Excited States of Dissolved Natural Organic Matter in Stormflow from Mixed-Use Watersheds., *Environ. Sci. Technol.*, 51(17), 9718–9728, doi:10.1021/acs.est.7b01914, 2017.
- McCabe, A. J. and Arnold, W. A.: Multiple linear regression models to predict the formation efficiency of triplet excited states of dissolved organic matter in temperate wetlands, *Limnol. Oceanogr.*, 63(5), 1992–2014, doi:10.1002/lno.10820, 2018.
- McGregor, K. G. and Anastasio, C.: Chemistry of fog waters in California’s Central Valley: 2. Photochemical transformations of amino acids and alkyl amines, *Atmos. Environ.*, 35(6), 1091–1104, doi:10.1016/S1352-2310(00)00282-X, 2001.
- Mckay, G., Huang, W., Romera-Castillo, C., Crouch, J. E., Rosario-Ortiz, F. L. and Jaffé, R.: Predicting Reactive Intermediate Quantum Yields from Dissolved Organic Matter Photolysis Using Optical Properties and Antioxidant Capacity., *Environ. Sci. Technol.*, 51(10), 5404–5413, doi:10.1021/acs.est.6b06372, 2017.
- McNeill, K. and Canonica, S.: Triplet state dissolved organic matter in aquatic photochemistry: reaction mechanisms, substrate scope, and photophysical properties., *Environ. Sci. Process. Impacts*, 18(11), 1381–1399, doi:10.1039/c6em00408c, 2016.
- McNeill, V. F.: Aqueous organic chemistry in the atmosphere: sources and chemical processing of organic aerosols., *Environ. Sci. Technol.*, 49(3), 1237–1244, doi:10.1021/es5043707, 2015.

- Monge, M. E., Rosenørn, T., Favez, O., Müller, M., Adler, G., Abo Riziq, A., Rudich, Y., Herrmann, H., George, C. and D'Anna, B.: Alternative pathway for atmospheric particles growth., *Proc. Natl. Acad. Sci. USA*, 109(18), 6840–6844, doi:10.1073/pnas.1120593109, 2012.
- Nguyen, T. K. V., Zhang, Q., Jimenez, J. L., Pike, M. and Carlton, A. G.: Liquid water: ubiquitous contributor to aerosol mass, *Environ. Sci. Technol. Lett.*, 3(7), 257–263, doi:10.1021/acs.estlett.6b00167, 2016.
- Ossola, R., Jönsson, O. M., Moor, K. and McNeill, K.: Singlet oxygen quantum yields in environmental waters., *Chem. Rev.*, 121(7), 4100–4146, doi:10.1021/acs.chemrev.0c00781, 2021.
- Park, S. S. and Yu, J.: Chemical and light absorption properties of humic-like substances from biomass burning emissions under controlled combustion experiments, *Atmos. Environ.*, 136, 114–122, doi:10.1016/j.atmosenv.2016.04.022, 2016.
- Parworth, C. L., Young, D. E., Kim, H., Zhang, X., Cappa, C. D., Collier, S. and Zhang, Q.: Wintertime water-soluble aerosol composition and particle water content in Fresno, California, *J. Geophys. Res. Atmos.*, 122(5), 3155–3170, doi:10.1002/2016JD026173, 2017.
- Paulson, S. E., Gallimore, P. J., Kuang, X. M., Chen, J. R., Kalberer, M. and Gonzalez, D. H.: A light-driven burst of hydroxyl radicals dominates oxidation chemistry in newly activated cloud droplets., *Sci. Adv.*, 5(5), eaav7689, doi:10.1126/sciadv.aav7689, 2019.
- Richards-Henderson, N. K., Pham, A. T., Kirk, B. B. and Anastasio, C.: Secondary organic aerosol from aqueous reactions of green leaf volatiles with organic triplet excited states and singlet molecular oxygen., *Environ. Sci. Technol.*, 49(1), 268–276, doi:10.1021/es503656m, 2015.
- Rolph, G., Stein, A. and Stunder, B.: Real-time Environmental Applications and Display sYstem: READY, *Environ. Model. Softw.*, 95, 210–228, doi:10.1016/j.envsoft.2017.06.025, 2017.
- Ross, F. and Ross, A. B.: Selected specific rates of reactions of transients from water in aqueous solution. III. Hydroxyl radical and perhydroxyl radical and their radical ions, *Historical Energy Database (United States)*, 1977.
- Rossignol, S., Aregahegn, K. Z., Tinel, L., Fine, L., Nozière, B. and George, C.: Glyoxal induced atmospheric photosensitized chemistry leading to organic aerosol growth., *Environ. Sci. Technol.*, 48(6), 3218–3227, doi:10.1021/es405581g, 2014.
- Schauer, J. J., Kleeman, M. J., Cass, G. R. and Simoneit, B. R.: Measurement of emissions from air pollution sources. 3. C1-C29 organic compounds from fireplace combustion of wood., *Environ. Sci. Technol.*, 35(9), 1716–1728, doi:10.1021/es001331e, 2001.
- Seinfeld, J. H. and Pandis, S. N.: *Atmospheric Chemistry And Physics: From Air Pollution To Climate Change*, 3rd ed., Wiley, Hoboken, New Jersey., 2016.
- Sharpless, C. M., Aeschbacher, M., Page, S. E., Wenk, J., Sander, M. and McNeill, K.: Photooxidation-induced changes in optical, electrochemical, and photochemical properties of humic substances., *Environ. Sci. Technol.*, 48(5), 2688–2696, doi:10.1021/es403925g, 2014.

- Silva, P. J., Liu, D.-Y., Noble, C. A. and Prather, K. A.: Size and Chemical Characterization of Individual Particles Resulting from Biomass Burning of Local Southern California Species, *Environ. Sci. Technol.*, 33(18), 3068–3076, doi:10.1021/es980544p, 1999.
- Smith, J. D., Kinney, H. and Anastasio, C.: Aqueous benzene-diols react with an organic triplet excited state and hydroxyl radical to form secondary organic aerosol., *Phys. Chem. Chem. Phys.*, 17(15), 10227–10237, doi:10.1039/c4cp06095d, 2015.
- Smith, J. D., Sio, V., Yu, L., Zhang, Q. and Anastasio, C.: Secondary organic aerosol production from aqueous reactions of atmospheric phenols with an organic triplet excited state., *Environ. Sci. Technol.*, 48(2), 1049–1057, doi:10.1021/es4045715, 2014.
- Stein, A. F., Draxler, R. R., Rolph, G. D., Stunder, B. J. B., Cohen, M. D. and Ngan, F.: Noaa's HYSPLIT atmospheric transport and dispersion modeling system, *Bull. Amer. Meteor. Soc.*, 96(12), 2059–2077, doi:10.1175/BAMS-D-14-00110.1, 2015.
- Tilgner, A. and Herrmann, H.: Tropospheric Aqueous-Phase OH Oxidation Chemistry: Current Understanding, Uptake of Highly Oxidized Organics and Its Effects, in *Multiphase environmental chemistry in the atmosphere*, vol. 1299, edited by S. W. Hunt, A. Laskin, and S. A. Nizkorodov, pp. 49–85, American Chemical Society, Washington, DC., 2018.
- Tong, H., Arangio, A. M., Lakey, P. S. J., Berkemeier, T., Liu, F., Kampf, C. J., Brune, W. H., Pöschl, U. and Shiraiwa, M.: Hydroxyl radicals from secondary organic aerosol decomposition in water, *Atmos. Chem. Phys.*, 16(3), 1761–1771, doi:10.5194/acp-16-1761-2016, 2016.
- Tratnyek, P. G. and Hoigne, J.: Oxidation of substituted phenols in the environment: a QSAR analysis of rate constants for reaction with singlet oxygen, *Environ. Sci. Technol.*, 25(9), 1596–1604, 1991.
- U.S. Geological Survey: Dissolved oxygen: U.S. Geological Survey Techniques and Methods, book 9, chap. A6.2, 33 p., <https://doi.org/10.3133/tm9A6.2>, 2020.
- Verma, V., Fang, T., Xu, L., Peltier, R. E., Russell, A. G., Ng, N. L. and Weber, R. J.: Organic aerosols associated with the generation of reactive oxygen species (ROS) by water-soluble PM<sub>2.5</sub>., *Environ. Sci. Technol.*, 49(7), 4646–4656, doi:10.1021/es505577w, 2015.
- Vicente, A., Alves, C., Calvo, A. I., Fernandes, A. P., Nunes, T., Monteiro, C., Almeida, S. M. and Pio, C.: Emission factors and detailed chemical composition of smoke particles from the 2010 wildfire season, *Atmos. Environ.*, 71, 295–303, doi:10.1016/j.atmosenv.2013.01.062, 2013.
- Wander, R., Neta, P. and Dorfman, L. M.: Pulse radiolysis studies. XII. Kinetics and spectra of the cyclohexadienyl radicals in aqueous benzoic acid solution, *J. Phys. Chem.*, 72(8), 2946–2949, doi:10.1021/j100854a044, 1968.
- Wang, G., Zhang, R., Gomez, M. E., Yang, L., Levy Zamora, M., Hu, M., Lin, Y., Peng, J., Guo, S., Meng, J., Li, J., Cheng, C., Hu, T., Ren, Y., Wang, Y., Gao, J., Cao, J., An, Z., Zhou, W., Li, G., Wang, J., Tian, P., Marrero-Ortiz, W., Secretst, J., Du, Z., Zheng, J., Shang, D., Zeng, L., Shao, M., Wang, W., Huang, Y., Wang, Y., Zhu, Y., Li, Y., Hu, J., Pan, B., Cai, L., Cheng, Y., Ji, Y., Zhang, F., Rosenfeld, D., Liss, P. S., Duce, R. A., Kolb, C. E. and Molina, M. J.: Persistent sulfate formation from London Fog to Chinese haze., *Proc. Natl. Acad. Sci. USA*, 113(48), 13630–13635, doi:10.1073/pnas.1616540113, 2016.

- Wang, H., Zhou, H., Ma, J., Nie, J., Yan, S. and Song, W.: Triplet photochemistry of dissolved black carbon and its effects on the photochemical formation of reactive oxygen species., *Environ. Sci. Technol.*, 54(8), 4903–4911, doi:10.1021/acs.est.0c00061, 2020a.
- Wang, X., Gemayel, R., Hayeck, N., Perrier, S., Charbonnel, N., Xu, C., Chen, H., Zhu, C., Zhang, L., Wang, L., Nizkorodov, S. A., Wang, X., Wang, Z., Wang, T., Mellouki, A., Riva, M., Chen, J. and George, C.: Atmospheric photosensitization: A new pathway for sulfate formation., *Environ. Sci. Technol.*, 54(6), 3114–3120, doi:10.1021/acs.est.9b06347, 2020b.
- Wenk, J. and Canonica, S.: Phenolic Antioxidants Inhibit the Triplet-Induced Transformation of Anilines and Sulfonamide Antibiotics in Aqueous Solution, *Environ. Sci. Technol.*, 46(10), 5455–5462, doi:10.1021/es300485u, 2012.
- Wenk, J., Eustis, S. N., McNeill, K. and Canonica, S.: Quenching of excited triplet states by dissolved natural organic matter., *Environ. Sci. Technol.*, 47(22), 12802–12810, doi:10.1021/es402668h, 2013.
- Wenk, J., von Gunten, U. and Canonica, S.: Effect of dissolved organic matter on the transformation of contaminants induced by excited triplet states and the hydroxyl radical., *Environ. Sci. Technol.*, 45(4), 1334–1340, doi:10.1021/es102212t, 2011.
- Wilkinson, F., Helman, W. P. and Ross, A. B.: Rate constants for the decay and reactions of the lowest electronically excited singlet state of molecular oxygen in solution. an expanded and revised compilation, *J. Phys. Chem. Ref. Data*, 24(2), 663–677, doi:10.1063/1.555965, 1995.
- Wong, J. P. S., Nenes, A. and Weber, R. J.: Changes in light absorptivity of molecular weight separated brown carbon due to photolytic aging., *Environ. Sci. Technol.*, 51(15), 8414–8421, doi:10.1021/acs.est.7b01739, 2017.
- Wong, J. P. S., Tsagkaraki, M., Tsiodra, I., Mihalopoulos, N., Violaki, K., Kanakidou, M., Sciare, J., Nenes, A. and Weber, R. J.: Effects of atmospheric processing on the oxidative potential of biomass burning organic aerosols., *Environ. Sci. Technol.*, 53(12), 6747–6756, doi:10.1021/acs.est.9b01034, 2019.
- Yu, L., Smith, J., Laskin, A., Anastasio, C., Laskin, J. and Zhang, Q.: Chemical characterization of SOA formed from aqueous-phase reactions of phenols with the triplet excited state of carbonyl and hydroxyl radical, *Atmos. Chem. Phys.*, 14(24), 13801–13816, doi:10.5194/acp-14-13801-2014, 2014.
- Zeinali, N., Oluwoye, I., Altarawneh, M. K., Almatarneh, M. H. and Dlugogorski, B. Z.: Probing the Reactivity of Singlet Oxygen with Cyclic Monoterpenes., *ACS Omega*, 4(9), 14040–14048, doi:10.1021/acsomega.9b01825, 2019.
- Zeng, L., Dibb, J., Scheuer, E., Katich, J. M., Schwarz, J. P., Bourgeois, I., Peischl, J., Ryerson, T., Warneke, C., Perring, A. E., Diskin, G. S., DiGangi, J. P., Nowak, J. B., Moore, R. H., Wiggins, E. B., Pagonis, D., Guo, H., Campuzano-Jost, P., Jimenez, J. L., Xu, L. and Weber, R. J.: Characteristics and evolution of brown carbon in western United States wildfires, *Atmos. Chem. Phys.*, 22(12), 8009–8036, doi:10.5194/acp-22-8009-2022, 2022.
- Zhang, X., Lin, Y.-H., Surratt, J. D. and Weber, R. J.: Sources, Composition and Absorption Ångström Exponent of Light-absorbing Organic Components in Aerosol Extracts from the Los Angeles Basin, *Environ. Sci. Technol.*, 47(8), 3685–3693, doi:10.1021/es305047b, 2013.

Zhao, R., Lee, A. K. Y., Huang, L., Li, X., Yang, F. and Abbatt, J. P. D.: Photochemical processing of aqueous atmospheric brown carbon, *Atmos. Chem. Phys.*, 15(11), 6087–6100, doi:10.5194/acp-15-6087-2015, 2015.

Zuo, Y. and Hoigne, J.: Formation of hydrogen peroxide and depletion of oxalic acid in atmospheric water by photolysis of iron(III)-oxalato complexes, *Environ. Sci. Technol.*, 26(5), 1014–1022, doi:10.1021/es00029a022, 1992.



## Chapter 6: Conclusion

This work provides a more comprehensive understanding of photochemistry and photooxidants in concentrated aqueous particle extracts as well as in aerosol liquid water. We found that the reaction of triplet with highly-substituted phenols can be an important source of aqSOA in biomass-burning influenced ALW. We also optimized a method to measure triplet concentrations in concentrated particle extracts. In addition, we quantified light absorption, and measured the steady-state concentrations, formation, and loss kinetics of three important photooxidants – hydroxyl radical ( $\bullet\text{OH}$ ), oxidizing triplet excited of organic matter ( $^3\text{C}^*$ ), and singlet molecular oxygen ( $^1\text{O}_2^*$ ) - in aqueous particle extracts. This work not only provided more data for photooxidants in aqueous extracts of different particle types, but also improves predictions of photooxidant concentrations in aerosol liquid water (ALW). This will enable us to better understand the reactivity of particle water as well as the relative importance of the three photooxidants in ALW conditions.

In chapter 2, we measured rate constants and SOA mass yields of six highly-substituted phenols that are potentially important in biomass-burning influenced ALW reacting with an atmospheric model triplet (triplet excited state of 3,4-dimethoxybenzaldehyde,  $^3\text{DMB}^*$ ). With phenol rate constants determined in this and previous work, we developed a quantitative structure-activity relationship with one-electron oxidation potentials, allowing rate constants of other phenols to be predicted. High aqSOA mass yields, ranging from 60% to 100%, indicate efficient aqSOA formation. Calculations of SOA formation rates using our data along with previous predicted oxidant concentrations indicate that phenols with high  $K_H$  can be an important source of aqSOA in ALW, with  $^3\text{C}^*$  typically the dominant oxidant.

In chapter 3, after examining 12 triplet probe candidates, we found that (phenylthiol)acetic acid (PTA) seems well suited for ALW conditions, with mild inhibition and fast rate constants with triplets. However, one weakness of this probe is that it has a pH-dependent reactivity with triplets. Comparing the performance

of both PTA and syringol as triplet probes in aqueous extracts of particles, PTA is less sensitive to inhibition than SYR. However, SYR captures both weakly and strongly oxidizing triplets, while PTA only reacts appreciably with strongly oxidizing triplets. Since the inhibition effect can be quantified by measuring inhibition factors, we decided to use both PTA and SYR as triplet probes for  $^3\text{C}^*$  concentration measurements, and then use inhibition factors to  $^3\text{C}^*$  concentration correction. Therefore, the ratio of  $^3\text{C}^*$  concentrations determined by PTA and SYR can be regarded as the fraction of strongly oxidizing triplets to the total oxidizing triplets.

In chapter 4, our experiments on photooxidant measurements as a function of particle dilution using winter (WIN) and summer (SUM) biomass burning particles is an extension of a previous study of winter particles,<sup>31</sup> but with higher DOC levels and of the addition of summer particles. With increasing particle mass concentration, the  $\bullet\text{OH}$  concentration in SUM linearly increases while in WIN it is relatively unchanged. This suggests that unimolecular reactions such as direct photodegradation of chromophores appear to be the major  $\bullet\text{OH}$  source in WIN, while in SUM bimolecular reactions might dominate. In our work, with more concentrated extracts, we observed a more distinct behavior of the suppression of  $^3\text{C}^*$  by organic matter, which is more significant than we expected. For the first time, we observed the leveling-off of  $^1\text{O}_2^*$  with the increasing particle mass concentration, which is attributed to  $^3\text{C}^*$  concentration suppression at higher DOC. Extrapolating to ALW conditions, predicted  $\bullet\text{OH}$  concentrations are on the order of  $10^{-14}$  M, similar to those in fog/cloud waters. In contrast, predicted concentrations of  $^3\text{C}^*$  and  $^1\text{O}_2^*$  in ALW are approximately 10 - 100 times higher than in cloud/fogs, with values of  $(4 - 9) \times 10^{-13}$  M and  $(1 - 6) \times 10^{-12}$  M, respectively. Comparing to previous work,<sup>31</sup> our predicted  $\bullet\text{OH}$  value is approximately 10 times higher,  $^3\text{C}^*$  is around 5 times higher than the best fit line, but more than 10 times lower than their high estimate. Because we now take into account the impact of plateauing  $^3\text{C}^*$  concentrations on  $^1\text{O}_2^*$  production, our  $^1\text{O}_2^*$  concentrations are 10 – 100 times lower than the previously predicted value. Although  $\bullet\text{OH}$  is often considered the main sink for organic compounds in the aqueous phase, the much higher concentrations of

$^3\text{C}^*$  and  $^1\text{O}_2^*$  in aerosol liquid water suggest these photooxidants can be more important sinks for many organics in particle water.

In chapter 5, to study the seasonal variation of photooxidants, we measured photooxidant concentrations in aqueous extracts of four types of particles: winter samples influenced by residential wood combustion (Win-Spr), summer fresh (FBB) and aged (ABB) biomass burning samples, and summer/fall samples with no biomass burning (Sum-Fall). FBB has the highest mass absorption coefficient, but lowest quantum yields for all three photooxidants, while aged BB particles tend to have higher quantum yields. DOC appears to be a good parameter to estimate  $^1\text{O}_2^*$  and  $^3\text{C}^*$  concentrations, which exhibit good linearity with DOC, independent of sample type. Win-Spr samples show the highest fraction of strongly oxidizing  $^3\text{C}^*$  to total oxidizing  $^3\text{C}^*$ . The predicted  $\bullet\text{OH}$  concentration in ALW is around  $8 \times 10^{-15}$  M, while  $^1\text{O}_2^*$  and  $^3\text{C}^*$  concentrations have ranges of  $(0.6 - 7) \times 10^{-12}$  M and  $(0.08 - 1) \times 10^{-12}$  M, respectively, showing a broader range of concentrations comparing to results in chapter 4. Photooxidant concentrations in the Win-Spr and Sum-Fall particles increase by factors of (5-22) from average particle extracts to ALW, while the enhancements in FBB and ABB are smaller ( $< 5$ ). Based on our estimated concentrations, lifetimes of organic compounds in ALW can be significantly shortened compared to foggy/cloudy conditions due to enhanced photooxidant concentrations.  $^3\text{C}^*$  can be a dominant oxidant for the processing of organic compounds in aerosol liquid water due to its high concentrations, while  $\bullet\text{OH}$  is more important for less reactive organics. The importance of  $^1\text{O}_2^*$  is enhanced in aerosol liquid water relative to fog/cloud water and it is more important for furans and other compounds that are highly reactive with  $^1\text{O}_2^*$ .

Though we reduced the uncertainties inherent in predicting ALW photooxidants compared to the only previous study, because of experimental limitations our extrapolation is still over a very wide range (approximately a factor of 600). For future work, to better predict photooxidant concentrations in ALW, more measurements of oxidants are needed in more concentrated particle extracts to improve our estimates. To obtain more concentrated particle extracts, will require rotary evaporation or other techniques to remove

water but not change the characterization of extracts. Since high particle mass concentrations can lead to significant light screening, using containers that have very short pathlengths for illumination experiments are recommended. In addition, approaches such as chamber and flow tube studies are needed to measure photooxidants and their chemical impacts under conditions more similar to ambient aerosols. Moreover, since most of our samples were influenced by biomass burning, investigation on photooxidant concentration and formation in particles from different sources including biogenic and anthropogenic sources such as fossil fuel combustion will provide a better understanding of oxidant kinetics across the particle population. Lastly, we found there is significant amount of highly light-absorbing water-insoluble brown carbon in particles. Their photochemistry and the ability of photooxidant formation has rarely been assessed, which also requires more studies in the future.